Influence of oxygen partial pressure on defect concentrations and on oxygen diffusion in UO2+x

Elisabetta Pizzi

Elisabetta Pizzi. Influence of oxygen partial pressure on defect concentrations and on oxygen diffusion in UO2+x. Other. Ecole Centrale Paris, 2013. English. NNT : 2013ECAP0059 . tel-00969106

HAL Id: tel-00969106
https://theses.hal.science/tel-00969106v1

Submitted on 2 Apr 2014

ÉCOLE CENTRALE DES ARTS
ET MANUFACTURES
« ÉCOLE CENTRALE PARIS »

THÈSE

présentée par

Mlle Elisabetta PIZZI

pour l'obtention du

GRADE DE DOCTEUR

Spécialité : Science des Matériaux

Laboratoire d'accueil : Structures, Propriétés et Modélisation des Solides (SPMS)

SUJET :

INFLUENCE DE LA PRESSION PARTIELLE D'OXYGENE SUR LES CONCENTRATIONS EN DEFAUTS ET SUR LA DIFFUSION DE L'OXYGENE DANS L'UO_{2+x}

soutenue le 24 octobre 2013 devant un jury composé de :

M. David Siméone	Expert senior CEA, responsable du LRC CARMEN	**Directeur de thèse**
M. Fiqiri Hodaj	Professeur INP	**Rapporteur**
Mme. Marie-France Barthe	Co-directrice CEMTHI	**Rapporteur**
M. Claude Petot	Professeur émérite	**Examinateur**
M. Grant Henderson	Professor of Earth Science, University of Toronto	**Examinateur**
M. Philippe Garcia	Encadrant de thèse, CEA	**Examinateur**
M. Hichem Dammak	Professeur Ecole Centrale Paris	**Examinateur**

2013ECAP0059

"La pacatezza è la vera forza.
La dedizione è silenziosa.
L'impegno non fa rumore,
ma è il motore del mondo."

Rita Levi Montalcini

To my dear and lovely mum and

To my dad, the brightest star of the sky

Acknowledgments

The list of people I want to thank here is surely quite long; however I hope you have the desire to read these pages in order to know all the people who helped me to realize my PhD.

First of all, thanks to all the members of my jury.

Thank-you to Mr. Fiqiri Hodaj and Mrs. Marie France Barthe to have been examiners of my thesis; I consider your jugements on my work quite important.

Thank-you to Mr. David Simeone, my PhD thesis director, to have welcomed me in Saclay each time I needed to make my diffusion and conductivity experiments.

Thank-you to Mr. Philippe Garcia, my CEA direct supervisor, that helped me to pursue all the studies reported in this thesis. I really appreciated the passion you have for your work and your precision in analysing the scientific pertinence of each result I presented to you.

A special thanks to Mr. Claude Petot, who honoured me to have accepted to be in my jury. I thank you and your wife Georgette for your incredible support in all the experimental activity concerning electrical conductivity and oxygen diffusion studies. The entire reconstruction of the experimental devices dedicated to these experiences wouldn't be possible without your precious help. Thank-you to have trasmitted me not only your huge knowledge on oxide transport properties but also to have shared with me your passion for the world of research.

Thank-you to Mr. Grant Henderson to have accepted to partecipate to my jury. Thanks also to have given me and Philippe Martin the possibility to carry out the XAS experiences in the Canadian syncrothron CLS.

Thank-you also to Mr. Hichem Dammak to be in my jury and to partecipate to my thesis defense.

A special thank-you to Mrs. Virginie Basini and Mrs. Carole Valot, the two chiefs of LLCC lab in which I worked, for the constant support.

Thank-you to Philippe Martin, that shared with me the interesting Canadian experiences. I appreciated your big scientific competence in XAS field and

your fruitful advices concerning my professional life.

Thank-you to Ben Moulton, that shares with me sleepless nights of work at the CLS synchrotron to collect XAS data and thanks also to all the team of the SGM beam-line of CLS for their competence, professionalism and sympathy.

Thank-you to Gaëlle Carlot to have helped me in sample transport organization and to have given me advices in all my practical and theoretical works needed to pursue my thesis.

Thank-you to Hervé Palancher and Lionel Desgranges, that helped me in the adventure of creating and characterizing higher oxides phases.

Thank-you to Michel Freyss and Emerson Vathonne to have furnished to me the *ab-initio* estimates of UO_2 DOS, to compare with my experimental XAS spectra.

Thank you to Gwenaëlle Cortes, to have organized all the missions I needed to do in order to carry out my experiments all over in the world.

Thank-you to all the LLCC lab, that accepted me and shared the every-day life of my PhD experience and thanks to Guido Baldinozzi, Laurence Launeville, Dominique Gosset and Suzy Fraczkiewicz of the LRC CARMEN lab of Saclay too.

Thank-you to the SA3C lab and in particular to Roure Ingrid, Claudine Pozo, Bertrand Pasquet and Philippe Bienvenue to have helped me to acquire and analyse SIMS and confocal microscopy data.

Thank-you to the UO_2 lab, in particular to Catherine Tanguy and Joseph Sanchez, to have introduced me to the world of the cutting and polishing samples, to Hélène Roquette for XRD sample characterization and to Letitia Silvestre and Pierre Matheron to have helped me to carry out iodine diffusion annealings.

Thanks to all my nearest collegues with who I shared our PhD experiences: Tam, Gaëlle, Amélie, Axel, Richard, Emerson, Dario, Remy, Boris, Mathieu, Tobias and Francisco (even if he shared only a small piece of my experience).

Thank-you also to Yann, Fernando, Cyril and Julie, my Parisian collegues. They shared with me difficulties and good moments I passed in these three years.

Thank-you to the dance section of the AS CEA, to have shared with me the passion of dancing for these three years. I spent with you a lot of good moments.

Thank-you to my italian collegues that let me feel home also in French territory: Patrizio, Benedetta, Sofia, Giorgio, Daniele, Claudia, Francesco and Saverio. Among them, I care to say a special thanks to you, dear Patrizio and

Benedetta: you helped and encouraged me in many occasions (you even convinced me to use LateX to write my thesis!!!) and you did and continue to share with me your friendship. Without you, my French experience wold have been much more poor... You are real good friends and I'm really grateful to you.
Last but not least, a huge THANK-YOU to my family, that shared from Italy my experience. They stayed always with me, they encouraged me in difficult moments and gave me all the pratical and moral help I needed to continue this, sometimes difficult, PhD adventure. Thanks to my mum, always willing to listen to me and to give me the right advices, to smile to me and to support me. Thanks to my dad: you left me and my family in the middle of my French staying but I'm sure you follow me from heaven. I hope that you continue to be proud of me like when you were alive. And thanks to my sister: I know that you love me, despite you never tell me.

Contents

Introduction

It is the aim of this work to further our understanding of atomic transport phenomena and mechanisms in uranium dioxide, which is the most widely used nuclear fuel in water reactors. Thermally or radiation induced transport properties impact practically all engineering aspects of nuclear oxide fuels, whether at the manufacturing stage, during in-reactor operation, or under long-term repository conditions. Oxygen transport in particular has a direct effect upon fuel performance. For example, oxygen redistribution within a fuel pellet alone can lead to local microstructural changes that will affect fission product diffusion and the thermodynamic properties of the fuel itself. Atomic transport is controlled by point defects, and since many other fuel properties that govern fuel performance are influenced by point defects and more generally the material microstructure, it is of high significance to investigate their thermodynamic properties and migration mechanisms.

Conversely and following for instance the work of Dieckmann [64] in binary and ternary transition metal oxides, measuring atomic transport and electrical properties is a means of determining the characteristics of point or complex defects that are responsible for those properties. UO_2 is reputed to be an oxygen deficient/excess oxide because deviation from stoichiometry is mainly accommodated by anion defects. Incorporation into the lattice of electronegative oxygen atoms is structurally possible but is accommodated electrically by a change in the valence state of uranium atoms. This also enables the presence of substitutional impurities or doping agents, mainly cations. Electronic and oxygen defects enter into quasi-chemical equilibria as a consequence of which their concentrations are strongly related. As a result, in certain situations, it is the impurity content that determines the composition of the material, hence defect concentrations and atomic transport properties. In the sixties and seventies, many studies relating to oxygen self-diffusion in UO_2 and UO_{2+x} have been carried out, but none unequivocally identified the mechanism or activation energy for its migration [30, 50, 142]. The main reason for this uncertainty lies in part in the difficulties in measuring all the thermodynamic variables influencing oxygen diffusion (*i.e.* oxygen partial pressure, impurity content and temperature). In fact, only recently was it demonstrated that a strict control of these three thermodynamic variables enables oxygen diffusion mechanisms to be identified. However, this approach concerned only slightly off-stoichiometric UO_2 [68, 78].

In the past many studies have also been carried out in relation to fission product diffusion. Among the elements produced following the fission of a heavy atom, iodine is one the most crucial: it is volatile and can induce stress corrosion cracking [52] during strong pellet - zircalloy cladding interactions. Contrary some other fission products such as xenon or krypton, the trace diffusion of iodine can be studied through depth profiling of low dose ion implantations but only the apparent activation energy for trace diffusion in stoichiometric UO_2 [165] has been assessed. To our knowledge, there still lacks a systematic study which would enable the determination of iodine diffusion mechanisms in $UO_{2\pm x}$.

In this framework, this thesis aims to characterize the nature and properties of charged defects involved in oxygen and iodine diffusion in $UO_{2\pm x}$. To this end, we will mainly study oxygen self-diffusion under broader temperature and oxygen potential ranges than those studied in the past [68, 78]. The focus upon the UO_{2+x} (as opposed to other oxide phases) is due to the broad range of conditions over which it is stable and because of its technological significance. In parallel to determining transport properties as a function of oxygen content, we also aim to characterise the effect controlled oxidation has upon the electronic structure of our material. The methodology adopted involves annealing UO_2 specimens under controlled thermodynamic conditions of temperature and pO_2 (oxygen partial pressure) in order to stabilise defect populations in the samples. Oxygen diffusion is then studied in regard to self-diffusion by using the isotopic exchange method using ^{18}O as a tracer element. For chemical diffusion, the kinetics with which equilibrium in the samples is restored following a change in the oxygen partial pressure is monitored from electrical conductivity measurements. The analysis of atomic and electronic transport property dependencies upon temperature and oxygen partial pressure should enable us to shear light upon the nature of the defects involved in the oxygen or iodine diffusion process in $UO_{2\pm x}$.

The first chapter critically reviews literature results concerning the structure, electronic structure, atomic transport properties and electrical conductivity of UO_{2+x}. Emphasis is put upon the importance of charged defects in this material and how oxidation is accommodated both structurally and in terms of electronic structure. Chapter two describes the characterisation techniques we have implemented.

Chapter three is devoted to the development of a point defect model that simultaneously reproduces electrical conductivity and deviation from stoichiometry data [162, 151] previously published. This provides us with a means to estimate different electronic and anion defects as a function of temperature, oxygen partial pressure and impurity content. Defect formation energies are determined and compared to recently published first principles results.

Experimental results relating to electrical conductivity, oxygen self- and chemical diffusion for two sample sets: Cr-doped and undoped polycrystalline UO_2 samples, are reported in chapter four.

The fifth chapter is devoted to X-ray Absorption Spectroscopy at the oxygen K- and uranium N- edges of UO_{2+x} and higher oxide phases. This enables us to determine electronic structure modifications induced by sample annealing and is based on the study of reference phases UO_2, U_4O_9 and U_3O_7.

The sixth chapter critically analyses and reviews the experimental data obtained in Chapters 4 and 5 in the light of the model developed in Chapter 3 and of electronic structure calculations. Consistency of the results obtained is verified and reliability of the approach used to study UO_{2+x} is discussed.

A general conclusion summarizes the major results obtained and defines some outlook necessary to complete this work.

Work on iodine is consigned to an Appendix, as only a preliminary study of its diffusion properties could be carried out. The experimental characterization of its transport properties is limited to the evaluation of the iodine diffusion coefficient dependence upon oxygen partial pressure at the fixed temperature of 1500°C.

Chapter 1

Literature review

UO_2 has been so extensively studied over the years that it is virtually impossible to draw up a comprehensive review of all the properties we are concerned with in this work. Rather, in this chapter we will try to emphasize how structural, point defect and electronic properties of the material are related to each other and to macroscopic properties. In the first part of this chapter we review some aspects of our knowledge of uranium oxides in their various forms: how deviation from stoichiometry is accommodated, the phase transitions it undergoes and the electronic structure of UO_2.

We then go on to review how temperature or oxygen partial pressure dependences of defect concentrations may be described using models based on defect equilibria in combination with defect formation energies provided from first principle calculations.

Part three is devoted to our current knowledge of electrical and oxygen diffusion properties of UO_{2+x} as they constitute very sensitive tracers of bulk electronic and atomic defects.

1.1 Structure and electronic structure in the U-O system

1.1.1 Deviation from stoichiometry and phase diagram

1.1.1.1 A complex phase diagram

UO_2 crystallizes in a fluorite structure: its space group is $Fm\bar{3}m$ and its cell parameter is equal to 5.47 Å at room temperature; its structure is represented in Figure 1.1.

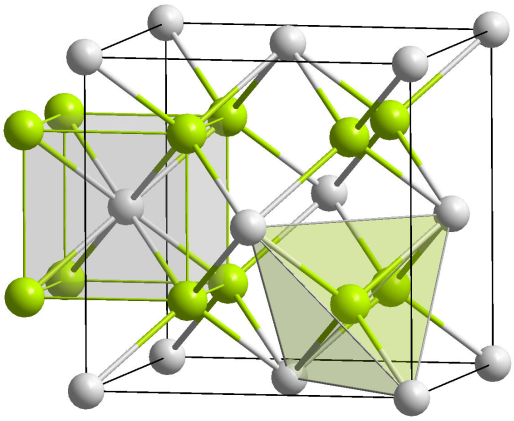

Figure 1.1: UO_2 fluorite structure; uranium atoms are represented in grey, oxygen atoms in green.

The uranium sublattice is of the Face Centred Cubic (FCC) type whereas the copenetrated anion sublattice has a simple cubic structure, with an O-O distance equal to half the cell parameter. A useful way of looking at this fluorite structure is to consider it as being made up of oxygen cubes, with every other cube containing a uranium atom in its centre. The centres of the empty oxygen cubes constitute the only interstitial site available. This site is usually referred to as octahedral site in relation to its position with respect to the cation sublattice and plays a crucial role in the behaviour of the fluorite structured materials. Data relating to neutron irradiated uranium oxide shows that the material can accommodate large quantities of crystalline defects and foreign atoms without changing structure. In a similar way, the composition of uranium oxide may deviate substantially from exact stoichiometry, which is usually represented as $UO_{2\pm x}$. At a given temperature and pressure, UO_2 will equilibrate with the surrounding atmosphere so that the activity of oxygen in the gas phase and the solid are equal. Therefore, oxygen being extremely mobile in UO_2 [30], the composition of the solid rapidly adapts to the oxygen partial pressure of the gas phase. As composition deviates from exact stoichiometry, a variety of higher oxide phases appear which explains the complex phase diagram indicated in Figure 1.2.

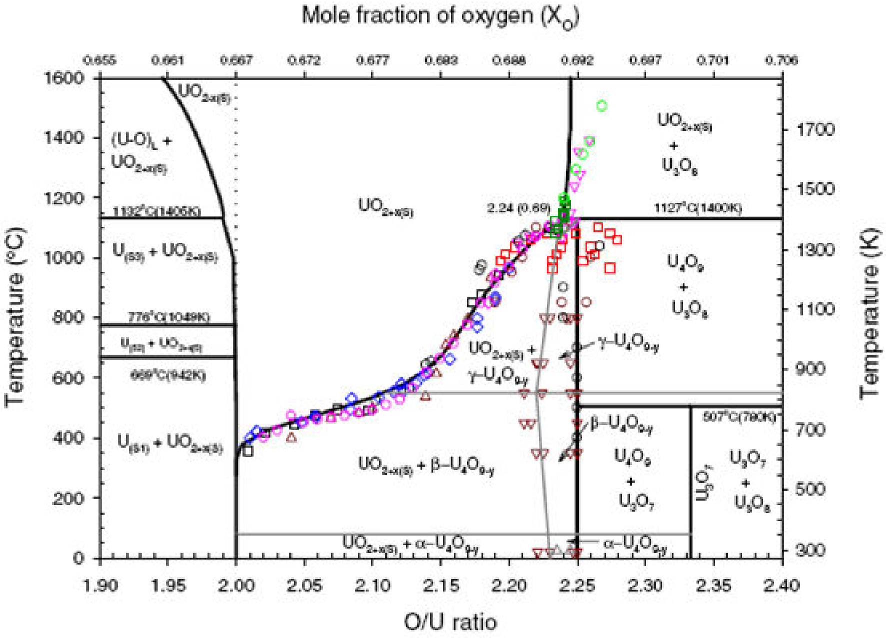

Figure 1.2: Phase-diagram of the U-O system, as reported by [92]

In this work, we are mainly concerned with the UO_{2+x} phase which exists over a broad range of compositions but also with higher oxide phases such as U_4O_9. The reason for this is twofold. Firstly, UO_{2+x} can decompose at lower temperatures into a two phase system so that when one characterises at room temperature samples equilibrated at high temperature, a proportion of the solid may comprise U_4O_9 [92, 180]. The second reason lies in that the structures of α-, β- and γ-U_4O_9 are actually quite similar to that of UO_2. U_4O_9 may be seen as resulting from a rearrangement of structural defects that are found in UO_{2+x} [15, 61]. This aspect will be detailed in the following sections.

1.1.1.2 Deviation from stoichiometry

Any thermodynamic representation of UO_{2+x} should be capable of capturing the actual dependence of oxygen composition upon oxygen partial pressure (pO_2) and temperature. There are many studies relating to this property and authors (see for instance [27, 45, 88, 105, 118, 125, 151]) have extensively critically reviewed these data in order to construct coherent thermodynamic representations of the system. It is of course not our aim to revisit these reviews but rather to look at this property (the chemical potential of oxygen), based on a restricted number of examples which illustrate the different compositional regions within the single $UO_{2\pm x}$ phase. This will later provide us with an insight into how the material accommodates deviation from stoichiometry. The data reported here essentially concern thermogravimetric analyses of $UO_{2\pm x}$ samples. This method consists in measuring at constant temperature the weight gain or loss of samples of known composition as they equilibrate with a gas phase which has a given oxygen partial pressure. Weight or gain loss is of course interpreted as gain or loss of oxygen. In addition to the absolute uncertainties in determining the value of deviation from stoichiometry, which requires an end or starting point of known composition, there are also uncertainties associated with the deviation from stoichiometry increments. Usually these uncertainties represent deviation from stoichiometry variations estimated between ± 0.002 and ± 0.01 [118].

Hyper-stoichiometry

Basically though, deviation from stoichiometry is made possible in this iono-covalent system by the property of uranium atoms to take on valence states which are greater than +4 [184]. In an ideally ionic representation, hyperstoichiometry which concerns a large region of the phase diagram, is thought to result from the incorporation of additional oxygen atoms at the interstitial sites described above and a concomitant oxidation of uranium atoms to a U^{5+} state. Note there are conflicting reports in relation to the existence of U^{6+}. Conradson [49, 48] claims that these may exist in U_4O_9 although more systematic absorption analyses would suggest that U^{6+} only appear in non-cubic phases [117]. Increase in average cation valence induces also local distortions of atomic environment and a shortening the U-O bonds (see §1.1.1.3).

Studies dealing with composition as a function of temperature and oxygen partial pressure have been extensively reported [22, 33, 82, 91, 110, 129, 130, 160]. Perron [151] carried out a review of these data, critically evaluating the validity and sensitivity of the experiments reported by different authors. He succeeded in constructing a simple function which, in the range of temperatures we are concerned with, provides us with an indication of the relationship between deviation from stoichiometry and oxygen partial pressure. It is encouraging that Perron's relationship is based on experimental data sets which have recently been reviewed and validated [27, 118]. Figure 1.3 therefore presents Perron's evaluation of the dependence of the oxygen to metal ratio (O/M) upon pO_2 in the temperature range 1073-1573 K.

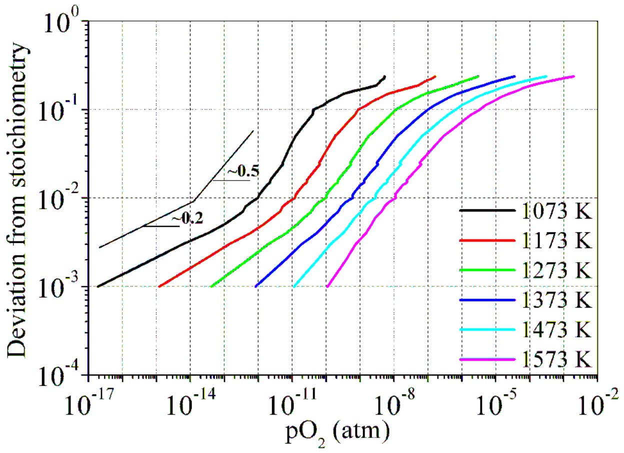

Figure 1.3: Deviation from stoichiometry dependence upon temperature and oxygen partial pressure as compiled by Perron [151].

This figure indicates that depending on the range of oxygen partial pressure there appears to be two (at the highest temperatures) or three (at the lowest temperatures) distinct regimes of deviation from stoichiometry which no doubt is a reflection of how, on the atomic scale, the material is accommodating hyperstoichiometry (see for instance [149]). There appears to be a transition from a $x \propto pO_2^{1/5}$ to a $x \propto pO_2^{1/2}$ at the lowest oxygen potentials and for the lowest temperatures, whereas at high deviations from stoichiometry, the O/M ratio levels off as the material approaches the transition to U_4O_9. Figure 1.3 shows also that for a fixed value of pO_2, lower temperatures correspond to higher deviations from stoichiometry.

Substoichiometry

The hypo-stoichiometric or substoichiometric material is only stable at high temperature and low oxygen partial pressures, as suggested in Figure 1.2 and is thought to be due mainly to the presence of oxygen vacancies [109, 143]. Because the conditions are difficult to obtain and control experimentally, few deviation from stoichiometry measurements exist. Those carried out in the past by Tetembaum and Hunt [173] and Javed [101] are represented in Figure 1.4. Although a certain scatter exists in the data, the results of Tetembaum [173] at temperatures in excess of 2000 K indicate a transition from $x \propto pO_2^{-1/2}$ to roughly $x \propto pO_2^{-1/4}$ as sub-stoichiometry increases. The results of Javed [101] on the other hand would tend to indicate $x \propto pO_2^{-1/2}$.

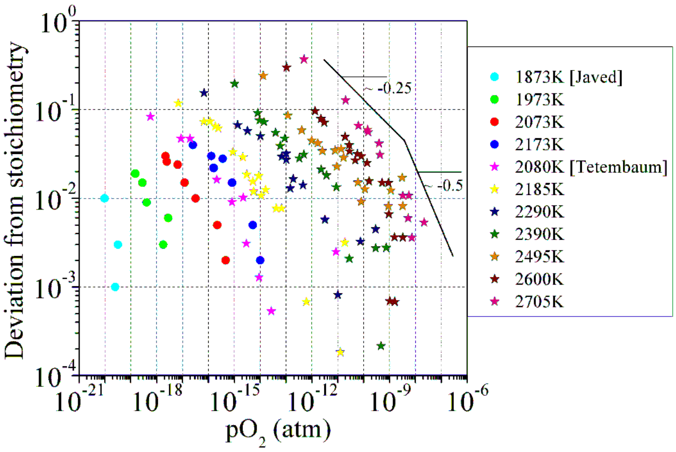

Figure 1.4: Dependence upon oxygen partial pressure of the deviation from stoichiometry x: comparison between data taken at different temperatures reported by Javed [101] and Tetembaum [173].

1.1.1.3 Higher oxide phases

In addition to hyperstoichiometric uranium dioxide, there is a range of higher oxide phases the composition of which may substantially deviate from exact stoichiometry depending upon temperature and oxygen activity. This is the case of cubic U_4O_9 and orthorhombic U_3O_8. The structure of these phases and the conditions under which they are stable are now relatively well known. Although X-Ray diffraction has extensively been used and continues to be to identify the formation of a new phase and establish details of the U-O phase diagram (see [85]) this technique may not be used to resolve the structure of uranium oxides completely. The reason for this is that scattering intensities of uranium atoms are far greater than those of oxygen. Willis [181] pioneered neutron diffraction work on uranium oxides, which, because oxygen and uranium atoms have similar neutron scattering intensities, enabled determining the positions of both uranium and oxygen atoms. In addition to this, because neutrons have a greater penetration depth than X-rays, they provide information relative to the bulk of the material rather than the surface. Willis [182] further carried out neutron diffraction experiments of a hyperstoichiometric $UO_{2.12}$ single crystal at 1100 K. His analysis showed that the simplest model which could account for the experimental data corresponded to the so-called 2:2:2 cluster. This aggregate involves four oxygen interstitials, 2 of which are displaced with respect to the cubic coordinated interstitial site along the <1 1 0> direction, and the remainder displaced from an ordinary oxygen site along the <1 1 1> direction. This is accompanied by the formation of two oxygen vacancies. In this work the uranium lattice was shown to remain undisturbed with respect to the fluorite structure. In particular Willis reported the absence of uranium vacancies [183].

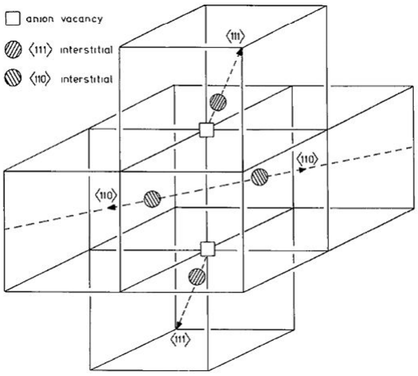

Figure 1.5: 2:2:2 cluster proposed by Willis based on neutron diffraction study [182].

Depending upon temperature but at temperatures below circa 1400 K (see Figure 1.2), oxidation of UO_{2+x} is reported to lead to the formation of α, β, or γ-U_4O_9, the structures of which are all based on the fluorite arrangement of UO_2. Cooper and Willis [51] only recently refined the structure of β-U_4O_9 which had been described earlier by Bevan [32]. In this phase, the uranium positions are close to those of the original fluorite phase but excess oxygen atoms are accommodated in so-called cuboctahedral clusters. These clusters proposed originally by Bevan (see Figure 1.6) comprise 12 oxygen atoms (instead of the eight illustrated in Figure 1.1) contained within the original FCC cation cell.

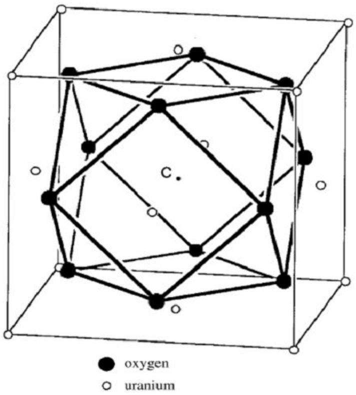

Figure 1.6: Oxygen cluster structure proposed by Bevan [32]

The presence of an additional interstitial oxygen atom sitting at the centre of the cuboctahedron has also been reported [61]. U_4O_9 may be considered as resulting from the long range ordering of these cuboctahedral clusters which gives rise to a cubic superstructure. α-U_4O_9, which is observed at lower temperatures, is a trigonal distortion of β-U_4O_9: Desgranges *et al.* [62] have recently proposed a refinement of this structure with a view to deriving a structural model for the oxidation of UO_2 to U_3O_8.

U_3O_8 is known to exist in two allotropic orthorhombic forms α and β [127] and was studied mainly since it constitutes the near highest oxide form of UO_2 [14, 62]. Also, it has been recognised for some time that U_3O_7 which has a tetragonal structure plays a key role in the low temperature oxidation process of UO_2 to U_3O_8 [137]. However U_3O_7 is a metastable phase [63]. This implies for example that if one heats a homogeneous sample with that composition and structure in a sealed environment, it will readily disproportionate depending upon temperature into U_4O_9 and U_3O_8 [94]. One very self-explanatory way of identifying its influence in the oxidation process to U_3O_8 is to carry out oxidation experiments during which structural features are characterised *in-situ*. A good example of this was reported by Rousseau *et al.* [161] who followed the structural evolution of UO_2 powders at 470 K under air using synchrotron radiation. Figure 1.7 reports some of the more striking results which show the emergence of the tetragonal distortion of the fluorite structure as an intermediate state between the fluorite U_4O_9 and the orthorhombic U_3O_8 phases. The details of the cluster arrangements in β-U_3O_7 were later published by Desgranges *et al.* [63] based on oxidation experiments monitored using neutron diffraction. They suggested that β-U_3O_7 actually resulted from cuboctahedra moving closer together which is responsible for the tetragonal distortion and shorter U-O bonds.

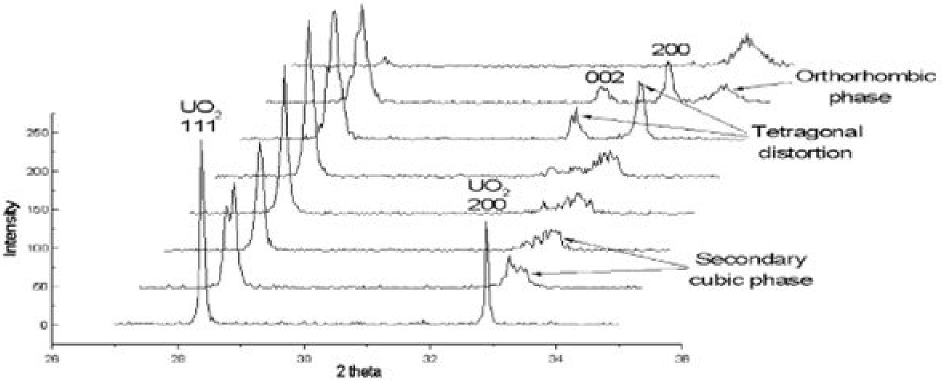

Figure 1.7: Structural evolution in time of a UO_2 powder exposed to air at a temperature of 250°C [161].

During the oxidation process, the reduction in U-O bond lengths is accompanied by an increase in the covalent nature of these bonds. In the UO_2 and U_4O_9

cubic fluorite structures, the U-O bonds can be considered partially ionic. As the oxidation process leads to higher oxide phases, the degree of covalence increases and the U-O atomic distances decrease to reach values typical of $(UO_2)O_2$ uranyl-groups. This is accompanied by a concomitant lowering of the crystal symmetry. While U_4O_9 keeps a cubic fluorite structure, U_3O_7 becomes tetragonal, U_3O_8 orthorhombic and UO_3 tetragonal with an uranyl geometry. In this latter phase uranium atoms are surrounded at a distance of about 2.3 Å by a 5 coplanar oxygen atoms which form a pentagon with 2 oxygen atoms placed along an axis perpendicular to this plane at a shorter distance (1.79 Å). It is quite natural to assume that methods for determining the electronic structure of the material (which is liable to characterise the nature of the bonds) will constitute a useful complement to the structural characterisations reported here. The next section aims at reviewing the most important features relating to the electronic structure UO_2 obtained both from theoretical and experimental methods.

1.1.2 Electronic structure

1.1.2.1 Introduction: the characteristics of UO_2 electronic structure

UO_2 has a complex electronic structure largely determined by the strong correlation effects of the Uranium 5f electrons. The UO_2 energy bands near the Fermi level are basically divided into four distinct regions:

1. A wide 3.7 eV valence band formed by hybridised O 2p with U 5f and U 6d orbitals [26];
2. A narrow 2.3 eV band containing two well-localized U 5f electrons, that lies just below the Fermi level [26];
3. A gap, estimated at 2.1±0.1 eV [166];
4. A wide conduction band whose lowest energy levels that spread over approximately 4 eV are composed of the hybridised O 2p and U 5f orbitals [187].

These characteristics were determined from a combination of different techniques used either to study the occupied sates (such as X-Ray Photoemission Spectroscopy - XPS) or the unoccupied states (such as Bremsstrahlung Isochromat Spectroscopy - BIS - and X-ray Absorption Spectroscopy - XAS). The first experimental study of UO_2 valence and conduction band features (see Figure 1.8) was carried out by Baer and Shoenes [26] who used XPS and BIS.

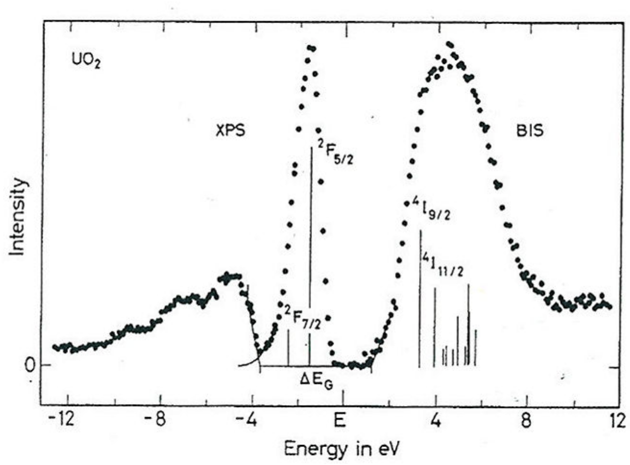

Figure 1.8: Experimental XPS ans BIS spectra of UO_2 [26]

Optical measurements carried out by Schoenes [166] may only reveal unoccupied 6d states because of the dipole selection rule. Based on that, Baer suggested that the unoccupied states observed in BIS also corresponded to such transitions [26]. However, as pointed out by Yu [187], the cross section for the f state is dominant at the high energy of the electrons used for BIS measurements and consequently it becomes implausible that BIS signal is originated from the 6d states. In fact, Yu succeeded in demonstrating with other techniques that the bottom of the conduction band is mainly composed of uranium 5f states (see Figure 1.10). In fact, a combination of X-ray Absorption Spectroscopy (XAS) and DOS *ab-initio* calculations demonstrated the f-type character of the unoccupied states observed [187] conferring unto UO_2 a f-f type semiconducting nature.

This shows that the combination of XAS and *ab-initio* simulations constitutes a powerful tool for determining the electronic structure of this material. In the following paragraphs we review our knowledge of the electronic structure of UO_2 based on these two techniques.

1.1.2.2 Growing contribution of *ab-initio* approaches

In recent years, *ab-initio* calculations which are based upon solving the Schrödinger equation, have been widely used to describe actinide oxide materials. In order to solve this equation and calculate the wave function associated with all the electrons in the system, practically all recent studies rely upon Density Functional Theory (or DFT). DFT is based upon two theorems established by Hohenberg and Kohn [96]. These theorems enable the ground state of a system to be determined not from the minimisation of the energy of the system with respect $3N$ unknowns (N wave functions of the N particles each with three degrees of freedom) but with 1 space dependent scalar function: the electronic density. However even with this formulation the problem remains untreatable, because the only known formulation for the kinetic energy term in the Schrödinger equation is that which corresponds to N independent electrons. Replacing a system comprising N interacting electrons with a system comprising N independent electrons is known as the Kohn-Sham approximation [108] in which all interaction terms between electrons are contained in the exchange-correlation functional. Various approximations have been used depending upon whether one assumes a uniform electron gas (Local Density Approximation or LDA) or whether the exchange-correlation functional is dependent upon the gradient of electronic density (Generalized Gradient Approximations or GGA).

Although efficient, exchange-correlation functionals in their standard formulation [96, 108] fail to entirely capture strong correlations. In particular these functionals predict UO_2 to be a metal when it is known to be a Mott-insulator (see previous section), the properties of which are to large extent determined by the strong correlations between 5f electrons. Improving the modelling of these strong correlations requires using approximations which go "beyond DFT". The most widely used alternative to standard DFT is known as DFT+U (where U is the Hubbard correction term) [20]. This approximation succeeds in opening a gap [89] and localising electrons on the 5f orbitals. However, the consequence of this is that the system may be trapped in a local energy minimum which does not correspond to the ground state. Dorado [65, 69] has recently suggested a method known as occupation matrix control which guarantees that the ground state is reached. These methods have been used with increasing success to reproduce both the electronic structure of UO_2 [65] (see section §1.1.2.3) and calculate defect formation and migration energies [18, 17, 65, 66] (see section §1.2.2).

1.1.2.3 UO_2 Oxygen K-edge XAS characterization

X-ray absorption spectroscopy is a technique used for characterising the absorption properties of a material as a function of the incident photon energy [147]. A compound absorption coefficient μ is strongly dependent upon its physical characteristics (density, atomic number and atomic mass) and upon the energy of the incident X-rays. Following the Fermi golden rule, for X-ray energies greater than the core-level binding energy, the photoelectric effect is activated and the promotion of one core electron to an excited state is possible. The excitation process follows the dipole selection rules, according to which an electron can jump to an excited level only with a change of the angular momentum ($\Delta l = \pm 1$) but no change of its spin ($\Delta s = 0$). Therefore, the absorption coefficient μ can be seen as the probability to induce a transition between these two quantum states. A XAS spectrum, at least close to the absorption edge, represents the density of unoccupied (*i.e.* available) states.

In particular, a XAS spectrum at oxygen K-edge corresponds to electronic transitions of oxygen 1s core electrons to unoccupied *n*p level, with $n \geq 2$. For energies up to 10 eV above the absorption edge the spectrum is mainly characteristic of 1s $\rightarrow$ 2p transitions. At higher incident photon energies, the photoelectron is energetic enough to actually leave the atom and multiple scattering occurs thus providing information relating to the local environment around oxygen atoms [86, 103, 131].

We now turn our attention to UO_2. In a purely ionic model one expects uranium and oxygen ions to take on the following configuration: $6p^6 5f^2 6d^0 7s^0$ for U and $2p^6$ for O. However, this representation does not reflect the true nature of the bonds. A degree of covalency gives rise to hybridized valence orbitals of type $5f^3\underline{L}$ and $5f^2 6d^1\underline{L}$, where $\underline{L}$ is an O 2p ligand hole. Therefore, in UO_2 the promotion of a 1s O electron to the 2p level produces a signature of the hybridized $5f^3$ and $5f^2 6d^1$ orbital configurations, modulated by the 1s O core hole attraction. Note that in a cubic crystal field, the d orbitals are split into two e_g and three t_{2g} orbitals, the last ones having higher energy levels [86, 103]. As a consequence, there are two possible configurations for the hybridised orbital $5f^2 6d^1$: $5f^2 6e_g{}^1$ or $5f^2 6t_{2g}{}^1$.

The first UO_2 O K-edge XAS spectrum was collected by Jollet *et al.* [103] and is represented in Figure 1.9.

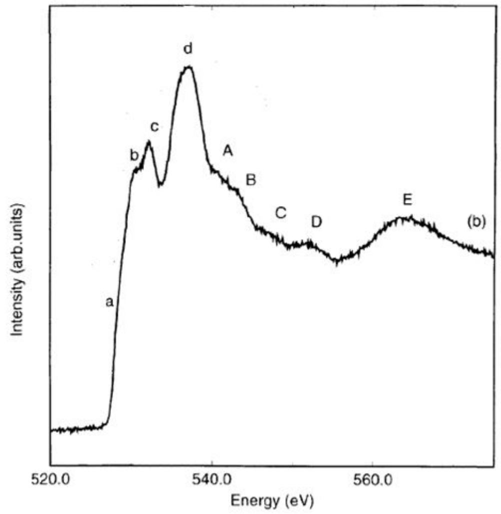

Figure 1.9: Oxygen K-edge XAS spectrum of UO_2: letters indicate peak positions; peaks indicated with normal letters give a picture of the electronic structure of the empty states of the oxygen atoms. Peaks indicated with capital letters instead are due to multiple scattering phenomena.

There is consensus [103, 187, 185] regarding features a and b which are attributed to the hybridization of the O 2p with the U 5f orbitals ($5f^3$ configuration). Peaks c and d are instead due to the more energetic U 6d orbitals ($5f^26e_g{}^1$or $5f^26t_{2g}{}^1$ configurations). This analysis is based on the comparison of the O K-edge XAS spectrum with *ab-initio* DOS calculations (see Figure 1.10) carried out using different approaches (LDA+U [103], GGA+U [187]) none of which took the core-hole effect inevitably present during a XAS experiment into account. In fact the promotion of a core electron into the conduction band leads to the appearance of a hole in the atomic core states. In principle, its presence induces modifications in the DOS probed by XAS and can only be reproduced using first-principles methods if an appropriate pseudopotential is used [100, 40, 136]. However in transition metal oxides, modifications to the oxygen DOS induced by the presence of the core-hole are limited, as the total unoccupied bands are more affected by the cation contributions [86]. Figure 1.10 illustrates this point made by De Groot [86]: in UO_2 the calculated O 2p orbital contribution to the DOS of the empty conduction band is much weaker than the cation one. As a consequence, an oxygen 1s core hole shouldn't strongly affect the empty DOS of UO_2 in an excited state.

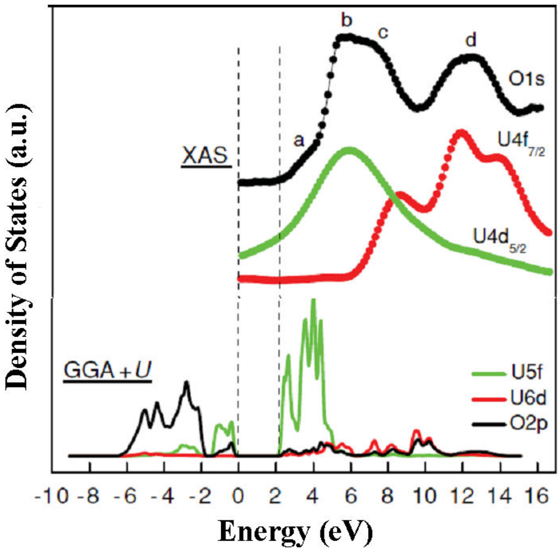

Figure 1.10: Comparison of the oxygen K- (black), uranium N_5- (green) and uranium N_7-edge (red curve) spectra with *ab-initio* oxygen 2p, uranium 5f and 6d DOS calculation carried out with the GGA+U approximation [187].

Oxygen K-edge spectra are strongly affected by the oxidation state of the cation. Two examples are given by Martin *et al.* [131] and Modin *et al.* [140] who respectively studied the modifications of UO_2 and PuO_2 O K-edge XAS spectra induced by supposed oxidation. In particular, the work of Martin *et al.* [131] on a UO_2 single crystal and polycrystalline samples seems to demonstrate that oxidation leads to the appearance of an intense peak at low energy. As seen in §1.1.1.2, UO_2 hyperstoichiometry is associated with the presence in the lattice of cations with a 5+ oxidation state. This work tended to preclude the presence of U^{6+} in UO_{2+x} samples although a definite conclusion could not be reached due to the fact that *ab-initio* calculated DOS were not available at the time.

A seen previously, interpretation of XAS spectra is based on their comparison with DOS calculated by *ab-initio*. In recent years substantial inroads have been made to provide reliable models capable of describing the complexity of UO_2 electronic structure.

1.2 Modelling point defect concentrations in transition metal oxides and in UO_{2+x} in particular

In literature, uranium dioxide has been the subject of many studies in relation to equilibrium point defect concentration estimates. We will be focusing here on two complementary approaches both of which are concerned with modelling various defect equilibria. Whereas the first approach focuses on adequately representing available experimental data to derive for instance chemical equilibrium constants, the second uses results from first principle calculations of defect formation energies as input data for the various defect equilibria envisaged. It is important to stress that these two approaches should at some stage converge to give a comprehensive and coherent picture of point defect concentrations and this essentially arbitrary distinction has been adopted here mainly to rationalise results available in the literature.

In the first approach, one is in principle capable of describing the effects upon defect concentrations of temperature and of the local oxygen activity in the solid in equilibrium with the surrounding gaseous atmosphere. The nature of defects is generally postulated based on ones knowledge of basic thermodynamic data such as the partial molar free energy of oxygen and its dependence upon composition and temperature. The models can be then assessed upon their ability to rationalise other basic material properties.

The second approach is found in studies primarily concerned with first principle modelling and is often presented as one of its most obvious applications: the determination as a function of composition and temperature of the concentration of point defects based on calculated point defect formation energies. The relevance of these applications is obviously intimately connected with the type of exchange correlation functional chosen (GGA, LDA, LDA+U, hybrid functionals, etc.) and is, because of the relatively recent availability of such techniques, still very much the subject of discussion. Even if it is still somewhat unrealistic to think that defect concentrations may be assessed essentially from first principles, we will see in what follows the capability of these *ab-initio* methods in their more advanced forms to reflect at least qualitatively some of the more complex aspects of our material's behaviour.

1.2.1 Thermodynamic models based on the analysis of experimental data

Thermodynamic models used to calculate equilibrium point defect concentrations in oxide materials in general are often based on the law of mass action. In this formalism, originally developed by Wagner and Schottky [111] using the Kröger and Vink formalism [113], the mass-action type equations describing equilibria between electronic and ionic defects are written under the assumption that defects are non interacting and infinitely diluted. With this approximation defect activities are simply expressed in terms of defect concentrations. To complete the model, electroneutrality and site conservation equations on both sublattices are added. Success of this theory is however mitigated by some important shortcomings [37]:

- The mass action law assumes defects as non-interacting species. However in oxide systems defects are usually charged and as a result subject to long range Coulomb interactions.
- Because the mass action law generally assumes infinite dilution, the configurational entropy contribution of the different defects in the Gibbs free energy of the system reduces to site fractions (*i.e.* the probability that an anion or cation site is occupied by a defect of a particular anionic or cationic type). However for high defect concentrations, defects are no longer statistically uncorrelated because the presence of a defect excludes others from sharing the same region in the lattice. This is known as the site exclusion effect and becomes increasingly relevant as the defect concentration in the material rises (high deviations from stoichiometry).

Authors [60, 98, 126, 139, 167, 170, 186] have therefore attempted to consider one or the other or both of these effects; *i.e.* defect interactions and site exclusion. Ling [126] for example proposed a general theory which he applied to the description of the behaviour of point defects in cerium oxide. The author claims the model reproduces deviation from stoichiometry data in $CeO_{2\text{-}x}$ even at high values of x. Despite their more physical description of the system, these approaches loose the attractive simplicity that characterizes the ideal mass action law approach.

This latter more simple approach has encountered reasonable success in rationalising experimental data such as non-stoichiometry, electrical conductivity or atomic transport properties and their dependence upon oxygen partial pressure for a wide range of oxides [71, 106, 111, 148, 174, 175], including uranium dioxide [73, 114, 145, 146, 149].

A. Nakamura and T. Fujino [145] and Park and Olander [149] used the model to reproduce the available partial oxygen enthalpy and entropy dependences upon oxide composition and temperature. M. Fraczkiewicz [73] attempted to simultaneously reproduce deviation from stoichiometry data as reviewed by Perron [151] and Ruello's electrical conductivity data [164].

Despite efforts made to understand the relationship between the presence of a given type of defect and atomic transport and/or thermodynamic properties of UO_2, these authors did not succeed in reproducing the entire range of available data. They provided some possible explanations for these shortcomings. For example, M. Fraczkiewicz suggested that an improved knowledge of the relative mobility of electrons with respect to holes could help rationalise deviation from stoichiometry and electrical conductivity data. A. Nakamura and T. Fujino instead suggested that the strong electrostatic interactions that exist between charged defects may play a crucial role. They attempted [146] to take this into account by considering the defect interaction and formation energies as dependent upon UO_{2+x} molar volume. They derived an extra enthalpy term called "excess enthalpy term", and recalculated the partial oxygen molar enthalpy and entropy of oxygen to find a better agreement between their model and the experimental data.

In relation to UO_2 at least, authors have nonetheless been able to derive defect formation energies from the analysis of the experimental data with such models. It is interesting to note that these defect formation energies actually characterise a given chemical equilibrium and as such are in principle directly comparable to values which may be computed from first principles.

In the following section, we focus on point defect models that incorporate defect formation energies calculated from first principles and assess the relevance of these approaches to capture the specificity of our material.

1.2.2 Models based on formation energies calculated from first principles

As mentioned in §1.1.2.2, methods which go beyond standard DFT have become increasingly useful not only for clarifying details relating to the electronic structure of UO_2 but also as will be seen later for shedding light upon the nature of point defects and their most stable configurations.

However, the first attempts at calculating defect concentrations from first principles were done with standard DFT (see [56] and [74, 75] respectively for LDA and GGA formalisms). These methods were shown to provide bulk properties (*e.g.* cell parameter, bulk modulus and cohesive energy) in reasonable agreement with experiment and despite the fact that these functionals were incapable of capturing the semi-conducting nature of UO_2, they were used to calculate defect formation energies. The energies were used in a mass action type model (originally proposed by Matzke [135] and Lidiard [121]) with the usual simplifying assumptions of infinite dilution. The defects accounted for were oxygen interstitials (O_i) and vacancies (V_O), uranium interstitials (U_i) and vacancies (V_U) and the equilibria modelled comprised oxygen and uranium

Frenkel disorder (FP_O and FP_U) and Schottky disorder (S_i). As one would expect, the energies associated with the different equilibria lay in the following order (of increasing energies): oxygen Frenkel (3.6 eV [74]or 3.9 eV [56]), Schottky (5.6 eV [74] or 5.8 eV [56]), uranium Frenkel pairs (11.8 eV [74] or 10.7 eV [56]). Also oxygen interstitials were calculated as forming much more readily than oxygen vacancies. When solved, the model predicts that the most abundant defects in the sub-stoichiometric regime are oxygen vacancies (as expected, see section §1.1.1.2), but in the hyperstoichiometric regime, uranium vacancies become the predominant defect species above deviations from stoichiometry of the order of 10^{-4}, in contradiction with Willis's neutron diffraction results (see section §1.1.1.3). There is one essential shortcoming with all these approaches that has its roots in the fact that with standard DFT it is impossible to model charged defects in UO_2 in contradiction with any basic description of the material behaviour. As a consequence of this all the defects accounted for in these approaches are by construction neutral defects and as an example, it is impossible to attempt to reproduce the electrical properties of the material.

Effect of charge

It is only with the advent of methods which go beyond standard DFT (*e.g.* DFT+U [18, 65, 69] or hybrid functionals [57]) that it has been possible to model charged defects and to try to reconcile approaches described in the previous section with first principle calculations. Table 1.1 reports the formation energies calculated using different approaches for isolated uranium and oxygen defects. Interpreting this table requires a number of points be kept in mind:

- Any comparison between the energy values that appear in this table should be made with great care. From one study to the other, energies may indeed correspond to different equilibria. This is the case in particular for Crocombette's values [57, 55]. The authors' values could have been modified to produce values comparable to other data but we have chosen to quote the data that appear in the original paper.

- The comparisons which are most significant are those that involve defects for which the formation equilibria do not require defining a reference state such as uranium and oxygen Frenkel pairs and Schottky defects. Authors often use reference states that are different or for which their approximations provide different values making it extremely tenuous to compare defect formation energies between studies.

- The Schottky defect formation energies reported refer to unaggregated Schottky disorder (the uranium vacancy and the two oxygen vacancies are uninteracting).

- The formation energies of the charged defects that are reported allude to doubly charged anion defects (O_i'' and $V_O^{\circ\circ}$) and uranium interstitials and vacancies have a +/-4 charge state.

Method	***Ref.***	O_i	V_O	FP_O	U_i	V_U	FP_U	S_i
Ab-initio - Neutral defects								
LDA	[56]	-2.9	6.7	3.9	7.3	3.3	10.7	5.8
GGA	[74]	-2.5	6.1	3.6	7.0	4.8	11.8	5.6
LSDA+U	[99]	-0.4	4.5	4.1	4.7	8.4	13.1	–
LSDA+U	[80]	-2.2	7.5	5.4	8.2	9.1	17.2	10.6
GGA+U	[65]	-0.05	5.36	4.96	5.38	10.43	15.81	10.66
LDA+U	[18]	–	–	5.26	–	–	–	10.15
Hybr. Funct.	[57]	-0.8	7	6.4	–	-3.5	–	9.9
Ab-initio - Charged defects								
LDA+U	[18]	–	–	3.32	–	–	–	6.00
LDA+U	[66]	-0.6	–	–	–	–	11.82	–
GGA+U	[66]	-0.45	–	–	–	–	–	–
Hybr. Funct.	[57]	–	–	4.8	–	–	–	5.8
Hybr. Funct.(*)	[55]	-1.4	5.6	4.2	–	-4.7	–	6.4
PDM - Charged defects								
	[149]	-2.17	6.7/9					
	[145]	-0.12/-0.5		5.3				
Experiments - Charged defects								
	[130]	-1.3						
	[46, 135]			3.0–4.6				6.0–7.0

(*)The formation energies of the defects O_i'', $V_O^{\circ\circ}$ and V_U'''' are calculated in the middle of the gap.

Table 1.1: Formation energies (in eV) of different defects calculated in the fluorite phase.

At a glance, one notices that all calculated interstitial formation energies are negative, as are also the available experimental values. It is also quite striking that all oxygen vacancy formation energies (including the sole available experimental value) are highly positive, roughly 5 eV. These observations are consistent with the fact that UO_2 readily oxidises whereas the substoichiometric phase is rather difficult to form and only appears at high temperatures under very reducing atmospheres (see section §1.1.1.2). Also consistent with our understanding of the material (see section §1.1.1.3 and Willis's neutron diffraction work [183]) is the fact that oxygen Frenkel pairs are less costly energetically than uranium Frenkel pairs which is an indication that oxygen disorder prevails over disorder on the cation sublattice.

The charge states of point defects also have a substantial effect upon their formation energy. Crocombette [57] was the first to have recently quantified this and his results are also reported in Table 1.1. It is striking for instance that the energy of a charged Frenkel pair lies between 1.6 eV and 2 eV below the formation energy of the Frenkel pair involving neutral defects. Andersson [18] reports (see Table 1.1) the same energy differences between charged and neutral oxygen Frenkel pairs. The same applies to formation energies of neutral and doubly charged oxygen vacancies.

Crocombette's work also enables us to have an idea of the charge of the most stable defect as a function of the Fermi level, which itself depends upon deviation from stoichiometry or indeed the level of aliovalent cation doping. In particular he observed that:

- The -4 charged uranium vacancy (V_U'''') is the most stable defect at practically all Fermi levels, hence deviations from stoichiometry.
- The -2 charged oxygen interstitial (O_i'') appears to be stable over a wide range of compositions.
- The +2 charged oxygen vacancy ($V_O^{\circ\circ}$) is more stable in the hyperstoichiometric region (Fermi level closer to the valence band) although singly charged and even neutral vacancies may prevail in the sub-stoichiometric region.

Note that unfortunately within the GGA+U approximation, no systematic data exist in relation to the effect of charge.

It is important to note that an attempt has recently been made to interpret uranium self-diffusion experiments in near stoichiometric material based on a point defect model for which defect formation energies have been determined within the GGA + U approximation [66]. The charge of the defects modelled are chosen of the strength of Crocombette's study and the point defect model that underpins the approach predicts that electronic disorder prevails over disorder on the oxygen sub-lattice which itself is more important than disorder on the uranium sublattice. In addition, the model enables the authors to rationalise the experimental data available in near stoichiometric material and to interpret these data based on the nature of the atmosphere under which the diffusion experiments are carried out and in particular the oxygen partial pressure.

Clustering

In hyperstoichiometric material, it was demonstrated experimentally (see §1.1.1.3) that increasing values of x will lead to a greater degree of covalency which is manifest in a shortening of U-O bonds. Using the hybrid functional approach, Crocombette [55] calculates that decreasing Fermi levels (*i.e.* increasing oxygen partial pressures) will favour oxygen clustering. In addition he showed that as the size of an oxygen cluster increases, its charge moves away from that expected based on a purely ionic model. The more stable cluster configurations obtained within the DFT+U approximation or using hybrid functionals are illustrated in Figure 1.11:

- The oxygen di-interstitial [19, 65] or the split di-interstitial [19, 44, 81, 80] are respectively represented in red and blue in Figure 1.11a). The former defect is composed by 2 O ions in 2 adjacent octahedral sites. The latter is by contrast composed of 3 oxygen interstitials in a {111} plane and 1 O vacancy. This kind of defect is calculated by Crocombette [55] to be energetically more stable if singly negatively charged.

- The oxygen quad-interstitial [17] is composed of two split di-interstitials (it is represented in Figure 1.11b) with blue and green spheres).

- The cuboctahedron (COT) [17, 44] corresponds to a cluster as described by Bevan [32], or possibly containing an additional oxygen interstitial in its centre as suggested by Desgranges *et al.* in [61] (see §1.1.1.3 for details). These defects containing 4 or 5 additional oxygen ions (COTv and COTo) are represented in Figure1.11c). Crocombette [55] calculated that both these defects bear a -2 charge instead of -8 or -10, as expect in a purely ionic model.

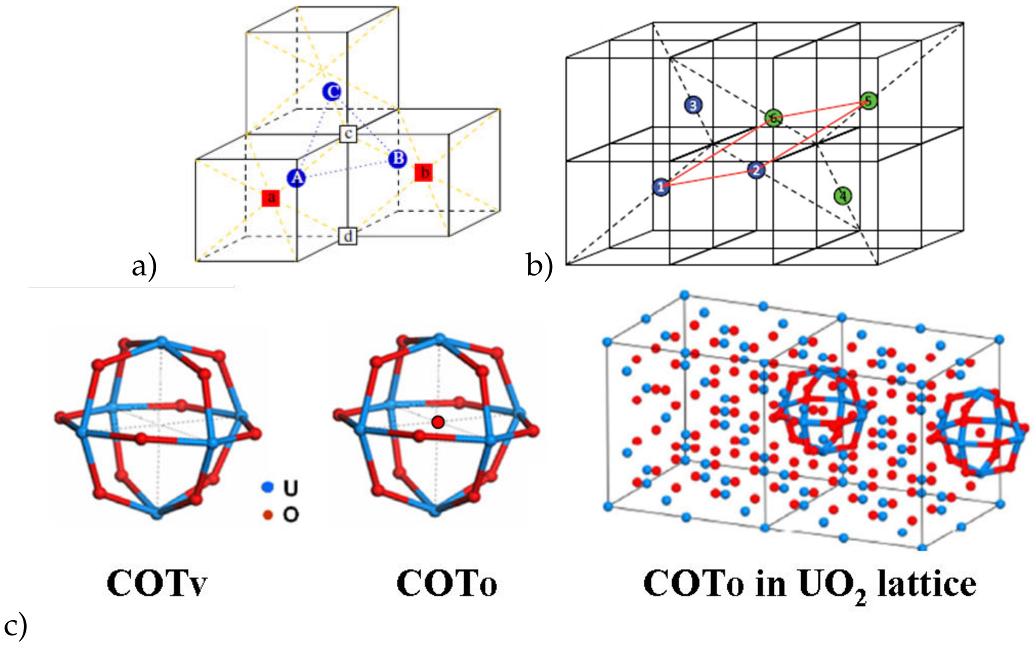

Figure 1.11: Representation of: a) an oxygen di-interstitial (represented in red), a split di-interstitial (in blue) [19]. b) an oxygen quadinterstitial, as calculated by Andersson *et al.* within the DFT+U formalism [17] c) the 2 possible types of cuboctahedra . [44]

1.2.3 Conclusions

To conclude this section, it appears that DFT provides defect formation energies that are broadly compatible (irrespective of the approximation) with the behaviour of the material. However, there are two aspects relating to point defects which a mechanistic approach should take into account:

- The charge of defects constitutes a key aspect of the behaviour of UO_2 to the extent that methods which go beyond standard DFT are necessary in any meaningful attempt to compare theoretical and experimental data. It seems that DFT+U in particular opens up the prospect of interpreting atomic transport properties quantitatively [66] and hybrid functional studies may guide us towards the nature of the defect which a point defect model should describe [57, 55].

- The effect of clustering of oxygen ions in the hyperstoichiometric region of the phase diagram appears also to be key to understanding the material's properties.

Point defect models have been developed in the past either based on the analysis of equilibrium properties or on first principles calculations. No attempt has, to our knowledge, been made to reconcile these approaches, *i.e.* to benchmark defect properties derived from the analysis of the material's properties to comparable values obtained from first principles. This aspect will be looked at in detail in Chapter 3. In the following section however, we examine in greater detail the type of property that may be used in order to derive basic quantities relating to point defects, *i.e.* defect formation and migration energies.

1.3 Experimental approaches to evaluate UO_{2+x} transport properties

As seen in paragraph §1.2.1, point defect models can be used to analyse thermodynamic equilibrium properties and derive quantitative information relating to point or complex defect populations. In past studies, they were essentially applied to reproduce deviation from stoichiometry data. However, these models should in principle be capable of reproducing the range of properties which show a strong dependence upon defect populations, such as electrical or atomic transport properties some of which are the focus of this section.

1.3.1 Electrical properties

In an oxide system, electrical conductivity can be ensured either by electronic defects (electrons or holes) or mobile ionic species. In UO_2, Bates *et al.* [29] observed no effect upon electrical conductivity measurements of using either direct or alternative currents at different frequencies and therefore concluded, as is now generally accepted, that the ionic contribution to the electrical conductivity is negligible. As a result, the electrical conductivity of UO_2 can be considered as the sum of two contributions, each corresponding to the product of the electronic defect concentration with its mobility [28, 111]:

$$\sigma = e \cdot (\mu_e \left[e^{'}\right] + \mu_p \left[h^{\circ}\right]) \cdot N_{s,U} = \mu_p \cdot e \cdot \left(\mu_{rel} \left[e^{'}\right] + \left[h^{\circ}\right]\right) \cdot \mathcal{N}_{Av} \cdot \frac{d}{M} \quad (1.1)$$

Here μ_e and μ_p are the electron and hole mobilities respectively, e the elementary electrical charge, μ_{rel} is the ratio of the electron to hole mobilities, $[e']$ and $[h^{\circ}]$ are respectively the electron and hole concentrations and $N_{s,U}$ is the number of uranium sites. Supposing all cation sites occupied, $N_{s,U}$ can be calculated as $\mathcal{N}_{Av} \cdot \frac{d}{M}$, where $\mathcal{N}_{Av}$ is the Avogadro's number and d and M are the density and the molar mass of UO_2 respectively. At a given temperature, electrical conductivity variations may therefore be seen as reflecting changes in the electronic charge carrier concentrations. Many studies have been dedicated to quantifying the electrical conductivity of UO_2 over a wide range of conditions.

1.3.1.1 Electrical conductivity dependence upon thermodynamic variables

P. Ruello [162] measured UO_2 single crystal electrical conductivity at different values of oxygen partial pressures and at seven different temperatures; his data are reported in Figure 1.12a).

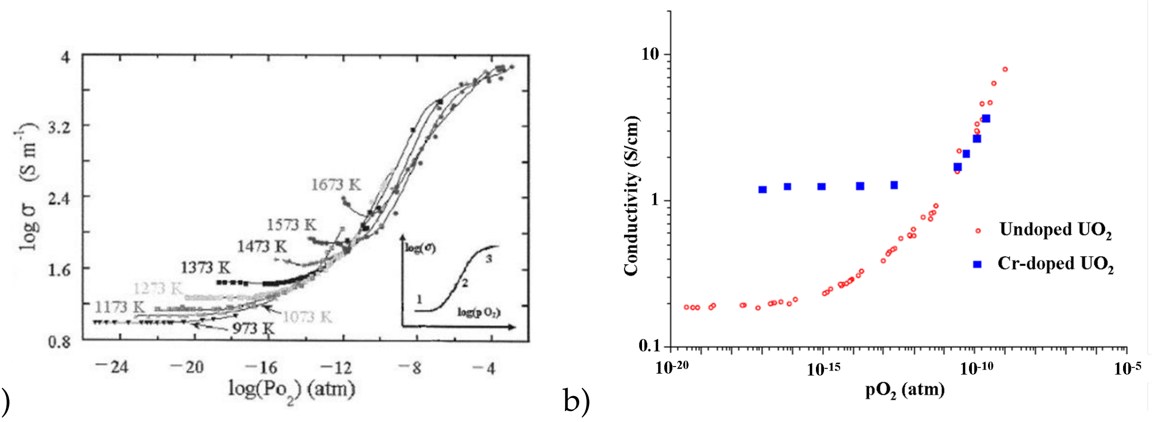

a) b)

Figure 1.12: a) Electrical conductivity data measured by Ruello [162, 164]. For each considered temperature, electrical conductivity is represented as a function of oxygen partial pressure. b) Comparison of Ruello's data with the conductivity measurements of a Cr-doped UO_2 polycristalline sample (Cr being presumably present as a 3+ ion on the cation sublattice [73, 132, 159]) collected by [73]. Each set of data was taken at 1273 K.

With a few reasonable assumptions, the UO_2 electrical conductivity curves reveal the dependence upon oxygen partial pressure and temperature of the nature and relative defect concentrations (see the insert of the Figure 1.12a)):

1. At low temperatures (less than *ca.* 1273 K) and oxygen potentials, under conditions where at a given temperature electrical conductivity is independent of oxygen partial pressure, electrical conduction in UO_2 has been demonstrated from Seebeck coefficient measurements [164] to be ensured by holes (*i.e.* p-type conduction) created for charge compensation reasons by impurities, hence reference to an extrinsic regime. These impurities have a valence less than +4 and are assumed to be present on the cation sublattice.

2. As the oxygen potential rises, the material incorporates negatively charged ions which cause a fraction of uranium ions to take on valences in excess

of +4. When the concentration of oxidised uranium ions created in this way becomes equivalent to that which compensates for the presence of aliovalent impurities, the electrical conductivity rises above the extrinsic plateau. Ruello observed a Log(σ) *vs.* Log(pO_2) slope of roughly 1/2 which he interpreted as being due to singly negatively charge oxygen di-interstitials. This interpretation also tallies with the 1/2 slope of the Log(x) *vs.* Log(pO_2) slopes mentioned in the previous section (see Figure 1.3). This change from a presumably purely ionic behaviour in which the absolute charge of a cluster increases by less than 2 as an additional oxygen atom is incorporated to it corroborates the calculations of Crocombette alluded to in the previous section and indicates an increase, as expected from our knowledge of the oxidation process, in the covalent nature of bonds (see §1.1.1.3).

3. Only at high temperatures does the behaviour become intrinsic for all accessible oxygen partial pressures (in Ruello's case this is noticeable at and above 1473 K). The authors showed through measuring Seebeck coefficients that the minimum the electrical conductivity goes through as a function of oxygen partial pressure corresponds to an n to p transition. Further assuming that electrons and holes have similar mobilities and that oxygen vacancies and interstitials have identical charges, the electroneutrality condition requires that the minimum corresponds to exact stoichiometry.

4. At all temperatures, as the oxygen partial pressures increases, the electrical conductivity appears to level off. Here deviation from stoichiometry is high enough that larger size oxygen clusters form and the author associates this with the onset of a phase transition towards U_4O_9. At those partial pressures, it is also noted that the time necessary to equilibrate UO_{2+x} samples increases substantially.

1.3.1.2 Mobility of the charge carriers

In UO_2 electrical conductivity is thought to occur via a small polaron hopping mechanism [43, 70, 144, 163, 184]. This mechanism applies to semiconductors in which the interactions between charge carriers and lattice vibrations (phonons) are strong. The charge carrier mobilities may be expressed depending on the nature of the process: adiabatic (respt. non-adiabatic) for which hopping occurs over a characteristic time shorter (respt. longer) than a lattice vibration [43]:

$$\mu_{p/e} = \frac{\mu_0}{T^q} \cdot \exp\left[-\frac{E_H}{k_B T}\right] \tag{1.2}$$

Where q is 1 (respt. 3/2) in the case of an adiabatic (respt. non-adiabatic) mechanism, E_H is the charge carrier migration barrier and μ_0 a pre-exponential factor.

Ruello [164] showed from electrical conductivity and Seebeck coefficient measurements that UO_2 is a p-type conductor below roughly 1273 K so that an analysis of conductivity data in this range can provide information relating to hole mobility. Dudney *et al.* [70] carried out electrical conductivity measurements on yttria-doped and pure uranium dioxide. Samples of containing varying quantities of yttria were prepared and characterised as a function of temperature and oxygen partial pressure. At a given temperature and in an extrinsic regime, the electrical conductivity appeared to have a linear dependence upon the mol fraction of yttrium oxide incorporated during the manufacturing process, whence the authors deduced based on equation 1.1 (and assuming that $[h^\circ]$ ~ mol fraction of yttrium) values of the hole mobility at four different temperatures. This analysis provided an estimate of μ_0 (554 cm^2.K/V.s) and E_H. Similarly in a p-type extrinsic regime, Ruello [162] analysed his conductivity data to estimate E_H for both mechanisms (adiabatic and non-adiabatic). In the former case, he found E_H to be 0.26 eV, in the latter E_H was estimated at 0.31 eV.

There exists a reasonable understanding of electrical properties of UO_2 which can be seen as providing an estimate of the concentration in electronic defects. In particular, it is possible to interpret at least qualitatively the data in terms of charge compensation due to the presence of impurities at low temperatures and oxygen partial pressures. It also appears at high temperatures that this property reflects changes in the oxygen defect populations with clusters emerging rapidly as the oxygen potential rises and so presumably oxygen interstitials and vacancies dominating at lower partial pressures. These qualitative results have however never been rationalised in the framework of a point defect model which is the aim and scope of Chapter 3. We now take a look at properties which potentially provide a more direct estimate of the oxygen defect population.

1.3.2 Self-diffusion and chemical diffusion of oxygen

1.3.2.1 Why study these properties?

We have just seen how electrical conductivity can be regarded as a measure of the electronic charge carrier concentrations and indirectly oxygen point defect concentrations. Self-diffusion properties have a more explicit dependence upon point defect concentrations and in certain cases, their study may provide migration mechanisms and associated energy barriers. Indeed in principle the self-diffusion coefficient may be written as follows (pag. 139 of [153]):

$$D_O^* = \sum_d f_d \cdot N_d D_d \tag{1.3}$$

which represents the sum of contributions over all types of defects on the oxygen sublattice responsible for the diffusion of oxygen and D_d the corresponding defect diffusion coefficient, D_O* the tracer diffusion coefficient of oxygen, N_d the corresponding oxygen defect concentration and f_d the correlation factor corresponding to mechanism *d*. Philibert then goes on to show that assuming a single type of defect responsible for diffusion predominates, then D_O* may be expressed in the following way:

$$D_O^* = \alpha\left(T\right) \cdot pO_2^m \tag{1.4}$$

where $\alpha(T)$ is an exponential function of temperature and *m* is characteristic of the defect and its charge.

Another important property we are interested in is diffusion in a chemical potential gradient otherwise know as chemical diffusion. We may use here Darken's equation in conjunction with the Gibbs-Duhem relation (see [31]) to derive an expression for the chemical diffusion of oxygen $\widetilde{D_O}$, assuming that oxygen self-diffusion is much greater than uranium self-diffusion in uranium dioxide [30]:

$$\widetilde{D_O} = x_U D_O^* \left(1 + \frac{\partial \ln\left(\gamma_O\right)}{\partial \ln\left(x_O\right)}\right) \tag{1.5}$$

where x_U and x_O are the mole fractions of uranium and oxygen and γ_O is the activity coefficient of oxygen in the solid. This activity coefficient is at equilibrium related to the oxygen partial pressure through the relation:

$$\ln\left(x_O \gamma_O\right) = \frac{1}{2} \ln\left(pO_2\right) \tag{1.6}$$

One can then derive an expression for $\ln\left(\gamma_O\right)$ based on equation 1.6 which can be inserted into equation 1.5 to yield:

$$\widetilde{D_O} = x_U D_O^* \cdot \frac{1}{2} \frac{\partial \ln (pO_2)}{\partial \ln (x_O)} \tag{1.7}$$

This equation shows that the chemical diffusion coefficient is a property which relates the self-diffusion coefficient to the thermodynamic factor, which characterises the dependence upon composition of the equilibrium oxygen partial pressure, a property extensively reported in sections §1.1.1 and §1.2.1 and obtainable via thermogravimetric measurements. A review of these properties in relation to UO_2 is now carried out.

1.3.2.2 Self-diffusion

Oxygen self-diffusion involves determining the diffusion coefficient of a tracer atom (usually use the ^{18}O isotope) in a homogeneous sample. Several techniques have been used to set up a tracer-atom concentration profile during a diffusion experiment amongst which the most frequently encountered are:

1. The solid-solid exchange method which involves a diffusion couple made up of two solid samples of identical chemical composition but different isotopic composition. Samples are placed face to face pressed and heated in an inert atmosphere in order to allow the isotopic exchange to take place.

2. The gas-solid exchange method: the sample is annealed under an atmosphere composed of a well defined H_2/H_2O or CO/CO_2 mixture, with one of the oxide gases enriched in ^{18}O. In this case the oxygen partial pressure is determined by one or the other of the following chemical equilibria: $H_2 + \frac{1}{2}O_2 \rightleftharpoons H_2O$ or $CO + \frac{1}{2}O_2 \rightleftharpoons CO_2$.

In both cases the molecular oxygen which results from these equilibria is enriched in ^{18}O, following which gas-solid exchange occurs at the surface of the sample that eventually leads to the establishment of an ^{18}O concentration profile.

The isotopic mixing that has occurred as a result of the diffusion process which determines the concentration profile can then be characterized by Nuclear Reaction Analysis – NRA – (using for example the reactions $^{18}O(p,\gamma)^{19}F$, $^{18}O(p,n)^{18}F$ or $^{18}O(p,\alpha)^{15}N$) [90] or by the Secondary Ion Mass Spectrometry – SIMS – [25, 30, 50, 78, 128, 141, 142]. Once the concentration profile is determined, the data is modelled using Fick's second equation. These methods have been widely used to deduce oxygen diffusion coefficients in near- and hyper-stoichiometric uranium dioxide.

The studies involving purportedly stoichiometric material [25, 30, 90, 128] showed a rather large scatter (see Figure 1.13) which Garcia *et al.* [78] and Dorado, Garcia *et al.* [68] have ascribed to two main factors:

1. In the past, experiments were carried with no particular control of the oxygen partial pressure of the carrier gas or measurement thereof. Using a reducing or neutral atmosphere is certainly conducive to maintaining the material close to stoichiometric composition. However, under those conditions, deviation from stoichiometry is likely to be different from one study to the next or actually be slightly modified as a result of the diffusion annealing process. Small compositional changes will induce very large variations of the oxygen activity in the sample, hence scattered results. The Markin and Bones data at 800°C [129, 130] reveals that a stoichiometry change of 2.5 10^{-3} is equivalent around stoichiometric composition to a four orders of magnitude change in the oxygen partial pressure. Since $D_O{}^*$ is proportional to $pO_2{}^m$ (see equation 1.4) this is likely to lead to large variations in the resulting tracer diffusion coefficient.
2. In the temperature range usually looked at in oxygen diffusion studies (up to about 1000°C) UO_2 behaves extrinsically. Therefore the hole concentration is likely determined by the aliovalent impurity content. Their study showed that this could lead to an extra order of magnitude scatter.

They further showed that by carrying out experiments over a range of oxygen partial pressures and temperatures whilst measuring the relative hole concentration by measuring the electrical conductivity of the samples, that one could rationalise tracer diffusion data obtained for samples containing different impurity concentrations. Indeed, if one assumes the two following mass balance equations (implying only isolated and doubly charged interstitials (negative) and vacancies (positive) coexist):

$$\begin{cases} \frac{1}{2}O_{2(g)} \rightleftharpoons O_i^{"} + 2h^\circ & K_{O_i} = \frac{\left[O_i^{"}\right]\left[h^\circ\right]^2}{\sqrt{pO_2}} \\ O_X \rightleftharpoons V_O^{\circ\circ} + O_i^{"} & K_{AF} = \frac{\left[V_O^{\circ\circ}\right]\left[O_i^{"}\right]}{2} \end{cases}$$

Equation 1.3 may be rewritten as follows:

$$D_O \propto \frac{K_{O_i}\sqrt{pO_2}}{\left[h^\circ\right]^2} \exp\left[-\frac{\Delta H_m^{O_i}}{K_B T}\right] + \frac{2K_{AF}\left[h^\circ\right]^2}{K_{O_i}\sqrt{pO_2}} \exp\left[-\frac{\Delta H_m^{V_O}}{K_B T}\right] \tag{1.8}$$

Where, $\Delta H_m^{O_i}$ and $\Delta H_m^{V_O}$ are respectively the migration enthalpies of oxygen interstitials and vacancies, $[h^\circ]$ the hole concentration, pO_2 the oxygen partial pressure, while K_{O_i} and K_{AF} are respectively the oxygen interstitial and the Frenkel pair formation reaction constants. In an extrinsic regime, $[h^{\circ}]$ is presumably independent of oxygen partial pressure so that at constant temperature, D_O is expected to be proportional to pO_2 to the exponent 1/2 or -1/2 depending on whether the diffusion mechanism is assisted by interstitials or vacancies (see Figure 1.14). This was taken as substanding both the interstitial mechanism for oxygen diffusion and the fact that interstitials are doubly charged, in line with the theoretical results of Crocombette [57] (see section §1.2.2). Based on these data they were also capable of estimating the sum of the oxygen formation and migration energies at roughly 0.6 eV.

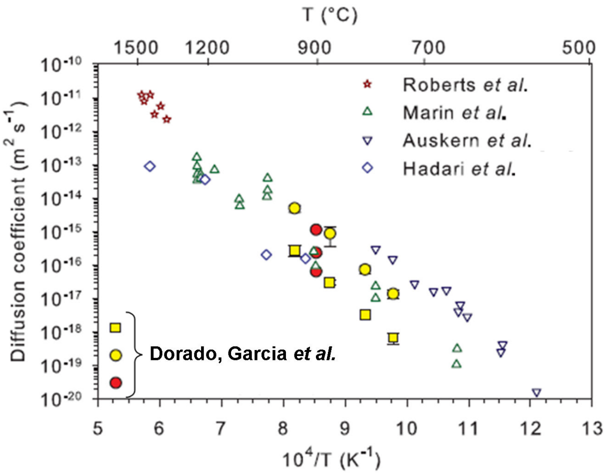

Figure 1.13: Arrhenius dependence of the O self-diffusion coefficient [68, 78]. Yellow circles and squares two UO_2 sample sets containing different impurity levels; red circles concern Cr-doped samples

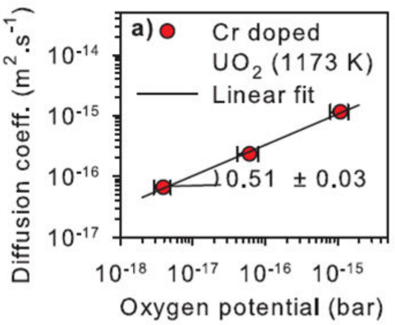

Figure 1.14: Oxygen diffusion coefficient dependence upon oxygen partial pressure evaluated at 1173 K for a Cr-doped UO_2 sample in an extrinsic regime [68].

Work has also been extensively carried out at higher deviations from stoichiometry.

In much the same way as for most of the stoichiometric work, self-diffusion was studied as a function of deviation from stoichiometry: Figure 1.15 represents the dependence of D upon x as reported by Contamin *et al.* [50] or reviewed by Belle [30].

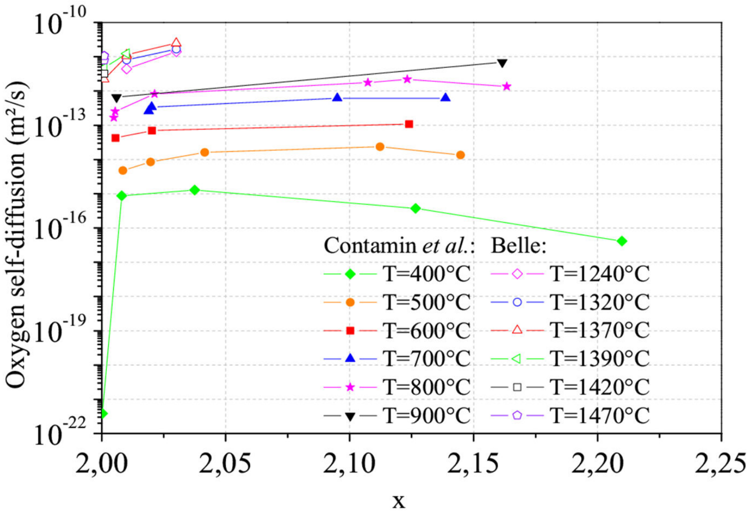

Figure 1.15: Dependence of oxygen self-diffusion coefficients upon deviation from stoichiometry: represented data are reported by Contamin *et al.* [50] and by Belle [30].

As shown in Figure 1.15, deviation from stoichiometry induces a strong increase in oxygen diffusion coefficients; however, all the authors [25, 30, 50, 128, 141, 142] agree that oxygen self-diffusion levels off beyond deviation from stoichiometry values of roughly 0.01. Few if any quantitative interpretations for these dependences have been proposed connecting the property to the nature of the defects responsible for oxygen self-diffusion. In particular no clear relation is made between the self-diffusion coefficient and the clustering of oxygen interstitials which inevitably occurs (as seen experimentally from electrical conductivity and neutron diffraction studies) in the range of deviation from stoichiometry reported in these studies. One qualitative explanation could be that as deviation from stoichiometry increases then so does the proportion of oxygen clusters with regard to the free oxygen interstitials responsible for diffusion.

On the strength of successes encountered with the studies involving oxygen tracer diffusion measurements as a function of oxygen partial pressure, it is probably worth conducting similar work at higher and lower oxygen partial pressures in an attempt to ascertain the influence either of oxygen vacancies or clusters on oxygen diffusion. Such a study is described in Chapter 4.

1.3.2.3 Chemical diffusion of oxygen

The oxygen chemical diffusion coefficient may be derived from the kinetics required for a sample to incorporate oxygen atoms as a result of a sudden increase of the equilibrium oxygen partial pressure. This may be done through thermogravimetric measurements [107] or as is more commonly found through electrical conductivity measurements. Jost *et al.* [104] have demonstrated that in the long time approximation, the conductivity change with time of the electrical conductivity of a parallelepipedic sample is related to the oxygen chemical diffusion coefficient by the following relationship:

$$\frac{\sigma(t)-\sigma_\infty}{\sigma_0-\sigma_\infty}=\left(\frac{8}{\pi^2}\right)^3\exp\left[-\pi^2\cdot\left(\frac{1}{a^2}+\frac{1}{b^2}+\frac{1}{c^2}\right)\widetilde{D_O}t\right] \tag{1.9}$$

Here σ is the conductivity at time t, σ_∞ and σ_0 are the asymptotic and initial conductivity values, is the initial value, $\widetilde{D_O}$ is the chemical diffusion coefficient, while a, b and c are the sample dimensions. The disadvantage of this method lies in the fact that the range of temperatures and oxygen partial pressures in which the conductivity is extrinsic is inaccessible.

Ruello [162] made some measurements of oxygen chemical diffusion in UO_{2+x}, within 2 different ranges in values of x: the first covers values between 0.005 and 0.01, while the second one covers values between 0.1 and 0.2. The results (reported in Figure 1.16) show that oxygen chemical diffusion coefficients follow roughly an Arrhenius dependence upon temperature and are strongly dependent upon the actual value of deviation from stoichiometry of the sample.

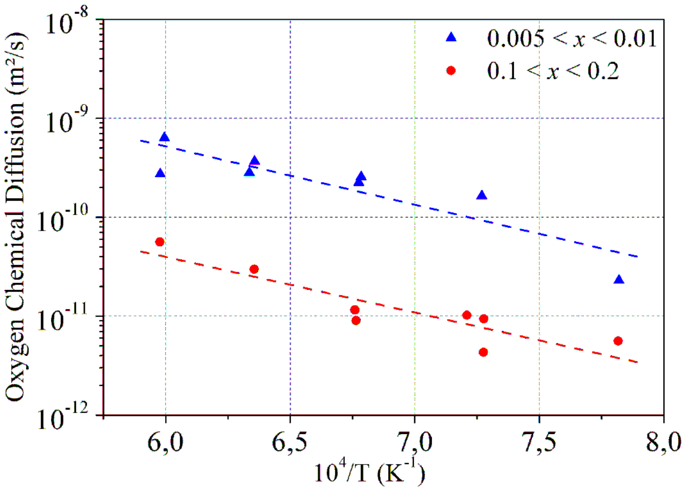

Figure 1.16: Arrhenius dependence of oxygen chemical diffusion coefficients evaluated by Ruello [162]

As illustrated in Figure 1.16, the chemical diffusion coefficient decreases as deviation from stoichiometry increases. Based on an asymptotic point defect model which assumes di-interstitial clusters to constitute the majority defect population, Ruello [162] estimates that the chemical diffusion coefficient should be roughly proportional to the ratio of the self-diffusion coefficient over deviation from stoichiometry x. Assuming the self-diffusion coefficient to level off above deviation from stoichiometry values of about 0.01, one would expect, from the $\frac{1}{x}$ dependency of the chemical diffusion coefficient, that it should decrease by about one order of magnitude when x increases by approximately the same amount. This is indeed what is observed in Figure 1.16.

As in self-diffusion studies, it would be interesting to analyse the dependence upon the oxygen partial pressure of the chemical diffusion coefficient.

1.3.3 Conclusions

We have shown here how electrical conductivity and atomic transport properties are intimately related to point defect populations in the crystal. Electrical conductivity reflects electronic defect concentrations. The study of such a property is important for three reasons: firstly under extrinsic conditions, it can help us evaluate the negatively charged substitutional cation impurity concentration and study the hole mobility. Secondly, electrical conductivity measurements under out-of-equilibrium conditions in an intrinsic regime enable us to study oxygen chemical diffusion as a function of oxygen partial pressure or sample composition. Finally, in the context of evaluating oxygen point defect concentrations via atomic diffusion measurements, the more important reason for measuring the electronic conductivity of a sample is to evaluate under precise temperature and oxygen partial pressure conditions the hole concentration, which enters in an equilibrium with anionic defects.

Another useful property for studying oxygen defect populations in UO_2 is to measure oxygen self-diffusion coefficients and combining these to electrical conductivity measurements. From the point of view of methodology, Garcia *et al.* [78] and Dorado, Garcia *et al.* [68] have demonstrated that analysing the dependence of oxygen self-diffusion coefficients upon oxygen potential is the better suited in the near stoichiometric composition region than monitoring oxygen content.

1.4 Conclusions

Many years of research have provided us with a great deal of knowledge about the U-O system, be it in terms of phase diagram (section §1.1.1), the nature of point defects (section §1.2), equilibrium properties (deviation from stoichiometry, electrical or atomic transport properties, section §1.3) or electronic structure (section §1.1.2). However, the most relevant phase from a technological standpoint remains the UO_{2+x} phase and there is no comprehensive analysis available that would enable us to connect a description of equilibrium properties (deviation from stoichiometry, electrical and atomic transport properties...) with the more recent electronic structure calculations via a point defect model. We have seen that this model should account for the presence of various electronic and charged point defects (section §1.2.1) and the clustering of interstitial oxygen ions (sections §1.1.1.3 and §1.2.2) and that electronic disorder should prevail over disorder on the oxygen sub-lattice. The aim of Chapter 3 is indeed to attempt to set up such a model which will constitute a useful guide for the remainder of this work.

There exists little quantitative data relating to the nature and concentration of the majority defect population in the UO_{2+x} phase and a picture of this emerges in Chapter 3. In order to build upon this picture and on the strength of results obtained in past for UO_{2+x} compositions close to stoichiometry, we have chosen to focus on two areas that are poorly documented in the literature: the range of oxygen partial pressures in which oxygen vacancies are present and conditions (based on results from Chapter 3), not far removed from the stoichiometric composition in which the majority defect population changes from isolated anion interstitials to oxygen clusters. Oxygen defects are monitored by combining electrical conductivity and self- or chemical diffusion experiments applied to samples containing different quantities of impurities. As seen in section §1.3, it is important to monitor experiments as a function of oxygen partial pressure as opposed to composition. Having presented the details of the experimental techniques used in the course of this work in Chapter 2, we go on to describe the results of the diffusion and electrical conductivity experiments in Chapter 4.

We have also seen in this chapter that oxidation of the material is accompanied by a change in the valence of uranium ions, a shortening of U-O bonds, both of which are manifestations of changes in the electronic structure of the material. In an attempt to characterise this, Chapter 5 is devoted to XAS experiments at the O K-edge and U N-edges that should, in addition to providing information about the electronic structure of the material as a function of oxygen contents, provide us with a detailed insight into rearrangements at the atomic scale. The aim that underpins this work is to correlate modifications of the transport properties observed in Chapter 4 with changes in the electronic structure. Results from Chapters 4 and 5 are interpreted in Chapter 6 using the approach in Chapter 3 as a guide.

Chapter 2

Materials and Methods

Measuring the atomic transport properties of UO_{2+x} constitutes an efficient means of understanding more about the nature and the behaviour of point or complex defects in the material. This type of measurement however requires properties to be measured as a function of the thermodynamic conditions, *i.e.* temperature and equilibrium oxygen partial pressure. We have seen that the sample impurity content also plays an essential role and that electrical properties may constitute a way of assessing the role of cation impurities. As a result of this we first focus in this chapter upon the techniques used for characterising the material properties carried out in the remainder of this work: oxygen diffusion and electrical properties. Because atomic diffusion is based upon characterisation of ^{18}O concentration profiles, a section is devoted to depth profiling using SIMS.

Also, as shown in section §1.1, the oxidation of UO_2 will modify the charge of uranium cations lead to structural changes and eventually the formation of new oxide phases. In this work structural changes due to oxidation was probed by X-Ray Diffraction (XRD). Variations in electronic density of states were characterised by X-ray Absorption Spectroscopy (XAS).

This chapter proposes firstly a detailed description of the sample preparation and annealing conditions under controlled atmospheres. The characterization techniques mentioned in this introduction are then detailed.

2.1 Sample characteristics and preparation

In this work we used two different types of polycrystalline samples: either pure or Cr-doped UO_2. Both kinds of samples were sliced from cylindrical pellets of 8.2 mm in diameter and roughly 1 cm in height. Undoped pellets were obtained by sintering a UO_2 powder at 1700°C under a dry Ar/5% H_2 atmosphere. These pellets have a theoretical density of roughly 98% of the theoretical value (10.96 g/cm^3) and a mean grain size of 6 µm. The Cr-doped UO_2 pellets were fabricated adding 1990 ppm of Cr_2O_3 to the UO_2 powder before the sintering process, performed at 1760°C under an oxygen potential of -396 kJ/mol. Chromium addition led to the growth of the grains to a size of *circa* 200 µm, probably as a consequence of the presence of a liquid CrO phase during sintering [73, 134]. Following sintering, Cr-doped UO_2 pellets were annealed at 1765°C under an oxygen potential of -392 kJ/mol (Ar/5%H_2 with 1240 ppm of H_2O). Figure 2.1 represents the thermodynamic conditions under which the thermal annealing cycles were carried out.

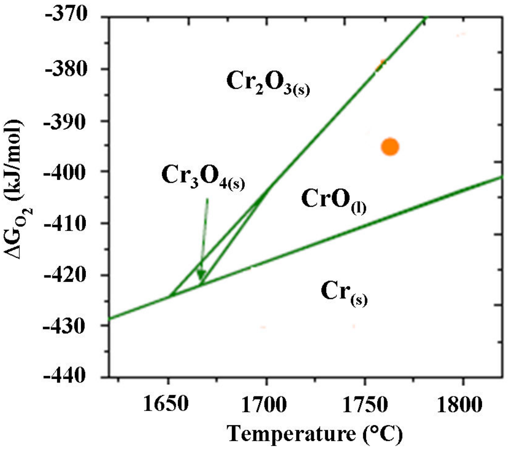

Figure 2.1: Thermodynamic conditions under which Cr-doped pellets were sintered and annealed (dot) as regards to the Cr-O predominance diagram [134]

To obtain our samples, these pellets were sliced into disks of 1 mm thickness. Each sample was then progressively polished with silicon carbide polishing disks of decreasing abrasive size and finally with a diamond paste with a 1 µm grain (mirror polishing). In addition, some Cr-doped samples were submitted to another polishing step carried out with a colloidal silica suspension of 50 nm of granulometry (OPU). Between each polishing step, the samples were placed in ethanol and cleansed using ultrasounds for three minutes at ambient temperature. Specimens used for electrical conductivity characterisations were cut into parallelepiped shapes, the faces of which were carefully polished only with the least abrasive silicon carbide polishing disk we had.

2.2 Oxygen diffusion experiments under controlled oxygen potential

In this work, when studying oxygen diffusion in UO_2, the sample oxygen composition has been controlled by controlling annealing conditions. Annealing cycles were performed in a furnace equipped with a system that constantly monitors the oxygen partial pressure in situ. We now present the experimental device (and its oxygen potential control system) used to anneal the samples dedicated to oxygen diffusion studies.

2.2.1 Thermal treatment device

The samples dedicated to the study of oxygen diffusion were submitted to two annealing stages. The first drives the oxide to a given composition by exposing it to an atmosphere with well controlled temperature and oxygen potential. The second is carried out under the same thermodynamic conditions but under an atmosphere enriched in ^{18}O. Chemical reactions at the sample surface enable an ^{18}O enrichment of the samples which sets up an isotopic concentration gradient or diffusion profile.

For this purpose, the oxygen diffusion setup was equipped with the following elements:

1. a furnace that consists of a hot zone in which the samples are annealed, and a cold zone, in which samples are moved to after extraction from the hot zone

2. a quenching system, which consists of a platinum sample holder mounted upon an alumina rod which enables a rapid transfer of the samples from the hot to the cold zone of the furnace. Samples are quenched so that their composition, and it is hoped their microstructure, remains unchanged with respect to the high temperature annealing conditions.

3. the oxygen potential control system, that consists of a zirconia probe. Depending on the device layout, it can be placed either inside the furnace in close proximity to the sample or in a furnace maintained at an optimal temperature through which the main gas flow may be diverted.

4. a gas mixture controller, composed of 4 fluxmeters that control the fluxes of the gases (Ar or Ar/10%H_2) sent into the furnace

5. two bubblers, one filled with distilled water, the other with water enriched to 98% of ^{18}O. When the gas mixture passes through a bubbler, it

is assumed that the water vapour pressure equilibrates to its equilibrium value.

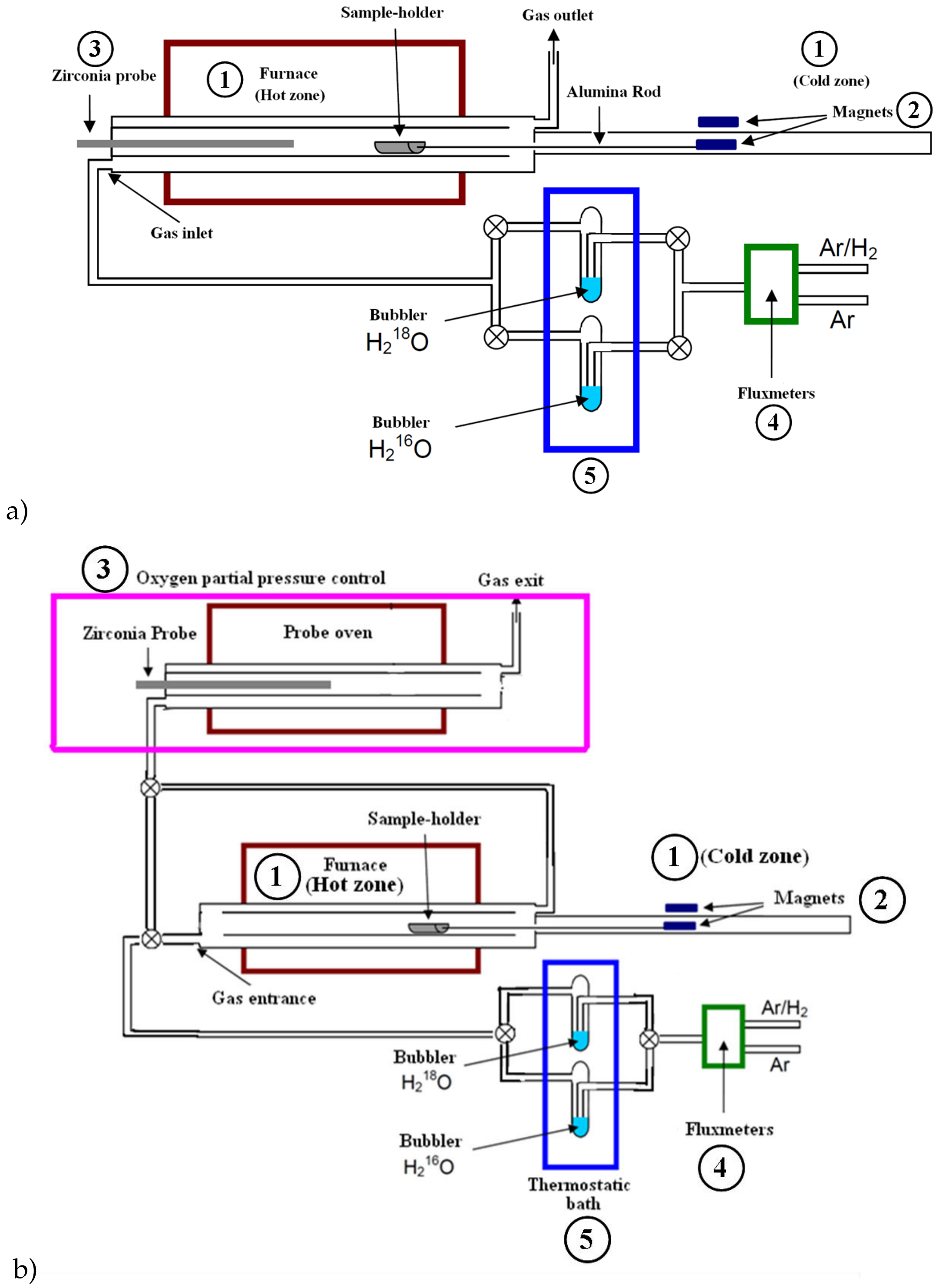

Figure 2.2: The oxygen diffusion setup with the zirconia probe placed in a standard (a) or in a “bypass” (b) configuration.

The oxygen diffusion setup was applied in two different configurations, schematically represented in Figure 2.2. At the beginning, the zirconia probe was placed at one extremity of the furnace (see Figure 2.2a)). The zirconia probe was later placed in a furnace maintained at 900°C which is the optimal temperature for probe operation, to which the main gas flow may be diverted. After this important change in configuration, a system calibration was performed. Section §2.2.2 reports how the response of the device to different gas compositions was evaluated.

In this oxygen diffusion setup, the oxygen partial pressure is fixed throughout the system by the redox couple H_2/H_2O (both of which are of course in a gaseous form) present in the Ar and Ar/10%H_2 mixture and which picks up water vapour after going through the bubblers. The hydrogen partial pressure is determined by the Ar and Ar/10%H_2 flow rates. The water vapour pressure is determined by the temperature at which the bubblers are maintained. The oxygen partial pressure is determined by the local temperature in the furnace (providing this temperature is high enough) and is fixed by the following equilibrium: $H_{2(g)} + \frac{1}{2}O_{2(g)} \rightleftharpoons H_2O_{(g)}$ (see Appendix A). The resulting oxygen partial pressure should not depend upon the oxygen isotope which composes the water molecules present in the bubblers [21]. The oxygen potential in the furnace atmosphere is constantly monitored by the zirconia probe.

2.2.1.1 Operation of a zirconia probe

This kind of gauge is in fact an electrochemical cell which consists of two Pt or Pt-Rh electrodes placed on either side of a purely ionic conductor. The ionic conductor in our case is made up of yttria doped zirconia (YSZ). Doping serves the dual purpose of stabilizing a particular form of zirconia and fixing via charge compensation processes the oxygen vacancy concentration. This gives the oxides ionic conducting properties at least up to 1100°C. Both sides of the electronic conductor are exposed to atmospheres of differing oxygen content only one of which is known and which constitutes the reference electrode. The following Figure schematically shows its functioning principle:

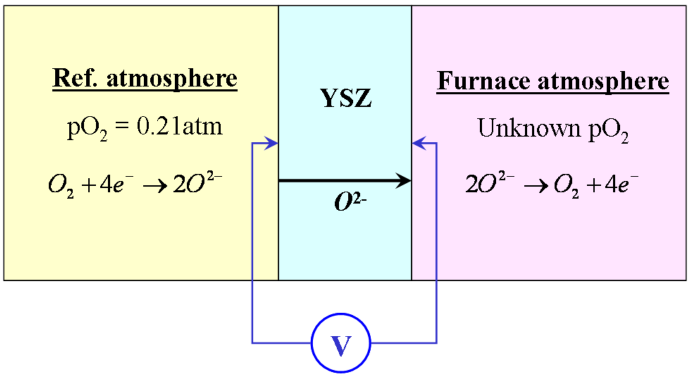

Figure 2.3: Functioning of a zirconia probe.

The following reaction occurs at both electrodes [41, 152]:

$$O_2 + 4e^- \rightleftharpoons 2O^{2-} \tag{2.1}$$

The oxygen potential difference on either side of the conductor creates a flux of oxygen ions across the thickness of the zirconia probe. In the present case, the reference atmosphere is simply air, the oxygen partial pressure of which is 0.21 atm. The other side of the probe is in contact with the furnace atmosphere, the oxygen partial pressure of which has to be measured. A potential drop across the ionic conductor ΔV is set up which is determined by the electrical properties of the electrolyte and the chemical potential of oxygen on either side of the electrolyte :

$$\Delta V = -\frac{t_{ion}}{n\mathcal{F}}\left(\mu_{O_2} - \mu^0_{O_2}\right) \tag{2.2}$$

This potential drop ΔV may be monitored using a high impedance voltmeter. With this type of device, measurements of the electrical potential difference are reliable as they are not affected by electrical contact resistances. Here, n is the number of electrons involved in the redox reaction (4 in this case according to Equation (2.1)), $\mathcal{F}$ is the Faraday constant, μ_{O_2} is the unknown oxygen potential that we are seeking to determine and $\mu^0_{O_2}$ is the oxygen potential of the reference atmospheres, while t_{ion} is the YSZ ionic number which represents the ratio of the ionic conductivity to the total conductivity [111]. Within the 650°C-1000°C temperature range , t_{ion} is equal to 1, *i.e.* the electronic contribution to the total conductivity is negligible.

If the probe is inserted into an oven maintained at constant temperature (900°C in the bypass configuration of oxygen device), both sides of the probe are at the same temperature. With this condition and expressing the oxygen activity as $\mu_{O_2} = RT\ln(pO_2)$, it comes:

$$\Delta V = \frac{RT}{4\mathfrak{F}}\ln\left(\frac{pO_2^0}{pO_2}\right) \tag{2.3}$$

which is also known as the Nernst relationship [153]. Knowing the oxygen partial pressure of the reference atmosphere and the electrical potential drop ΔV across the solid electrolyte, it is possible from Equation 2.3 to estimate the oxygen potential of the furnace atmosphere.

2.2.2 Calibration of the setup in bypass configuration

2.2.2.1 Oxygen partial pressure

Oxygen partial pressure in the furnace is dependent upon the temperature and the partial pressures of water and hydrogen in the gas stream. Appendix A explains in detail how pO_2 is estimated from the various experimental conditions, *i.e.* the gas flow rates and the temperature at which the bubblers operate. We report here the simplified relationship used to estimate pO_2:

$$pO_2^f = r^2\left[\frac{pH_2O}{(1-pH_2O)\cdot K(T_f)}\right]^2 \tag{2.4}$$

Where pO_2^f is the oxygen partial pressure at temperature T_f, pH_2O is the water partial pressure assumed to be roughly equal to the saturation water pressure at the temperature at which the bubblers are maintained (roughly 278 K), $K(T_f)$ is the water formation equilibrium constant at furnace temperature T_f: its value is determined from well reported relationships [116]; *r* is the ratio of the hydrogen and argon flow rates over the hydrogen flow rate:

$$\frac{1}{r} \equiv \frac{0.1\cdot \dot{V}_{Ar/10\%H_2}}{\dot{V}_{Ar}+\dot{V}_{Ar/10\%H_2}} \tag{2.5}$$

where $\dot{V}_{Ar}$ and $\dot{V}_{Ar/10\%H_2}$ are the argon and the Ar/10%H_2 flow rates respectively.

Relationship 2.4 shows that the oxygen partial pressure may be estimated from

1. Flow rate values

2. The saturation water vapour pressure which is dependent upon the temperature at which bubblers operate

3. The equilibrium constant for the formation of water vapour from reaction between oxygen and hydrogen

In order to qualify the setup, it is important to ascertain the extent to which relationship 2.4 is valid. We therefore measured for different *r* values, obtained for different values of the Ar and Ar/10%H_2 flow rates, the oxygen partial pressure with our zirconia probe maintained at 900°C and compared it to the theoretical value obtained from application of relationship2.4. The results are plotted in Figure 2.4.

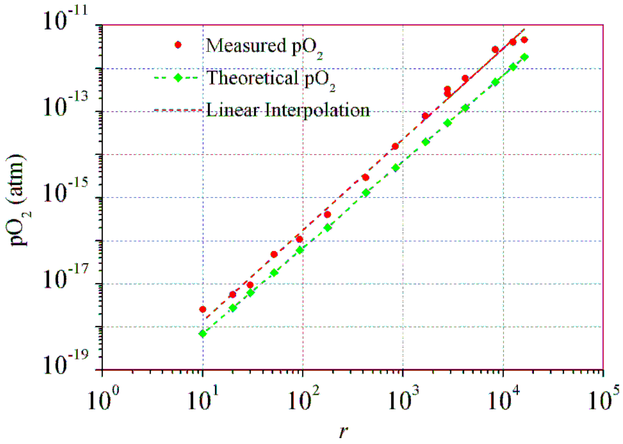

Figure 2.4: Comparison between the oxygen partial pressures that were measured and calculated with the theoretical formula 2.4.

In this log-log representation, experimental values are roughly aligned and the slope of the corresponding line has been estimated at 2.11 (±0.04), as expected from Equation 2.4. This calibration shows that the setup enables oxygen partial pressures to be adequately controlled over practically seven orders of magnitude. However there appears to be a systematic deviation between theoretical and experimental values which is difficult to explain. It could be ascribed to contact resistances between the electrodes and the solid electrolyte. However an offset was set on the voltmeter whilst measurements were carried out under air, so that the electrical potential drop under those conditions was zero. Nevertheless this qualification is deemed adequate in view of the fact that properties we intend to measure are usually dependent upon oxygen partial pressures via a power law. The crucial issue is the value of the exponent which will be no different if oxygen partial pressures are measured to within a constant factor.

2.2.2.2 Control of the temperature in the furnace

The sample holder itself is not equipped with a thermocouple. However the resistance furnace is and this thermocouple is closer to the resistances than the samples are and does not provide a satisfactory estimate of the temperature inside the quartz tube. It is therefore necessary to determine the relationship between the temperature in the hot zone of the furnace (*i.e.* where the samples are placed) as a function of the temperature picked up by the thermocouple of the furnace. To this end, a type K thermocouple is inserted in the hot zone of the furnace where the sample holder is meant to sit. Under different Ar fluxes, the furnace temperature is then progressively increased from 760°C to 1027°C and the temperature measured by the type-K thermocouple recorded. Interpolation of the measured values provides a linear relationship which is then used to determine the sample temperature T_{sample} based on the temperature measured by the furnace thermocouple T_{fc}:

$$T_{sample} = 0.9209 \cdot T_{fc} + 41.603 \tag{2.6}$$

We checked that the sample temperature was unaffected by variations in gas flow rates in the range of those that were used throughout this work. The uncertainty related to the annealing temperature measure is only related to the capability of the furnace to maintain temperature T_{fc} at a stable value. This uncertainty is estimated to be ±5°C.

2.3 Electrical conductivity measurements

Electrical conductivity measurements are carried out under controlled thermodynamic conditions. They provide equilibrium concentrations of the electronic defects present in UO_2 samples. This section describes the four-point bridge method used to perform the measurements.

2.3.1 Physical principle

Electrical conductivity measurements are performed using a double Kelvin Bridge [1] and the 4-point method. The corresponding electrical circuit is shown in Figure 2.5.

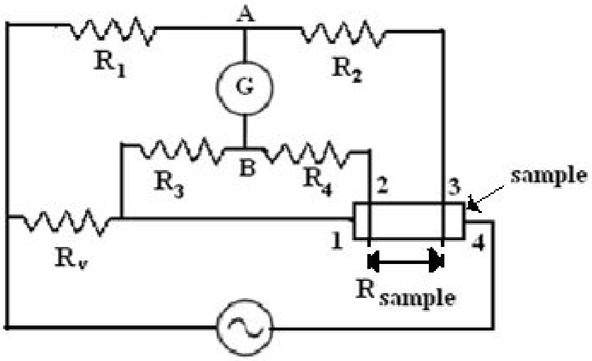

Figure 2.5: Schematic diagram of the double Kelvin bridge used to measure the sample resistance (between the contacts 2 and 3).

The 4-point method consists in evaluating an unknown resistance (R_{sample}) by adjusting the variable resistance R_v until the bridge is completely balanced (*i.e.* until the potential difference between the nodes A and B in Figure 2.5 is zero). If the resistances also fulfil the condition $\frac{R_1}{R_2} = \frac{R_3}{R_4}$, the sample resistance can be calculated using the following relationship:

$$R_{sample} = R_v \cdot \frac{R_1}{R_2} = R_v \cdot \frac{R_3}{R_4} \tag{2.7}$$

In practice, R_1 and R_2 are much greater than R_v and R_{sample}, in order that most of the current passes through the sample. The bridge is also sensitive to small sample resistances if R_3 and R_4 are lower than R_1 and R_2. But, in this case, the contributions of the contact resistances are no longer negligible. For this reason, R_3 is usually set equal to R_1, and R_4 to R_2.

2.3.2 Presentation of the device

The device used for electrical conductivity measurements (shown in Figure 2.6) is based on the electrical circuit represented in Figure 2.5.

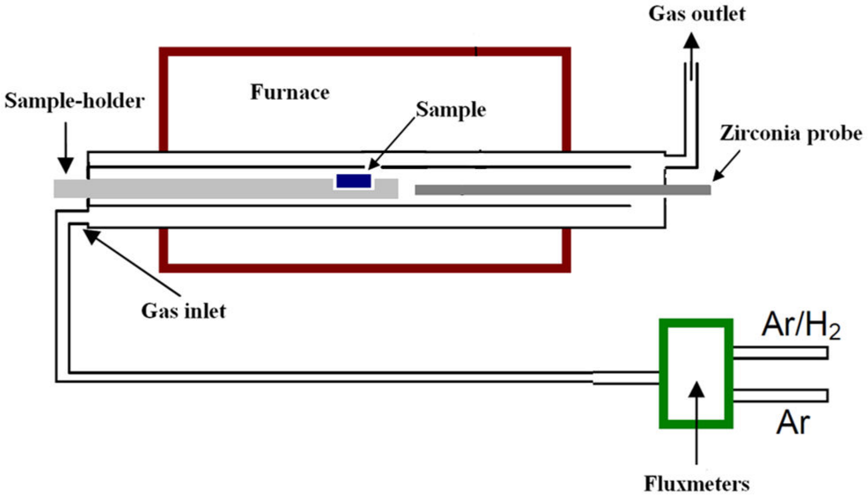

Figure 2.6: Schematic diagram of the device used for electrical conductivity masurements.

The sample-holder is inserted into the alumina rod shown in Figure 2.6. This element is placed in a dedicated furnace in order that electrical conductivity measurements be carried out at high temperatures (up to 1600°C). The control of the oxygen potential of the atmosphere surrounding the sample is carried out using a zirconia probe, located in the furnace just after the specimen. Contacts 1 and 4 are platinum meshes between which the samples are clamped. Contacts 2 and 3 are made of two Pt wires wrapped around the sample: they have to be parallel so that the cell coefficient may be calculated simply and to adhere properly to the parallelepipedic sample faces. All contacts 1, 2, 3 and 4 are connected to the bridge by additional Pt wires. Calibrated electrical resistances are used for R_1, R_2, R_3 and R_4: in our case, R_1 and R_3 are equal to 100 kΩ, and R_2 and R_4 to 1 kΩ. R_v is a variable resistance that can reach at maximum 1 kΩ. The bridge is balanced with the help of a lock-in amplifier. This electronic component is also the generator of the electric signal that supplies the bridge. The principle of the method is to multiply an AC signal provided by the generator with the voltage difference that we wish to measure and to integrate the resulting signal over time. The system relies upon the orthogonality properties of sinusoidal functions and eventually enables the low signal (tension AB) intensity to be properly amplified. This guarantees an optimal system sensitivity and enables low currents to be extracted from the noise which do no more interfere with the actual measurement [2, 3].

2.3.3 Uncertainty associated to an electrical conductivity measurement

Generally sample electrical conductivity is estimated through the following relationship [73]:

$$\sigma = \left(\frac{1}{R_{sample}} \cdot \frac{l}{S} \right) \cdot \frac{1}{(1 - f_{por})} \tag{2.8}$$

Here, σ is electrical conductivity, f_{por} is the fraction of porosity in the sample (2% in our case - see §2.1), while R_{sample}, l and S are respectively sample resistance, length and surface measured between the contacts 2 and 3 (see Figure 2.5).

Following Equation 2.8, sample electrical conductivity is therefore determined by measuring R_{sample}, l and S:

- R_{sample} is reliably measured with the double Kelvin bridge (see §2.3.1). Its relative uncertainty mainly corresponds to the ratio between its value and the resistance of contacts wrapped on the sample [73]. Supposing the contact resistance and R_{sample} respectively of the order of 1 kΩ and 1 Ω, sample resistance would have a relative uncertainty of 10^{-3} and can be neglected in the data analysis.

- Sample section S is directly measured once specimen is prepared.

- Distance l is measured once sample is placed in the sample-holder (see Figure 2.7).

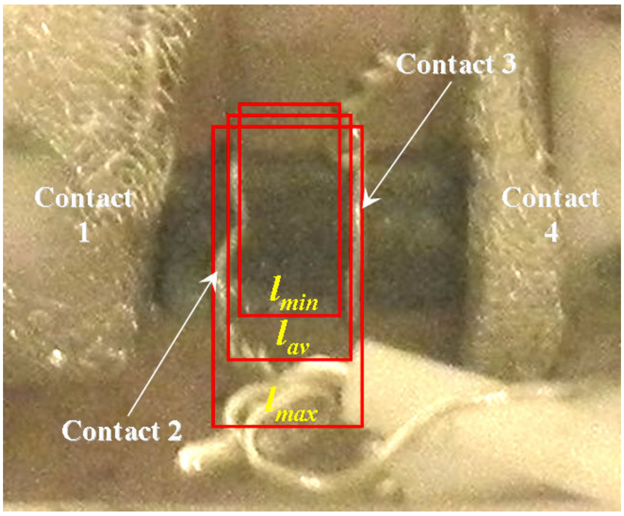

Figure 2.7: Measurement of the distance between contact 2 and 3 wrapped on a parallepipedic UO_2 sample.

As indicated in Figure 2.7, the *l* estimate is based on the measurements of the average, the minimum and the maximum distance between the Pt wires constituting contacts 2 and 3. The average value of *l* enables us to simply estimate an average value of sample electrical conductivity; measure uncertainty rather depends on the extreme values of *l* and it usually reaches 10-15%. This method of distance evaluation therefore constitutes the major source of uncertainty of an electrical conductivity measurement. Moreover, besides this systematic error, Pt wire positions can vary during a sample anneal caused by sample thermal dilatation and Pt wire creep.

2.4 Sample characterization techniques

This paragraph presents all the techniques used to characterize the polycrystalline UO_2 samples studied in this work.

2.4.1 X-Ray Diffraction (XRD) and its application to our polycrystalline samples

X-ray diffraction (XRD) [87, 150] is a non-destructive technique used to identify the crystalline structure of solid materials, *i.e.* it is sensitive to the long range ordering of atoms. It basically uses Bragg's law which relates the wavelength λ of the incident X-Rays, the angle between the incident and diffracted X-Rays $2\cdot\vartheta_{hkl}$ and the inter-reticular distance d_{hkl} between planes of Miller indices (*h*, *k*, *l*):

$$2d_{hkl}\sin\left(\theta_{hkl}\right) = n\cdot\lambda,\ \ n\,\epsilon\,\mathbb{N} \tag{2.9}$$

where *n* is an integer.

Measuring the intensity of X-rays diffracted by a single crystal sample requires a complex instrumentation. Indeed, for single crystals, diffraction only concerns a few points located on a sphere centred on the sample. Specific configurations between the X-ray source, the sample and the detection system are required so that the Bragg conditions be verified. For polycrystalline samples on the other hand, many crystalline orientations can be found within the specimen and in the ideal case (referred to as "powder") it can be assumed that diffracted rays form a cone only defined by the diffraction angle associated with an (*h*, *k*, *l*) Bragg line and the vector normal to diffracting planes. Therefore for polycrystalline sample analyses, movement between the source, the sample surface and the detector can be significantly simplified: basically the source and detection system only need to move around a circle with sample in its centre.

Laboratory diffractometers have X-ray sources often based on a Coolidge tube principle[1]. In this work a Bruker D8 advance diffractometer located at the "Laboratoire UO_2" facility at the Cadarache nuclear centre was used. It is equipped with Cu tube which delivers two characteristic lines (Cu $K_{\alpha 1}$ and Cu $K_{\alpha 2}$, respectively equal to 8046.6 and 8026.7 eV).

We have used two distinct configurations for analysing our samples. The first and more common setup involves what is known as the Bragg-Brentano geometry or "ϑ-2ϑ" configuration (see Figure 2.8) in which the detector moves with respect to the sample on a circle centred on the sample. This results in different volumes being probed at each angular position and requires of course the samples to be homogeneous. In the case where one wishes to characterise surface effects, a different setup known as "ϑ_{in}-ϑ_{out}" is used. In this configuration, the incident X-Ray beam angle is fixed with respect to the sample at a low value (typically a few degrees) and an angular detector scan enables X-Rays diffracted by different atomic planes to be intercepted.

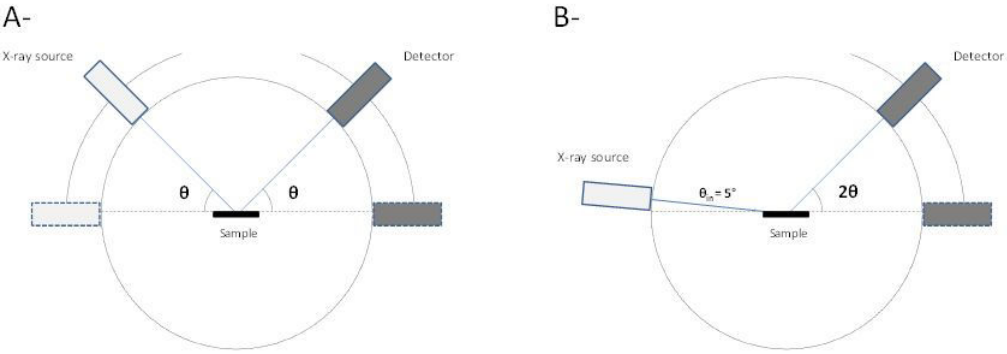

Figure 2.8: The Bragg-Brentano configuration in the "ϑ-2ϑ" (A) or in the "ϑ_{in}-ϑ_{out}" (B) XRD analysis.

Different detectors were used for both data collection configurations (low incidence angle, 5°, and "ϑ-2ϑ" scans).

Regarding the low incidence angle configuration, a point detector was used whereas a 1D solid state LYNX EYE detector was preferred for the "ϑ-2ϑ"

---

[1] The Coolidge tube is composed of a tungsten cathode and a metallic anticathode (composed for example of Mo, Cu, Co or Fe). The electrons emitted from the cathode hit the anticathode provoking the emission of X-rays. Their energy spectrum is characterized by characteristic lines (K_α and K_β) of the metal composing it and by the *bremmstrahlung* radiation. A superimposed filter removes the background radiation and selects the monochromatic X-rays of energy K_α. Remark however that at the exit of the Coolidge tube the X-rays have two energetic components, called $K_{\alpha 1}$ and $K_{\alpha 2}$, that differ in energy less than 20 eV and that the filter cannot separate.

scans. In our experiments, we collected diffraction patterns on different uranium oxide phases both in the "ϑ-2ϑ" and in "ϑ_{in}-ϑ_{out}" configurations. In all cases, the sample was set in rotational motion around an axis perpendicular to its surface during the data collection in order to ensure good sampling statistics.

The intensity of rays diffracted by a given (*h*, *k*, *l*) set of planes is actually proportional to the square of the norm of the structure factor corresponding to this family of planes. This factor is entirely determined by where (location) and what (site occupancy and atomic number) atoms are present in the diffracting planes. Analysing XRD diffraction patterns requires determining a structural model that best reproduces the intensity of diffracted rays.

The XRD diffraction patterns were quantitatively analysed using the Rietveld method [4] which enables this optimisation process to be carried out[2]. The Fullprof software package [5] was used to deduce sample compositions and phase lattice parameters.

We have shown using Electron Backscattered Diffraction that our polycrystalline samples did not exhibit any texture [154]. It is also important to note that the grain size of our undoped samples is roughly 6 µm whilst a millimetre size X-Ray beam is used in our analyses. As a result, XRD analyses on these samples may be considered as powder diffraction.

2.4.2 X-Ray Absorption Spectroscopy (XAS)

Unlike XRD technique, X-ray Absorption Spectroscopy (XAS) is sensitive to the short-range ordering of atoms constitutive a solid target [147]. In particular, this characterization technique measures the absorption of X-rays by various atoms in a sample depending on the incident X-ray energy. During a XAS spectrum collection, monochromatic X-rays are sent to the sample to induce atomic excitations through the photoelectric effect. When this phenomenon is activated, X-rays have a sufficient energy to let some core-electrons reach the energy continuum (Figure 2.9a)). Once excited, the atoms tend to come back

---

[2] The Rietveld method consists in a simulation of the diffractogramme peak intensities, positions and widths to obtain information on the microstructure and composition of a sample. The simulation takes into account the experimental setup, the reflections of sample phases, sample X-ray absorption and diffusion and the radiation background. The theoretical curve that best simulates the experimental XRD spectra is found by minimising X^2, *i.e.* the difference between the measured data and the calculated intensities:

$$\chi^2 = \sum_i w_i \cdot \left[y_{i,exp} - y_{i,cal}\left(\vec{\beta}\right)\right]^2 \tag{2.10}$$

where i is the number of experimental points, w_i is the inverse of the variance associated to the $y_{i,exp}$ experimental observations, $y_{i,cal}$ is the simulated value dependent on the model parameters $\vec{\beta}$.

in their ground state: their electrons drop from their higher energetic levels to fill the core-holes created by the X-ray absorptions. The energy released from this de-excitation process leads the atoms either to emit X-rays of a well defined energy (de-excitation by fluorescence - see Figure 2.9b)) or to promote a second electron into the energy continuum (Auger effect - see Figure 2.9c)).

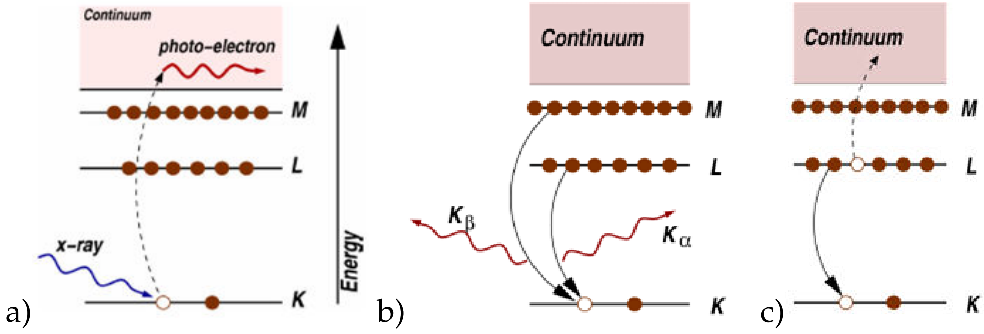

Figure 2.9: Atom excitation by X-ray absorption (a) and subsequent de-excitation by fluorescence (b) or by the Auger effect (c).

As already said, after the excitation process, the photo-electrons travel into the energy continuum. The photo-electron wavefunctions (the wavelengths of which are dependent upon their kinetic energy) propagate in the local environment of the excited atoms. The electrons of their neighbouring atoms can scatter the travelling photo-electrons inducing their retrodiffusion. This phenomenon modulates the amplitudes of the photo-electron wavefunctions and modulates the X-ray absorption probability of the absorbing atoms. In this sense XAS (in particular with the EXAFS spectra) is an atomic probe and can provide a practical way to determine the chemical state and local atomic structure for a selected atomic species (see Figure 2.10).

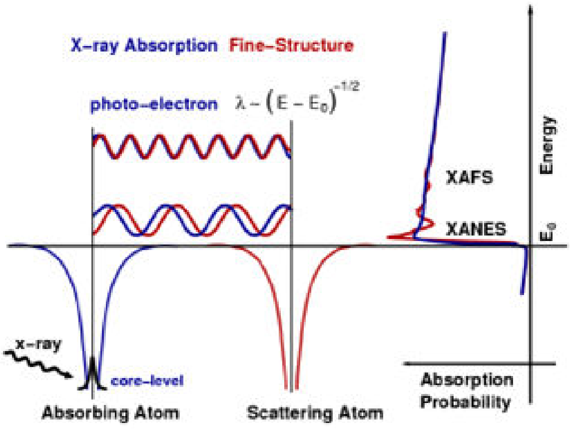

Figure 2.10: Modification (indicated in red) of the normal photoelectron wavelength (in blue) due to the presence of a neighbouring atom. Its influence modifies the X-ray absorption probability.

Generally the absorption of an homogeneous material can be deduced from the Beer's law:

$$I = I_0 \cdot \exp\left(-\mu \cdot t\right) \tag{2.11}$$

Here, I is the sample transmitted X-ray intensity, I_0 the X-ray intensity sent on the sample, t the sample thickness and μ its absorption coefficient. μ can be calculated using the Fermi golden rule, that expresses the probability of the transition between the ground and the excited state of atoms:

$$\mu\left(E\right) = \frac{2\pi}{\hbar} | < i|\mathcal{H}|f > |^2 \delta\left(E_f - E_i - \hbar\omega\right) \tag{2.12}$$

Here the δ function takes care of the energy conservation in an atomic excitation process, while the squared matrix element gives the transition rate between the initial ground state and the final excited state of the atom, respectively indicated with i and f. $\mathcal{H}$ is the Hamiltonian operator that describes the X-ray absorption. This equation demonstrates that μ depends upon f, *i.e.* the unoccupied (*i.e.* available) Density Of States (hereafter called DOS) of the excited atom. Consequently, a XAS spectrum is an experimental evidence of these empty states, modulated by the presence of the core-hole presence.

The absorption coefficient μ can be measured in the transmission mode: in this case, μ is directly given through the Beer law (see equation 2.11), measuring the incoming and the transmitted X-ray beam energies. Otherwise, μ can be measured either in the fluorescence or in the total electron modes. As X-ray absorption induces the electronic reorganisation of the excited atom, it also influences its de-excitation. Therefore, both the fluorescence and the Auger electrons emission phenomena are proportional to its X-ray absorption cross-section. As a consequence, in the fluorescence mode μ is estimated from the X-ray fluorescence yield (fY), *i.e.* detecting the characteristic X-rays produced during atomic de-excitations. Conversely, in the Total electron Yield (TeY) mode XAS spectra are collected by detecting the Auger electrons.

Just above the absorption energy threshold (*i.e.* up to 30-50 eV), photo-electrons are emitted from the absorber atoms with small kinetic energies: this fact induces photo-electrons, consequently to the Heisenberg uncertainty relationship $\Delta E.\Delta t \sim \hbar$, to have long life-times. In this case, photo-electrons are scattered many times by the first neighbours of the excited atoms before being retrodiffused towards their originating atoms. This phenomenon, called multiple scattering, prevails in the low energy part of a XAS front, called X-Ray Absorption Near Edge Structure (XANES) spectrum. For energies much higher than the absorption threshold (ranging from 50 to 1000 eV), the created photo-electrons have relatively short life-times and they are usually retrodiffused by only the first or second neighbours of the excited atoms through a single diffusion phenomenon. Due to these short life-times, at the highest energies the XAS spectra present attenuated oscillations: this part of the spectra is called the EXAFS (Extended X-Ray Absorption Fine Structure) signal. The EXAFS spectra provide information on distances between the atoms present in the lattice and on their coordination number, as they depend upon the atom neighbourhood.

2.4.2.1 Experimental details of our experiences

In this work, all our XAS characterizations were carried out at the SGM beam-line of the Canadian synchrotron CLS [6] (see Figures 2.11 and 2.12). This beam-line (placed in ultra-high vacuum 10^{-10}- $5{\cdot}10^{-9}$ torr) provides users with a high flux and high resolution photon beam with photon energies between 250 and 2000 eV. This low energy range is particularly suited for studying the electronic structure of light elements (such as oxygen) containing samples through core level excitation. In our case, samples were characterized acquiring XANES spectra at the following edges:

- Oxygen K-edge (532 eV): this edge probes the electronic transition 1s $\rightarrow$ 2p. Spectra are collected in the energy range 520 – 580 eV.

- Uranium $N_{4,5}$-edges (respectively at 778.3 and 736.2 eV): these edges correspond respectively to the electronic transition $4d^{3/2}\rightarrow 5f^{5/2}$ and $4d^{5/2} \rightarrow 5f^{7/2}$. Their spectra are collected in the energy range 720 – 810 eV.

- Uranium $N_{6,7}$-edges (respectively at 388.2 and 377.4 eV): these edges correspond respectively to the electronic transition $4f^{5/2} \rightarrow 6d^{3/2}$ and $4f^{7/2} \rightarrow 6d^{5/2}$. Their spectra are collected in the energy range 360 – 420 eV.

For each edge, Fluorescence Yield (fY) and Total Electron Yield (TeY) spectra were simultaneously collected.

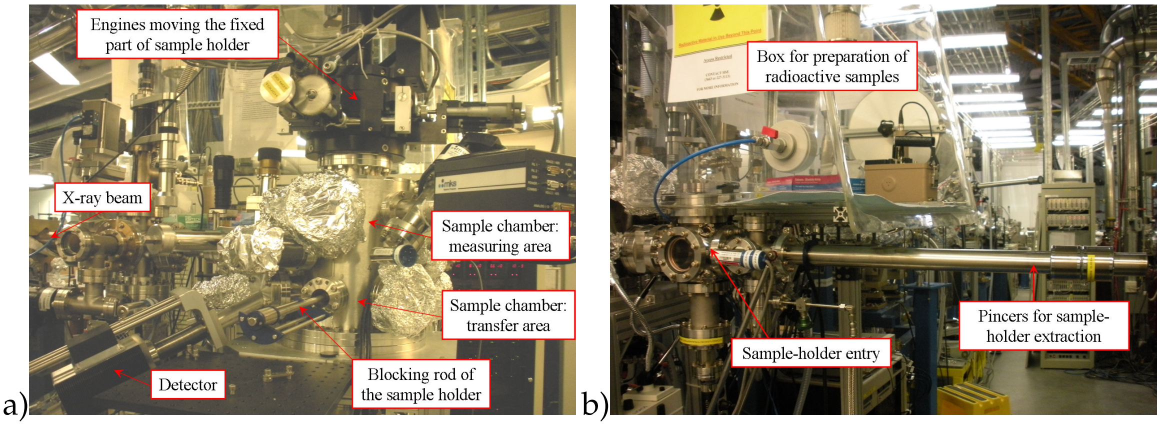

Figure 2.11: The endstation of the SGM beamline of the Canadian synchrotron CLS.

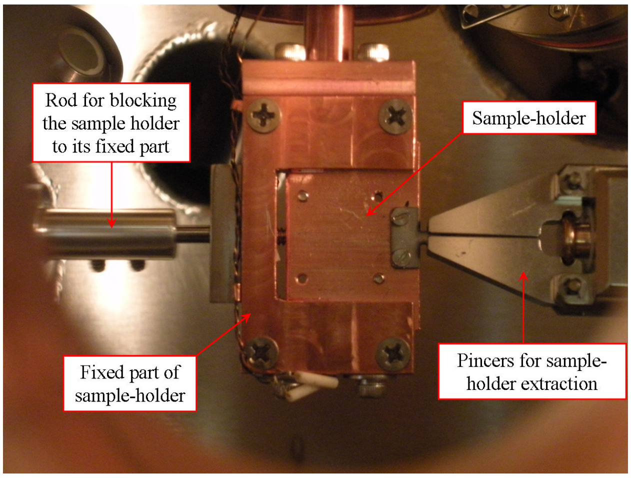

Figure 2.12: An insight of the the sample chamber of which the SGM beam-line is equipped.

2.4.2.2 XANES data processing

Analysis of XANES spectra passes through the normalization of the collected raw data. This operation consists in 3-steps data processing, represented in Figure 2.13a). Firstly, a pre-edge function have to be subtracted from $\mu(E)$ to get rid of the matrix absorption (indicated in Figure 2.13a) with a green line). Secondly, the threshold energy E_0 has to be identified, typically as the energy value where the maximum first derivative of $\mu(E)$ falls (indicated with a orange point on the black curve of Figure 2.13a)). Lastly, a normalization range has to be defined to normalize $\mu(E)$ from 0 to 1 (indicated in Figure 2.13a) with red circles). In this way the so-normalised XANES spectra (see the example in Figure 2.13b)) are completely independent on the concentration of the probed atoms and are ready to be analysed.

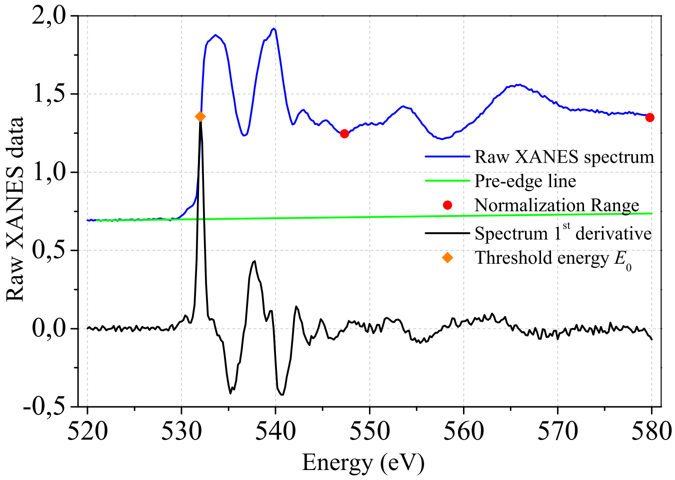

a)

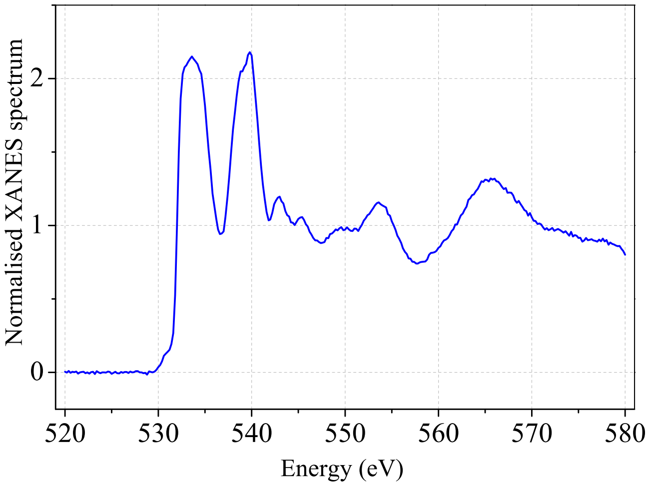

b)

Figure 2.13: Normalisation of a raw XAS spectrum: processing of raw data (graph a) and the final result (normalised spectrum - graph b).

2.4.3 Secondary Ion Mass Spectrometry (SIMS)

Secondary ion mass spectrometry is a partially destructive local isotopic and chemical analysis technique. A beam of energetic Cs^+ or O^{2+} ions (10-15 keV) sputters and ionizes atoms at the sample surface. The secondary ions produced are then extracted and separated using a magnetic sector mass spectrometer [24, 58, 59, 13, 155]. The mass resolution for a IMS 6f such as that used in our studies is of the order of 10^3. Therefore isotopes such as ^{16}O and ^{18}O can easily be separated. Figure 2.14 is a schematic diagram of the shielded Cameca IMS 6f SIMS instrument at the LECA STAR laboratory CEA – Cadarache.

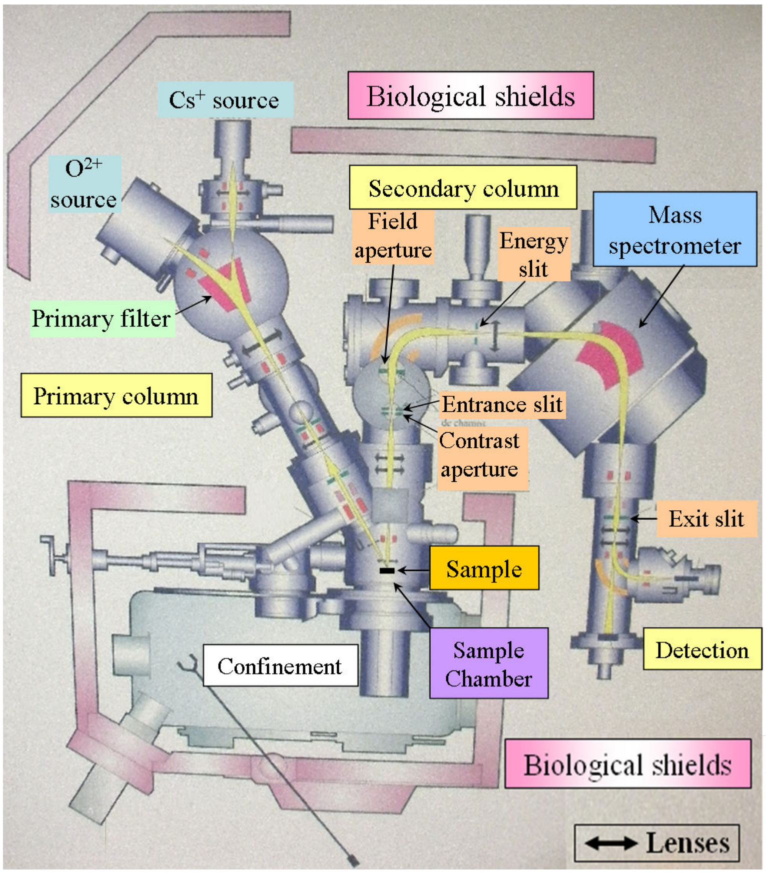

Figure 2.14: Scheme of CAMECA IMS-6f SIMS device of the LECA STAR laboratory of CEA Cadarache.

The main components of a SIMS are placed under high vacuum (10^{-3}-10^{-7} Pa). As we can see in Figure 2.14, they are:

- the ion source (Cs^+, O^{2+}), that produces the primary beam
- the primary column, that enables the focusing of the primary beam
- the sample chamber, in which samples are placed and analysed
- the secondary column, through which the secondary ions produced are accelerated
- the mass spectrometer, that separates ions.

The CAMECA SIMS used in our work enables several modes to be implemented. The mode we are most concerned with in our study is depth profiling. In this configuration, a primary beam is focused upon the surface of the sample and rastered over an area typically between 50x50 to 250x250 μm^2. Typical technical characteristics are nanometric scale depth resolution, a low ionic detection limit (of the order of magnitude of the ppb for some elements, depending on the matrix) and a high mass resolution (10^3). This technique is very appropriate for characterising elemental concentrations in a material. The main drawback with SIMS resides in the fact that the method basically provides relative isotopic distributions and that the methodologies for deriving quantitative data can prove complex to control.

The reason for this is that not all atoms of a given species that are sputtered from the sample surface actually contribute to the ion current detected by the mass spectrometer [24, 179]. These two quantities (*i.e.* isotopic concentration and secondary ion current of a given isotope) are connected through a set of proportionality factors which we will now introduce.

As primary ions hit the surface of the material, atoms of the sample are sputtered from the surface. Sputtering depends on many factors, such as the current intensity of the primary beam (called I_P hereafter), the angle with which the primary beam hits the sample surface and the sample composition and texture (*e.g.* polycrystal or single crystal) [97]. Assuming a steady state sputtering regime is reached, the composition of sputtered atoms is identical to the composition of the material. Let Y_{sput} be the total sputtering yield under a given set of experimental conditions and C_A be the concentration of atoms A we are trying to detect, the total number of sputtered A atoms per second may be expressed as $Y_{sput} \cdot I_P \cdot C_A$.

Of these atoms only a restricted set will actually be ionised. If Y_i is the ionization yield, *i.e.* the probability that a sputtered A atom is ionised, then the total number of ionised A atoms is: $Y_i \cdot Y_{sput} \cdot I_P \cdot C_A$. Y_i is of course dependent upon the experimental conditions but also upon the nature of atoms A and the composition of the matrix (*i.e.* matrix effect).

Of these ionised A atoms, only a fraction is actually detected. This contribution to the secondary ion current is termed collection factor Y_c and covers a wide range of effects: extraction, transmission, detection of secondary ions. It is dependent upon the nature of A, experimental conditions and essentially the secondary part of the SIMS set-up (transmission characteristics of the secondary system). If Y_c represents the proportion of secondary A ions that are detected, then the secondary A-ion current $I_{A^{+/-}}$ can be written:

$$I_{A^{+/-}} = Y_c \cdot Y_i \cdot Y_{sput} \cdot I_P \cdot C_A = K_A \cdot C_A \tag{2.13}$$

The product of the sputtering, ionization and collection (*i.e.* extraction, transmission and detection) yields with the primary ion current is called the absolute sensitivity factor K_A, and connects the concentration of each atomic species of the analysed sample to its measured secondary ionic current:

$$\begin{cases} K_A = Y_c \cdot Y_i \cdot Y_{sput} \cdot I_P \\ I_{A^+} = K_A \cdot C_A \end{cases} \tag{2.14}$$

Note that collected ion currents strongly depend upon SIMS experimental conditions. If a matrix element of the sample (the concentration of which is known) behaves in a similar way to that of the ions one is attempting to characterise the concentration, then the ratio between the ion current of the isotope of interest (termed A in the example) and the ion current of the matrix ion (called B) is not influenced by experimental conditions. This data processing leads to the definition of another parameter, called relative sensitivity factor, here indicated as K_{AB}:

$$\frac{I_{A^+}}{I_{B^+}} = K_{AB} \cdot \frac{C_A}{C_B} \tag{2.15}$$

In Equation 2.15 I_{A^+} and I_{B^+} are the measured currents of the ions A^+ and B^+, while C_A and C_B are the concentrations of the atoms A and B in the sample. The parameter K_{AB} opens up the prospect of SIMS constituting a quantitative analysis.

Oxygen 18 characterisations represent a simple situation. Indeed, in this case one is capable of normalising the ^{18}O signal to the total oxygen signal (^{18}O + ^{16}O). Unless transmission effects are notably different for one or the other isotope (which should not be the case) then one is capable of eliminating all collection and ionisation caveats because oxygen is a matrix component. Therefore $\frac{^{18}O}{^{16}O+^{18}O}$ actually represents the ^{18}O concentration.

Finally, in depth-profiling mode, SIMS collects signals as a function of the sputtering time. To convert this signal into a depth profile, the depth of SIMS craters have to be measured. We have done this using an optical technique (chromatic confocal microscopy) which is described in paragraph §2.4.4. The next sub-section provides useful information relative to the optimization of SIMS settings.

2.4.3.1 Optimisation of SIMS conditions

In this subsection we describe how SIMS settings are optimised for quantitative depth profiling.

After a succinct optimization of the primary beam the secondary beam is first adjusted. The secondary beam is made up of single atom or molecular ions sputtered from the sample and of charged molecules produced from the interaction between beam and sample ions. It may be advantageous to analyse these molecules as in some cases, they can help to eliminate matrix effects which we know are important in UO_2. It is known that the energy spectra of these ionic molecules are narrower than the ones of single ions. This leads to an improved ion energy resolution and to an increase of the extraction and detection yields [24, 58, 59]. In this work the MCs^+ method was tested: oxygen isotopes and dopant concentrations were measured through the detection of the molecules formed by the sample atoms of interest and the Cs^+ ions from the incident beam.

The main settings relative to the secondary column are: the contrast and the field aperture, the energy slit, the entrance and the exit slits (see Figure 2.14 for their placement). In general all these parameters enable optimisation of the collection yield (see § 2.4.3) and the quality of the detected signal:

- The contrast aperture affects the quantity of ions that can enter into the mass spectrometer. In our setup it is equal to 400 µm and corresponds to a widely opened window, which guarantees a high signal intensity. However, if the signal is too intense and saturates, the contrast aperture can be set to a lower value.

- The mass spectrometer separates ions depending upon their mass to charge ratio $\frac{M}{q}$ as expected from the Lorentz equation which relates this parameter to the magnetic field and the charged particle trajectory. Following the application of a calibration procedure, a relationship is established between the applied magnetic field and the mass of the ions detected. Counts may then be monitored as a function of the mass of detected ions as indicated in Figure 2.15 for $^{16}O^{133}Cs^+$, $^{18}O^{133}Cs^+$, $^{52}Cr^{133}Cs^+$, $^{235}U^+$ by modifying the magnetic field continually. Note that these curves have shapes that approach that of a rectangular window function. This is extremely desirable since during subsequent analyses, the count rate will be unaffected by slight modifications of the magnetic field thus providing a very stable signal. It is during this optimisation process that the desired mass resolution is chosen. To this end, the entrance slits may be closed generally in such a way that separation of close peaks is satisfactory as illustrated in Figure 2.15 a) and b). This also substantially contributes to having ion count rate signals with flat peak tops that resemble window functions. However adjusting the entrance slits is necessarily a compromise between mass resolution (Figure 2.15 shows that our setup guarantees a mass resolution $M/\Delta M$ of about 100-150) and count rate.

- The exit slits usually have to be 2.5 times more open than the entrance one, to avoid optical aberrations and to enable almost all the ions to reach the detector.

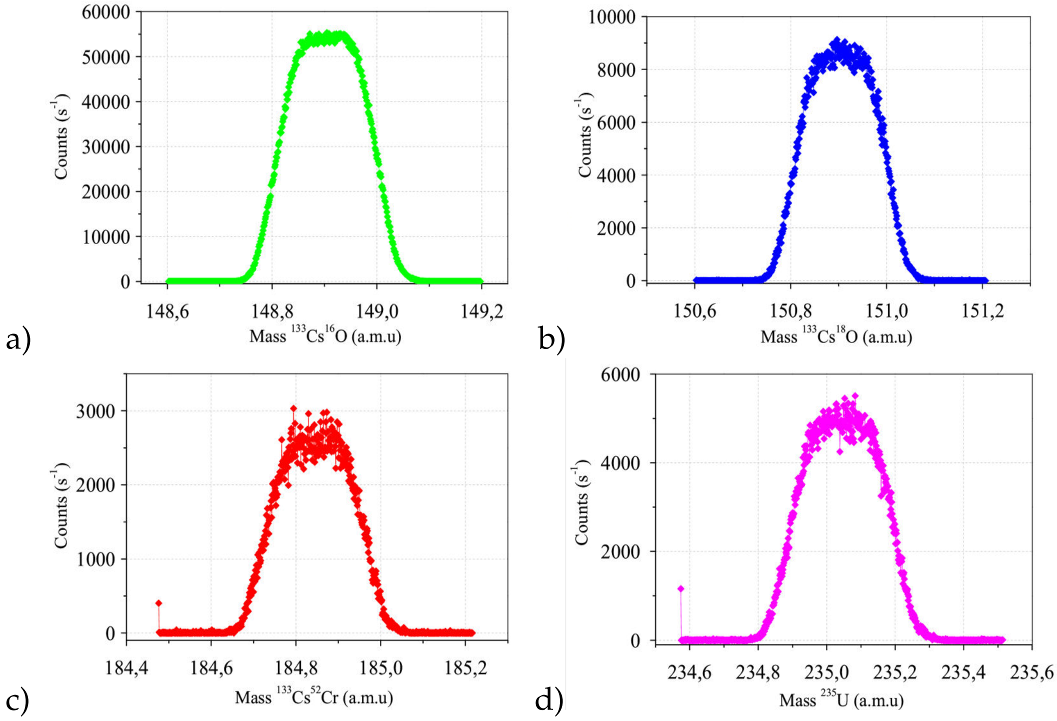

Figure 2.15: Mass calibration for the ionic species chosen to be detected during a SIMS experiment: $^{16}O^{133}Cs^{+}$ (a), $^{18}O^{133}Cs^{+}$ (b), $^{52}Cr^{133}Cs^{+}$ (c) and $^{235}U^{+}$ (d).

- Secondary ions of a given type are generally produced over a wide energy spectrum. The energy slit is used to select ions in a small energy range. This sometimes helps eliminate matrix effects (*e.g.* texture) and contributes to providing quantitative analyses. This slit is placed before the magnetic sector of the mass spectrometer. A greater energy resolution (which one obtains by closing these slits) also helps improve the resolution of the mass spectrometer. In our oxygen diffusion experiments it is set to select ions with an energy spread in the range of ±20 eV (see Figure 2.16).

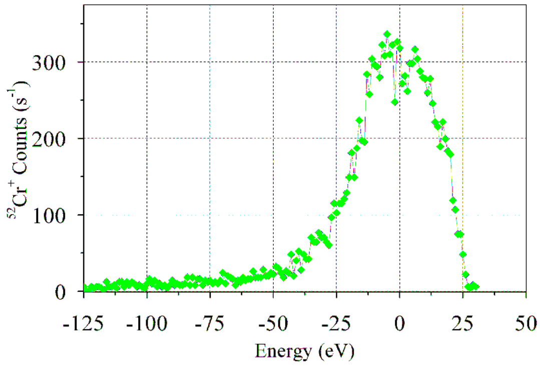

Figure 2.16: Energy calibration of the $^{52}Cr^{+}$ ion. The energy slits are positioned to collect ions within an energy range of ±20 eV.

The primary beam is then optimised. Four electrostatic lenses are used to focus and control the intensity of the incident caesium beam. The one nearest the sample is the first to be adjusted. The three others affect the primary beam intensity. The lens nearest to the primary ion source controls the beam density and alignment in the primary column. The deflectors positioned just after the source are adjusted so that the primary beam is homogeneous and as small as possible.

Beam alignment and focusing on the sample are firstly obtained in a fixed probe mode for a small value of the primary beam current. Primary beam current is then continuously increased up to the desired optimal (usually highest) value: alignment, dimensions and shape of the beam have to be continuously monitored and optimised during this stage. Typical beam size under conditions investigated is 10-20 µm.

Once all parameters are properly set, the profiling conditions for the depth-profiling mode must be optimised. In this mode, a primary beam rastered over a square area at the sample surface. Because the sides of the crater are slanting, it is important that the detected signal comes from an area much smaller than the crater size. Indeed if this is not the case ions will contribute to the signal that originates from depths different from the crater bottom inducing substantial errors. To avoid crater side effects, it is also important that the beam size be much smaller than the crater size. An accepted rule of thumb is that the crater size should be at least equal to the analysed area plus four times the beam size. For a 30 µm analysed area, the crater should have sides of between 80 and 100 µm [13]. This choice is ideal for Cr-doped UO_2 samples, as they comprise grains which can reach 200 µm in size (see §2.1). In this case in fact, the size of the rastered area is smaller than the grain dimensions which means that craters usually remain within one grain. In case of undoped samples, grains have an average size of only 6 µm. These small dimensions make it impossible to analyse with SIMS a single grain in case, it is best to average the contribution over many grains. An analysed area of about 60 µm is the most suited to select and consequently the crater size is increased up to 150 µm.

2.4.4 Chromatic confocal Microscopy

Chromatic confocal microscopy is here used to characterize the topology of the sample craters produced by the incident SIMS ion beam. The system used is made up of white light source, a lens, the sample one wishes to characterise, mirrors and a spectrometer capable of analysing visible wavelengths (see Figure 2.17). The method relies on the chromatic aberrations of the optical system that are such that if the light beam is focused at a point of the surface of the sample, the elevation at that point will be in the focal plane for a single wavelength only. The wavelength reflected back to the spectrometer is therefore related to the elevation of a given point on the surface of the sample. Points of the surface located at different depths are detected as different colours.

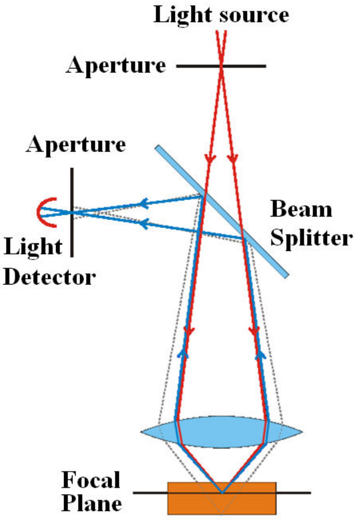

Figure 2.17: Schematic diagram of a confocal microscope.

Cartographies are obtained by rastering the light source over the sample surface in predetermined steps of the order of the size of the light beam (1 µm steps). The SurfaceMap and SPIP softwares [7] are used to save and analyse the data generated with this technique.

2.5 Determination of diffusion coefficients

Oxygen diffusion coefficients are estimated by simulating changes in depth profiles obtained during an isothermal annealing cycle. Depth profiles are obtained from SIMS time-dependent signals. The sputtering rate which we can check is constant is estimated in order to correlate the SIMS sputtering time to a given crater depth. Confocal microscopy observations provide an estimate of the sputtering rate. Its determination and the subsequent depth profile simulation are described in the following subsections.

2.5.1 SIMS sputtering rate

Here the methodology developed to estimate the sputtering rate is presented.

After having straightened the confocal microscopy image, two areas within these images are selected. The first is taken at the centre of the crater bottom and has a circular shape (its surface corresponds roughly to the area from which secondary ions are extracted). The second is made of portions of the sample surface and constitutes the reference altitude. From these areas a depth distribution is determined with points of the surface constituting the reference and points located at altitudes corresponding to the crater bottom, as shown in Figure 2.18:

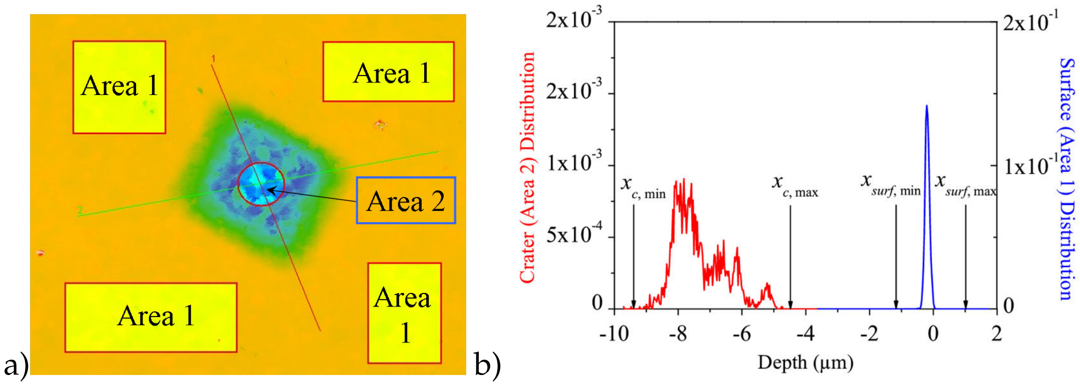

Figure 2.18: Selection of areas at the sample surface and at crater bottom (a) and the corresponding depth distribution (b).

The two portions of the depth distribution, related to the crater bottom and to the sample surface, are normalized to obtain two distribution functions:

$$\begin{cases} \int_{x_{c,\min}}^{x_{c,\max}} f_{crater}\left(x\right) dx = 1 \\ \int_{x_{surf,\min}}^{x_{surf,\max}} f_{surface}\left(x\right) dx = 1 \end{cases} \tag{2.16}$$

Their convolution represents the crater depth distribution function:

$$f\left(\delta\right) = \int_{x_{surf,\min}}^{x_{surf,\max}} f_{crater}\left(x + \delta\right) \cdot f_{surface}\left(x\right) dx \tag{2.17}$$

Here, δ is the crater depth, $x_{surf,\min}$ and $x_{surf,max}$ are respectively the lowest and the highest possible surface altitudes, while $f_{crater}(x+\delta)$ and $f_{surface}(x)$ are the depth distribution functions respectively of the crater bottom and of the sample surface.

If the SIMS primary beam current remains constant during the analysis, the crater depth distribution $f(\delta)$ function is proportional to the sputtering rate distribution. From $f(\delta)$ are deduced the average sputtering rate $\bar{v}$ and its standard deviation, which defines the depth resolution. From $\bar{v}$, the average instantaneous depth $\bar{z}\left(t\right)$ at sputtering time t is calculated as follows :

$$\bar{z}\left(t\right) = \bar{v} \cdot t \tag{2.18}$$

Now, our analysis is not restricted by the fact that the primary beam current, hence sputtering rate, remains constant during the analysis. Indeed, assuming that the sputtering rate at a given point of the surface *i* is proportional to the SIMS primary beam current (*i.e.* $v_i(t) = \alpha_i \cdot I_p(t)$, with $\alpha_i \epsilon \mathbb{R}^+$), it comes that at a given sputtering time *t*, the altitude corresponding to point *i* is given by:

$$z_i(t) = \int_0^t v_i(t)\, dt = \alpha_i \cdot \int_0^t I_p(t)\, dt \tag{2.19}$$

If $I_p(t)$ is determined from the experimental data or assumed to be proportional to a measured physical quantity (such as the ion current corresponding to a matrix species), then α_i may be obtained from applying the previous relationship for a time corresponding to the total analysis time t_{an}:

$$\alpha_i = \frac{z_{i,crater}}{\int_0^{t_{an}} I_p(t)\, dt} \tag{2.20}$$

Here $z_{i,crater}$ is the final crater depth measured by confocal microscopy at point *i* at the sample surface and $I_p(t)$ is the primary ion beam current. Hence at any given sputtering time *t* depth z_i may be obtained from relationship 2.19.

For each sample, several depth profiles are characterised in order to check both the reproducibility of the method and the homogeneity of the sample composition. Depth profile changes resulting from sample annealing are simulated using Fick's law whence diffusion coefficients are derived for the element analysed.

2.5.2 Simulation of oxygen depth profiles

Diffusion coefficients are deduced by solving Fick's second law:

$$\frac{\partial c(x,t)}{\partial t} = D \cdot \frac{\partial^2 c(x,t)}{\partial x^2} \tag{2.21}$$

In Equation 2.21, *D* is supposed to be independent on concentration.

In the oxygen studies, the relatively low temperatures imposed during annealing enables us to neglet the phenomenon of the sample surface evaporation (see Appendix B). The initial and the two boundary conditions are set as follows:

$$\begin{cases} \left[\frac{\partial c(x,t)}{\partial x}\right]_{x=0} = \frac{K}{D} \cdot (c(0,t) - c_{gas}) \\ c(\infty,t) = c_0 \\ c(x,0) = F(x) \end{cases}$$

In this system, D represents the diffusion coefficient, K the parameter used to describe the exchange of atoms between the sample surface and the gaseous atmosphere, c_{gas} the ^{18}O concentration in the atmosphere (during the diffusion annealing stage, it is equal to 0.98, *cf.* section §2.2.1), c_0 corresponds to the natural abundance of ^{18}O (roughly 0.002), $c(x,t)$ is the time and space dependent ^{18}O concentration and $F(x)$ is the initial depth profile prior to annealing.

Analytical solutions to this equation are reported in simple cases (as, for example, when $F(x)$ is a constant) [153, 168]. Tarento [171] succeeded however in finding an analytical solution to this partial differential equation for any function $F(x)$ (see Appendix B for details).

Ideally, the initial condition $c(x,0)$ is equal to the natural abundance of ^{18}O (c_0). However, the furnace atmosphere used to bring samples to equilibrium was sometimes polluted by the ^{18}O adsorbed during the previous experiments. In this case, the ^{18}O tracer penetrates inside the UO_2 bulk also during the annealing step of sample equilibration. In this case, we need firstly to simulate the phenomenon of contamination to obtain the initial ^{18}O depth profile $F(x)$. A second simulation provides an oxygen self-diffusion coefficient estimate.

Chapter 3

A point defect model for UO_{2+x} based on electrical conductivity and deviation from stoichiometry measurements

Although uranium dioxide has been extensively studied for over 50 years [25, 114] there still does not exist a comprehensive understanding of prevailing point or complex defects or how these defects control most of its physical properties. As seen in §1.1.1, the reason for that is probably to be found in the complexity of the material which is stable over a very wide range of deviation from stoichiometry. This comes about through modifications mainly in oxygen related defect concentrations [182, 183] and is made possible by the property uranium has of existing under different charge states (3+, 4+, 5+ and 6+). In relation to this, we have seen in §1.2.2 that reliable determinations of point defect formation or migration energies are only just emerging [19, 69] and rely upon an improved description of the strong correlations which exist between the uranium 5f electrons. The nature of point defects may be obtained through structural characterisations of the material (see §1.1.1) or application of first principles methods (see §1.2.2). Another very complementary approach is to study the material's physical properties as a function of temperature, equilibrium oxygen partial pressure, possibly impurity concentrations (see §1.3) and develop a point defect model or theory capable of reproducing these properties (§1.2.1). Many atomic transport properties can be analysed in this way (see for instance [64]) but we focus here on electrical conductivity and to a lesser degree on deviation from stoichiometry measurements. In this chapter, we attempt to develop a comprehensive point defect model, based on defect chemistry which reproduces these data and which we will later use in Chapter

6 to analyse the atomic transport data described in Chapter 4. The first part of this work is devoted to laying out the principles and hypotheses that underpin the model. Particular attention is paid to building into the model our knowledge of the electrical properties of UO_2 but also, following Kröger [115], of the relationship between deviation from stoichiometry and oxygen partial pressure. We then go on to derive the model equations and how the model parameters are determined, initially from an asymptotic analysis of the available experimental data. Finally, we discuss the ability of the model to reproduce the electrical conductivity measurements of Ruello [164] between 973 K and 1673 K and to provide an estimate of each defect concentration dependence upon oxygen partial pressure. Particular attention is devoted to comparing the activation energies of the mass balance equations involving the defects to defect formation energies derived from first principles.

3.1 Modelling hypotheses in relation to our knowledge of UO_2

The model developed is similar to others reported in the past (notably Kröger [115] and Park Olander[149]) and is based on defect chemistry. In this type of formulation, charged defect concentrations are governed by a set of simultaneous equations amongst which so-called mass-action laws are the expression of thermodynamic equilibrium. This approach is in the general case invalid because applicable in principle only to a limited range of defect concentrations, *i.e.* a limited region of the $UO_{2\pm x}$ phase diagram (see §1.2.1). Hence the equations described below are applicable in theory to low deviations from stoichiometry only but we boldly apply them to deviations from stoichiometry in excess of this value.

We follow here the assumption of many other authors [70, 164] that thermally activated electronic disorder is controlled by the disproportionation of two U^{4+} ($5f^2$) ions into one U^{5+} ($5f^1$) ion and one U^{3+} ($5f^3$) ion. U^{5+} ions may also be formed through a charge compensation mechanism on introduction of an oxygen interstitial or vacancy as suggested from recent electronic structure calculations [68]. As reported in §1.3.1, UO_2 electrical conductivity is expressed as the sum of an electron and a hole contribution and occurs via the small polaron hopping. Supposing this mechanism adiabatic and coupling together Equations 1.1 and 1.2, UO_2 electrical conductivity can be generally expressed as follows:

$$\sigma = \frac{\mu_0}{T} \exp\left[-\frac{\Delta H_m}{K_B T}\right] \cdot e \cdot N_{s,U} \cdot \left(\mu_{rel}\left[e'\right] + \left[h^{\circ}\right]\right) \tag{3.1}$$

where T represents temperature, μ_0 is a constant and ΔH_m is the charge migration enthalpy. Although no direct measurement of the hole mobility μ_p (see Equation 1.2) is reported for UO_2, an estimate can be obtained from an analysis of the temperature dependence of electrical conductivity data at low oxygen partial pressures and at temperatures below the transition from an intrinsic behaviour (see §1.3.1.2). As a result of Equation 3.1, the Arrhenius dependence of σT provides an estimate of the hole mobility, *i.e.* ΔH_m and the product of μ_0 with the impurity concentration. Dudney [70] proposed a value for μ_0 of 0.0554 $m^2 \cdot K \cdot V^{-1} \cdot s^{-1}$ (widely used) and Ruello [162] an activation energy of 0.26 eV for the study of a particular type of single crystal sample. This activation energy can be determined unequivocally from Ruello's data. On the other hand, μ_0 cannot and only the product of μ_0 with y (the extrinsic carrier concentration) may be determined directly from the data. We will see below how considering deviation from stoichiometry data may help provide a more appropriate estimate of μ_0. We also assume following Ruello [162] that the electron and hole mobilities are similar (*i.e.* $\mu_{rel} \sim 1$) although this inference is essentially indirect, *i.e.* no straightforward measurement of the electron mobility has ever, to our knowledge, been carried out for UO_2. The relevance of such a hypothesis will be looked at in the discussion section. In the following, we use Kröger-Vink notation to express thermodynamic equilibria between the various point defect species. To respect this notation, equations have to guarantee mass equilibrium. The disproportionation equation provides the following relationship:

$$2U_U^X \rightleftharpoons U_U^{5+} + U_U^{3+} \text{ ou } \varnothing \rightleftharpoons h^{\circ} + e^{'} \tag{3.2}$$

where U_U^X designates a uranium atom on an ordinary uranium lattice site (U^{4+}) with the superscript X indicating a neutral defect. The second relationship of equation 3.2 supposes that electronic defects, as well as vacancies, are defects without mass.

As described in §1.3.2.2, the recent analysis of oxygen self-diffusion experiments [68, 78] has shown the existence of doubly charged oxygen interstitials. This work also highlighted the relevance for UO_2 at least for small deviations from stoichiometry of the following defect equilibrium equation which describes the introduction in the material of an oxygen interstitial from the gas phase:

$$2U_U^X + \frac{1}{2}O_2 + V_i^X \rightleftharpoons O_i'' + 2U_U^{5+} \text{ ou } \frac{1}{2}O_2 \rightleftharpoons O_i'' + h^{\circ} \tag{3.3}$$

The model presented here also enables the description of the sub-stoichiometric region of the phase diagram. Section §1.1.1.2 describes how substantial (*i.e.* measurable) deviation from stoichiometry in the sub-stoichiometric region is only observed at high temperature (greater than 1873 K) and very low oxygen partial pressures [101], which corresponds to conditions that in the main lie outside those of the electrical conductivity data used to validate the model. Following the majority of previous authors (*e.g.* Murch [143] and Kim [109]), we assume that sub-stoichiometry is due to the presence of oxygen vacancies. Assuming oxygen vacancies of charge +*p* constitute the predominant anion-type defect population, one would expect (see §3.3.1) that deviation from stoichiometry follows a power law dependence of oxygen partial pressure with an exponent of -½ close to stoichiometry (*i.e.* when *e′*~*h*°) and this irrespective of the charge of the point defect, so long as O_i'' are the interstitial species. As *x* decreases still further and electrons become the predominant electronic defect species, the slope of this property is expected to be close to $-\frac{1}{2(p+1)}$. Based on this analysis, the results of thermogravimetric experiments of Tetembaum [173] (see Figure 1.4) suggest a singly charged oxygen vacancy at least at large deviations from stoichiometry. The results of Javed [101] on the other hand would tend to indicate for the oxygen vacancy a charge of +2. To state on the effective charge of oxygen vacancies, we turned also to recent charged defect calculations of Crocombette and co-workers [57] (see §1.2.2). Even if in their work oxygen vacancy charge is calculated to vary as a function of Fermi energy level, we surmise here the existence of doubly charged positive vacancies only. Oxygen disorder on the anion sublattice is therefore assumed to result from the following Frenkel equilibrium:

$$O_O^X + V_i^X \rightleftharpoons O_i'' + V_O^{\circ\circ} \tag{3.4}$$

where V_i^X is a vacant interstitial site.

It has long been demonstrated for UO_2 that in the hyperstoichiometric region of the phase diagram, excess oxygen atoms readily agglomerate to form so-called clusters (see §1.1.1.3). Here we consider the existence of complex Willis defects in the so-called 2:2:2 configuration (see Figure 1.5 in §1.1.1.3), which we rename *W* in the remainder of this work. There remains to determine an appropriate charge for this defect. Again we turn to Ruello's data [164] with which we aim to remain consistent. The author showed a square root dependence of electrical conductivity upon oxygen potential above 1273 K and at high oxygen potentials in a region where the material has an intrinsic behaviour (see Figure 1.12a) in §1.3.1.1). Assuming n excess oxygen atoms make up the defect and that a single type of defect predominates, then it is quite straightforward to prove that the electrical conductivity is proportional to oxygen partial pressure to the power $\frac{n}{2(p+1)}$ where $-p$ is the apparent charge of the defect. Assuming, as suggested by Willis that n equals two, a charge of -1 for this type of cluster is compatible with the experimental results. The mass balance equation describing the formation of such a cluster may be written as follows:

$$O_2 + 2O_O^X + 2V_i^X + U_U^X \rightleftharpoons W' + U_U^{5+} \tag{3.5}$$

It is quite probable that clusters of different composition exist in UO_2 and that their proportion varies depending upon oxygen potential and temperature (see §1.1.1.3 and §1.2.2) but for sake of keeping this model simple and in the absence of straightforward experimental evidence, we choose here to consider only one type of cluster. Based again on Willis neutron diffraction results [183] (see again §1.1.1.3), we assume here that uranium vacancies constitute a minority defect for all deviations from stoichiometry. Table 3.1 summarises the nature of defects described by the model.

Notation	***Effective Charge***	***Nature***
U_U^X	0	Uranium atom on an ordinary cation lattice site
h°	+1	Hole, *i.e.* U^{5+} ion
$e^{\prime}$	-1	Electron, *i.e.* U^{3+} ion
O_O^X	0	Oxygen atom on an ordinary anion lattice site
O_2	0	Oxygen molecule present in the gas phase
$O_i^{"}$	-2	Doubly charged oxygen interstitial
V_i^X	0	Vacant interstitial site
$V_O^{\circ\circ}$	+2	Oxygen vacancy
$W^{\prime}$	-1	Di-Oxygen cluster

Table 3.1: Defects considered in the model.

3.2 Model equations

In the dilute limit approximation, the configurational entropy terms for each of the chemical potentials of the different defect species are given by the corresponding site fractions. If ΔG_α designates the Gibbs free energy of defect formation equation (α), then thermodynamic equilibrium determines relationships between the activities, *i.e.* site fractions under our approximations. Site fractions are proportional to defect concentrations and it can be shown that the equilibrium constants are expressed as a function of defect concentrations normalized to the uranium site concentration. Thermodynamic equilibrium is therefore expressed as four relationships, each corresponding to the four chemical equilibria described in the previous section:

$$K_e = \frac{\left[U_U^{5+}\right]\left[U_U^{3+}\right]}{\left[U_U^X\right]^2} = \exp\left[-\frac{\Delta G_e}{k_B T}\right] \tag{3.6}$$

$$K_{O_i} = \frac{\left[O_i^{''}\right]\left[U_U^{5+}\right]^2}{\left[U_U^X\right]^2\left[V_i^X\right]\cdot\sqrt{pO_2}} = \exp\left[-\frac{\Delta G_{O_i}}{k_B T}\right] \tag{3.7}$$

$$K_W = \frac{\left[W^{'}\right]\left[U_U^{5+}\right]}{\left[O_O^X\right]^2\left[V_i^X\right]^2\left[U_U^X\right]\cdot pO_2} = \exp\left[-\frac{\Delta G_W}{k_B T}\right] \tag{3.8}$$

$$K_{AF} = \frac{\left[O_i^{''}\right]\left[V_O^{\circ\circ}\right]}{\left[O_O^X\right]\left[V_i^X\right]} = \exp\left[-\frac{\Delta G_{AF}}{k_B T}\right] \tag{3.9}$$

where the square brackets represent defect concentrations normalised to the uranium site concentration $N_{s,U}$ and pO_2 the equilibrium oxygen partial pressure.There are eight unknowns to this problem and in addition to the four defect equilibrium relationships, one guarantees electroneutrality and three additional equations express the constraints imposed by the crystalline structure:

$$y^{'} + 2\left[O_i^{''}\right] + \left[e^{'}\right] + \left[W^{'}\right] = \left[h^{\circ}\right] + 2\left[V_O^{\circ\circ}\right] \tag{3.10}$$

where y represents the extrinsic charge carrier concentration due to aliovalent cations present on the uranium sub-lattice. In case of Chromium-doped uranium dioxide, y is affected by an effective charge of -1, and therefore in Equation 3.10 it is expressed as y'. These impurities are responsible for the extrinsic behaviour observed at low oxygen partial pressures and temperatures. Additional constraints are written as follows:

$$y^{'} + \left[e^{'}\right] + \left[h^{\circ}\right] + \left[U_U^X\right] = 1 \tag{3.11}$$

$$\left[O_O^X\right] + 2\left[W^{'}\right] + \left[V_O^{\circ\circ}\right] = 2 \tag{3.12}$$

$$\left[O_i^{''}\right] + \left[V_i^X\right] + (2+\alpha)\left[W^{'}\right] = 1 \tag{3.13}$$

An empirical parameter α is introduced at this point that limits deviation from stoichiometry to a value of the order of 0.25 which correspond to a phase transition towards U_4O_9. At this phase limit, if the di-interstitial cluster constitutes the majority defect population then deviation from stoichiometry is simply approximately $2\left[W'\right]$ which limits the cluster concentration to 0.125. At this point there are no interstitial sites readily available to accept additional interstitials and equation 3.13 yields a value of approximately 6. The physical reason why cluster concentrations are limited is probably to be found in the fact that as their concentration increases they are brought closer and closer to each other and Coulombic interactions are no longer negligible. At this point, strong electrostatic repulsive forces appear between these complexes. The levelling off of deviation from stoichiometry and electrical conductivity observed at high oxygen potentials is probably related to this. In fact, it was experimentally demonstrated by [61] that the formation of the more complex defect of type cuboctahedra induces a deep rearrangement of anionic sublattice and the consequent UO_2 phase transition towards U_4O_9 (see §1.1.1.3). It is also possible that clusters of different composition and charge exist: the actual details of how, why and indeed if the majority defect population in UO_{2+x} changes from a (2:2:2) to a cuboctahedron configuration are unknown.

The conductivity is obtained from relationship 3.1. Also, an estimate of deviation from stoichiometry x may be calculated, assuming uranium vacancies to be negligible in comparison to oxygen defect populations:

$$\left[O_i''\right] + 2\left[W'\right] - \left[V_O^{\circ\circ}\right] = x \tag{3.14}$$

3.3 Asymptotic model approach

3.3.1 Asymptotic model in an intrinsic, substoichiometric regime dominated by oxygen vacancies

In this paragraph we derive simplified expressions for deviation from stoichiometry and electrical conductivity under certain limiting conditions. We assume the majority anion-type defect is the oxygen vacancy but treat the general case where the formal charge of the oxygen vacancy is $+p$. The electroneutrality equation may be expressed as:

$$2\left[O_i''\right] + \left[e'\right] = \left[h^{\circ}\right] + p\left[V_O^{p\circ}\right] \tag{3.15}$$

Frenkel equilibrium (*i.e.* equation 3.9) has to be re-written to take into account a charge state for the oxygen vacancy which may differ from +2:

$$O_O^X + V_i^X + (2-p)\,U_U^X \rightleftharpoons O_i'' + V_O^{\mathrm{p}^\circ} + (2-p)\,h^\circ \tag{3.16}$$

This equilibrium yields a general expression for K_{AF}:

$$K_{AF} = \frac{\left[O_i''\right]\left[V_O^{\mathrm{p}^\circ}\right]\left[h^\circ\right]^{2-p}}{2} \tag{3.17}$$

We continue to assume equilibrium 3.3. Substituting the expression for $[O_i'']$ from equation 3.3 into the relationship 3.17 yields:

$$\left[V_O^{\mathrm{p}^\circ}\right] = \frac{2K_{AF}\left[h^\circ\right]^p}{K_{O_i}\sqrt{pO_2}} \tag{3.18}$$

Two limiting cases are then considered. If $\left[h^\circ\right]$ predominates over anion-type defects, as is typically the case close to stoichiometry; then equation 3.15 reduces to $\left[e'\right] \sim \left[h^\circ\right]$ and $\left[h^\circ\right] = \sqrt{K_e}$. Substituting this expression into equation 3.18 yields:

$$\left[V_O^{\mathrm{p}^\circ}\right] = \frac{2K_{AF}K_e^{p/2}}{K_{O_i}\sqrt{pO_2}} \tag{3.19}$$

If $x \sim \left[V_O^{p^\circ}\right]$, then Log($x$) vs. Log($pO_2$) must bear a slope of approximately -0.5. If anion type defects predominate, then $\left[e'\right] = \frac{K_e}{\left[h^\circ\right]} = p\left[V_O^{\mathrm{p}^\circ}\right]$ which yields after substitution into equation 3.18:

$$\left[V_O^{\mathrm{p}^\circ}\right] = \left(\frac{1}{p}\right)^{\frac{p}{p+1}}\left(\frac{2K_{AF}}{K_{O_i}}\right)^{\frac{1}{p+1}} K_e^{\frac{p}{p+1}}\, pO_2^{-\frac{1}{2(p+1)}} \tag{3.20}$$

In which case the Log(x) vs. Log(pO_2) must bear a slope of approximately $-\frac{1}{2(p+1)}$.

3.3.2 Analysis of electrical conductivity data of Ruello with an asymptotic model approach

The electrical conductivity of Ruello was reported in detail in Chapter 1 – §1.3.1.1 and indeed we follow his analysis of these data. We assume UO_{2+x} is an electronic conductor and therefore that electrical conductivity reflects the level of electronic disorder. The difficulty with this type of analysis lies in determining a set of model parameters that reproduces the experimental data over a wide range of oxygen partial pressures and temperatures adequately but also in demonstrating this set is unique. To do this we need to determine ranges of temperature and oxygen potential over which it is reasonable to assume only a restricted set of defects predominate and all other defects may be neglected in the analysis. We first focus on the low temperature electrical conductivity data (*i.e.* 973 K, 1073 K, 1173 K) because as indicated from Ruello's Seebeck coefficient measurements, under all oxygen partial pressures studied, there is no risk of there being a transition from a n to p type conduction. As a result, we can be relatively sure that only h°, O_i'' and W' defects need be considered.

3.3.2.1 Analysis of the low temperature data (973 K, 1073 K, 1173 K)

At a given temperature, we consider 3 regions depending upon oxygen partial pressure. At low oxygen partial pressures, *i.e.* in the so-called p extrinsic region, where electrical conductivity is independent of oxygen partial pressures, the hole concentration is determined by the level of aliovalent impurities which in turn determines the extrinsic charge carrier concentration $y^{'}$. This region is known as region 1. In this region electroneutrality condition reduces to:

$$y^{'} = \left[h^{\circ}\right] \tag{3.21}$$

Assuming the equilibria 3.3 and 3.4, we can express oxygen vacancies as dependent upon the aliovalent impurity concentration $y^{'}$:

$$\left[V_O^{\circ\circ}\right] = \frac{2K_{AF}}{K_{O_i}\sqrt{pO_2}} \cdot y'^2 \tag{3.22}$$

As a consequence, an increase in the doping agent amount leads to an increase of oxygen vacancy concentration in UO_2, extending its hypo-stoichiometric domain.

As the oxygen partial pressure rises, but before oxygen interstitials form complex defects, the appropriate electroneutrality equation is instead given by:

$$y^{'} + 2\left[O_i^{''}\right] = \left[h^{\circ}\right] \tag{3.23}$$

A transition occurs at the point where isolated oxygen interstitials predominate over extrinsic electronic defects, *i.e.* when $y^{'} \sim 2.[O_i'']$ and σ is equal to

2.σ_{plat}, where σ_{plat} is the electrical conductivity in the purely extrinsic regions. Figure 3.1 indicates that electrical conductivity data exists beyond this transition oxygen partial pressure only at 1173 K. The region in which isolated oxygen interstitials constitute the majority anionic defect is known as region 2.

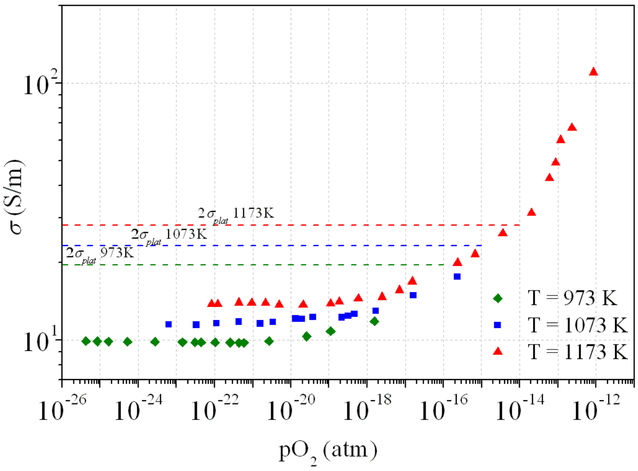

Figure 3.1: Electrical conductivity data at the three lowest temperatures 973, 1073 and 1173 K.

With increasing oxygen partial pressures and as extrinsic carriers become negligible, the appropriate electroneutrality equation becomes $\left[W'\right] + 2\left[O_i''\right] = \left[h^{\circ}\right]$ and a transition to region 3 in which oxygen complexes become the predominant oxygen species must occur at an oxygen partial pressure noted $pO_{2,trans}$ for which $[W']\sim 2.[O_i'']$. Combining this latter relationship with equations 3.7 and 3.8 yields:

$$K_{O_i} = 4\sqrt{2}pO_{2,trans}K_W^{3/2} \tag{3.24}$$

In region 3, assuming complex oxygen clusters of the W' type constitute the majority oxygen defect population, electroneutrality may be approximated by $[h^{\circ}]\sim[W']$. As a result, from equation 3.8 it follows (assuming $V_i^X \sim U_U^X \sim \frac{O_O^X}{2} \sim 1$) that deviation from stoichiometry may be expressed as:

$$x \approx 2\left[W'\right] \approx 4 \cdot \sqrt{K_W \cdot pO_2} \tag{3.25}$$

which suggests Log(x) varies as ½.Log(pO_2). Note that under those assumptions, Log(σ) has the same dependence upon Log(pO_2). The problem now comes down to determining μ_0, y', K_{O_i}, K_W unequivocally. These four quantities are intimately connected. Indeed if μ_0 is known, then y' is determined from the analysis of the extrinsic electrical conductivity data which provides an estimate of ($\mu_0 \cdot y' \cdot e$). A simple model may then be developed that accounts for the oxygen defects that are isolated only. This model uses equations 3.23 and 3.7 (with $V_i^X \sim U_U^X \sim 1$) the combination of which yields:

$$\left[h^{\circ}\right]^3 - y' \left[h^{\circ}\right]^2 = 2K_{O_i}\sqrt{pO_2} \tag{3.26}$$

K_{O_i} may then be determined from comparison of experimental electrical conductivity measurements to the theoretical results obtained from solving equation 3.26. K_W may then be determined through the equation 3.24. Equation 3.26 may be rendered adimensional by dividing both sides of the equation by y'^3. For any value of the oxygen potential pO_2, if a different value of $y^{'}$ (*i.e.* z') hence μ_0 is considered, one sees that the electrical conductivity given by the model is identical, providing the $K_{O_i}{}'$ is chosen proportional to K_{O_i} and such that $K'_{O_i} = K_{O_i}\frac{z'^3}{y'^3}$. Indeed, the adimensional form of equation 3.26 is:

$$x^3 - x^2 = 2\frac{K_{O_i}}{y'^3}\sqrt{pO_2} = \gamma\sqrt{pO_2} \tag{3.27}$$

For a given value of $y^{'}$, the value of K_{O_i} that provides an adequate fit of the model to experimental conductivity values corresponding to regions 1 and 2 is unique, and so the theoretical curve that fits the data is unique and independent of $y^{'}$. In order to determine $pO_{2,trans}$ at a given temperature from experiment, it is necessary that for some values of the oxygen potential defects W' and O_i'' exist. Of the three lower temperatures, only the 1173 K data would answer this criterion. Firstly, γ is determined so the solution to equation 3.27 reproduces as many experimental data points (σ/σ_{plat}, where σ_{plat} is the electrical conductivity value in the extrinsic region) as possible. Figure 3.2 shows the results obtained for $\gamma \sim 5.10^7$. It was further assumed that the experimental data point obtained at this temperature and at the highest oxygen partial pressure corresponds to region 3 were clusters constitute the majority defect. Electrical conductivity may therefore be approximated beyond this point by a straight line in a Log–Log representation with a slope of 0.5 which goes through this last data point. The intersection between this line and the optimised theoretical curve provides an estimate of $pO_{2,trans}$ (~10^{-13} atm, see Figure 3.2).

Note at this point that with a value of μ_0 of 0.0554 $m^2 \cdot K \cdot V^{-1} \cdot s^{-1}$ as suggested by Dudney [70], y' is estimated at $2.4.10^{25}$ m^{-3} based on experimental data in the extrinsic region, which in turn yields a value (based on relationship 3.27) of K_{O_i} of roughly $2.4.10^{-2}$. With a value of $pO_{2,trans}$ of 10^{-13}, one may estimate K_W

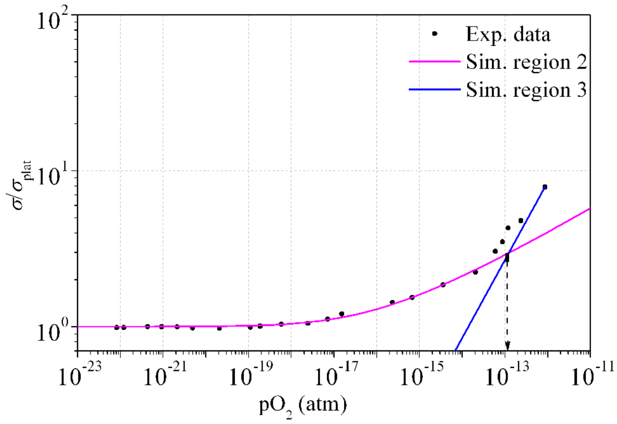

Figure 3.2: Adimensional analysis of electrical conductivity data taken at 1173 K: $pO_{2,trans}$ falls at the intersection between the two simulation curves.

from relationship 3.24 at roughly $1.5.10^7$. We turn now to the deviation from stoichiometry data compiled by Perron [151] at 1173 K. Figure 3.3 indicates these experimental data along with deviation from stoichiometry estimated from relationship 3.25 and the previous estimate of K_W .

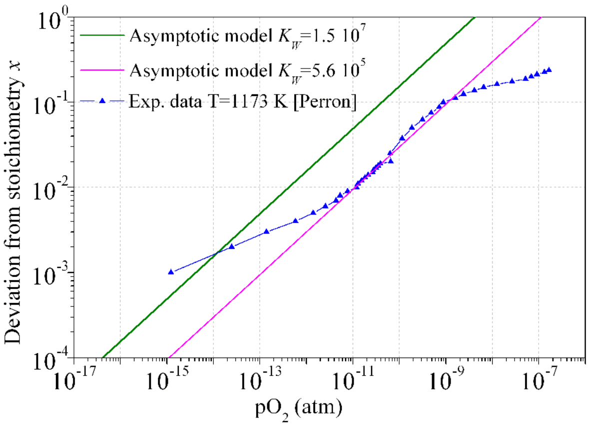

Figure 3.3: Deviation from stoichiometry estimates based on asymptotic model and different values of K_W.

A discrepancy is seen which may be cancelled by assuming a different value for K_W of $5.6.10^5$ as seen in Figure 3.3. In other words assuming a pre-exponential factor for hole mobility of 0.0554 $m^2 \cdot K \cdot V^{-1} \cdot s^{-1}$ renders electrical conductivity measurements inconsistent with deviation from stoichiometry values. If K_W is assumed to be approximately $5.6.10^5$ as suggested from deviation from stoichiometry measurements only, K_{O_i} is once again estimated from equation 3.24 to be $1.7.10^{-4}$. The value of γ determined previously then enables an estimate of y and finally μ_0 to be made. Application of relationship 3.27 yields y for the afore mentioned value of K_{O_i}, and from the Arrhenius representation of Log (σT), the product (μ_0 x y) is determined. This analysis yields values of $4.6.10^{24}$ m^{-3} and 0.29 $m^2 \cdot K \cdot V^{-1} \cdot s^{-1}$for y and μ_0 respectively. At this stage, a model that takes into account only impurities, oxygen interstitials and complex defects was applied to optimise the values of parameters μ_0, K_{O_i} and K_W at 1173 K. A value of 0.26 ±0.05 $m^2 \cdot K \cdot V^{-1} \cdot s^{-1}$ is determined for μ_0 which appears to be approximately five times the value suggested by Dudney. From the quantity (μ_0 $\cdot$ y), y is estimated at $5.2.10^{24}$ m^{-3}. We then reproduce the data at 973 K and 1073 K considering this last estimate of μ_0 using a simplified model and relationships 3.7 and 3.8.

***T* (K)**	***Simplified Model***		
	μ_0	K_{O_i}	K_W
1173	0.26	$2.5\ 10^{-4}$	$6.3\ 10^{5}$
1073	0.26	$3.2\ 10^{-4}$	$7.9\ 10^{6}$
973	0.26	$1.3\ 10^{-3}$	$1.6\ 10^{8}$

Table 3.2: Best estimate determination of equilibrium constants K_{O_i} and K_W obtained using a simplified model with a value of μ_0 of 0.26 $m^2 \cdot K \cdot V^{-1} \cdot s^{-1}$

Figure 3.4a), b) shows the experimental data and corresponding model results at 973 and 1173K. These results are consistent with the fact that at those temperatures, electrons and oxygen vacancies are negligible in comparison with holes and oxygen interstitials or clusters.

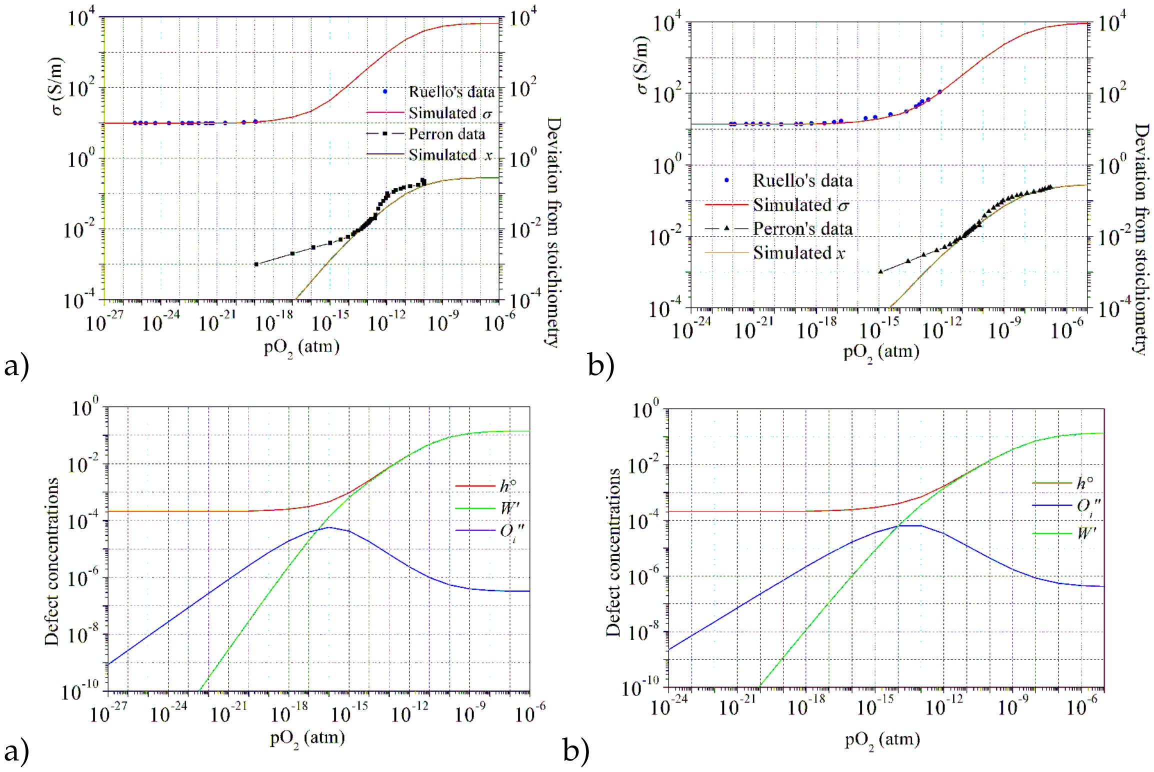

a) b)

a) b)

Figure 3.4: Experimental data and corresponding simplified model results at 973 (a), and 1173K (b).

3.3.2.2 Analysis of the high temperature data (1473 K, 1573 K, 1673 K)

We follow Ruello's [162] hypotheses in the sense that electrons and holes are assumed to have similar mobilities. As a result, a combination of equations 3.1 and 3.6 suggests that electrical conductivity data shows a minimum for values of $[h^{\circ}]$ given by:

$$\left[h^{\circ}\right] \approx \left[e^{'}\right] \approx \sqrt{K_e} \tag{3.28}$$

Minima in the conductivity data are only clearly observed above 1473 K, which is why estimates of K_e and K_{AF} are only attempted at those temperatures. Based on our previous estimate of μ_0, we can now estimate K_e at all three temperatures from the actual value of the minimum electrical conductivity data:

$$K_e = \left(\left[h^{\circ}\right]\right)^2 = \left(\frac{\sigma_{min} T}{2 \cdot e \cdot \mu_0 \exp\left[-\frac{\Delta H_m}{K_B T}\right] \cdot \mathcal{N}_{Av} \cdot \frac{d}{M}}\right)^2 \tag{3.29}$$

Further assuming that the material behaves intrinsically at those temperatures, the electroneutrality equation reduces to:

$$\left[O_i''\right] \sim \left[V_O^{\circ\circ}\right] \tag{3.30}$$

Noting $pO_{2,min}$ the value of the oxygen potential at which the minimum electrical conductivity is obtained, combining equations 3.28, 3.29, 3.7 and 3.9 yields:

$$K_{AF} = \frac{K_{O_i}^2 pO_{2,min}}{2K_e^2} \tag{3.31}$$

Note that $pO_{2,min}$ may also be considered as the oxygen partial pressure at which exact stoichiometry is obtained. However, because of the shape of the electrical conductivity curves, there is probably a relatively large uncertainty in the determination of $pO_{2,min}$ and hence K_{AF}. Table 3.3 indicates all estimated values of K_{O_i} , K_W, K_e and K_{AF} either obtained directly from the data analysis or extrapolated at lower or higher temperatures with values of μ_0 and y as indicated in the previous section ($0.26\ m^2\cdot K\cdot V^{-1}\cdot s^{-1}$and $5.2.10^{24}\ m^{-3}$) respectively. Note that if electrons and holes are assumed to have different mobilities, then the analytical expressions derived from the asymptotic model are modified as follows:

$$K_e = \frac{1}{\mu_{rel}} \left(\frac{\sigma_{min} T}{2 \cdot e \cdot \mu_0 \exp\left[-\frac{\Delta H_m}{K_B T}\right] \cdot \mathcal{N}_{Av} \cdot \frac{d}{M}} \right)^2 \tag{3.32}$$

$$K_{AF} = \frac{K_{O_i}^2 pO_{2,min}}{2\mu_{rel}^2 K_e^2} + \frac{K_{O_i}\sqrt{pO_{2,min}}}{4\mu_{rel}^{3/2}\sqrt{K_e}} \left(1 - \mu_{rel}\right) \tag{3.33}$$

3.4 Results and sensitivity analysis

The aim of the analysis of Ruello's data [164] with this model is to determine whether values of defect equilibrium constants may be determined that simultaneously reproduce electrical conductivity and deviation from stoichiometry data adequately. A mathematical model was therefore set up that solves equations 3.6 to 3.13 simultaneously for given values of the equilibrium constants, α and μ_0. Because of the number of physical constants involved, it was necessary to devise a method for providing a starting estimate of these constants based on the asymptotic model approach described in the previous section (§3.3.2). This involves analysing the electrical conductivity of Ruello and previously obtained deviation from stoichiometry data simultaneously with assumptions relative to the predominance of a given defect population. Equilibrium constants, for which whenever possible the asymptotic analysis provides starting values, and the α parameter are adjusted for a data set at a given temperature in order to minimise the difference between the model and the experimental data points. Greater emphasis is given to the electrical conductivity data. Table 3.3 provides a summary of model parameters determined from the asymptotic analysis and obtained from fitting the data with the complete model. As can be seen, values of the estimates are very close to the model parameter values obtained upon considering the model in its complete form. Also indicated in Table 3.3 are the uncertainties associated with each of the model parameters based on an estimated relative error of ±10% for electrical conductivity data and ± 5.10^{-3} postulated for deviation from stoichiometry data. These uncertainties are estimated from the minimum and maximum values of equilibrium constants that reproduce the experimental data within the uncertainties postulated for both these properties (deviation from stoichiometry and electrical conductivity).

T [K]	K_{O_i}		K_W		K_e		K_{AF}	
	Initial	**Fit**	**Initial**	**Fit**	**Initial**	**Fit**	**Initial**	**Fit**
973	**$1.3\ 10^{-3}$**	**$1.3\ 10^{-3\pm0.4}$**	**$1.6\ 10^{8}$**	**$1.6\ 10^{8\pm0.4}$**	**$1.8\ 10^{-12}$**	**$2.0\ 10^{-10\pm0.2}$**	**$5.6\ 10^{-13}$**	**$5.0\ 10^{-15\pm0.4}$**
1073	**$3.2\ 10^{-4}$**	**$3.2\ 10^{-4\pm0.4}$**	**$7.9\ 10^{6}$**	**$7.9\ 10^{6\pm0.4}$**	**$3.1\ 10^{-11}$**	**$5.0\ 10^{-10\pm0.2}$**	**$5.2\ 10^{-12}$**	**$4.0\ 10^{-14\pm0.4}$**
1173	**$2.5\ 10^{-4}$**	**$2.0\ 10^{-4\pm0.4}$**	**$6.3\ 10^{5}$**	**$6.3\ 10^{5\pm0.4}$**	**$3.3\ 10^{-10}$**	**$1.0\ 10^{-10\pm0.2}$**	**$3.4\ 10^{-11}$**	**$1.3\ 10^{-13\pm0.4}$**
1273	**$1.1\ 10^{-4}$**	**$1.3\ 10^{-4\pm0.4}$**	**$7.7\ 10^{4}$**	**$4.0\ 10^{4\pm0.4}$**	**$2.4\ 10^{-9}$**	**$5.0\ 10^{-9\pm0.2}$**	**$1.6\ 10^{-10}$**	**$4.0\ 10^{-13\pm0.4}$**
1373	**$6.5\ 10^{-5}$**	**$7.9\ 10^{-5\pm0.4}$**	**$1.3\ 10^{4}$**	**$1.8\ 10^{4\pm0.4}$**	**$1.3\ 10^{-8}$**	**$1.6\ 10^{-8\pm0.2}$**	**$6.1\ 10^{-10}$**	**$1.0\ 10^{-12\pm0.4}$**
1473	**$4.1\ 10^{-5}$**	**$5.6\ 10^{-5\pm0.4}$**	**$2.7\ 10^{3}$**	**$6.3\ 10^{3\pm0.4}$**	**$6.3\ 10^{-8}$**	**$6.3\ 10^{-8\pm0.2}$**	**$1.7\ 10^{-9}$**	**$4.0\ 10^{-9\pm0.4}$**
1573	**$2.7\ 10^{-5}$**	**$2.4\ 10^{-5\pm0.4}$**	**$6.9\ 10^{2}$**	**$1.6\ 10^{3\pm0.4}$**	**$1.6\ 10^{-7}$**	**$1.7\ 10^{-7\pm0.2}$**	**$6.6\ 10^{-9}$**	**$1.0\ 10^{-8\pm0.4}$**
1673	**$1.9\ 10^{-5}$**	**$1.3\ 10^{-5\pm0.4}$**	**$2.1\ 10^{2}$**	**$3.2\ 10^{3\pm0.4}$**	**$7.1\ 10^{-7}$**	**$7.1\ 10^{-7\pm0.2}$**	**$1.1\ 10^{-8}$**	**$3.2\ 10^{-8\pm0.4}$**

Table 3.3: Model parameters determined from the asymptotic analysis presented in section 3.3.2 ("Initial" column) and obtained from comparison of the model in its complete form to the data ("Fit" column). The hole mobility is assumed at 0.26 $m^2 \cdot K \cdot V^{-1} \cdot s^{-1}$. Initial estimates of equilibrium constants are indicated in red; initial extrapolated values are in blue.

The main conclusions one may draw from this analysis and results from section §3.3.2 are as follows:

1. If the mobility pre-exponential factor μ_0 is postulated, adjusting the model parameters to reproduce the electrical conductivity data alone provides a unique set of equilibrium constants. However, deviation from stoichiom-

etry will in general not be properly reproduced because electrical conductivity data alone provides an estimate of $(\mu_0 \cdot y)$ only.

2. It is the combined analysis of deviation from stoichiometry and electrical conductivity data that enables us to determine all model parameters (equilibrium constants, α and μ_0) unequivocally. A best-estimate value of 0.26 $m^2 \cdot K \cdot V^{-1} \cdot s^{-1}$ was derived from the data analysis.

3. In principle deviation from stoichiometry measurements should be carried out on the same set of samples as those used to measure out electrical conductivity since as now widely reported, impurity content will modify these material properties. However, we only consider deviations from stoichiometry in excess of about 5.10^{-3} simply because it basically constitutes the minimal error associated with this kind of measurement. In this region most samples are expected to behave intrinsically unless purposefully doped.

4. Our analysis shows that K_{AF} and K_e cannot be determined from the low temperature electrical conductivity data (*i.e.* 973 K, 1073 K, 1173 K). This is also the case for K_W with the exception of the 1173 K data. However, K_W may be estimated with reasonable accuracy in the low temperature range based on deviation from stoichiometry measurements. Conversely because of the presence of impurities and the limited impact of isolated oxygen interstitials upon deviation from stoichiometry, K_{O_i} may not be determined from deviation from stoichiometry measurements alone.

Figure 3.5 a) and b) gives an example of both calculated and measured electrical conductivity and deviation from stoichiometry data at 1173 K and 1573 K. Also shown in 3.6 a) and b) are the corresponding defects concentrations.

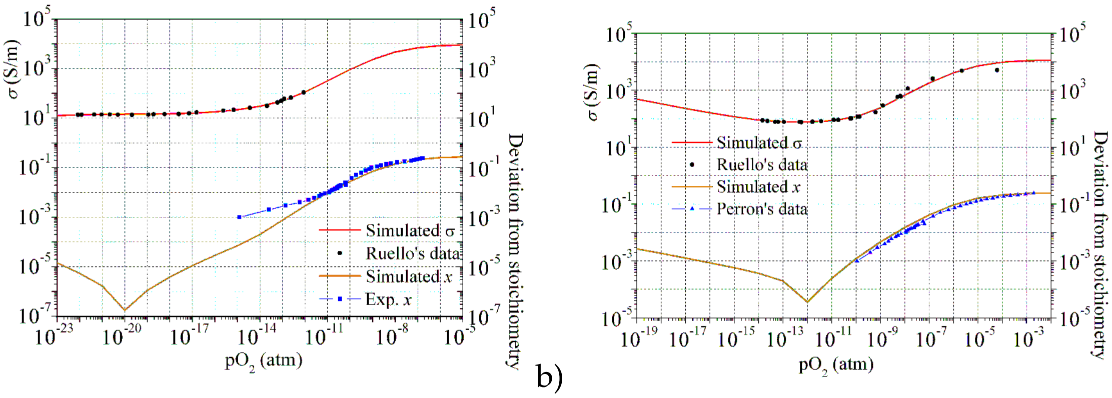

a) b)

Figure 3.5: Fit of electrical conductivity and deviation from stoichiometry data taken at 1173 K (a) and 1573 K (b).

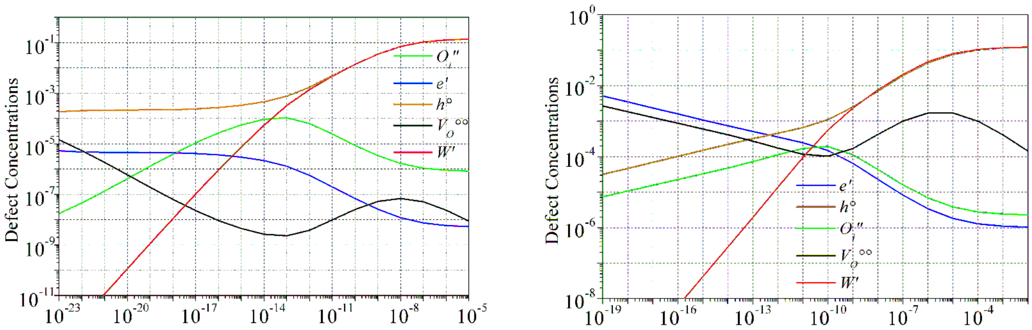

a) b)

Figure 3.6: Calculated defect concentrations at a temperature equal to 1173 K (a) and to 1573 K (b).

As expected, at 1173 K, complex anion clusters only appear at the highest oxygen potential values. Electronic defects constitute the majority defect population at all temperatures and oxygen partial pressures. The equilibrium constants determined from the data analysis are plotted in an Arrhenius representation in Figure 3.7 a, b, c and d.

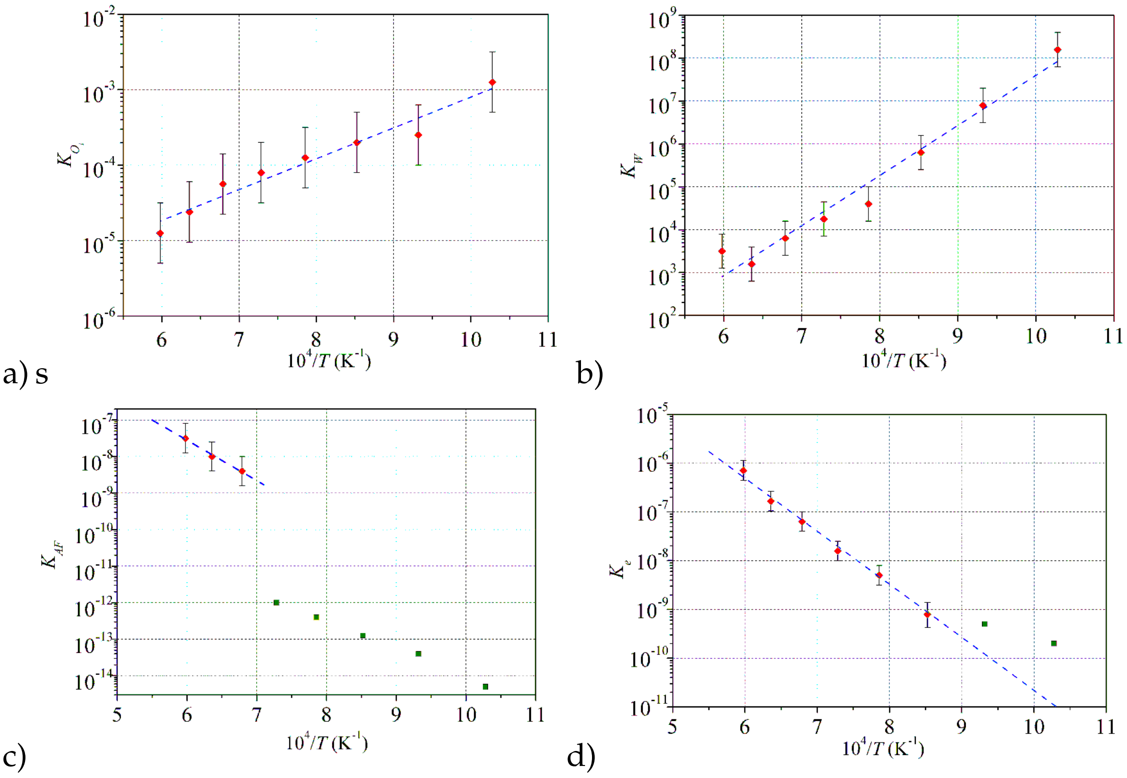

Figure 3.7: Arrhenius representation of the defect formation constants: graph a) refers to K_{O_i}, b) to K_W, c) to K_{AF} and d) to K_e.

Activation energies are reported for all four equilibrium constants in Table 3.4.

K	***Associated defect***	***Formation Energy* (eV)**	**Ab-initio *Calculations* (eV)**
K_e	Pair h°-e'	2.2 ± 0.1	1.8 **[18]**
K_{AF}	Oxygen Frenkel pair	2.2 < E < 6.5	3.5 **[18]**
K_{O_i}	Oxygen interstitial	-0.8 ± 0.1	-0.6 [66]
K_W	Willis defect	-2.3 ± 0.2	-1.9 [65]

Table 3.4: Comparison of first principle estimates of defect formation energies [18, 65] with results form the analysis of electrical conductivity data.

3.5 Discussion

3.5.1 Determination of equilibrium constants

As Figure 3.7 indicates, the equilibrium constants are roughly aligned when plotted in an Arrhenius representation which gives credit to the activation energies derived. It is however worth mentioning that not all equilibrium constants may be determined at all temperatures. Indeed, an accurate determination of equilibrium constants can only be derived first if a defect involved in this equilibrium is actually present in substantial quantities under the conditions investigated and if the property is actually sensitive to the presence of that defect. Electrical conductivity is more directly sensitive to charge carrier concentrations and deviation from stoichiometry to disorder on the oxygen sublattice. In relation to the di-interstitial constant for instance, analysing deviation from stoichiometry data at high oxygen potentials with a very simple asymptotic model, provides very good estimates of the corresponding equilibrium constant because di-interstitials constitute the majority defect population and that property is sensitive to it. Another good example is the mono-interstitial formation constant. Figure 3.8 indicates the experimental data at 1173 K in comparison with model calculations assuming the presence of both di-interstitials and mono-interstitials on the one hand, and di-interstitials alone on the other.

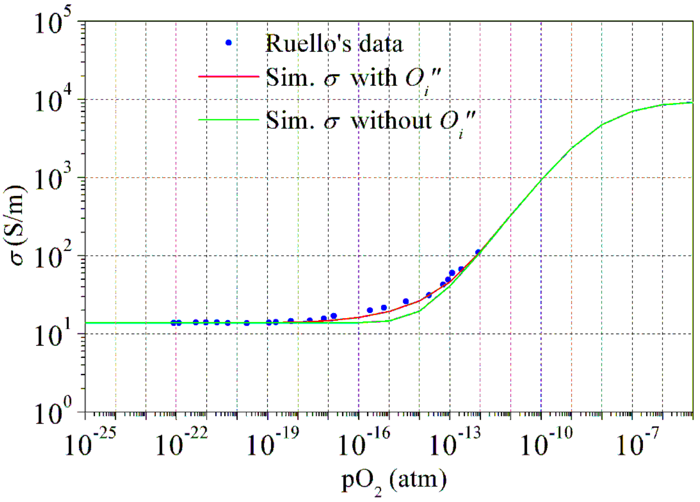

Figure 3.8: Simulation of conductivity data at 1173 K assuming the presence of both di- interstitials and mono-interstitials (red curve) on the one hand, and di-interstitials alone on the other (green curve).

This figure illustrates that electrical conductivity measurements are sensitive, albeit in a small range of partial pressures, to the presence of oxygen mono-interstitials, which gives credit to any defect characteristics derived from this property analysis. Conversely, Figure 3.5a) shows that because of the accuracy one may assume for thermogravimetric measurements, deviation from stoichiometry estimates are too insensitive in the region where mono-interstitials prevail for any meaningful data to be derived in relation to these defects. If improved accuracy were possible then it would be necessary to measure deviation from stoichiometry and electrical conductivity on identical sets of samples to draw combined, coherent conclusions. Along these lines, it is important to note that at the lowest temperatures for example, the Frenkel defect or the electron hole formation constants may be discounted altogether with no loss in terms of model representation. In other words it is impossible to determine Frenkel equilibrium constants from the lowest temperatures. The green points reported in Figure 3.7 represent upper values for the formation constants (oxygen Frenkel and electron-hole formation) above which the model cannot reproduce the experimental data adequately. Regarding the Frenkel disorder equilibrium constant in particular, its influence is only notable at the highest temperatures and its determination relies on an estimate of the oxygen potential at which electrical conductivity is minimal (with the added hypothesis that electrons and holes have similar mobilities, see section §3.3.2). The electrical conductivity data shows that it is difficult to determine this partial pressure adequately. So it is expected that using electrical conductivity measurements (or indeed deviation from stoichiometry) will lead to a generally poor estimate of the Frenkel formation constant.

3.5.2 Nature of defects, formation energies and comparison with theoretical approaches

Figure 3.6a) shows that the crossover point from a regime where mono-interstitials predominate to a regime where di-interstitials become the majority defect population occurs at 1173 K at an oxygen potential between 10^{-14} atm and 10^{-13} atm. The corresponding deviation from stoichiometry lies between 10^{-4} and 10^{-3} which is very low indeed. Beyond that crossover point, the charge of the di-interstitial defect does not follow the value expected from a purely ionic model, in coherence with the work of Crocombette and co-workers [57, 55] (see Chapter 1 - §1.2.2). For instance, the most stable di-interstitial (IX2) reported in [55] at high oxygen partial pressures has a charge of -1, as transpires from the present analysis. We can also compare quantitatively the results of our data analysis to these theoretical approaches based on Density Functional Theory. The results of Andersson and co-workers [18] are reported in Table 3.4. A good agreement is noted for both the electron-hole formation energy and the doubly charged mono-interstitial. One may also note the very close agreement with the band gap of 2.1±0.1 eV determined from optical methods by Schoenes [166]. A lack of accuracy in the Frenkel pair formation constant makes comparisons difficult between experiment and theory. We have also used results derived from Dorado's work [65] to estimate the formation energy of di-interstitial clusters. This exercise is also extremely encouraging since it shows very close theoretical and experimental values (2.3 eV vs. 1.9 eV for the experimental and theoretical values respectively).

Such close agreement between experimentally determined formation energies and electronic structure calculations has never, to our knowledge, been demonstrated to this point. Both approaches are therefore encouraging. Also, interesting indications stem from the close inspection of Figure 3.4 which indicates deviation from stoichiometry as calculated by the model and corresponding experimental data at 973 K. As the oxygen partial pressure rises the slope of Log(x) vs. Log(pO_2) curves changes from roughly ½ to 1 possibly indicating the emergence of a defect population of charge p and containing n excess oxygen atoms such that $\frac{n}{2(p+1)} \sim 1$. Assuming a single negative charge would indicate that the cluster may be made up of roughly 4 excess oxygen atoms as would be expected for a cuboctahedron (see [61]).

Finally, the fact that this simple defect equilibrium approach is capable of reproducing properties over a wide range of temperature and oxygen partial pressure would indicate that uranium defects play a negligible part. By default, it therefore corroborates the broadly accepted view that electronic defects are present at a greater concentration than defects on the anion sublattice which themselves are more concentrated than defects on the cation sublattice. As in Ruello's analysis [162], in the work detailed in the previous sections we have assumed that the electron and hole mobilities are equivalent. This hypothesis is expected to have an impact upon the data analysis, hence the equilibrium constants derived; at high temperature mainly since it is at the higher temperatures (above 1473 K) that conduction undergoes a transition from p to n type conduction as the oxygen partial pressure decreases. In fact, as seen in section §3.3.2.2, K_e and K_{AF} are the constants mainly affected by the hypothesis of similar hole and electron mobilities. We have checked that a five fold modification of the electron relative mobility does not substantially modify values of K_W or K_{O_i}, nor does it in general modify the activation energies of any of the equilibrium constants, as suggested from the analysis in section §3.3.2.2.

3.6 Conclusions

In this work a simple point defect model has been developed based on point defect equilibria. It very satisfactorily reproduces electrical conductivity and deviation from stoichiometry data over a wide range of temperatures and oxygen partial pressures. In this model, defects on the cation sublattice are neglected other than electronic defects which is consistent with the generally held view in relation to UO_2 that electronic disorder dominates over anion disorder, which itself is more significant than cation disorder. A rather large value for the preexponential factor of the hole mobility is deduced from this analysis (0.26 $m^2K\ V^{-1}s^{-1}$), approximately 5 times greater than the value suggested by Dudney [70]. Based on the temperature analysis, it appears that formation energies for mono-interstitials, di-interstitials, and the electron-hole pairs can be determined with reasonable accuracy. The energy of oxygen Frenkel pair however cannot, probably because under the conditions examined, oxygen vacancies constitute the minority defect. Furthermore, the energies derived for the mono-interstitials and the electron-hole pair are shown to be close to values derived from first principles. In addition to this, the charge and apparent composition of di-interstitials is well in line with the more recent DFT+U calculations which predict a decrease in the charge per additional oxygen interstitial that makes up the cluster. Our results show that in relatively pure material, oxygen clustering is predominant at very low levels of hyperstoichiometry. Although encouraging, these conclusions should be backed up by further investigations. In particular, mobility measurements should be carried out even at low temperatures in order to confirm the conduction mechanism and the value of the hole mobility used at high temperature. It would be most enlightening to have an idea of the effect upon hole mobility of the nature and concentration of dopants. In a similar vein, the electron mobility should be sort to be determined through doping our material with pentavalent cations. It is also quite obvious that our analysis in principle requires that electrical conductivity and deviation from stoichiometry measurements be carried out on samples from identical batches. This is all the more true when samples are doped purposefully.

We have seen in this chapter how electrical conductivity and deviation from stoichiometry data may be rationalised using a point defect model for which equilibrium constants are thought to be characteristic of the material. Defect concentration calculations (Figure 3.6) tell us that we can expect rather radical changes in the oxygen self-diffusion coefficient as the majority defect population changes from mono-interstitials to di-interstitial clusters. Also the model tells us (see equation 3.22) that an increase in the dopant concentration is conducive to stabilising oxygen vacancies. In the next Chapter we study oxygen self-diffusion over a range of oxygen partial pressures in materials doped with trivalent ions in order both to characterise the effect of a change in the predominant defect population upon this property (for the higher oxygen partial pressures) and to ascertain whether oxygen vacancies may indeed be stabilised at the lowest oxygen partial pressures in the hope of improving our estimates of the Frenkel pair formation constant. Later in Chapter 6 we will attempt to interpret these experimental data quantitatively and ascertain whether they are compatible with the model outlined in this chapter.

Chapter 4

Electrical conductivity, oxygen chemical and self-diffusion coefficient measurements in UO_{2+x} as a function of temperature and oxygen partial pressure

In Chapter 3, we saw that the analysis of electrical conductivity and deviation from stoichiometry data provided us with an estimate of formation energies of bulk defects. This of course only applies in an intrinsic region in which electrical conductivity is essentially an indirect means of tracking the behaviour of oxygen point defects. In particular, the analysis of existing data in an extrinsic region does not enable us to derive reliable information relating to oxygen vacancies.

The study of atomic transport properties is extremely complementary to this because this property is always sensitive to disorder on the oxygen sub-lattice. Oxygen self-diffusion coefficient measurements (see Chapter 1 - §1.3.2.2) which are the main object of this chapter are liable to confirm the point defect analysis presented previously, enhance our knowledge of certain defect equilibria and possibly even enable us to derive defect migration barriers.

In this chapter self-diffusion measurements are carried out with two essential objectives:

- Determining data (formation and migration energies) which are meaningful to oxygen vacancies. To this end we define and study a range of conditions (impurity content, temperature and oxygen partial pressures) which we consider as being favourable to the stabilisation of oxygen vacancies, despite the relatively low temperatures accessible with our current equipment (*i.e.* below 1273 K). Doping with a trivalent cation such as chromium has the effect of increasing the oxygen potential value at which the material changes from substoichiometry to hyperstoichiometry (see Chapter 3, §3.3.2.1).

- Determining the transition region between a regime where mono-interstitials dominate to a regime in which di-interstitials constitute the majority oxygen defect population. This transition point is not well documented (other than from the results of Chapter 3) and we attempt to use oxygen self-diffusion coefficient measurements to determine it. Self-diffusion data at exact stoichiometry and at high deviations from stoichiometry exist but not at this transition point (as shown in §1.3.2.2, Figure 1.15).

In this chapter, we measure oxygen self-diffusion coefficients over a wide range of oxygen partial pressures and between 800°C and 1000°C. As was demonstrated from previous studies [68, 78], it is essential when doing this to ascertain the charge carrier concentrations by determining the electrical conductivity of the samples under identical conditions to those in which self-diffusion is measured. The technique used for electrical property measurements is the four point Kelvin bridge method outlined in Chapter 2, §2.3.1. Self-diffusion measurements are carried out by first equilibrating samples under the prescribed temperature and oxygen partial pressure and subsequently annealing under identical conditions in an atmosphere enriched with ^{18}O thus enabling isotopic exchange to occur. Diffusion coefficients are derived from the ^{18}O depth profiles determined from SIMS (see §2.5).

4.1 Conditions under which experiments are carried out

4.1.1 Choice of experimental conditions

In order to increase the chance of characterising vacancy assisted migration, we have chosen to study chromium doped samples (see paragraph §3.3.2.1). This serves the added advantage of prescribing the hole concentration as demonstrated in previous studies [68, 78], thus simplifying the analysis of the dependence upon oxygen partial pressure of the oxygen self-diffusion coefficient. This nonetheless requires determining the electrical conductivity of the material to provide an estimate of the hole concentration. In these samples an oxygen diffusion study was carried out at four temperatures (between 750°C and 950°C) and at the lowest oxygen partial pressure possible. Based on these results, an analysis at 800°C was carried out as a function of oxygen partial pressure to ascertain the effect of oxygen vacancies. These samples were also studied at 900°C and 1000°C at higher oxygen potentials (see Chapter 3) in the hope of characterising a change from a mono-interstitial to a di-interstitial regime. The higher temperatures were motivated on the grounds that this would guarantee shorter periods of time to reach equilibrium.

In parallel to this, relatively pure polycrystalline samples were looked at and their electrical and self-diffusion properties were characterised at 900°C and 1000°C and identical oxygen partial pressures to those at which our 900°C and 1000°C annealed chromium doped samples were studied. Because the materials were known to contain only small levels of impurities, they were also earmarked for a chemical diffusion study that could potentially enable us to determine the thermodynamic factor γ (see Chapter 1, §1.3.2), which would enable further validation of the point defect model developped in Chapter 3.

The following provides a summary of the type of samples (either chromium doped or undoped polycrystalline samples) characterised and the conditions under which each property (electrical conductivity, chemical diffusion and self-diffusion) was studied.

4.1.2 Electrical and chemical diffusion experiments

Electrical conductivity as a function of temperature

Table 4.1 reports the experimental conditions under which the electrical conductivity of Cr-doped and undoped samples were characterised. The aim here was to determine the hole mobility and estimate the impurity or doping content in in both sets of samples studied. To this end, parallelepipedic samples were prepared from both sample sets and exposed to a reducing atmosphere ($Ar/10\%\ H_2$ or Ar cleansed of its oxygen using an electrochemical pump [41]) at different temperatures in the 500-1000°C temperature range; the oxygen partial pressure of the gas was always monitored using a zirconia probe located in the gas flow just beyond the sample holder (see electrical conductivity device layout in Figure 2.6).

Nature of sample studied	*Employed Gas*	*T* (°C)	pO_2 (atm)
Undoped UO_2	$Ar/10\%H_2$	692	$4.4\ 10^{-23}$
		793	$2.9\ 10^{-21}$
		893	$2.3\ 10^{-19}$
		893	$3.4\ 10^{-19}$
		937	$9.2\ 10^{-19}$
		993	$2.9\ 10^{-18}$
Cr-doped UO_2	Ar cleansed of its residual oxygen using an electrochemical zirconia pump and such that the pO_2 at 650°C was roughly 10^{-22} atm	533	$9\ 10^{-27}$
		626	$1.8\ 10^{-23}$
		721	$9.8\ 10^{-21}$
		817	$1.8\ 10^{-18}$
		912	$1.5\ 10^{-16}$
		1003	$5.2\ 10^{-15}$

Table 4.1: Thermodynamic conditions under which the dependence upon temperature of the electrical conductivity was evaluated.

Electrical conductivity as a function of oxygen partial pressure for subsequent chemical diffusion measurements

The following table presents the thermodynamic conditions in which electrical conductivity either of Cr-doped or un-doped UO_2 sample was characterized as a function of oxygen partial pressure. In particular, we evaluated electrical conductivity for oxygen partial pressures ranging between 10^{-19} atm and 10^{-11} atm and at two temperatures: 893°C and 993°C.

Any variation of conductivity is an indication that the composition of the sample is changing. As a consequence, if the sample behaves intrinsically, any variation of annealing atmosphere induces a change of the recorded electrical conductivity signal. When a sample is at equilibrium with the atmosphere, its composition and in particular its oxygen content is homogeneous. If a change occurs in the composition of the surrounding atmosphere, the oxygen surface concentration changes and the kinetics with which the sample eventually reaches a new equilibrium (tracked by the electrical conductivity measurement) is determined by the oxygen (chemical) diffusion coefficient.

The thermodynamic conditions indicated with an asterisk in Table 4.2 are those in which both electrical conductivity and chemical diffusion coefficient measurements were carried out.

_T_ (°C)	**pO_2 (atm)**		**_T_ (°C)**	**pO_2 (atm)**	
	Undoped UO_2	***Cr-doped UO_2***		***Undoped UO_2***	***Cr-doped UO_2***
893	2.3 10^{-19}	1.0 10^{-19}	993	2.3 10^{-18}	1.9 10^{-18}
	3.4 10^{-19}	2.1 10^{-18}		2.8 10^{-15}	5.9 10^{-18}
	2.8 10^{-18}(*)	1.3 10^{-17}		2.9 10^{-13} (*)	3 10^{-17}
	2.3 10^{-17}(*)	1.3 10^{-16}		8.4 10^{-13} (*)	9.2 10^{-17}
	2.4 10^{-16}(*)	6.2 10^{-16}		4.3 10^{-12} (*)	3.5 10^{-16}
	1.2 10^{-15} (*)	1.2 10^{-15}			1.7 10^{-15}
	9.4 10^{-16}	4.5 10^{-15}			1.2 10^{-14}
	6.8 10^{-15}(*)	2.5 10^{-14}			7.9 10^{-14}
	2.4 10^{-13}(*)	8.2 10^{-14}			2.5 10^{-13}
	5.7 10^{-13} (*)	1.4 10^{-13}			1.0 10^{-12}
	2.1 10^{-12} (*)	4.3 10^{-13}			6.3 10^{-12}

Table 4.2: Thermodynamic conditions at which we estimated electrical conductivity (and in same cases oxygen chemical diffusion coefficients) dependence upon oxygen partial pressure.

4.1.3 Self-diffusion experiments

Oxygen self-diffusion dependence upon temperature

Table 4.3 presents the experimental conditions under which the oxygen self-diffusion coefficients of chromium doped samples were characterised as a function of temperature. Four temperatures were studied at the lowest possible oxygen potential. The carrier gas used is a mixture of Ar/10%H_2, which is then humidified by bubbling in water containing either ordinary distilled water or enriched in ^{18}O and maintained at a temperature of 5°C. The system set up is that reported in Figure 2.2a) and the oxygen partial pressure was monitored using an *in-situ* yttria stabilised zirconia probe placed at the furnace inlet in close proximity to the sample holder.

Nature of sample studied	**_T_ (°C)**	***^{16}O equilibrating anneal***		***^{18}O diffusion anneal***	
		_t_ (h)	**pO_2 (atm)**	**_t_ (h)**	**pO_2 (atm)**
Cr-doped UO_2	748	14.3	2.8±1 10^{-22}	3	4.8±2 10^{-22}
Cr-doped UO_2	800	5	1.2±0.4 10^{-20}	2.11	1.3±0.5 10^{-20}
Cr-doped UO_2	870	3.42	2.0±0.6 10^{-19}	3	3.1±1 10^{-19}
Cr-doped UO_2	950	4.15	4.8±1.5 10^{-18}	3	7.3±2.3 10^{-18}

Table 4.3: Thermodynamic conditions imposed for annealing dedicated to the oxygen self-diffusion activation energy study.

Oxygen diffusion dependence upon pO_2 at 800°C at low oxygen potentials

An identical experimental setup was used for the following diffusion experiments involving chromium doped samples.

Nature of sample studied	*T* (°C)	*^{16}O equilibrating anneal*		*^{18}O diffusion anneal*	
		t (h)	*pO_2* (atm)	*t* (h)	*pO_2* (atm)
Cr-doped UO_2	800	5	$1.2\pm0.4\ 10^{-20}$	2.11	$1.3\pm0.5\ 10^{-20}$
Cr-doped UO_2	800	2.5	$2.1\pm0.9\ 10^{-20}$	16	$2.1\pm0.9\ 10^{-20}$
Cr-doped UO_2	800	6	$1.3\pm0.5\ 10^{-19}$	14,3	$1.1\pm0.4\ 10^{-19}$
Cr-doped UO_2	800	3.15	$2.8\pm0.8\ 10^{-19}$	2.05	$3\pm1\ 10^{-19}$
Cr-doped UO_2	800	12	$2.6\pm0.9\ 10^{-17}$	1	$2.9\pm0.8\ 10^{-17}$

Table 4.4: Thermodynamic conditions dedicated to the study of the oxygen self-diffusion dependence upon oxygen partial pressure at a temperature of 800°C.

Oxygen diffusion dependence upon pO_2 at 890°C and 990°C and at high oxygen potentials

In the following set of experiments the configuration described in Figure 2.2b) was used. In particular, the oxygen partial pressure was not only monitored *in-situ* but also measured prior to the beginning and following the end of an annealing sequence by diverting the humidified carrier gas over a short period of time through a furnace maintained at 900°C and containing an air reference yttria stabilised zirconia probe. During annealing, the gas outlet was continually monitored using this system.

Table 4.5 reports the thermodynamic conditions and anneal time applied during the equilibration period and ^{18}O-diffusion annealing carried out.

N°	*Nature of sample*	*T* (°C)	*^{16}O equilibrating anneal*			*^{18}O diffusion anneal*		
			t (h)	*pO_2 before TT* (atm)	*pO_2 after TT* (atm)	*t* (min)	*pO_2 before TT* (atm)	*pO_2 after TT* (atm)
1	Cr-doped	890	5	$1.0\pm0.3\ 10^{-15}$	$9.4\pm3\ 10^{-16}$	30	$7.1\pm2\ 10^{-16}$	$6.8\pm2\ 10^{-16}$
	Undoped							
2	Cr-doped	890	5	$7.4\pm2\ 10^{-15}$	$8.6\pm2\ 10^{-15}$	30	$5.5\pm1\ 10^{-15}$	$5.5\pm1\ 10^{-15}$
	Undoped							
3	Cr-doped	890	5	$6.3\pm2\ 10^{-14}$	$6.9\pm2\ 10^{-14}$	30	$1.2\pm0.3\ 10^{-13}$	$1.2\pm0.3\ 10^{-13}$
	Undoped							
4	Cr-doped	890	5	$9.5\pm3\ 10^{-13}$	$8.9\pm2\ 10^{-13}$	30	$1.0\pm0.3\ 10^{-12}$	$1.9\pm0.5\ 10^{-12}$
	Undoped							
5	Cr-doped	987	2.5	$2.5\pm0.6\ 10^{-15}$	$2.6\pm0.6\ 10^{-15}$	15	$3.7\pm0.9\ 10^{-15}$	$3.6\pm0.8\ 10^{-15}$
	Undoped							
6	Cr-doped	987	2.5	$1.1\pm0.3\ 10^{-13}$	$1.2\pm0.3\ 10^{-13}$	15	$1.2\pm0.3\ 10^{-13}$	$1.2\pm0{,}3\ 10^{-13}$
	Undoped							
7	Cr-doped	987	2.5	$5.9\pm1\ 10^{-13}$	$6.7\pm2\ 10^{-13}$	15	$8.0\pm2\ 10^{-13}$	$8.3\pm2\ 10^{-13}$
	Undoped							
8	Cr-doped	987	2.5	$1.2\pm0.3\ 10^{-11}$	$1.6\pm0.4\ 10^{-11}$	15	$1.3\pm0.3\ 10^{-11}$	$1.4\pm0.3\ 10^{-11}$
	Undoped							

Table 4.5: Oxygen partial pressures and temperatures for all self-diffusion measurements at the highest oxygen partial pressures.

A typical annealing sequence corresponding to experiments described in Table 4.5, is shown in Figure 4.1. It shows the oxygen partial pressure prior to any treatment, during the equilibration period and following it, prior to the diffusion anneal, during the diffusion anneal and following it.

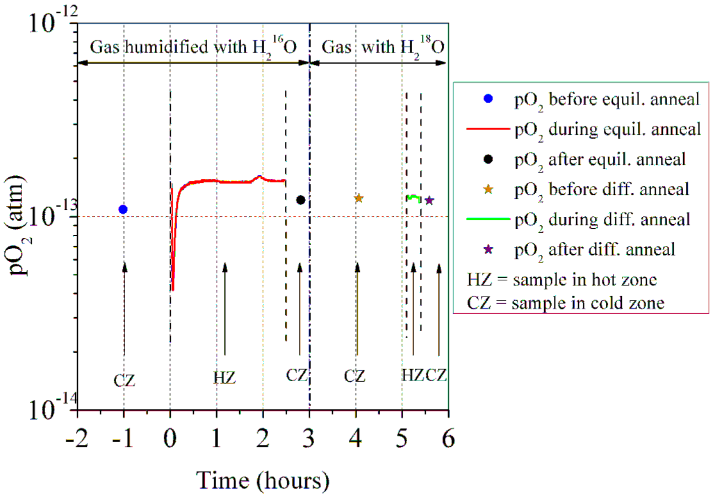

Figure 4.1: Example of pO_2 monitoring during diffusion experiment N°6 (987°C, 10^{-13} atm).

Figure 4.1 shows that in the first instants of the equilibration period, the oxygen partial pressure drops substantially. The oxygen partial pressure returns to its expected value in about half an hour; this observation was systematic and could be the result of adsorption of hydrogen molecules at the surface of the sample holder and alumina rod on which the sample holder is attached (see Figure 2.2), during the prolonged period when they are located in the cold region of the furnace and exposed to a flowing gas mixture containing hydrogen.

Special care was taken to make sure that the samples were equilibrated under exactly the same conditions as those used for the diffusion sequence proper, *i.e.* isotopic exchange.

4.2 Results of electrical conductivity and oxygen chemical diffusion measurements

4.2.1 Electrical conductivity

As seen previously, electrical conductivity provides an estimate of the hole concentration in the sample which is related to the oxygen point defect concentration and hence its self-diffusion coefficient. This underlines importance of collecting electrical conductivity data on the same sample sets as those used for oxygen self-diffusion studies. Figure 4.2 reports the electrical conductivity measurements as a function of oxygen partial pressure collected at the two temperatures of 893 and 993°C on Cr-doped and undoped UO_2 samples. The quality of such data is very much dependent upon the fact that sufficient time is allowed for stable thermodynamic conditions to be reached. For aim of comparison, we added to our measurement points the literature data collected by Ruello at 1000°C [162].

Compared to the undoped samples, the high amount of doping agents in our Cr-doped sample set induces an increase of electrical conductivity of about one order of magnitude. The collected data enables us also to verify the oxygen partial pressure range in which our Cr-doped samples show an extrinsic behaviour. For a temperature equal either to 893°C or 993°C electrical conductivity is fixed by the doping agent concentration up to oxygen partial pressures which may be estimated at between 10^{-12} and 10^{-11} atm. This fact will be useful for the analysis of oxygen self-diffusion coefficients. In fact, even at high val-

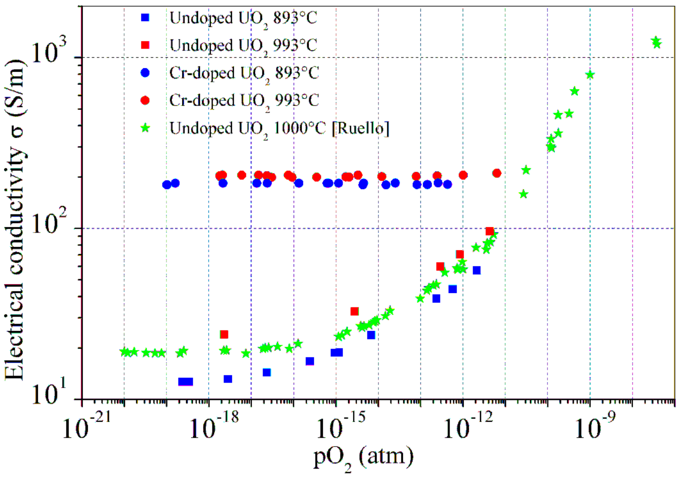

Figure 4.2: Electrical conductivity of un-doped and Cr-doped UO_2: dependence upon oxygen partial pressure at different values of temperatures and comparison of the data with those of Ruello [162]

ues of oxygen partial pressures, the hole concentration is a constant function of oxygen potential and has the same impact upon the oxygen self-diffusion coefficient at all oxygen partial pressures (as suggested by equation 1.8). However, the chemical diffusion coefficient cannot be determined in a range of oxygen partial pressures in which the electrical conductivity of the sample does not change.

Conversely, our undoped polycrystalline UO_2 sample behaves differently. As we can see in Figure 4.2, the extremely low impurity content present inside this type of samples induces a transition to the intrinsic region at much lower oxygen partial pressures than our Cr-doped samples. Comparison of our data with those of Ruello [162] demonstrates that impurities are present in both these samples in similar quantities.

Electrical conductivity data obtained by exposing the sample to the most reducing atmosphere allows to evaluate the characteristics of hole mobility. Next sections aims to present our results and compare them to the data of Fraczkiewicz [73] who studied similar sample sets.

4.2.2 Hole mobility study

The study of the hole mobility can be carried out by analysing conductivity data collected under the most reducing atmosphere. In fact, if the contribution of electrons is negligible compared to that of holes, Equation 3.1 can be written as follows:

$$\log(\sigma T) = \log(\mu_0 e [h^\circ]) - \frac{\Delta H_m}{\ln(10) \cdot k_B T} \tag{4.1}$$

Therefore, following equation 4.1, the Arrhenius representation of the quantity $\log(\sigma T)$ allows to directly deduce hole mobility activation enthalpy ΔH_m and to indirectly estimate the hole concentration $[h^\circ]$ assuming μ_0 to be known (evaluated in Chapter 3 at roughly 0.26 $m^2K/V{\cdot}s$). Note that if the material behaves extrinsically, $[h^\circ]$ is determined by the impurity content y (see Equation 3.21).

Figure 4.3a) and b) reports the Arrhenius dependence of $\log(\sigma T)$ we found respectively for our Cr-doped and undoped specimens together with the data collected by M. Fraczkiewicz [73] on the same sample sets.

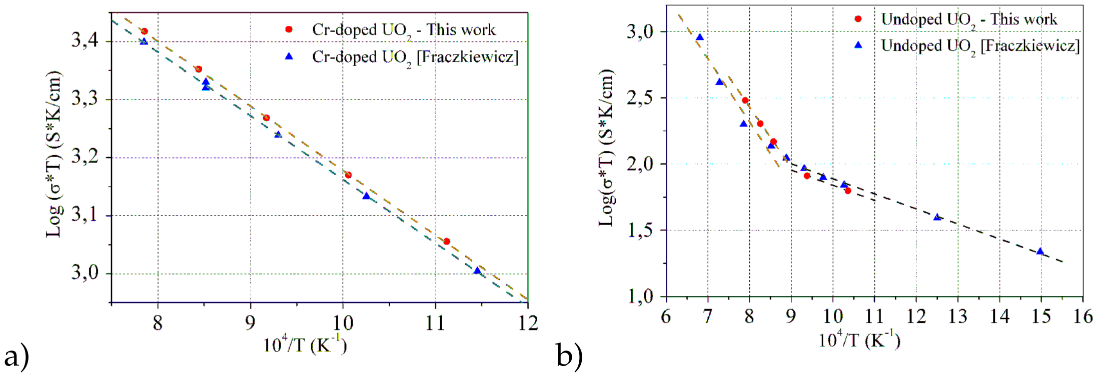

Figure 4.3: Dependence of Cr-doped (a) or undoped (b) UO_2 sample conductivity upon temperature

Our values of conductivity are identical to those of Fraczkiewicz [73], within the 10% systematic uncertainty which is estimated based on the precision with which one is capable of determining the distances between connecting wires (see Chapter 2, §2.3.3). The extrinsic behaviour of our Cr-doped sample is clearly visible in Figure 4.3a). Conversely, Figure 4.3b) shows that the contribution of the thermally activated holes becomes comparable to those produced by impurities at about 800°C. Consequently, an estimate of the impurity content of the undoped samples can be carried on only with the analysis of the data collected at low temperatures (dash black curve of Figure 4.3b)).

Table 4.6 reports our estimates of ΔH_m and of $(\mu_0 \cdot y)$. Our values are in great correspondence with the ones found by Fraczkiewicz.

Sample kind	**ΔH_m (eV)**		**($\mu_0 \cdot y$) (at·K·m^{-1}·V^{-1}·s^{-1})**	
	This work	**[73]**	***This work***	**[73]**
Cr-doped UO_2	0.22	0.22	1.2 10^{25}	1.1 10^{25}
Un-doped UO_2 (LT)	0.23	0.23	6.1 10^{23}	6.6 10^{23}
Un-doped UO_2 (HT)	0.91	0.95	8.0 10^{26}	8.5 10^{26}

Table 4.6: Hole activation enthalphy and (μ_0 x y) estimates obtained based on electrical conductivity data: our values are compared to those of Fraczkiewicz [73] assuming an adiabatic hopping process.

4.2.3 Oxygen chemical diffusion

As seen in Chapter 1, oxygen chemical diffusion (hereafter indicated as $\tilde{D}$) measurements are also an indication of the defects present in non-stoichiometric UO_{2+x}. Out of equilibrium electrical conductivity measurements following an abrupt change in the oxygen potential surrounding the sample enabled us to estimate this physical quantity.

To estimate $\tilde{D}$, we proceed as follows: the electrical conductivity of the sample is measured every 5 minutes following a change in the gas flow rates to an appropriate value, until it stabilises to a different value. Data are analysed by plotting the natural logarithm of the ratio $\frac{\sigma(t)-\sigma_\infty}{\sigma_0-\sigma_\infty}$ against time (see Equation 1.9 in Chapter 1): the slope of the graph obtained provides an estimate of $\tilde{D}$. The next figure shows an example of this analysis.

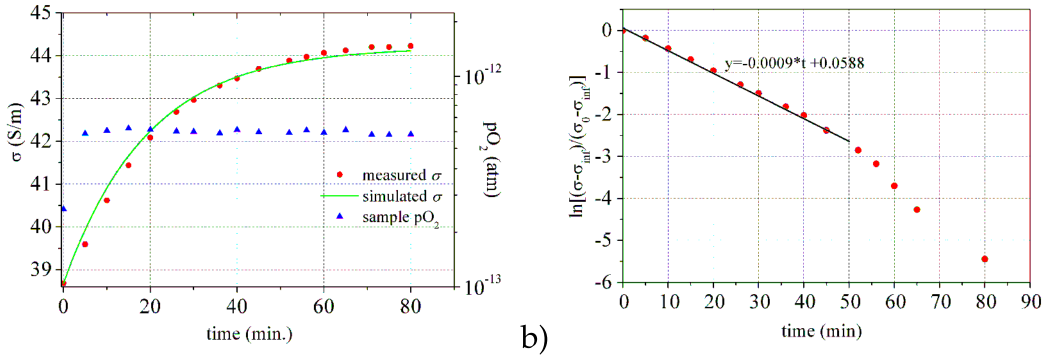

a) b)

Figure 4.4: Change with time of the conductivity of an un-doped UO_2 sample maintained at 893°C following a change in the oxygen partial pressure from $2.3 \cdot 10^{-13}$ to $5.3 \cdot 10^{-13}$ atm: a) Comparison between the simulated and the experimental curve; b) Determination of the oxygen chemical diffusion.

Table 4.7 reports the values obtained for chemical diffusion coefficients of un-doped samples.

***T* = 893°C**		***T* = 993°C**	
***Rejoined* pO_2 (atm)**	**$\tilde{D}$ (m²/s)**	***Rejoined* pO_2 (atm)**	**$\tilde{D}$ (m²/s)**
$2.8\ 10^{-18}$	$5.4\ 10^{-10}$	$2.9\ 10^{-13}$	$1.1\ 10^{-9}$
$2.3\ 10^{-17}$	$7\ 10^{-10}$	$8.4\ 10^{-13}$	$8.4\ 10^{-10}$
$2.4\ 10^{-16}$	$6.1\ 10^{-10}$	$4.3\ 10^{-12}$	$3.6\ 10^{-10}$
$1.2\ 10^{-15}$	$6\ 10^{-10}$		
$6.8\ 10^{-15}$	$5.3\ 10^{-10}$		
$2.4\ 10^{-13}$	$3.9\ 10^{-10}$		
$5.7\ 10^{-13}$	$3.1\ 10^{-10}$		
$2.1\ 10^{-12}$	$1.4\ 10^{-10}$		

Table 4.7: Estimates of oxygen chemical diffusion coefficients for different values of pO_2.

Figure 4.5 shows the oxygen chemical diffusion coefficients reported in Table 4.7 as a function of the final oxygen partial pressure. The major source of uncertainty for all data reported here is given by the error affecting electrical conductivity measurements (we remind again to Chapter 2, §2.3.3 for details).

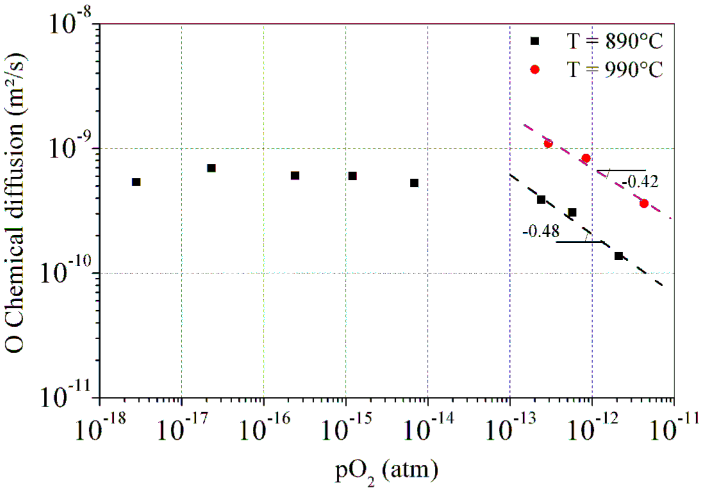

Figure 4.5: Dependence of UO_{2+x} oxygen chemical diffusion coefficient upon pO_2 at two different temperatures: 890°C and 990°C.

While at low oxygen partial pressures oxygen chemical diffusion remains more or less independent of oxygen partial pressure, it appears to decrease substantially at the higher oxygen potentials, *i.e.* in the intrinsic region proper. For both temperatures studied (893°C and 993°C), the last three points collected appear to form a straight line the slope of which is estimated at -0.48 and -0.42. These values seems to indicate that for oxygen potentials between 10^{-13} and 10^{-11} atm $\tilde{D}$ is proportional to $pO_2^{-1/2}$. However, following Equation 1.7, a through analysis of the oxygen chemical diffusion requires the determination of the oxygen self-diffusion coefficients in undoped samples annealed under identical thermodynamic conditions and the evaluation of the thermodynamic factor γ. Analysis of the data in Figure 4.5 is therefore deferred to Chapter 6. The next section reports the determination of oxygen self-diffusion coefficients.

4.3 Results of oxygen self-diffusion experiments

As reported in Chapter 2, oxygen tracer diffusion profiles are determined experimentally by depth profiling with Secondary Ion Mass Spectrometry. Crater depths required to determine the sputtering rates are characterised using chromatic confocal microscopy. Oxygen diffusion coefficients are then determined by fitting Fick's 2nd law to the experimental tracer profile. The next sub-sections present the results obtained; interpretations are postponed to Chapter 6.

4.3.1 Experimental determination of ^{18}O diffusion profiles

Sample characterisations were carried out using the SIMS IMS 6f Cameca instrument at CEA Cadarache. The optimisation of ion-beam conditions is a relatively long and delicate process: paragraph §2.4.3.1 provides all the details required prior to carrying out an oxygen depth profile. In our experiments the collected secondary ions are the oxygen isotopes ^{16}O and ^{18}O and some ionic species characteristic of sample matrix, such as ^{235}U and ^{52}Cr. The ^{18}O relative concentration profile is then determined by calculating the ^{18}O isotope fraction of the total oxygen content (sum of the ^{16}O and ^{18}O signals). Note that a quantitative analysis is therefore possible as the ionisation yields for both these isotopes are identical.

Once the time-dependent SIMS data is converted into depth profiles (see §2.5.1), ^{18}O profiles were successively simulated using Fick's law (see section §2.5.2 or Appendix B for details). Two examples of the profiles obtained are reported in the following Figure.

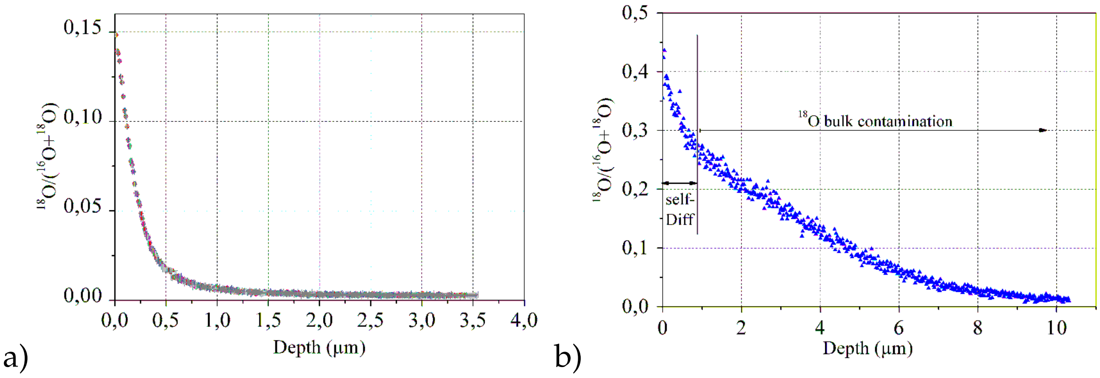

Figure 4.6: Example of an ideal ^{18}O depth profile (a) and one corresponding to a sample that has suffered from ^{18}O bulk contamination during the equilibrium annealing sequence (b): profile a) is that of a sample annealed at 800°C, 1.3 10^{-20} atm; the profile b) is of a sample annealed at 890°C, 5.5 10^{-15} atm.

As indicated in Figure 4.6, in some cases (Figure b), the collected ^{18}O depth profiles do not follow a simple erf function: ^{18}O is present at relatively high concentrations in the bulk of the sample. The reason for this is assumed to be that the sample was contaminated with ^{18}O during the equilibration stage due to residual ^{18}O adsorbed during previous experiments onto the surrounding materials (quartz tube and alumina sample holder rod). This residual ^{18}O may then be released during the equilibration stage and may contaminate the sample. During this equilibration stage, the carrier gas mixture is humidified with ordinary distilled water ($H_2{}^{16}O$). Under such circumstances, the oxygen self-diffusion phenomenon corresponding to the diffusion anneal proper is visible only on the first points of the ^{18}O depth profile. We have therefore deduced self-diffusion coefficients, whenever contamination was apparent, by reproducing the first few data points only; we assume in this case that the initial conditions are given by depth profiles determined towards the tail end of the ^{18}O profile.

Diffusion coefficients and isotopic exchange coefficients were determined for up to three or four SIMS depth profiles per sample. From a set of values corresponding to a single sample (*i.e.* several craters), an average diffusion coefficient and its corresponding standard deviation is evaluated. In some cases, a more complex procedure was applied which involved generating for a given crater up to twenty depth profiles, obtained from the experimentally determined sputtering rate distribution (which constitutes the main source of error, see Chapter 2) and determining for each of these depth profiles a different diffusion coefficient.

In the following subsections, the oxygen diffusion coefficients are presented as a function of the thermodynamic conditions.

4.3.2 Oxygen diffusion dependence upon temperature

The oxygen diffusion coefficients for samples annealed in conditions presented in Table 4.3 are reported in an Arrhenius representation in Figure 4.7. This figure also shows the oxygen diffusion coefficients previously published [68] for UO_2 sample sets containing different impurity levels.

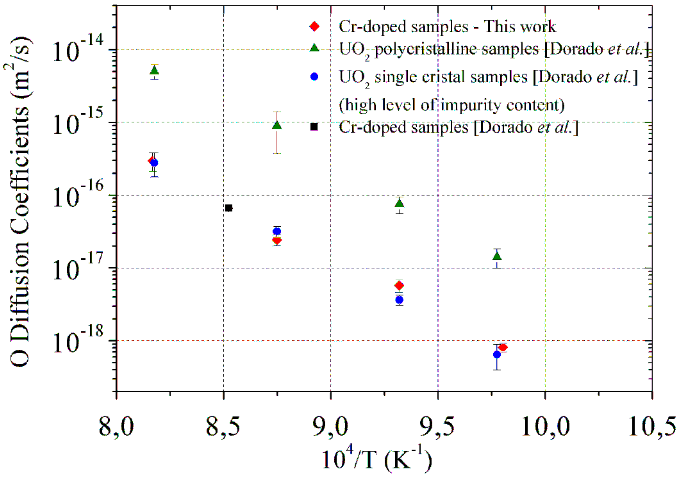

Figure 4.7: Comparison between oxygen diffusion coefficients evaluated for Cr-doped samples with the ones reported in [68] for different UO_2 samples containing different impurity levels. Single crystals are characterized by a high level of impurity content.

Figure 4.7 shows that oxygen diffusion coefficients of our Cr-doped samples follow an Arrhenius dependence quite similar to the one found for UO_2 samples containing high levels of impurities. The slope gives an indication of the oxygen diffusion activation energy: in the case of our doped sample, activation energy is equal to 3±0.2 eV, quite comparable to the estimates found by Dorado *et al.* [68] for their un-doped sample sets (equal to 3.26 and 3.22 eV). However one should employ extreme caution when interpreting such activation energies (as explained in Chapter 3) since this activation energy is primarily due to the dependence upon the oxygen partial pressure of the defect concentration in the samples.

4.3.3 Oxygen diffusion dependence upon pO_2 at low temperature (800°C)

Here we report the results relative to the oxygen diffusion coefficient dependence upon pO_2 at 800°C. The following figure shows the oxygen diffusion coefficients obtained and their comparison to the results of B. Dorado *et al.* [68] at 900°C. Comparison is possible because as the Cr-doped samples used in this study were manufactured and their surface prepared in the same way as those previously studied [68] (samples were cut and progressively polished with silicon carbides cloths, diamond paste and OPU paste - see section §2.1).

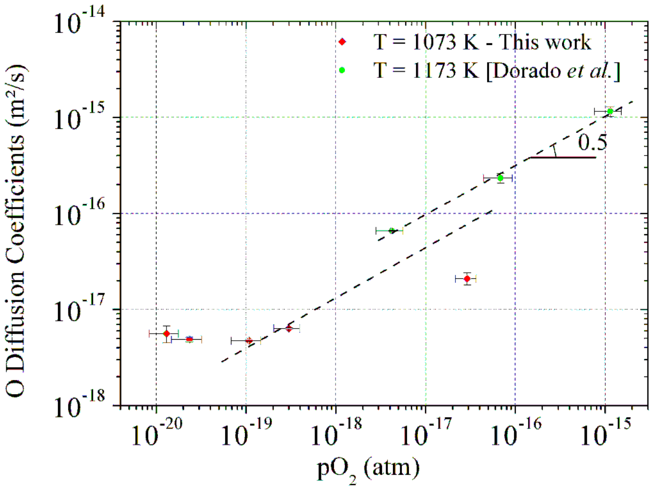

Figure 4.8: Comparison of the oxygen diffusion coefficient dependence upon pO_2 obtained at 800°C with results obtained for samples annealed at 900°C [68].

Figure 4.8 allows us to visualize the strong differences that exist between the pO_2 dependences at the two analyzed temperatures. It shows that the 900°C published data are on a straight line the slope of which is ½, fact that suggests an interstitial controlled diffusion mechanism. At 800°C however, our oxygen self-diffusion coefficient does not follow a similar trend possibly indicating the presence of a different type of defect. At the four lowest oxygen partial pressures, oxygen self-diffusion coefficients have similar values (roughly $5\ 10^{-18}$ m^2/s). Also at higher oxygen partial pressures, the data do not seem to line up in a straight line with a slope of ½. In Chapter 6 we attempt to rationalise these results using the model presented in Chapter 3.

4.3.4 Oxygen diffusion dependence upon pO$_2$ at high oxygen potentials

Figures 4.9 and 4.10 indicate the oxygen self-diffusion coefficients measured for different oxygen partial pressures at 890°C and 990°C respectively. For the lowest temperature, the data corresponding to our Cr-doped samples are plotted together with previously published results [68] for comparison. Note however that samples studied here were not subjected to the last OPU polishing stage as were those presented in [68].

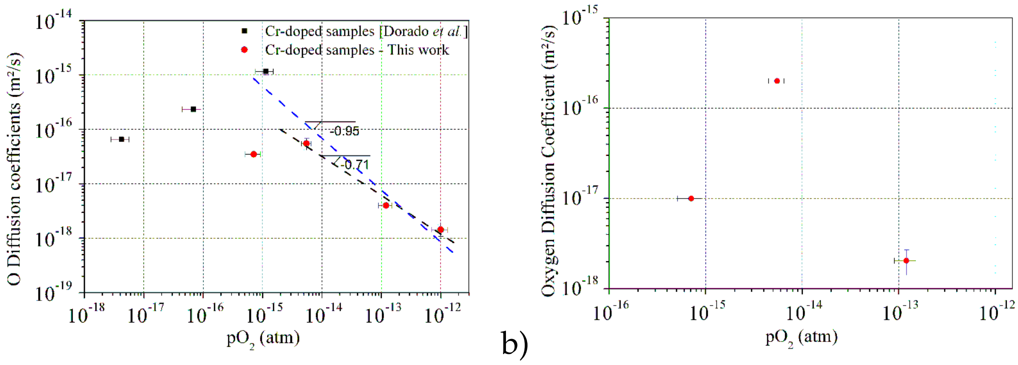

a) b)

Figure 4.9: Oxygen self-diffusion coefficient dependence upon oxygen partial pressure for an annealing temperature of 890°C: graph a) corresponds to Cr-doped samples; graph b) to undoped samples.

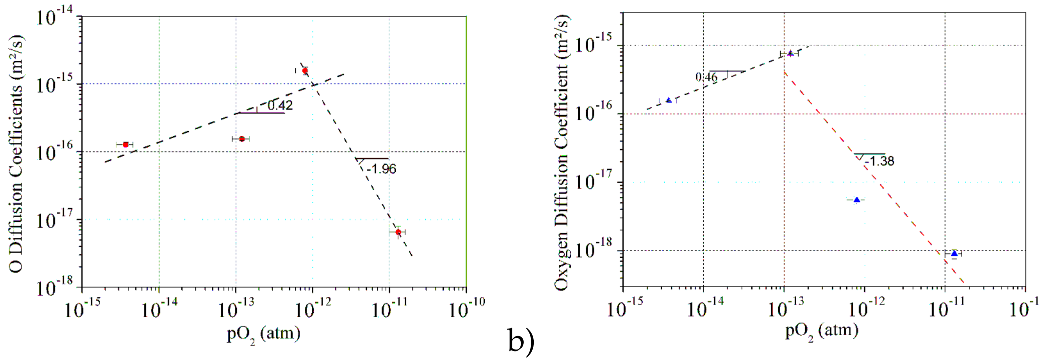

a) b)

Figure 4.10: Oxygen self-diffusion coefficient dependence upon oxygen partial pressure for an annealing temperature of 990°C: graph a) corresponds to Cr-doped samples; graph b) to undoped samples.

As we can see in Figures 4.9 and 4.10, the absolute values of oxygen diffusion data found in this work at 890°C and 990°C differ significantly from the data previously published by [78, 68]. It is difficult at this stage to explain the discrepancies observed in Figures 4.9 and 4.10 and we shall differ the discussion relative to the possible causes of these discrepancies until Chapter 6.

At 890°C the trend followed by the O diffusion coefficient for Cr-doped samples changes beyond an oxygen partial pressure of 10^{-15} atm. We can therefore imagine that beyond 10^{-15} atm the predominant oxygen defect is no longer the isolated interstitial. The trend followed by undoped samples is similar: oxygen diffusion strongly lowers between 5.5 10^{-15} and 1.2 10^{-13} atm.

At 990°C oxygen diffusion behaves differently. For Cr-doped samples, as we can see in Figure 4.10a), until 10^{-12} atm the diffusion coefficients increase for increasing values of oxygen partial pressure; then, at about 10^{-11} atm, they decrease substantially. Undoped samples follow a similar trend: the slope of 0.46 seems to confirm the interstitial mechanism for oxygen diffusion for oxygen potentials as high as 1.2 10^{-13} atm. Beyond this value, oxygen diffusion coefficients progressively decrease with increasing values of oxygen partial pressures.

To conclude, we can say that for both the sample sets studied there appears to be an oxygen potential threshold beyond which oxygen diffusion coefficients decrease substantially. In other words, at high oxygen potentials oxygen self-diffusion in UO_2 appears to be inhibited. We attempt to interpret these observations in Chapter 6.

4.4 Conclusions

This chapter is dedicated to the study of oxygen and electrical transport properties in UO_{2+x}: in particular, we assessed UO_{2+x} oxygen self- and chemical diffusion coefficients and their dependence upon temperature and oxygen potential in an attempt to probe the nature of defects and their influence upon oxygen diffusion phenomena. Cr-doped and undoped UO_2 polycrystalline samples were annealed under controlled atmospheres and quenched to fix their composition. Oxygen diffusive spreading was studied using ^{18}O tracer isotopes characterized following each experiment with SIMS. The experimentally evaluated profiles were simulated using Fick's 2nd law and oxygen self-diffusion coefficients were evaluated.

Basically two studies were performed, one for which oxygen self-diffusion coefficients were measured at fixed temperature (800°C, 890°C and 990°C) as a function of oxygen partial pressure. These experiments were carried out on Cr-doped and un-doped samples at 890°C and 990°C and on Cr-doped samples only at 800°C. Electrical conductivity of Cr-doped and undoped samples were determined in parallel as a means to estimate hole concentrations. At both temperatures studied, Cr-doped samples behave extrinsically until 10^{-12}-10^{-11} atm *circa*. Since in the range of pO_2 in which the diffusion coefficients are measured the hole concentration is determined by the Cr concentration, the evaluation of oxygen self-diffusion dependence upon oxygen potential can be evaluated by directly plotting the estimated oxygen diffusion coefficients as a function of oxygen partial pressures. Conversely, the low impurity content polycrystalline material shows an intrinsic behaviour at 890°C and 990°C. This enabled us to estimate the oxygen chemical diffusion coefficients. In agreement with [162], we showed that oxygen chemical diffusion decreases for increasing values of oxygen potentials.

The second study involved measuring diffusion coefficients for doped samples only as a function of temperature in an extrinsic regime in order to generate data relative to activation energies. The activation energy for Cr-doped samples in this regime was estimated at 3±0.2 eV which is quite comparable to the values reported in literature for samples [68] containing various levels of doping agents.

The interpretation of oxygen transport data presented here is carried out in Chapter 6: we base our analysis on the use of the point defect model developed in Chapter 3. This general discussion of results, established in the light of oxygen transport property measurements, is enriched with results from the characterisation of the electronic structure of UO_{2+x} which is the object of the following Chapter. In it, we look at results from X-ray Absorption Spectroscopy experiments carried out on higher oxide reference phases and UO_{2+x} samples to gain insight into the effect of oxidation upon the electronic structure of UO_{2+x} and the local environment of oxygen atoms.

Chapter 5

Evaluation of the oxidation effect on the electronic structure of uranium oxides by XAS

This chapter aims to evaluate how oxidation impacts the electronic structure of different phases of the U-O system, *i.e.* the modifications of the density of states (electronic structure) that are induced by hyperstoichiometry and associated atomic local environments.

The first part of this chapter is dedicated to our reference oxide phases. After a description of the sample preparation and XRD characterization, XAS results at the oxygen K- and uranium N-edges are detailed. The experimental results obtained are compared to *ab-initio* simulations and existing neutron diffraction experiments.

The second part of this chapter is dedicated to the electronic structure of UO_{2+x} specimens based on the analysis of our reference samples.

5.1 Sample preparation and XRD analysis of U_4O_9 and U_3O_7 reference phases

Our aim now is to produce stoichiometric reference samples (U_4O_9 and U_3O_7) so that UO_{2+x} data may be analysed. In the first part of this section a brief review of literature studies relative to the oxidation of UO_2 is carried out to determine the most adapted procedure for producing these phases. Thermally treated samples are then characterized by XRD to evaluate their structure. Higher oxide phases will be the object also of the XAS characterization: XAS spectra of our specimens are used as reference to interpret XAS spectra collected on UO_{2+x}. But despite their importance, no literature data on U_4O_9 and

U_3O_7 are available; in fact, past studies report XAS O K- and U N-edges data on UO_2 only [103, 131, 187].

5.1.1 Choice of the most relevant method for transforming UO_2 into higher oxide phases

As seen in section §1.1.1.3, the transformation of UO_2 to U_3O_8 can be easily attained: for example, U_3O_8 powder can be obtained by heating a sintered UO_2 sample at low temperature (*i.e.* 250°C) under air. However, producing U_4O_9 and U_3O_7 requires a stricter control of the thermodynamic conditions. Three methods were initiallty selected:

1. Garrido *et al.* [79], W. Van Lierde *et al.* [123, 124] and Masaki and Ishii [133] produced a U_4O_9 single crystal by the method of "oxygen transfer". Calculated amounts of stoichiometric UO_2 single crystals and U_3O_8 powders were placed in a quartz tube and heated for one month at T=1100°C under vacuum so that the final composition was expected to be 2.242 ± 0.001. This results in the oxidation of the UO_2 single crystal into U_4O_{9-y} by the excess oxygen. The induced phase transition was then checked by the mentioned authors characterizing the oxidised sample by neutron diffraction.

2. Willock and Pearce [180] annealed UO_2 polycrystalline samples under different oxygen potentials (corresponding to an O/M ratio between 2.05 and 2.12) and at different temperatures (in the 600°C-1200°C range). Following annealing, samples were cooled down very slowly to the ambient temperature. With this method, authors observed by XRD that UO_2 and U_4O_9 phases coexist, as expected from the phase diagram shown in Figure 1.2 of Chapter 1. SEM analyses demonstrated also that needles of U_4O_9 are located at the boundaries of UO_2 grains.

3. U_3O_7 or U_4O_9 layers on a UO_2 substrate can be created by annealing UO_2 specimens at low temperatures (T<400°C) under oxidising atmospheres (*i.e.* air or Ar + 150 ppm of O_2). This method was applied to pellets [34, 137, 172, 178, 158] or powders [23, 95, 137, 156, 161].

X-rays corresponding to the oxygen K-edge have an energy of 532 eV (see §2.4.2.1) and can penetrate the sample over 0.1 µm only [131]. At these energy conditions, XAS characterization can be considered a surface technique and consequently, a surface layer 1 µm thick is quite sufficient for our XAS experiments. Safety rules at the CLS (Canadian Light Source) beamline where experiements were carried out require bulk samples to be used as opposed to powders.

5.1.2 Production of a higher oxide layer on UO_2 specimen substrate

Our choice of conditions to produce either U_4O_9 or U_3O_7 was defined through the analysis of weight gain curve of UO_2 annealed in air. One such example is given in Figure 5.1.

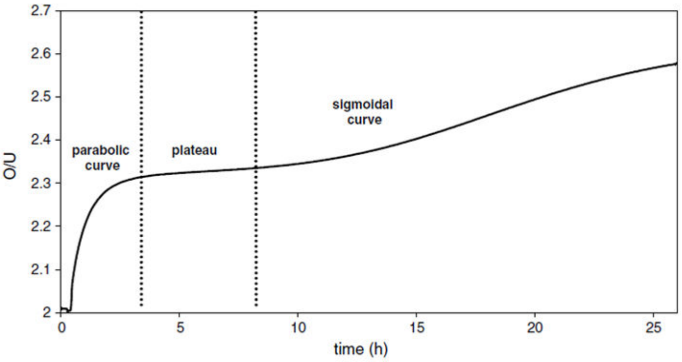

Figure 5.1: Weight gain curve of a UO_2 powder annealed at 250°C under air [161].

It was demonstrated [161] that under air and below 250°C UO_2 powders oxidize to U_4O_9 before transforming into U_3O_7 (see Figure 1.7). However, the annealing conditions to produce U_4O_9 exclusively cannot be deduced from a UO_2 weight gain curve (as the one presented in Figure 5.1). In fact, a sample with an O/M ratio equal to 2.25 can be either exclusively composed of U_4O_9 or a mixture of UO_2 and U_3O_7. Conversely, the U_3O_7 phase unequivocally corresponds to an O/M ratio equal to 2.33 (see the *plateau* region of Figure 5.1): as a consequence, the annealing conditions to obtain a U_3O_7 phase can be more easily determined from a weight gain curve.
Several attempts were made at producing either U_4O_9 or U_3O_7 from UO_2 samples. Following Rousseau *et al.* [161]'s study of UO_2 powders, two thermal treatments of 3 and 5 hours at 250°C were carried out. In addition to them, the thermal treatment suggested in [63] of 90 minutes at 300°C was also tested.
Concerning U_4O_9 three different annealing conditions were tested. Firstly, we applied the conditions reported by C. Viaud in [178] who demonstrated that a

20 hour annealing at 170°C does not lead to the production of a U_3O_7 layer on a UO_2 substrate. Secondly, a UO_2 sample was annealed at 250°C for 1 hour. In a powder sample these annealing conditions seem to correspond to an O/M ratio equal to 2.25 [161] (see Figure 5.1). Because the oxidation kinetics of a powder is exepected to be much greater than that of a sintered sample [137] hour attempt to oxidize the surface of a UO_2 sample to U_4O_9 was carried out at a lower temperature (200°C) with 1 hour of hold time. Table 5.1 summarizes the conditions tested.

Sample N°	*Annealing conditions*		*Desired phase*
	Temperature **(°C)**	*Duration* **(h)**	
1	250	3	U_3O_7
2	250	5	
3	300	1.5	
4	170	20	U_4O_9
5	250	1	
6	200	1	

Table 5.1: Annealing conditions used to produce a oxidised layer on a UO_2 substrate under air.

All of these thermal treatments are carried out on UO_2 samples in a furnace under air. At the end of the annealing period, samples were quenched by extracting them as quickly as possible. The oxidised samples were observed by optical microscopy to determine whether annealing had affected the sample surface. Figure 5.2a) is representative of our annealed samples, while Figure 5.2b) represents the surface of a sample converted into U_3O_8 [158].

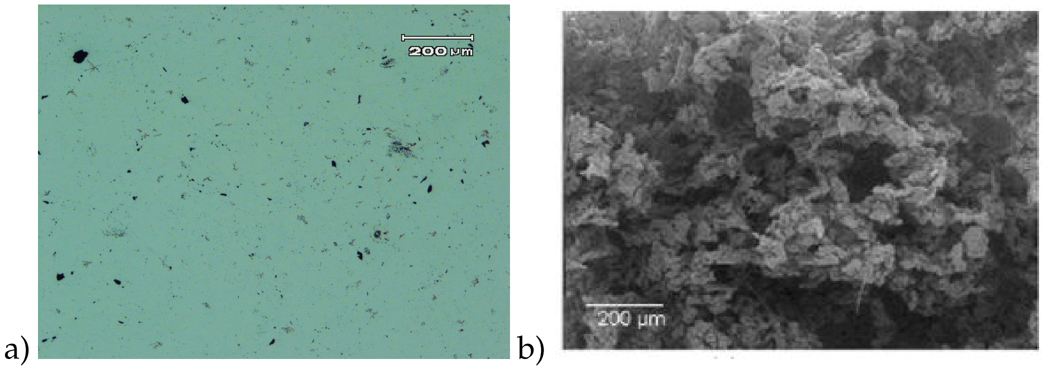

a) b)

Figure 5.2: Comparison between the optical microscopy images of the our annealed UO_2 sample surface (case of sample n°4) - image a) - and of the surface of sample whose surface has been transformed to U_3O_8 [158] - image b).

As shown in Figure 5.2a), our samples are homogeneous: their surface shows no obvious microstructural modifications. Conversely, Figure 5.2b) shows that oxidation of UO_2 into U_3O_8 induces the exfoliation and cracking of the sample surface. Consequently, the comparison of these two images leads us to suppose the complete absence of the U_3O_8 phase in our annealed samples.

5.1.3 XRD characterization

5.1.3.1 Results

XRD characterization in the ϑ-2ϑ Bragg-Brentano configuration confirmed the absence of the U_3O_8 phase. A slight contamination by $CaCO_3$ was nevertheless observed in all our annealed samples. As shown in Figure 5.3, in the ϑ-2ϑ configuration we were able to verify the appearance of a thick U_3O_7 layer on specimens n°2 and n°3. Conversely, the diffractogrammes collected on the other annealed samples show no significant differences with the one collected on UO_2 reference.

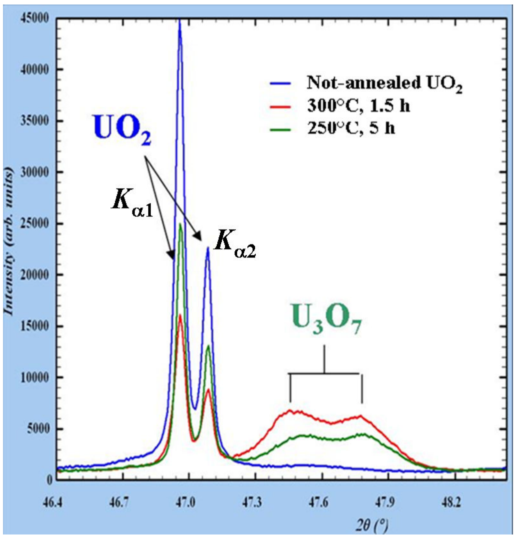

Figure 5.3: Comparison between the 220 Bragg line acquired on samples n°2 and n°3 with the UO_2 reference.

In the ϑ-2ϑ configuration with ϑ=47° (corresponding to the UO_2 220 Bragg line) we probed a sample thickness of 1.22 µm. In a ϑ_{in}–ϑ_{out} configuration, a smaller incidence ϑ_{in} enhances the contribution of the atomic layers closer to the sample surface (see §2.4.1). Therefore, this configuration should help to characterise the possible presence of a higher oxide layer on the UO_2 annealed surface. After fixing ϑ_{in} at 5°, we were able to probe a sample thickness of only about 0.26 µm. The best results obtained are represented in Figure 5.4: there, we compare the 220 Bragg line collected on the reference sample with the one corresponding to specimens n°1, 4, 5 and 6.

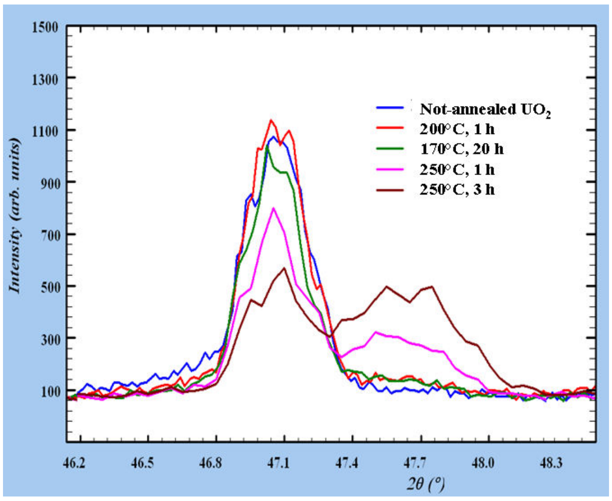

Figure 5.4: Comparison between the 220 Bragg line corresponding to annealed samples with the UO_2 reference. Annealing at 250°C leads to the formation of U_3O_7, while the counting statistics doesn't allow us to conclude as to the possible presence of U_4O_9 formed during annealings done at the two lowest temperatures.

5.1.3.2 Discussion of XRD results

As reported in §1.1.1.3, the U_3O_7 phase is tetragonal. Its crystalline features induce a splitting of some diffraction peaks (such as the Bragg lines 200, 220, 131). Therefore, the split peaks positioned at 47.45° and 47.8° in the ϑ-2ϑ diffractogrammes of Figure 5.3 enables us to conclude that a U_3O_7 layer has formed on annealed samples n°2 and n°3.

The diffractogrammes collected with the ϑ_{in}–ϑ_{out} geometry (see Figure 5.4) do not clearly indicate the presence of a U_4O_9 layer. The similar lattice parameters and the same cubic structure of UO_2 and U_4O_9 result in Bragg lines positionned at almost identical angles. Moreover, Figure 5.4 demonstrates the presence of U_3O_7 on all samples annealed at 250°C; for the same annealing temperature the increase in annealing time induces an increase of the oxidized layer thickness. To discuss these results critically, all the collected diffractogrammes were analysed with the FullProf software [5] in the FullPatternMatching mode. This analysis consists in reproducing with an analytical function the collected XRD spectra through the refinement of the lattice parameters of the phases that the sample contains. The refinement procedure was applied to the diffractogrammes collected on the annealed and reference specimens. Figures 5.5

and 5.6 report the simulation of the XRD spectra collected for samples n°3 and n°6, while the determined lattice parameters are indicated in Table 5.2. Once again, we cannot clearly detect a U_4O_9 phase from the diffractogrammes collected on the UO_2 samples annealed at 170°C and 200°C. Their simulations are however carried out with the insertion of the U_4O_9 phase.

Sample N°	X^2	***UO_2***	***U_4O_9***	***U_3O_7***	
		a (nm)	*a* (nm)	*a* (nm)	*c* (nm)
2	27.8	0.547	—	0.538	0.542
3	26.8	0.547	—	0.539	0.542
4	2.2	0.547	0.545	—	—
6	5.5	0.546	0.545	—	—
UO_2 Reference	57	0.547	—	—	—
Theoretical values	—	0.547	0.544	0.533	0.553

Table 5.2: FullProf estimates of the lattice parameters of the phases present in annealed samples.

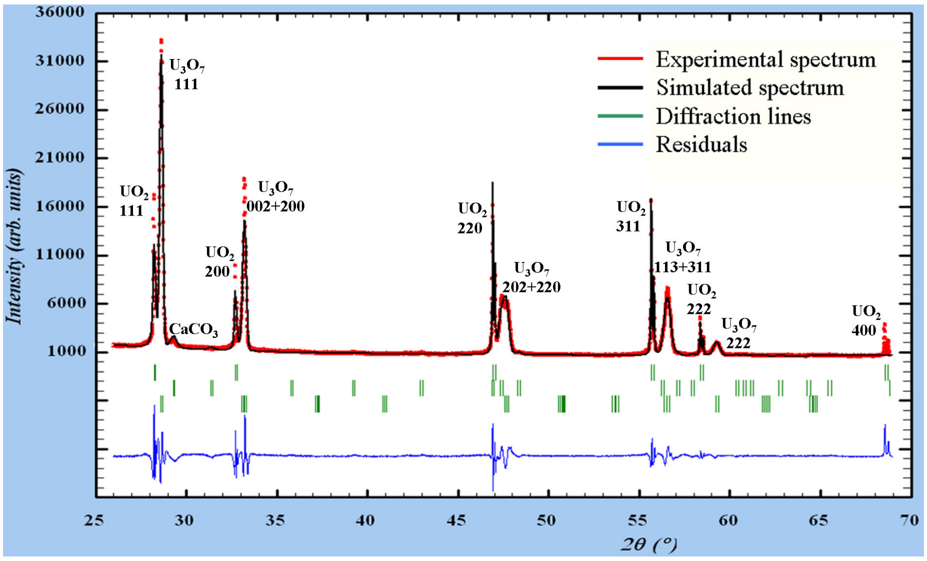

Figure 5.5: Simulation with the tool provided by the FullProf software of the diffractogramme acquired on the sample annealed at 300°C for 1 hour and half. It shows the presence of three phases: UO_2 (substrate), $CaCO_3$ (impurity) and U_3O_7 (created layer).

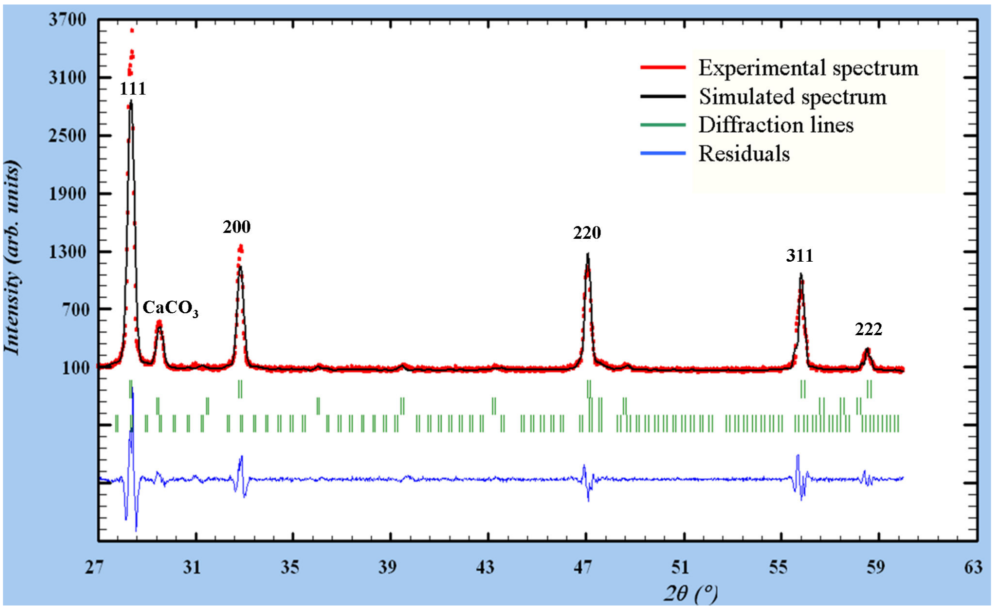

Figure 5.6: Simulation with FullProf software of the diffractogramme acquired on the sample annealed at 200°C for 1 hour. The fitting procedure was developed using three phases: UO_2 (substrate), $CaCO_3$ (impurity) and U_4O_9.

Results concerning U_3O_7 phase are in agreement with literature. As reported in [63, 161], under our annealing conditions this oxide phase is expected to form. Moreover, the refinement shows clearly that the created U_3O_7 phase is distorted along the c axis. In fact, the c parameter of the surface layer (0.542 nm) is close to the lattice parameter of UO_2, but different from its theoretical value (0.553 nm), which demonstrates in agreement with [61, 161] that the growth of U_3O_7 on a UO_2 substrate is accommodated through a distortion of the FCC lattice.

On the other hand, the presence of U_4O_9 on the samples annealed at the two lowest temperatures cannot be either confirmed or excluded. However, from Figure 5.4, the probable presence of U_3O_7 traces on the samples lead us to expect the formation of a U_4O_9 layer on the UO_2 substrate as U_4O_9 is an intermediate oxidation product between UO_2 and U_3O_7 [161].

As a conclusion, we can confirm that we have succeeded in producing samples with a U_3O_7 layer. Conversely, XRD results on the samples dedicated to the production of U_4O_9 are not conclusive. The XAS spectra collected at the oxygen K- and uranium N-edges on these samples will allow us to conclude as to the presence of U_4O_9. XAS characterization of all of these samples is described in the following section.

5.2 XAS characterisation on the reference compounds UO_2, U_3O_7 and intermediate phase

This section summarizes the most important XAS characterisation results of samples presented in the previous section . All our annealed samples (the ones reported in Table 5.1) together with a UO_2 reference were characterized at the oxygen K edge (electronic transition: 1s→2p) and uranium $N_{4,5}$ (transitions: $4d^{3/2} \rightarrow 5f^{5/2}$ and $4d^{5/2} \rightarrow 5f^{7/2}$) and $N_{6,7}$ edges ($4f^{5/2} \rightarrow 6d^{3/2}$ and $4f^{7/2} \rightarrow 6d^{5/2}$), to respectively probe the oxygen 2p and uranium 5f and 6d orbitals. We refer the reader back to section §2.4.2 (Chapter 2) for the technical details relating to this type of characterization.

5.2.1 Oxygen and Uranium local environment in UO_2 and higher oxides

The local environment of oxygen and uranium atoms in UO_2, U_4O_9 and U_3O_7 was estimated inserting in the Artemis software [8] the spatial coordinates of all the atoms constituting the elementary cell of each phase considered. For UO_2, the spatial coordinates of uranium and oxygen are respectively taken equal to (0, 0, 0) and ($\frac{1}{4}$, $\frac{1}{4}$, $\frac{1}{4}$). For U_4O_9 and U_3O_7, the atomic arrangements given by L. Desgranges *et al.* [61] were used. For the elementary cell of U_4O_9, the authors determined the atomic coordinates of 14 oxygen and 7 uranium atoms. For U_3O_7 they defined the atomic coordinates of 44 oxygen and 16 uranium atoms. All the reported atomic coordinates were inserted in the Artemis program to calculate the coordination spheres around each oxygen or uranium atom present in the elementary cell of these phases. Oxygen and uranium neighbour polyhedra are here represented using the VESTA [9] software.

First we focus our attention on oxygen: Figure 5.7 represents the first two coordination spheres of oxygen atoms in UO_2.

As shown in Figure 5.7a), in UO_2 oxygen are firstly surrounded by 4 uranium atoms, disposed at the vertexes of a tetrahedron at a distance of 2.369 Å. Figure 5.7b) describes the second coordination sphere, with 6 oxygen atoms at a distance of 2.375 Å. The local environment of oxygen in U_4O_9 and U_3O_7 is more complicated to picture, because of the high number of atoms composing their elementary cells: 828 for U_4O_9 and 848 for U_3O_7. Despite this, in U_4O_9 many of the defined oxygen atoms have a local environment quite similar to that of UO_2. In fact, they are firstly surrounded by 4 uranium atoms, at a distance ranging between 2.25-2.6 Å; their second neighbours are 6 or 7 oxygen atoms at a distance ranging between 2.6 and 3 Å. These atomic coordination shells is consistent with the fact that U_4O_9 keeps a cubic symmetry, although

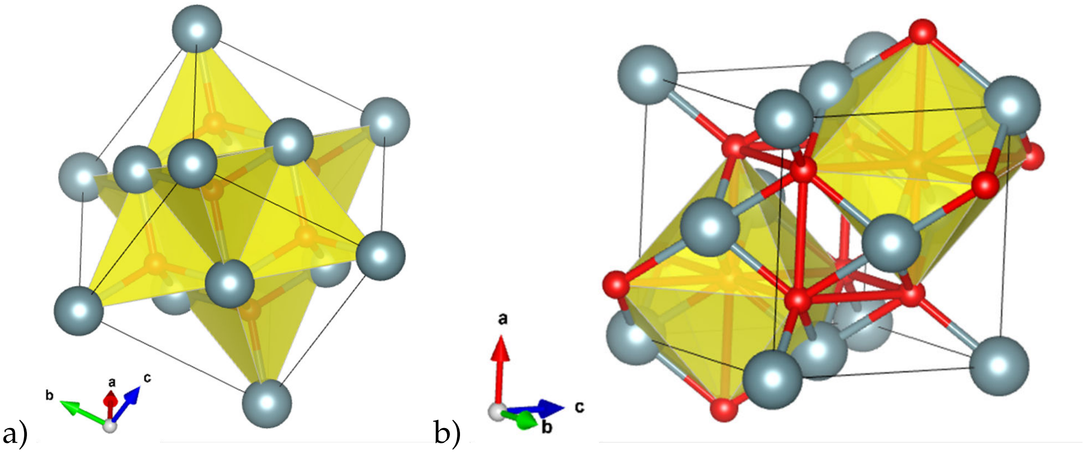

a) b)

Figure 5.7: Representation of the first (graph a) and second (graph b) neighbours of oxygen in UO_2. Oxygen is represented in red, uranium in grey and coordination polyhedra in yellow.

it contains a higher number of oxygen atoms. The oxygen local environment in U_3O_7 is more difficult to ascertain because of the high number of oxygen atoms in the elementary cell (594) and the departure from cubic symmetry.

Figure 5.8 represents the local environment of uranium in the UO_2 phase.

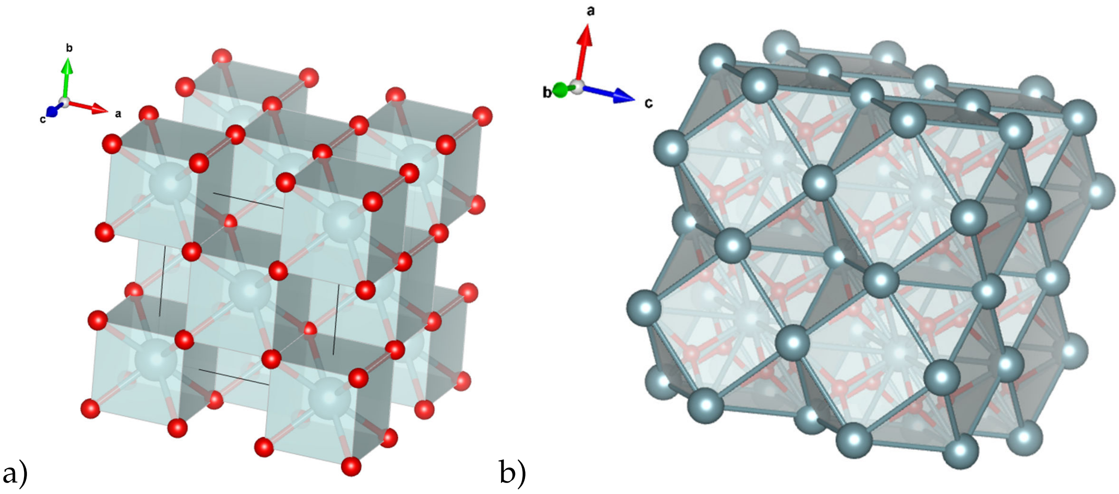

a) b)

Figure 5.8: Representation of the first (graph a) and second (graph b) neighbours of uranium in UO_2.

As represented in Figure 5.8, in UO_2 a uranium atom is firstly surrounded by eight oxygen atoms, disposed at the verteces of a cube at a distance of 2.369 Å. Then come 12 uranium atoms, at a distance of 3.868 Å. In the higher oxides phases considered here, a uranium atom is always surrounded by more than eight oxygen atoms. In U_4O_9 there are ten, eleven or twelve depending on the uranium atom considered in the elementary cell; in U_3O_7, their number ranges between 11 and 16. All these oxygen atoms are at variable distances from the central uranium atom: in U_4O_9 the distances range between 2.2 and 3.6 Å, while in U_3O_7 they range between 1.7-4 Å. Also in this case all these anions are disposed in a geometry that is difficult to determine. Like in UO_2, in these higher oxides, the second neighbours of uranium are always twelve uranium atoms. Both in U_4O_9 and U_3O_7 they lie between 3.7-4.3 Å away.

To conclude, in higher oxides, cation coordination shells are almost identical to the ones in UO_2 and composed by the same number of uranium atoms, while the number of nearest neighbour oxygen atoms increases and their positions are strongly modified by oxidation.

5.2.2 Calculation details

First principle simulations of UO_2 and UO_{2+x} have been used to guide us in the interpretation of the XAS data as they provide electronic structure information which may be compared to experimental data. These DOS calculations were carried out in the laboratory by E. Vathonne under the supervision of M. Freyss [176]. The following systems were studied :

- UO_2 with a perfect fluorite structure (reference DOS)
- UO_2 with an oxygen interstitial
- UO_2 with an oxygen di-interstitial

These calculations are performed in the framework of DFT using the projector augmented wave (PAW) method implemented in the VASP code [35] in the GGA approximation. The DFT+U formalism [122] was used to account for the strong Coulomb interactions between 5f electrons. In all calculations, the U and J parameters of the DFT+U approximation were set to 4.5 and 0.5 eV respectively as estimated from analyses of X-ray Photoemission Spectra carried out by Kotani [112].

Calculations were carried out on a 96 atom supercell. The actual paramagnetic order observed above the Néel temperature (30 K) [119] is approximated by a 1k AntiFerromagnetic order [16, 72]. Calculation of oxygen and uranium DOS were made both with neutral and negatively charged supercells. However, only simulations carried out for neutral supercells are reported in this chapter. Such supercells are more representative of our system: in neutral supercells in fact local charge compensation occurs on uranium atoms adjacent to the oxygen defect, inducing the uranium valence to increase for the presence of additional charged defects. Conversely, negatively charged cells forces cations to assume a valence of 4+ and don't allow us to appreciate the influence of cation valence variation on UO_2 electronic structures.

All the DOS hereafter represented are calculated additioning all the electronic structures respectively of oxygen or uranium atoms present in the supercell. This representation is the most representative of our system, as oxygen (or uranium) XAS signal convolutes all the anions (or cations) constituting the sample. In case of oxygen, XAS averages the contributions of both atoms of the lattice and the defects. In case of uranium, XAS averages the signals coming from cations with a 4+ valence with the ones of valence 5+.

Because the experiments provide a picture of the empty electronic states, the DOS are plotted from the top of the valence band only.

5.2.3 Experimental and theoretical results obtained for UO_2

We now compare the UO_2 XAS spectra to the calculated DOS with the results available in literature. Figure 5.9 reports the fluorescence (fY) and total electron yield (TeY) O K-edge XAS spectra collected on our reference presumably stoichiometric UO_2 which we compare to the total electron yield spectrum reported by Jollet *et al.* [103]: note this spectrum was shifted of 2.3 eV to enable a direct comparison to our data. Table 5.3 summarizes the peak position energies: the error associated with reported energies is ±0.1 eV.

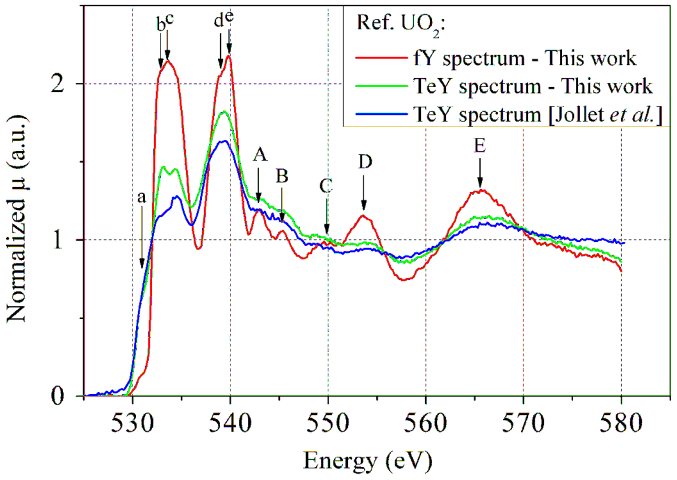

Figure 5.9: UO_2 oxygen K-edge XAS spectra: comparison between our data (collected in fY and TeY modes respectively) and the TeY spectrum reported by Jollet [103]

Spectrum	***Peak Positions***				
	a	**b**	**c**	**d**	**e**
fY mode - this work	531.0	533.0	533.6	539.0	539.8
TeY mode- this work	531.2	533.2	534.4	—	539.4
TeY mode [103]	530.85	532.95	534.5	—	539.2
	A	**B**	**C**	**D**	**E**
fY mode - this work	542.9	545.3	550.0	553.6	565.8
TeY mode- this work	543.2	545.4	549.4	553.6	566.2
TeY mode [103]	543.2	545.4	549.15	554.15	566.35

Table 5.3: Positions (in eV) of the oxygen K-edge resonances: comparison between our fY and TeY data with the data (shifted by 2.3 eV) of Jollet *et al.* [103]. Energies are affected by an error of ±0.1 eV.

As detailed in Chapter 2, a TeY spectrum corresponds to Auger electrons. Because Auger electrons has a shorter range of penetration than fluorescence photons (10 nm instead of 0.1 μm probed by X-ray photons [103, 131]), these spectra are much more sensitive to the sample surface than fluorescence spectra. The TeY and fY spectra in Figure 5.9 present the same resonances: the electronic structure of oxygen atoms at the surface and in the bulk are similar. However, the peaks in the TeY spectrum, with the exception of feature a, are much less intense than the resonances seen in fluorescence mode. This is an indication of differing oxydation states between the sample surface and bulk: in fact, as pointed out by McEachern and Taylor [138], a UO_2 sample has oxidised surface layers which host many foreign atoms and contaminants (*e.g.* hydroxyl groups or water molecules). The differences between fY and TeY collected spectra would appear to indicate that the TeY spectrum is characteristic of the surface not the bulk as sometimes previously assumed [103].

Based on these results, we would suggest taking the fluorescence spectrum indicated in Figure 5.9 as a reference for oxygen DOS in UO_2, being the most representative of the sample bulk.

Covalent bonding between atoms induce the oxygen 2p and the uranium 5f and 6d orbitals to hybridize. The DOS of these three orbitals calculated by *ab-initio* are represented in Figure 5.10a). Experimentally, uranium 5f and 6d orbitals are probed by $N_{4,5}$ and $N_{6,7}$ uranium edges. Figure 5.10b) shows the fY spectra corresponding to uranium N_5 and N_7 edges together with the oxygen K-edge spectrum: each XAS spectrum is translated along the abscissa of the minimum energy value necessary to activate the electronic transition.

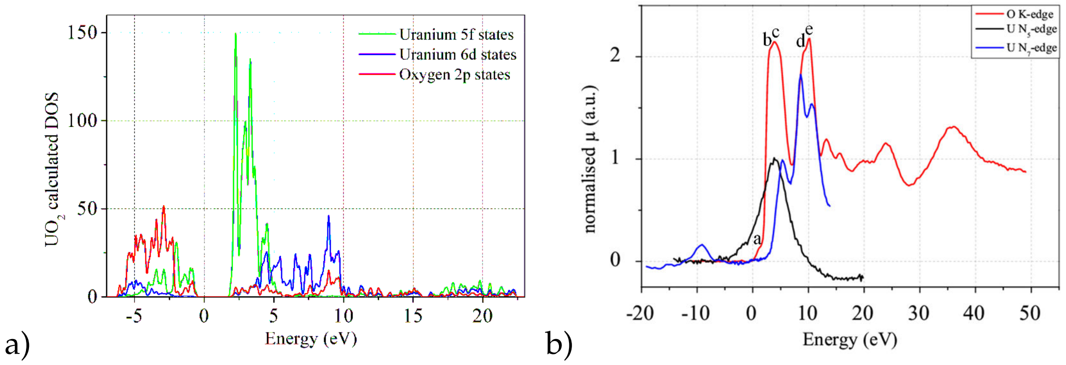

Figure 5.10: a) UO_2 uranium 5f, 6d and oxygen 2p DOS calculated by *ab-initio*; b) Comparison between the spectrum collected at the O K-edge with the U N_5 and N_7 edges.

Our experimental and theoretical DOS results reported in Figure 5.10 are in agreement with the study of Yu *et al.* [187]. In fact, Figure 5.10a) and b) show that the first part of the O K-edge spectrum is due to the hybridisation of the oxygen 2p and U 5f orbitals. The DOS calculations (Figure 5.10a) show that in these hybridized orbitals the 5f cation states are predominant. The hybridised O 2p/U 6d orbitals on the other hand are observed at higher energies and induce the c, d and e resonances of the O K-edge spectrum (Figure 5.10b).

As indicated in Chapter 2 - §2.4.2, a XAS spectrum represents the available density of states of the absorber atom modulated by its core-hole attraction. Core-hole lifetime depends on the energy at which the electronic transition takes place. In our case (see §2.4.2.1 for details), oxygen K, uranium N_5 and uranium N_7 edges are respectively activated at 532, 736.2 and 377.4 eV. The lifetime of the core hole created during the atomic excitation phenomenon respectively provokes a broadening of 0.22, 5.62 and 0.27 eV [8]. Figure 5.10b) shows that the energy broadening at the N_5 edge is greater than that observed at the oxygen K and uranium N_7 edges. In fact, the N_5 edge promotes the transition $4d^{5/2} \rightarrow 5f^{7/2}$ that is activated at higher energies.

Figure 5.11 shows the fY experimental spectrum of the reference UO_2 sample and the calculated partial DOS of oxygen 2p orbitals. We have added to DOS resonances a Lorentzian contribution of 0.22 eV to take into account the core hole lifetime broadening and a Gaussian contribution of 0.2 eV to account for the dispersion corresponding to the energy resolution of the experimental set-up.

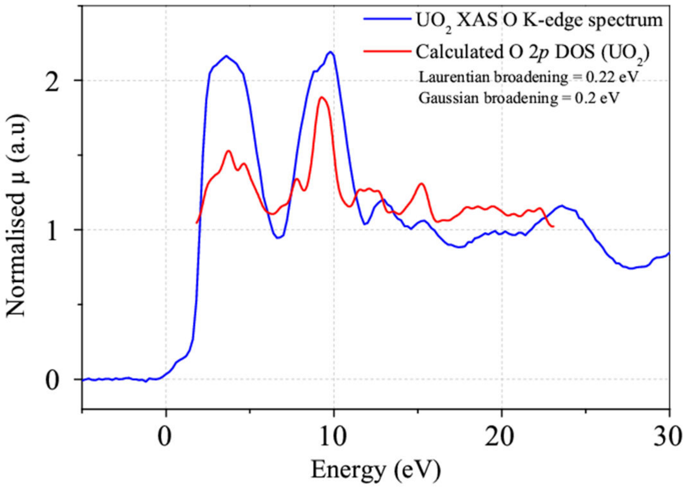

Figure 5.11: Comparison between our experimental XAS spectrum for UO_2 collected at the oxygen K-edge and the oxygen 2p DOS calculated by *ab-initio*.

As shown in Figure 5.11, the experimental spectrum is comparable with the calculated electronic structure of UO_2 for the first 10 eV: this part of the spectrum probes the empty oxygen electronic states directly. For energies higher than 10 eV, the XANES spectrum is not only the result of the empty states but also of multiple scattering phenomenona: the photo-electrons promoted in the continuum have enough kinetic energy to be scattered several times by the neighbour atoms before they backscatter to the excited atom. In fact, at energies higher than 10 eV the calculated DOS doesn't exactly reproduce the experimental evidence. Figure 5.11 shows also that the "a" feature of experimental fY XAS spectrum is not present in the calculated DOS. This difference points to the fact that in our UO_2 sample, the density of states of oxygen atoms differs slightly from the one present in a perfect fluorite structure. As already said to describe the Figure 5.9, resonance "a" can be ascribed to sample oxidation: sample exposure to air induces a slight oxidation of the surface which may induce the the small pre-edge peak observed. **It appears therefore, as one may have expected, that oxidation induces variations in the electronic structure of our material**. The next sections are therefore dedicated to evaluating how the UO_2 electronic structure changes as the material oxidises to U_4O_9 or U_3O_7.

5.2.4 XAS results on higher oxide phases

5.2.4.1 Oxidation effects on oxygen K-edge spectra

U_3O_7

As described in §5.1.3, the annealed samples n°1, 2, 3 and 5 present an oxidised U_3O_7 layer. In Figure 5.12 the fY Oxygen K edge spectra of all these samples are compared to the reference spectrum.

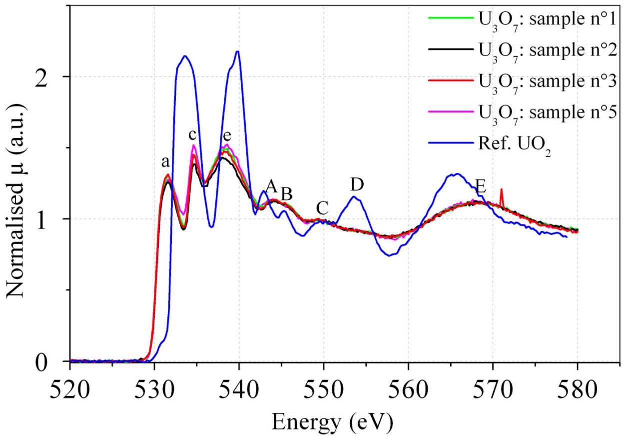

Figure 5.12: O K-edge XAS spectra of the samples whose XRD diffractogrammes show the presence of a U_3O_7 layer; comparison with the reference UO_2 spectrum

As shown in Figure 5.12, the oxygen K-edge spectra of samples n°1, 2, 3 and 5 share the same features. Therefore, each of these samples shares the same oxygen local environment. This fact is in agreement with the XRD results which showed these samples have a U_3O_7 layer at their surface. Figure 5.12 shows also the effect of oxidation on UO_2. UO_2 oxidation is due to the incorporation of oxygen defects in the lattice. Insertion of additional oxygen atoms charged negatively is compensated by an increase of the average uranium valence. This corresponds to an increase in the hole concentration in the valence band, which, in higher oxide phases, induces a decrease in the band gap. The fact that the U_3O_7 oxygen XAS spectrum starts 1 eV before the spectrum relative to UO_2 demonstrates experimentally the decrease of the band gap occurring in U_3O_7. Moreover, section §5.2.3 shows that the less energetic part of the spectrum is given by the hybridization of the O 2p and U 5f orbitals. Therefore, the appearance of the pre-edge peak “a” is a sign of the more available hybridised O 2p/U 5f states in the conduction band. As oxygen valence state is fixed at -2, we can assume that the presence of this peak indirectly probes the uranium valence increase occurring when UO_2 transforms to U_3O_7. Figure 5.12 shows also that transformation of UO_2 to U_3O_7 leads peaks b, d and D to disappear and induces a strong intensity decrease of all the other peaks. Broadening of the higher energy peaks is indicative of radical changes in the multiple scattering phenomena (*i.e.* local environment of oxygen) with an increase in the number of paths photo-electrons can travel. All these features can be considered as the spectroscopic signature of the phase transition from the UO_2 cubic phase to the tetragonal U_3O_7.

Intermediate Phase (IP)

fY Oxygen K-edge spectra of UO_2, U_3O_7 and of the samples purported to have a U_4O_9 layer are compared in Figure 5.13. Recorded peak positions for UO_2, the two IP and U_3O_7 are reported in Table 5.4: compared to the UO_2 peak positions, resonances of the IP spectra show shifts in energy significantly smaller than the ones relative to the U_3O_7 spectra.

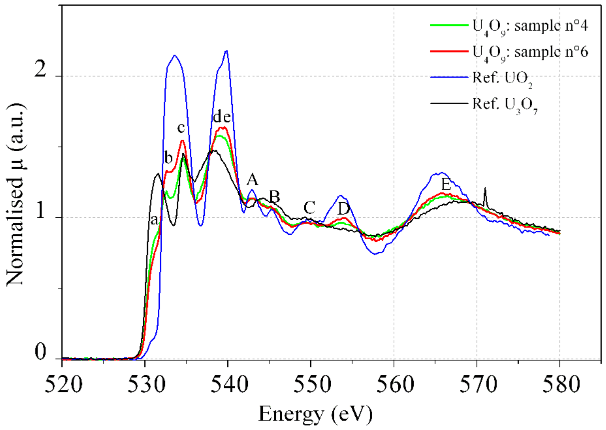

Figure 5.13: Comparison between the oxygen K-edge spectra of samples which possibly have a U_4O_9 layer (samples n°4 and 6) and the spectra of our reference phases UO_2 and U_3O_7.

Phase	***Peak Positions***									
	a	**b**	**c**	**d**	**e**	**A**	**B**	**C**	**D**	**E**
UO_2	531.0	533.0	533.6	539.0	539.8	542.9	545.3	550.0	553.6	565.8
IP	531.4	532.8	534.5	—	539.2	542.9	545.3	550.0	554.0	566.1
U_3O_7	531.6	—	534.7	—	538.5	544.3	545.3	550.0	—	568.5

Table 5.4: Positions (in eV) of the resonances present in the oxygen K-edge spectra of UO_2, IP (sample n°6) and U_3O_7 phases. Energy positions have an associated error of ±0.1 eV.

The trend observed in our XAS spectra reported in Figure 5.13 and in Table 5.4 is consistent with the oxidation mechanisms $UO_2 \rightarrow U_4O_9 \rightarrow U_3O_7$ described in literature [161]. For example, in the spectra of annealed samples n°4 and 6, resonance "a" is more intense than in UO_2; however, it still constitutes a pre-edge shoulder to the spectrum and it is not a well formed peak like in U_3O_7. Oxygen XAS spectra of IP samples present intermediate characteristics between UO_2 and U_3O_7. As in U_3O_7, all their resonances are less intense than for UO_2. However, they still maintain the same features as the ones observed in the reference UO_2 spectrum: this characteristic demonstrates that oxygen electronic structure and the local environment in the annealed specimens are similar to those of UO_2. Similar positions of peaks in UO_2 reference and oxidised sample spectra are compatible with the conservation of the cubic crystalline structure typical of U_4O_9. Therefore, from the spectra collected for the IP samples we can deduce that our annealing conditions led to oxidation of the sample surfaces and may have created layers composed of UO_2 and U_4O_9. However note that from Figure 5.13, spectra for samples n°4 (annealed at 170°C for 20 hours) and n°6 (annealed at 200°C for 1 hour) are not identical: the same resonances are observed (peak positions) but their relative intensities are different. If the same line of reasoning as in §5.2.3 is applied, sample n°6 would appear to be less oxidised than sample n°4. We therefore assume the spectrum collected on sample n°6 is more characteristic of the intermediate UO_2/U_4O_9 phase than that of sample n°4: later on this work we consider sample n°6 as the only reference for IP.

5.2.4.2 Oxidation effects on uranium N-edge spectra

We now try to correlate changes in the oxygen K-edge spectra to the XAS characterisation at the uranium edges. In fact, to respect the electroneutrality rule, the insertion of negatively charged oxygen defects in the UO_2 lattice induces an increase of the average valence of uranium atoms. Consequently, XAS spectra collected at uranium edges should follow similar trends to the oxygen ones. We therefore acquired the XAS spectra of the three phases UO_2, IP and U_3O_7 at the uranium $N_{4,5}$ edges to probe the 5f orbitals and at the uranium $N_{6,7}$ edges to probe the 6d states. At this stage, comparison of the penetration depths of the X-rays used to characterize the oxygen 2p and uranium 5f and 6d orbitals is necessary to determine the thickness of the sample layer probed in both cases. While the attenuation length of the X-rays used to probe oxygen is estimated at 0.18 μm, the X-rays sent on samples to probe the $N_{4,5}$ and $N_{6,7}$ edges are respectively equal to 0.12 and 0.42 μm [10]. Based on these values we say that the sample thickness probed during oxygen K-edge and uranium

N$_{4,5}$-edges XAS characterisations are almost identical. With a greater attenuation length, the X-rays used to probe the uranium N$_{6,7}$-edges travel further into UO$_2$ samples. Despite this fact, in all three cases considered, the X-ray penetration depth is smaller than the thickness of the oxidised layer grown on the UO$_2$ substrate (see §5.1.1). As a consequence, the XAS results presented in this section are representative of the higher oxide phases grown on the UO$_2$ substrate. For both the anionic and cationic sublattice we can therefore compare results obtained for IP or U$_3$O$_7$ with results obtained for UO$_2$.

Intermediate phase (IP)

While Figure 5.14a) and b) compares the results obtained for UO$_2$ with our IP, Table 5.5 summarizes their peak positions.

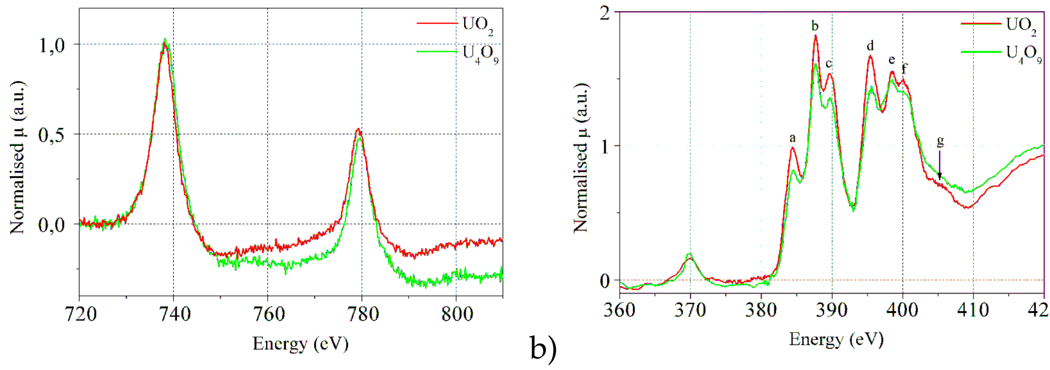

a) b)

Figure 5.14: Uranium spectra at the N$_{4,5}$ (a) and N$_{6,7}$ (b) edges of our references: UO$_2$ (red) and IP (green). In (b), peak near 370 eV can be ascribed to the N$_5$ uranium second harmonic.

Phase	*N$_5$*	*N$_4$*	*N$_7$*			*N$_6$*			
			a	**b**	**c**	**d**	**e**	**f**	**g**
UO$_2$	738.2	779.4	384.4	387.6	389.6	395.4	398.6	400.1	405.3
IP	738.4	779.6	384.5	387.7	389.7	395.6	398.5	400.0	—

Table 5.5: Peak positions (in eV) relative to the uranium XAS spectra collected at the N$_{4,5}$ and N$_{6,7}$ edges. N$_{4,5}$ resonance positions have an error bar of 0.15 eV, while the resolution associated at N$_{6,7}$ edges is 0.08 eV.

As we can see from Table 5.5 and in Figure 5.14a) and b), uranium N-edges spectra are consistent with the results obtained at the oxygen K-edge. Oxidation shifts the N$_{4,5}$ edge peaks to higher energies slightly: this fact is consistent with a uranium valence change. From litterature we know that higher oxides have uranium XAS resonances placed at higher energies and that U_4O_9 cation valence doesn't assume values higher than 5+ [117]. As a consequence, we can assume that the 0.2 eV shift of $N_{4,5}$ edge peaks is due to the valence increase from 4+ to 5+. Figure 5.14b) demonstrates that uranium $N_{6,7}$ edge XAS spectrum of the IP sample has features similar to UO_2: the presence of the same resonances confirms that in both these phases uranium keeps the same local environment. As already seen in Chapter 1 - §1.1.2.3, a cubic lattice induces the splitting of the uranium 6d states into the e_g and t_{2g} orbitals, the energetic levels of which differ by 2.8 eV [166]. A comparison of the experimental and calculation results (see Figure 5.15), reveals that peaks a and b may be associated to the e_g and t_{2g} ,orbitals respectively. With this association, we found a splitting of 3.2±0.1 eV, comparable to the literature value; this splitting is also indicative that our IP sample conserves the same cubic symmetry of UO_2. We derived also an estimate of the e_g/t_{2g} orbital splitting from the uranium 6d DOS calculated by *ab-initio* (the blue curve represented in Figure 5.10a)). We convoluted the theoretical curve with a Lorentzian and a Gaussian contribution respectively of 0.3 eV and 0.2 eV, to take into account both the effects of core hole lifetime and experimental broadening and we compared this curve with our XAS uranium N_7 edge spectrum.

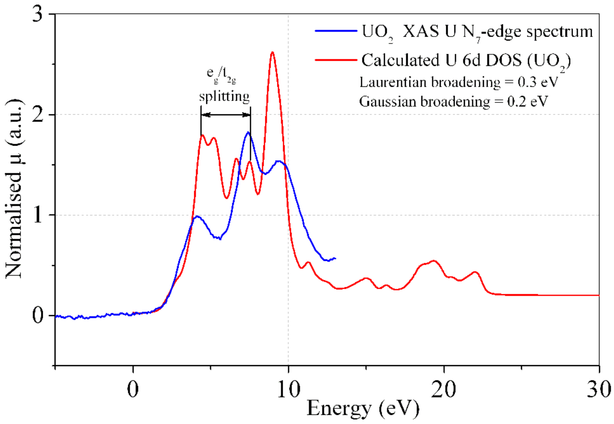

Figure 5.15: Comparison between our experimental XAS spectrum of UO_2 collected at the oxygen N_7-edge with the uranium 6d DOS calculated by *ab-initio*.

As shown in Figure 5.15, splitting between the uranium e_g and t_{2g} orbitals is estimated to be 3.1 eV. This value is in complete agreement with the experimental values reported above. Note however that comparison between experiment and calculations is only qualitatively. There are several reasons for this. Firstly, DFT is well suited for ground state calculations and less reliable when used to study excited states. Also, in our DFT calculations, the core hole effect is not taken into account. Finally, we have not eliminated the empty states from the calculations which correspond to electronic transition forbidden as a result of selection rules (see Chapter 2 - section §2.4.2). Considering these limitations, Figure 5.15 shows that calculated uranium 6d states well matches with the spectra acquired at the N_7 edge; note that no contribution of multiple scattering phenomena in the uranium N_7 edge spectra is clearly visible because of the adiacent presence of the N_6 edge.

U_3O_7

The same analysis carried out for IP is now developped for the U_3O_7 phase.

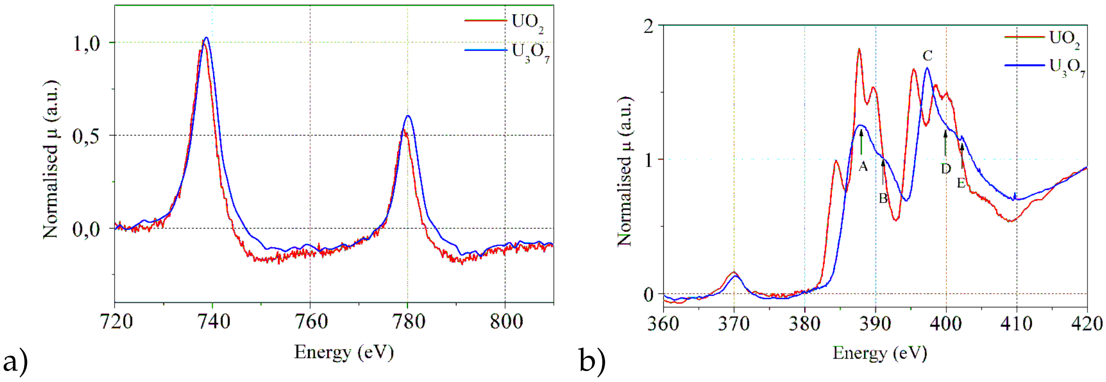

Figure 5.16: Uranium spectra at the $N_{4,5}$ (a) and $N_{6,7}$ (b) edges of our reference phases UO_2 (red), and U_3O_7 (blue).

Phase	***N_5***	***N_4***	***N_7***		***N_6***		
			A	**B**	**C**	**D**	**E**
U_3O_7	738.8	780.1	388	391	397.3	400.7	402.2

Table 5.6: Peak position energies (in eV) relative to the uranium XAS spectra collected at the $N_{4,5}$ and $N_{6,7}$ edges.

As shown in Figure 5.16a), the phase transition to U_3O_7 induces a shift of the $N_{4,5}$ energies greater than the shift observed for IP: in U_3O_7 the number of uranium atoms which have a valence higher than 4+ is greater. Actually, Figure 5.16b) shows a profound change in the uranium 6d states has occurred due to the phase transition from UO_2 to U_3O_7. This higher oxide phase spectrum in fact presents less well defined and broader peaks than for UO_2. This feature in indicative of a change in the uranium local environment and its electronic structure: the delocalisation of the U_3O_7 6d orbitals is greater than in for UO_2 and our IP sample. The observation of the $N_{6,7}$ edge spectrum is entirely consistent with the loss of the cubic symmetry in U_3O_7. As crystallography would predict, U_3O_7 because it is tetragonal leads to the disappearance of the 6d splitting into e_g and t_{2g} orbitals.

5.2.4.3 Oxidation effects evaluated by *ab-initio*

This section aims to determine to what extent the *ab-initio* calculated DOS of uranium dioxide with increasing deviations from stoichiometry follows the oxidation-induced observations.
For each supercell (perfect, containing one oxygen interstitial, one di-interstitial), Figure 5.17 represents the calculated DOS of the oxygen 2p orbitals, while Figure 5.18a) and b) reports respectively the DOS of uranium 5f and 6d orbitals of the empty energy levels (conduction band).

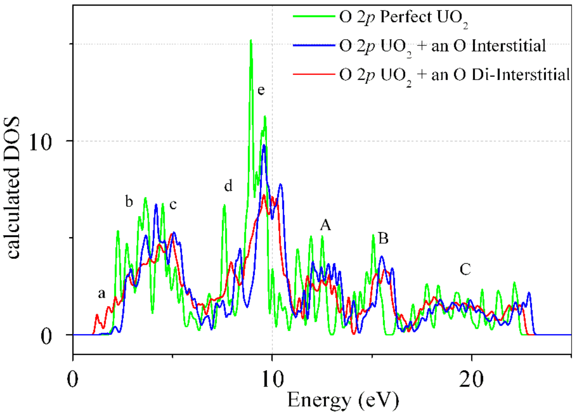

Figure 5.17: Comparison between Oxygen 2p DOS of UO_2 with a perfect lattice (green), an oxygen interstitial (red) and an oxygen di-interstitial (blue).

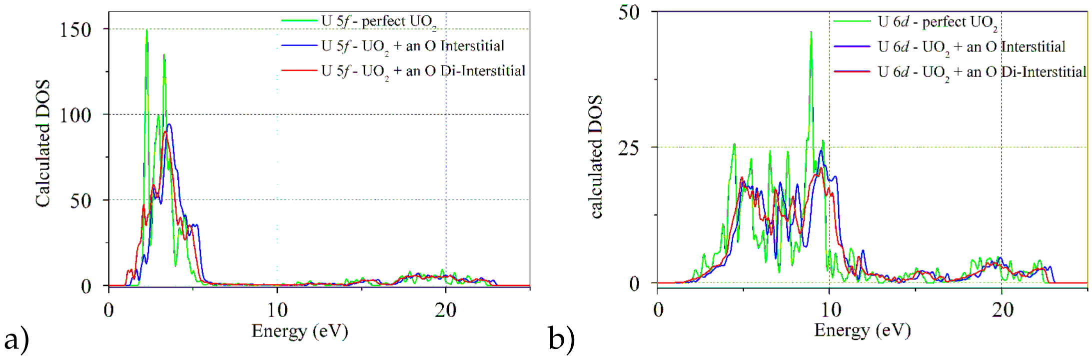

Figure 5.18: Comparison between Uranium 5f (a) and 6d (b) DOS of UO_2 with a perfect lattice (green), an oxygen interstitial (red) and an oxygen di-interstitial (bleu).

In presence of oxygen defects, partial UO_2 O 2p DOS shows the growing of a pre-peak at the beginning of the conduction band (see Figure 5.17). This pre-peak can be associated with peak "a" observed experimentally. Calculated 5f and 6d uranium DOS of the perfect UO_2 (see Fig. 5.18) are positioned at lower energies than the defective supercells. Moreover, with the exception of peak a in the oxygen DOS, all the other peaks of both the anion and cation electronic structures are less defined and intense (see Figures 5.17 and 5.18) as is observed in experiments demonstrating the relevance of these electronic structure calculations.

5.3 Discussion relative to XAS results obtained for reference phases

XAS characterization technique directly probes the empty electronic states. As a consequence of this, a XANES spectrum is sensitive to atomic bonding of the absorber atom, allowing us to deduce its local atomic environment (at a distance of 6-8 Å) and, in certain cases, the symmetry of the crystal field it is inserted in. Until now in fact we have seen that this technique enabled us to determine experimentally the DOS both of UO_2 and U_3O_7. An interesting feature of the DOS for U_3O_7 is the impact the change of symmetry from cubic to tetragonal has upon it. However the composition of our IP phase remains uncertain and we now further investigate this point.
With the Athena [8] software we reproduced the oxygen K-edge XAS spectrum of our IP phase using a linear combination of spectra relative to UO_2 and U_3O_7. With a fit quality factor X^2=0.326, the spectrum is composed of 34.9% of UO_2 and of 65.1% of the U_3O_7 spectra; these percentages are affected by 0.7% error.

In §5.2.4 we showed that our IP sample conserves a cubic structure. One may further state, on the grounds of the phase diagram, that it is quite probably composed of a mixture of UO_2 and U_4O_9. As oxidation induces also a cation valence increase, the same linear combination found to reproduce the oxygen spectrum is applied to estimate the average cation valence of the IP sample. Theoretical uranium valences of UO_2 and U_3O_7 are 4+ and 4.66+ respectively: based on the proportions of both spectra found in that of the IP, one can estimate the cation valence of our IP sample at approximately 4.43+, corresponding to an average O/M ratio of 2.215. From the phase diagram in chapter 1 - Figure 1.2, one further estimates the proportion of substoichiometric U_4O_9 in the IP at a value in excess of 90%. This result is consistent with a important change in the electronic structure of oxygen atoms (see Figure 5.13) but a conservation of the cubic symmetry as deduced from the splitting of the

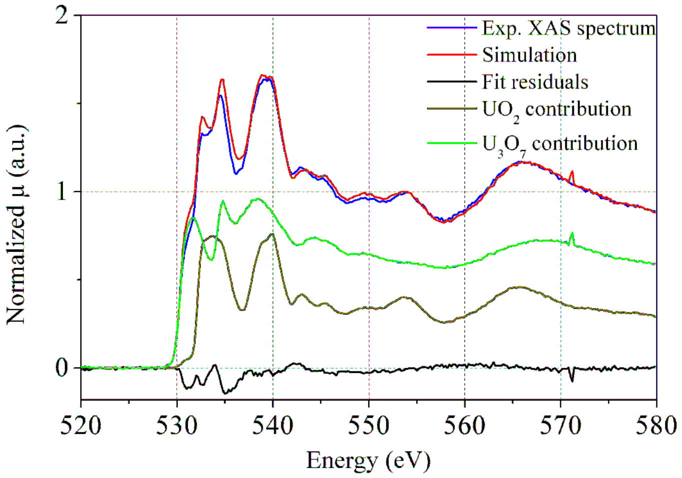

Figure 5.19: Reproduction of the U_4O_9 O K-edge spectrum with a linear combination of the UO_2 and U_3O_7 spectra.

e_g/t_{2g} orbitals seen at N_7 edge (see Figure 5.16b). It is therefore reasonable to assume that the spectrum of the IP is that characteristic of U_4O_9.

Figure 5.19 demonstrates also that the contribution of U_3O_7 is necessary to reproduce U_4O_9 spectrum adequately. As a consequence, local environments of U_4O_9 and U_3O_7 should share similar features. Each O K-edge XAS spectrum collected on uranium oxide phases has mainly two contributions (the first given by the anions of regular lattice sites, the second by the oxygen atoms constituting the defects): the reproduction of our U_4O_9 reference phase spectrum with a linear combination of UO_2 and U_3O_7 can be seen as a confirmation that the oxygen defects present in U_3O_7 and in U_4O_9 phases are equal and that only their concentration differs.

These results are consistent with the structural analyses of Desgranges *et al.* [61] on similar phases. Through the simulation of the neutron diffraction data of U_4O_9 and U_3O_7, they showed that UO_2 transforms to U_4O_9 before taking on the more distorted tetragonal structure typical of the U_3O_7 phase. This modification is induced by inserting an increasing number of oxygen cubocthaedral defects in the lattice. They observed also that in the phase change from U_4O_9 to U_3O_7 the number of complex oxygen defects increases whilst their composition remains essentially unchanged. Despite these two phases having different crystalline symmetries, their atomic lattices accommodate the same kind of oxygen defects.

Good reproduction of our IP sample spectrum with the linear combination found here is consistent also with the U_4O_9 oxygen and uranium local environments discussed in §5.2.1. In that section we showed that in U_4O_9 the disposition of atoms around oxygen has features similar to UO_2 and that each oxygen or uranium of the elementary cell is surrounded by a higher number of oxygen atoms.

5.4 XAS study of UO_{2+x} specimens

We also carried out XAS characterisations of our UO_{2+x} samples. These samples were prepared and annealed in pairs, the second sample being dedicated to oxygen self-diffusion studies (annealing conditions are reported in Table 4.5). Two sets of specimens were analysed: the undoped and the Cr-doped UO_2 polycrystalline samples. As an example we report in Figure 5.20 and Figure 5.21 the oxygen K- and at uranium $N_{4,5}$-edge XAS spectra collected on undoped samples annealed at 890°C at four oxygen potentials (7.1 10^{-16} atm, 5.5 10^{-15} atm, 1.2 10^{-13} atm and 1.0 10^{-12} atm). Figure 5.20 reports the relative intensity of peak a for all the UO_{2+x} spectra. Each reported value is calculated as the ratio between the intensity of peak a of the UO_{2+x} sample to that measured on the U_3O_7 reference phase.

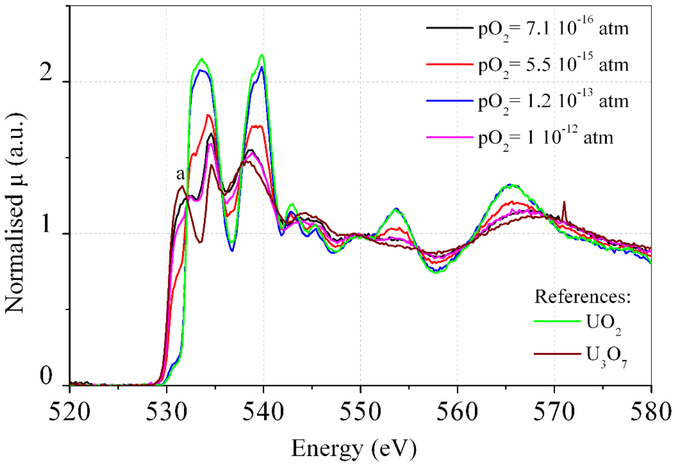

pO_2 (atm)	$I_{a,rel}$ (%)
7.1 10^{-16}	91.8
5.5 10^{-15}	56.2
1.2 10^{-13}	11.3
1.0 10^{-12}	81.5

Figure 5.20: fY XAS spectra respectively collected at the O K-edge on UO_2 undoped samples annealed at 890°C at four increasing oxygen potentials. The table reports the relative intensities of peak "a" measured for all the reported spectra.

From Figure 5.20, we see that the UO_2 sample annealed at the lowest pO_2 has an oxygen K-edge spectrum that shows the strongest signs of oxidation. As the equilibrium partial pressure rises to 1.2 10^{-13} atm, oxidation effects gradually decrease: the intensity of peak "a" gradually decreases while the other peaks increases their intensity. Above 1.2 10^{-13} atm (*i.e.* at 1.0 10^{-12} atm) the spectrum resembles that of U_3O_7. The spectra relative to the $N_{4,5}$ edge (see Figure 5.21) show trends similar those observed at the O K edge with strong signs of oxidation: peaks shift towards higher energy values for the lowest oxygen partial pressure.

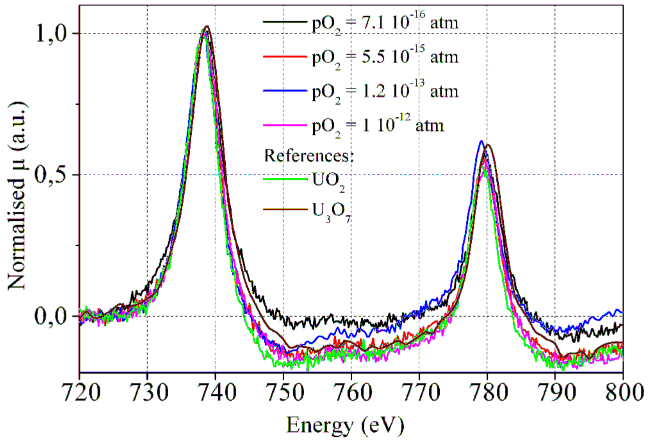

Sample	*N_5*	*N_4*
UO_2	738.2	779.4
U_3O_7	738.8	780.1
7.1 10^{-16} atm	738.6	779.8
5.5 10^{-15} atm	738.3	779.6
1.2 10^{-13} atm	738.2	779.4
1.0 10^{-12} atm	738.4	779.7

Figure 5.21: XAS spectra collected at the uranium $N_{4,5}$ edges on UO_2 undoped samples annealed at 890°C at four oxygen potentials. The table summarizes the resonance energy positions.

These observations are of course completely counter intuitive since higher equilibrium partial pressures should lead to more and more obvious signs of oxidation.

The O K-edge spectra of each annealed sample were reproduced by a linear combination of UO_2 and U_3O_7 spectra to quantify their degree of oxidation. Table 5.7 reports the quality factor of each fit and the percentages of UO_2 and U_3O_7 necessary to reproduce the spectrum for each annealed UO_{2+x} specimen. Figure 5.22 represents only the calculated contribution of U_3O_7 as a function of the annealing oxygen partial pressure for each temperature.

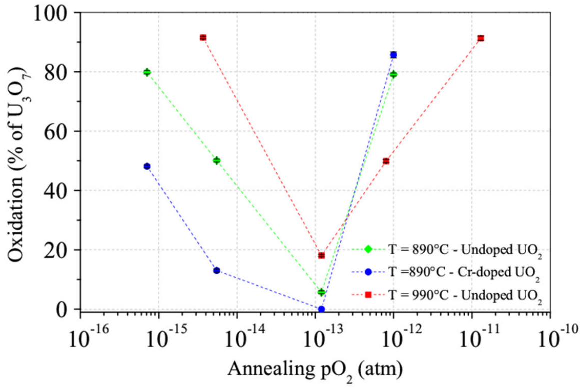

Figure 5.22: Quantification of the oxidation degree of UO_{2+x} samples.

Before analysing the trends in spectrum modifications induced by oxidation, we aim to briefly describe the results reported in Table 5.7. Figure 5.23

Annealing		*Sample*	X²	*Percentage*	
T (°C)	*pO_2* (atm)			*UO_2*	*U_3O_7*
890	$7.1\ 10^{-16}$	Cr-doped	0.2	52	48
	$5.5\ 10^{-15}$		0.144	87	13
	$1.2\ 10^{-13}$		0.336	1	0
	$1.0\ 10^{-12}$		0.627	14	86
890	$7.1\ 10^{-16}$	Undoped	0.294	20	80
	$5.5\ 10^{-15}$		0.162	50	50
	$1.2\ 10^{-13}$		0.19	94	6
	$1.0\ 10^{-12}$		0.21	21	80
990	$3.7\ 10^{-15}$	Undoped	0.090	9	92
	$1.2\ 10^{-13}$		0.070	82	18
	$8\ 10^{-13}$		0.146	50	50
	$1.3\ 10^{-11}$		0.347	9	91

Table 5.7: UO_2 and U_3O_7 contributions used to best reproduce the experimental spectra of the UO_{2+x} specimens. Percentages are affected by an error of 1%. X² is a value indicative of the quality of the fit.

reports the simulation of the two spectra that respectively have the best and the worst X² value.

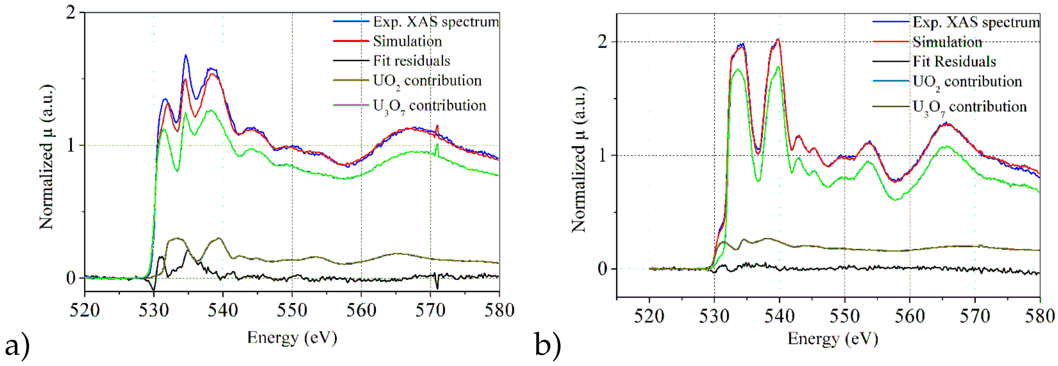

Figure 5.23: Comparison of XAS spectra of the Cr-doped sample annealed at 890°C, 10^{-12} atm (a) (worst X²) and of the undoped UO_{2+x} sample annealed at 990°C, $1.2\ 10^{-13}$ atm (b) (best X²) to the best-fit linear combination of UO_2 and U_3O_7 reference spectra.

We can see from figure 5.23a), that the greater differences between the experimental and the simulated curves are located in the lower part of the spectra (in the energy range 530-540 eV). However, it appears from Table 5.7 and Figure 5.23, that the fits are enough good to allow a reliable quantification of the sample oxidation induced by our annealing conditions.

The unexpected results outlined in Figure 5.22 require identifying of all the parameters that are liable to affect the collected XAS spectra:

- The sample annealing conditions. Annealing conditions are designed to control and modify the deviation from stoichiometry of the sample. As seen in the previous sections, XAS signals are strongly dependent upon the sample oxidation induced by annealing.

- The quenching stage of annealing. After being annealed, samples are quenched so that the UO_{2+x} microstructure supposedly remains in a state close to what it is at high temperature. UO_{2+x} in fact is a phase stable only at temperatures higher than 400°C (see the phase diagram reported in Chapter 1, Figure 1.2); depending upon cooling rate, UO_{2+x} should form a two phase compound comprising UO_2 and U_4O_9 as it cools.

- The impurity concentration present in the samples. At low pO_2, Cr doping fixes the sample hole concentration and consequently modifies the concentration of isolated point defects by the relationship 3.7 (see Chapter 3) so long as equilibrium is kinetically possible.

- The incorporation of point defects as a result of exposure to air. It is reported by [138] that the exposure of UO_2 samples to air provokes an oxidation of the first atomic layers of the sample including at ambient temperature. However oxidation of UO_2 is known to occur less readily as the sample deviation from stoichiomerty increases.

If one compares as in Figure 5.22 the XAS spectra of Cr-doped and undoped samples, it would appear that the annealing conditions have a first order impact upon the oxidation state of the sample surface subsequently characterised at room temperature. The comparison of Cr-doped and undoped samples enables us also to demonstrate the influence upon the DOS of the presence of trivalent chromium ions (see Figure 5.24).

As seen in Figures 5.24a) and 5.22, until the oxygen partial pressure exceeds 10^{-13} atm, XAS signals of Cr-doped samples show slightly smaller signs of oxidation than the undoped ones. This is consistent with the dependence of oxygen interstitial concentrations upon the charge carrier concentrations given by Equation 3.7. When isolated defects predominate, at identical oxygen partial pressures, an increase in hole concentration due to the presence of a trivalent doping agent induces a decrease in oxygen interstitial content. Conversely, at the highest pO_2 Figure 5.24b) demonstrates that the two analysed specimen own have identical spectra hence DOS. This is consistent with the fact that at high oxygen partial pressures samples behave intrinsically (see Chapter 3) and

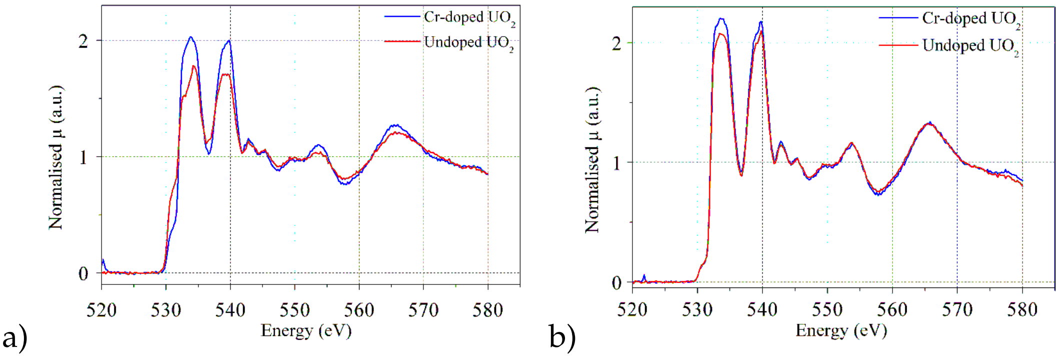

Figure 5.24: Comparison between the oxygen K-edge spectra of a Cr-doped sample with the one collected on an undoped specimen; these two samples were annealed at the same time and were therefore exposed to identical thermodynamic conditions. Samples were annealed at 890°C: Graph a) corresponds to annealing at a pO_2 of 5.5 10^{-15} atm, Graph b) to 1.2 10^{-13} atm.

it is not surprising that DOS loose their dependence upon doping concentrations.

Exposure to air in the first instants after quenching may influence the collected XAS signals. At low oxygen pressures, sample compositions are nearer to stoichiometry and consequently sample surface is more reactive to the presence the oxygen of the atmosphere. Additional oxygen atoms can penetrate into the first atomic layers of the surface inducing a strong variation in the probed XAS spectra. This fact explains the first part of the curves plotted in Figure 5.22: spectra of samples annealed at lower oxygen partial pressure show stronger signs of oxidation. Conversely, it seems that the oxidation effects induced by annealings become visible only after overcoming an oxygen potential threshold. This phenomenon can be associated with the predominance of oxygen clusters in the samples annealed at high pO_2. As seen in Chapter 4, these defects inhibit bulk diffusion of oxygen in UO_2 , preventing the incorporation of oxygen atoms contained in the surrounding gaseous environment. The pO_2 value at which DOS modifications begin to linearly follow the oxidising annealing conditions can be therefore interpreted as the pO_2 at which oxygen clusters become predominant over isolated defects. From these XAS results, it would appear that the transition oxygen partial pressure at which isolated oxygen interstitials become negligible in comparison to clusters is in the range 5.5 10^{-15} and 1.2 10^{-13} atm at 890°C, and at 10^{-13} atm *circa* at 990°C. This interpretation is however in contradiction with the fact that the reference sample for the stoichiometric UO_2 phase exhibits the characteristics of unoxidised UO_2. As shown in Chapter 2 - §2.1, its preparation protocol aims only that is sliced from sintered pellets and carefully polished, but doesn't forecast a post-polishing annealing. The reason for this contradiction is with no doubt to be found in the fact that all the other samples studied were annealed under an argon hydrogen mixture made to bubble through distilled water. It is likely that the water molecules adsorbed at the surface of the samples is crucial in increasing the reactivity of the surface. So the XAS characterisation of the surface layers of UO_2 is the subtle consequence of changes in the bulk and surface reactivity of the material.

Following this interpretation, the presence of a smaller concentration of oxygen interstitials in Cr-doped samples at low oxygen potential would induce their XAS signals to present stronger signs of oxidation. Conversely, Figure 5.24a) shows an opposite behaviour, *i.e.* samples seems to be less oxidised than the undoped specimens. This fact may be due to the presence of Chromium, that leads sample surface reactivity to decrease and consequently disables oxygen atoms to be incorporated in the lattice.

As for U_4O_9, the spectra collected on UO_{2+x} samples are successfully reproduced using a linear combination of UO_2 and U_3O_7 references. This fact indicates that oxygen defects are of the same kind in both hyperstoichiometric samples and in the higher oxide phases U_4O_9 and U_3O_7. As explained in the previous section (§5.3), comparison of our XAS spectra with the published neutron diffraction results demonstrates that both in U_4O_9 and U_3O_7 lattices additional oxygen atoms are disposed on cubocthaedra or on cluster defects sharing part of their structure (such as the Willis one).

5.5 Conclusions

In this chapter we evaluated the impact of the oxidation of UO_2 upon its electronic structure. Experimental DOS characterization of hyperstoichiometric samples was possible only after the detailed analysis of the XAS spectra of higher oxide phases, taken as references. Annealing a sample at low temperatures under air enabled the formation of a U_4O_9 or U_3O_7 layer on a UO_2 substrate that was subsequently characterized by XAS.

The high energy resolution provided us with high quality oxygen K-edge XAS reference spectra. Moreover, their comparison with uranium $N_{4,5}$ and $N_{6,7}$-edge spectra was used to show the hybridisation phenomenon that occurs between the O 2p and the U 5f and 6d orbitals. We succeeded also in collecting the first reference XAS spectra relative to U_4O_9 and U_3O_7 phases and in demonstrating experimentally that oxidation induces strong modifications of the electronic structure of uranium oxides. It appears that a change in the XAS oxygen K-edge spectrum is always coupled to a variation in the uranium N-edge spectra, as expected from simple charge compensation arguments. Oxidation induces also a progressive variation in the oxygen local environment: its modifications are consistent with the neutron diffraction results [61]. DFT+U calculations [176] compare very favourably with the experimental DOS for UO_2 or its higher oxide forms, to the extent that we have been able to use these theoretical approaches to interpret the experimental data.

Also in hyperstoichiometric UO_{2+x} samples oxygen and uranium local environments and density of states are direcly affected by sample composition, *i.e.* by their impurity content and thermodynamic conditions under which they are equilibrated. The influence of trivalent doping content on XAS spectra correlates both the fact that doping agents let decrease not only the oxygen isolated defect concentration but also the sample surface reactivity to air.

We have also seen that the degree of oxidation of hyperstoichiometric samples is not an increasing function of the oxygen potential as would be expected. Only XAS spectra of samples annealed at the highest pO_2 follow this expected trend. We interpret this as being due to the fact that the degree of surface oxidation is the result of a subtle combination of surface reactivity and transport in the bulk material. Specimens annealed at low pO_2 but in the presence of water vapour appear to be more reactive than those annealed at higher partial pressures providing that isolated oxygen interstitials constitute the majority defect population. We therefore interpret the pO_2 at which UO_{2+x} XAS spectra show the minimum signs of oxidation as the transition oxygen partial pressure at which clusters begin to dominate.

The intimate relationship existing between the impurity concentration, sample deviation from stoichiometry and thermodynamic conditions imposed during sample annealings continues to be analysed in the next chapter. In Chapter 6 in fact we will calculate the trivalent impurity concentration present in our samples from the conductivity data reported in Chapter 4. Then, for each kind of sample studied, we will simulate these conductivity data with the model developed in Chapter 3 to theoretically estimate oxygen defect concentrations and the transition pO_2 between isolated oxygen defects and defect clusters.

Chapter 6

Discussion of experimental results

In Chapter 4 we presented the experimental results relative to electrical conductivity, oxygen self- and chemical diffusion in UO_2 under various thermodynamic conditions. In particular we investigated the dependencies of these three properties upon oxygen potential, temperature and impurity content. Chapter 5 was devoted to the characterisation using XAS of the effect of oxidation upon electronic structure and attempted to relate to it local environment variations induced by the insertion of additional oxygen atoms. Now, the major aim of this chapter is to analyse the results obtained and to check their overall consistency.

Firstly, electrical conductivity data collected on several different types of samples are analysed in the light of the point defect model developed in Chapter 3. Application of the model to different specimens, *i.e.* specimens containing different types of additives and at different concentrations, is a guarantee the model may be used to estimate defect concentrations.

In the second part of this chapter we go on to determine fundamental defect properties (migration energies in particular) based on the combination of defect concentration calculations and self-diffusion measurements. We analyse data reported from previous studies and extend this analysis to the data reported in Chapter 4. In particular, we discuss the influence of increasing oxygen partial pressures upon self-diffusion and interpret this influence on the grounds of defect clustering and concentrations.

6.1 Analysis of conductivity data

The point defect model developed in Chapter 3 allows us to determine defect concentration dependencies upon oxygen potential by simulating electrical conductivity and deviation from stoichiometry data from literature [162, 151].

In particular, we showed that simulations of such data allows us to unequivocally determine the Arrhenius dependencies of each defect formation reaction constant considered in the model and the pre-exponential term of the hole mobility μ_0 estimated at 0.26 $m^2 \cdot K \cdot V^{-1} \cdot s^{-1}$ (see §3.3.2.1 and 3.4). There is no reason why the values determined for the reaction constant of a given type of defect should depend upon the nature or concentration of the doping agent. With no evidence to the contrary we similarly assume that the pre-exponential term μ_0 is also independent of doping agent nature and concentration. However, differences may arise in the nature of the complex oxygen interstitial aggregates which may form as the oxygen partial pressure increases.

In order to determine the influence of doping agents and to further test the scope of our point defect model, we analyse the electrical conductivity measurements of Gadolinium-doped UO_2 collected by Veziteu *et al.* [177] and the measurements carried out on our own both chromium doped and undoped samples (see Chapter 4).

6.1.1 UO_2 samples doped with trivalent doping agents

6.1.1.1 Gd-doped UO_2 samples

We assume that substitutional gadolinium atoms remain trivalent. The experimental data relating to these samples were collected and studied by Veziteu *et al.* [177]. These samples were obtained by sintering for 72 hours at 1400°C and in an Ar/H_2 atmosphere, a mixture of UO_2 powder with 0.5 mol.% of Gd_2O_3. The electrical conductivity data were collected as a function of oxygen partial pressure at 1000°C, 1100°C and 1200°C. They are presented in Figure 6.1a) and an Arrhenius representation of ($\sigma . T$) in the extrinsic region is given in Figure 6.1b).

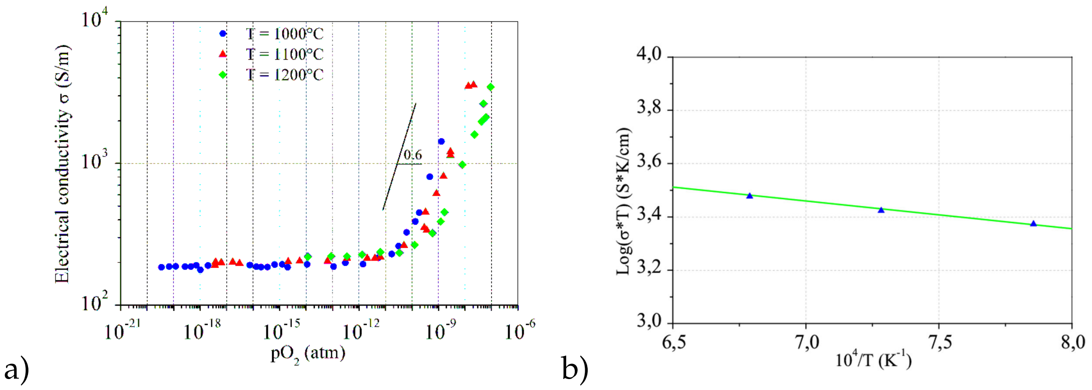

Figure 6.1: a) Gd-doped UO_2 electrical conductivity curves collected by Veziteu [177]. b) Arrhenius dependence of ($\sigma . T$) in the extrinsic region.

The hole migration barrier (E_H) and the negative cation concentration (y') were estimated from the Arrhenius relationship in Figure 6.1b) at 0.21 eV and 3.76 10^{25} at·m^{-3}. Note that the estimate of y' strongly depend on the value taken for the electron mobility μ_0 and can be compared to the effective doping agent concentration present in the samples. Also, from Figure 6.1a) we note that the slope of the electrical conductivity curve in the intrinsic region as a function of log(pO_2) is steeper than the one observed in Ruello's study. In fact, the slopes relative to the Gd doped data have a value of 0.6 rather than 0.5, as reported previously (Chapter 3). In Chapter 3, we saw these slopes were determined by the nature of the majority defect. Similarly, a slope of 0.6 is compatible with an oxygen complex defect that has 2 additional oxygen atoms and a fractional charge -2/3. The formation reaction constant for this defect (named W_b hereafter) can be written as follows:

$$O_2 + 2O_O^X + 2V_i^X + \frac{2}{3}U_U^X \rightleftharpoons W_b^{2/3'} + \frac{2}{3}U_U^{5+} \tag{6.1}$$

Note that for the same number of additional oxygen atoms, the apparent charge of the defect is less than that determined for a material containing impurity cations at lower concentrations (see Chapter 3) as would be expected in a material at high deviations from stoichiometry [55].

We simulated the entire set of data relative to the Gd-doped UO_2 material considering defect W_b and with values of E_H and y reported above. An example of the results obtained at 1100°C is shown in Figure 6.2.

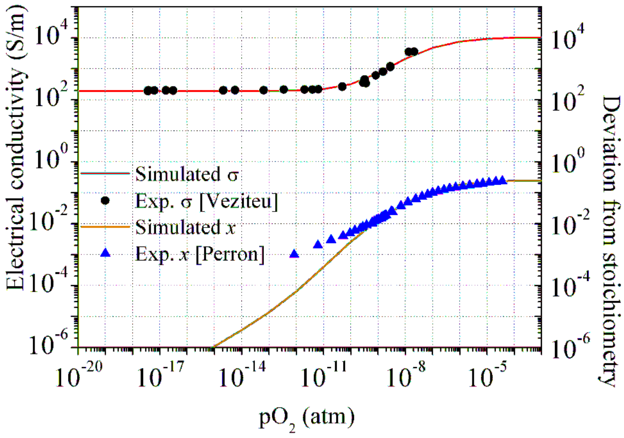

Figure 6.2: Simulation of Gd-doped electrical conductivity data taken at 1100°C.

6.1.1.2 Cr-doped UO_2 samples

We have also modelled the conductivity data relative to Cr-doped samples presented in Chapter 4 collected at 893°C and 993°C. From the hole mobility study reported in Table 4.6 and Figure 4.3a) we estimated the parameters of the hole activation energy E_H and y' due to Cr doping: they were found equal to 0.22 eV and 4.3 10^{25} at·m^{-3}.

Figures 6.3a) and b) show the calculation results. Note that we assumed the same defect cluster for Cr doped material as for Gd doped.

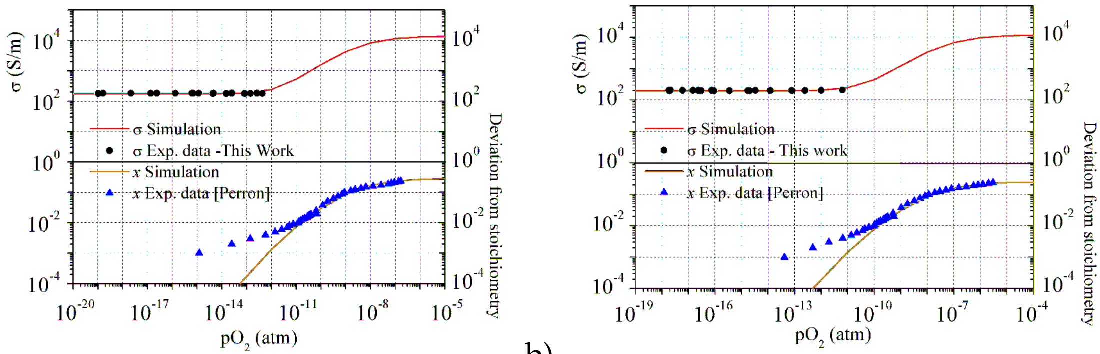

a) b)

Figure 6.3: Fit of electrical conductivity and deviation from stoichiometry data taken at 893°C (a) and 993°C (b) for chromium doped material.

Figures 6.4a) and b) report the corresponding defect concentrations.

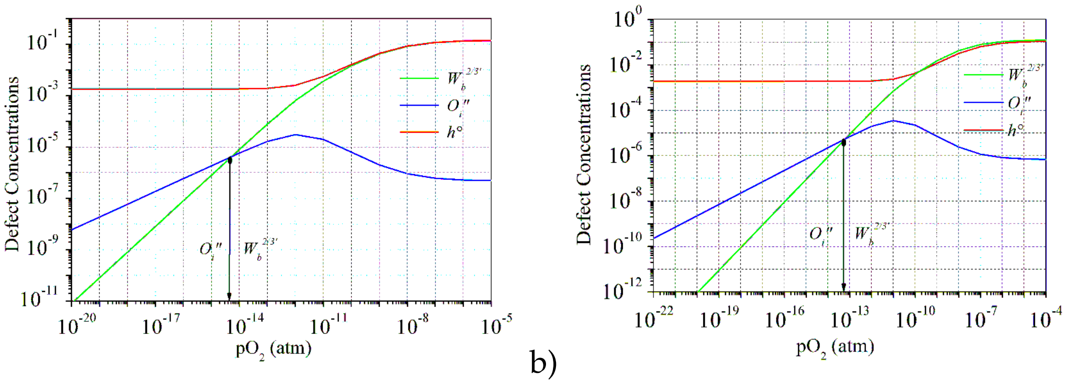

a) b)

Figure 6.4: Calculated defect concentrations at a temperature equal to 893°C (a) and to 993°C for chromium doped material (b).

From the calculated defect concentrations, we were able to estimate (see Table 6.1) the oxygen partial pressure at which oxygen clusters begins to predominate over oxygen interstitials.

Temperature (°C)	*Model* $pO_{2,trans}$ (atm)
800	$3.6\ 10^{-17}$
893	$5\ 10^{-15}$
993	$6.6\ 10^{-14}$

Table 6.1: Theoretically calculated pO_2 at which a transition occurs between oxygen interstitials and defects clusters for Cr-doped samples.

6.1.1.3 Equilibrium constant for W_b

As mentioned previously, as regards the Gd-doped samples, the physical parameters that characterise the model are obtained from electrical conductivity data. Concerning Cr-doped samples, no electrical conductivity data exists at high oxygen partial pressures. However, we assume the effect of doping agents upon clustering to be similar in both cases and K_{W_b} values are therefore determined from deviation from stoichiometry data. The equilibrium constants K_{W_b} obtained from the data analysis (*i.e.* electrical conductivity data for Gd-doped samples and deviation from stoichiometry data at the temperatures Cr-doped samples are studied) are presented in Figure 6.5.

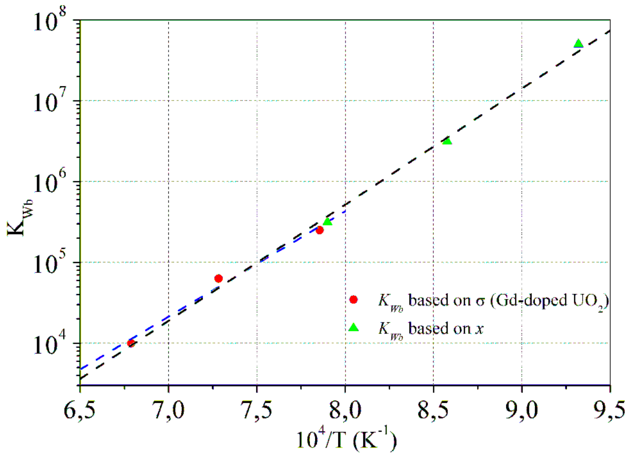

Figure 6.5: Arrhenius representation of the formation constant of the complex defect W_b present in Gd-doped UO_2 sample.

From this, it is possible to derive formation energies and entropies corresponding to the assumed defect cluster. A value of -2.9±0.1 eV is found for the formation energy of the more complex oxygen cluster which is less than the value of -2.2 eV obtained for the di-interstitial assumed from data analyses in Chapter 3. This is entirely consistent with the theoretical results of Crocombette [55]: the stability of a complex oxygen defect increases as the (absolute) charge to oxygen ratio of the defect decreases.

6.1.2 Undoped UO_2 samples

As shown in Figure 4.2, our polycrystalline samples behave quite similarly to the UO_2 single crystal specimen studied by Ruello [162]: in the extrinsic region, conductivities are similar. We choose to model the system with di-interstitial clusters as in Chapter 3.

Values of E_H and y characteristic of our undoped UO_2 sample set were derived in Chapter 4 from the low temperature conductivity study (see Table 4.6 and Figure 4.3b). Values derived are 0.23 eV and 2.4 10^{24} at·m^{-3} for E_H and y respectively. In order to reproduce the data collected at 893°C and 993°C, K_e, K_{O_i} and K_W need to be determined. This was done by implementing the method outlined in Chapter 3 and Figures 6.6a), b) and c) indicate the values obtained for these reaction constants.

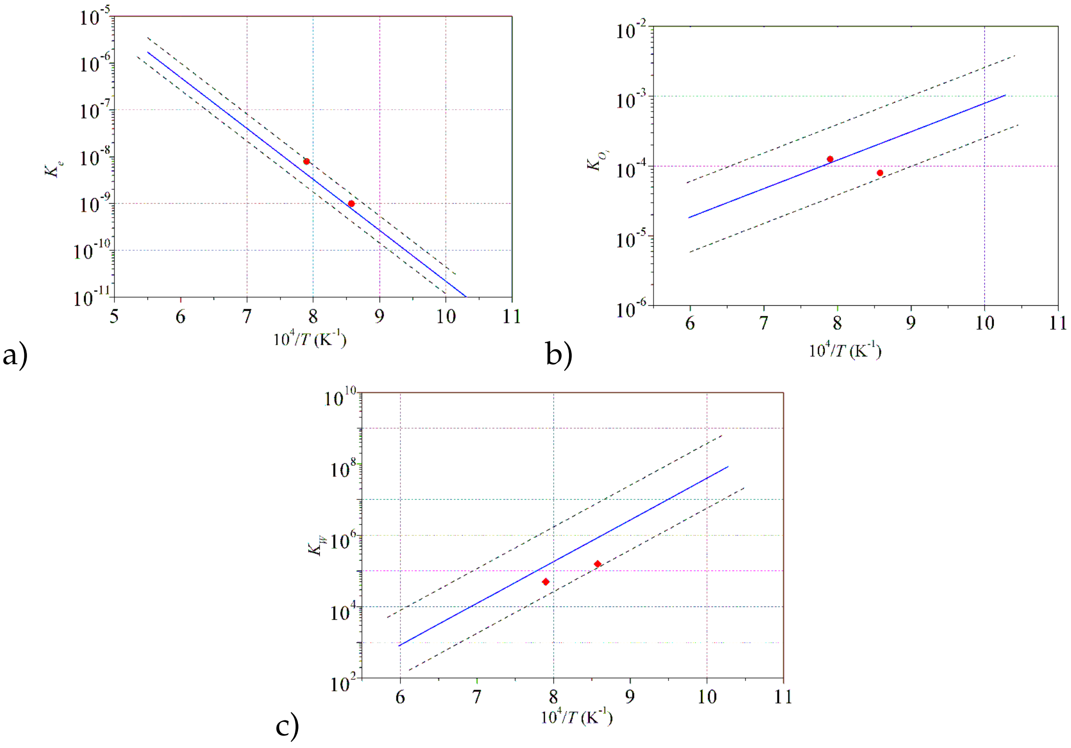

Figure 6.6: Optimized K_e(a), K_{O_i} (b) and K_W (c) reaction constants to fit electrical conductivity data of our undoped samples: comparison with their linear trends found in Chapter 3.

Experimental data are compared to the best-fit calulated values in Figure 6.7.

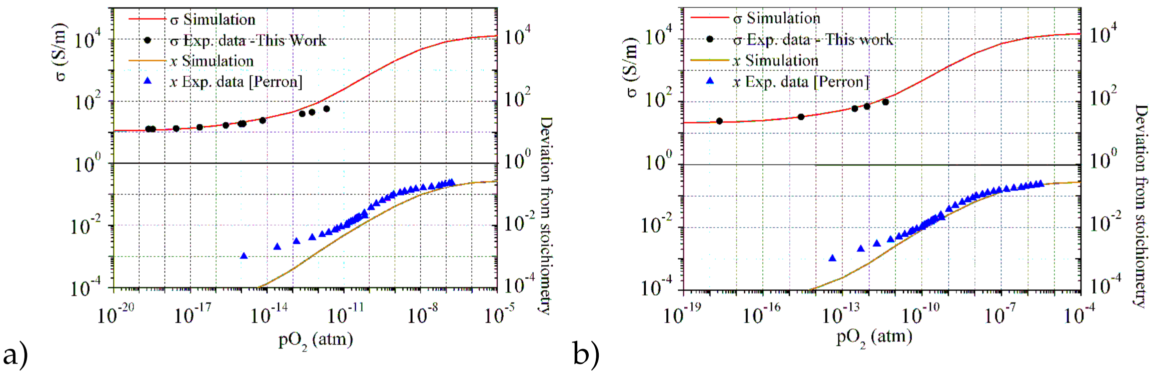

a) b)

Figure 6.7: Measured and modelled electrical conductivity and deviation from stoichiometry at 893°C (a) and 993°C (b).

As can be seen in Figure 6.7b), the model reproduces the 993°C data adequately. At 893°C on the other hand, the impression derived from Figure 6.6 is confirmed since reproduction of experimental data is less satisfactory. No clear cause may be given other than an experimental caveat.

The defect concentration changes with pO_2 estimated at 893°C and at 993°C are presented in Figure 6.8.

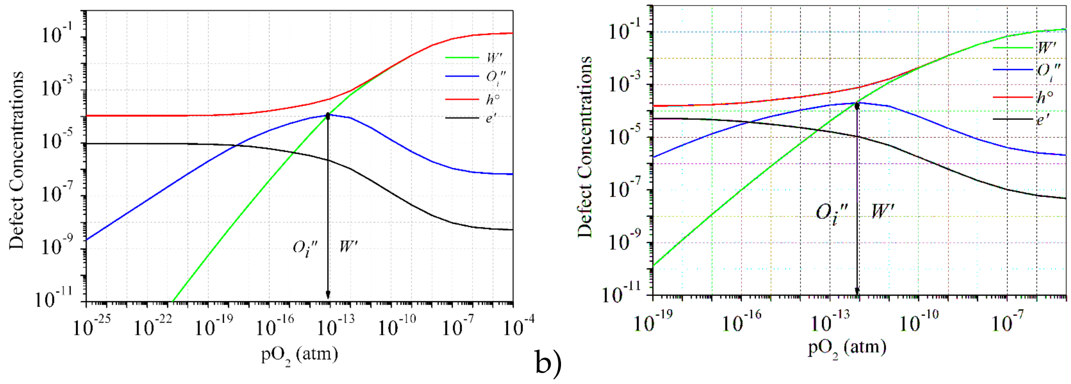

a) b)

Figure 6.8: Calculated defect concentrations at a temperature equal to 893°C (a) and to 993°C (b).

From figures 6.8 a) and b) we can estimate the oxygen partial pressure at which oxygen interstitials become less abundant than di-interstitial clusters. These values are summarised in Table 6.2.

Temperature **(°C)**	***Model*** $pO_{2,trans}$ **(atm)**
893	$8.5\ 10^{-14}$
993	$7.4\ 10^{-13}$

Table 6.2: Theoretically calculated pO_2 for the transition between isolated oxygen defects and defect clusters for undoped samples.

6.1.3 Conclusions

The methodology we have derived in Chapter 3 in which we analyse changes in electrical conductivity and composition as a function of oxygen partial pressure and temperature can be applied to uranium dioxide systems containing various doping agents and at different concentrations.

Regarding gadolinium doped samples, it appears that electrical conductivity values above 1000°C point to the existence of an oxygen cluster for which the absolute charge to oxygen ratio is less than for the di-interstitial identified in Chapter 3. Data relating to Cr-doped material are interpreted assuming a similar type of aggregate and a corresponding formation energy is estimated at -2.9 eV. This is in qualitative agreement with first principal results which predict this decrease with a decrease in the charge to atom ratio of the cluster as alluded to in Chapter 1 - §1.2.2. For undoped samples, the di-interstitial formation constant is close to that determined in Chapter 3 for a different low impurity sample.

It is reasonable to assume that the method applied in Chapter 3 and here provides appropriate estimates of defect concentrations. Their dependence upon temperature, oxygen potential and impurity content enables us to theoretically estimate the oxygen partial pressure ranges in which each kind of oxygen defect predominates. In particular, we can evaluate the minimal value of pO_2 at which oxygen clusters start to predominate over isolated defects. The theoretical evaluations reported in Tables 6.1 and 6.2 can now be used to analyse oxygen self- and chemical diffusion coefficients.

6.2 Interpretation of oxygen diffusion coefficients

In this section we combine defect concentration calculations and oxygen self-diffusion coefficient measurements to estimate migration mechanisms and barriers.

6.2.1 Oxygen interstitial diffusion coefficients based on previous studies

B. Dorado and co-workers [68] report an oxygen diffusion coefficient study at low oxygen partial pressures in which the diffusion mechanism is identified as being interstitial. The model developed previously (see Chapter 3 and previous section) enables us to estimate defect concentrations based upon reported electrical conductivity data. Although it is in principle preferable to have electrical conductivity data that covers both the extrinsic and intrinsic regions, it is possible to estimate defect concentrations at the temperature and oxygen partial pressures at which tracer diffusion coefficients were determined based upon:

1. the reaction constants determined in Chapter 3 and in the previous section for chromium doped samples, extrapolated at the relevant temperature
2. μ_0 determined from the analysis in Chapter 3
3. parameters y and E_H determined from the electrical conductivity values reported by the authors [68]

If oxygen interstitials constitute the majority defect population then the tracer diffusion coefficient (Chapter 1, Equation 1.3) may be expressed as:

$$D^*_O = f_{O_i} \cdot D_{O_i} \cdot [O_i"] \tag{6.2}$$

where f_{O_i} is the correlation factor for an interstitialcy mechanism, D_{O_i} is the oxygen interstitial diffusion coefficient and $[O_i"]$ the oxygen interstitial concentration. Based upon the tracer diffusion coefficients reported by the authors [68] and defect concentrations calculated as outlined above, one may estimate the defect diffusion coefficient (dependent upon temperature only) assuming a correlation factor of 0.7391 as suggested by Compaan and Haven [47] for this type of diffusion mechanism. The results are given in Table 6.3 where tracer diffusion coefficients, corresponding thermodynamic conditions indicated and values of D_{O_i} estimated from Equation 6.2 are reported. D_{O_i} values are then plotted in an Arrhenius representation in Figure 6.9.

Sample	**{*T* (°C), *p*O_2 (atm)}**	**D^*_O (m²/s)**	**[O_i"]**	**D_{O_i}(m²/s)**
Set 1	{750, 2.8 10^{-22}}	1.4 10^{-17}	3.0 10^{-8}	6.3 10^{-10}
	{800, 4.3 10^{-21}}	7.5 10^{-17}	8.3 10^{-8}	1.2 10^{-9}
	{870, 1.6 10^{-19}}	8.9 10^{-16}	3.1 10^{-7}	3.9 10^{-9}
	{950, 5.2 10^{-18}}	5.0 10^{-15}	9.7 10^{-7}	7.0 10^{-9}
Set 2	{750, 2.8 10^{-22}}	6.5 10^{-19}	2.6 10^{-9}	3.3 10^{-10}
	{800, 4.3 10^{-21}}	3.6 10^{-18}	6.9 10^{-9}	7.1 10^{-10}
	{870, 1.6 10^{-19}}	3.2 10^{-17}	2.5 10^{-8}	1.7 10^{-9}
	{950, 5.2 10^{-18}}	2.8 10^{-16}	8.0 10^{-8}	4.7 10^{-9}
Set 3	{900, 4.2 10^{-18}}	6.6 10^{-17}	1.2 10^{-7}	7.2 10^{-10}
	{900, 6.8 10^{-17}}	2.3 10^{-16}	5.0 10^{-7}	6.4 10^{-10}
	{900, 1.1 10^{-15}}	1.2 10^{-15}	2.0 10^{-6}	7.7 10^{-10}

Table 6.3: Oxygen interstitial diffusion coefficients and concentrations under different temperature and oxygen partial pressure conditions.

D_{O_i} is given by the following relationship [153]:

$$D_{O_i} = D_{0,O_i} \cdot \exp\left[-\frac{\Delta H^m_{O_i}}{k_B T}\right] \tag{6.3}$$

where D_{0,O_i} is the pre-exponential factor and $\Delta H^m_{O_i}$ the migration enthalpy for the diffusion of the defect.

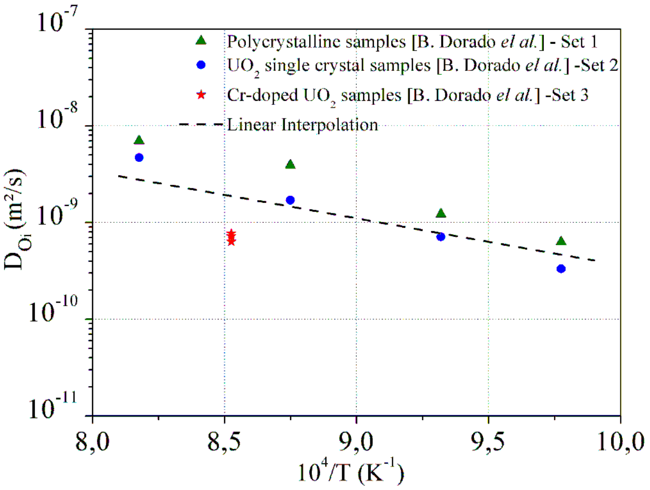

Figure 6.9: Arrhenius relationship of the oxygen interstitial self-diffusion coefficient.

$\Delta H^m_{O_i}$ is estimated from this Figure at 1±0.4 eV and the pre-exponential factor at 2.5 10^{-5} m²/s. The figure begs a number of comments. Firstly there appears to be some dispersion related to the nature of the samples. However, the migration barrier deduced from sample set 1 in Figure 6.9 is very close to the value related to sample set 2 ($\Delta H^m_{O_i}$ ~ 1.3±0.1 eV and $\Delta H^m_{O_i}$ ~ 1.4±0.03 eV for sample sets 1 and 2 respectively). Also, because the chromium doped data in Figure 6.9 were obtained at different oxygen partial pressures, the results in this Figure seem to confirm the fact that in Equation 6.2 only $[O_i'']$ is dependent upon oxygen partial pressure. The dispersion that appears in Figure 6.9 could be due to variations in the hole mobility which may be a consequence of differences in doping agents and concentrations. The factor of 5 dispersion observed in figure 6.9 in the defect diffusion coefficient could be explained by a variation of hole mobility by a factor of 2 only, since the interstitial concentration varies as $\frac{1}{[h^\circ]^2}$. This further justifies the need to carry out hole mobility measurements.

Note that the migration barrier estimated from Figure 6.9 (1±0.4 eV) is comparable to the value of ~ 0.9 eV, reported from first principle estimates for an interstitialcy mechanism [68].

The pre-exponential factor D_{0,O_i} is estimated from Figure 6.9 at 2.5 10^{-5}m²/s. Assuming this term is given by:

$$D_{0,O_i} = f_{O_i} \cdot a^2 \cdot \nu \cdot \exp\left[\frac{\Delta S^m_{O_i}}{k_B}\right] \tag{6.4}$$

where f_{O_i} is the correlation factor (0.7391), a is the jump distance (7.7 10^{-10} m) and ν is close to the Debye frequency (~ 10^{13} s^{-1}). From this equation, $\frac{\Delta S^m_{O_i}}{k_B}$, the migration entropy, is estimated at roughly 1.8.

6.2.2 Analysis of data collected at low oxygen potential on Cr-doped samples

In this section we focus on oxygen self-diffusion data obtained on Cr-doped samples (see §4.3.2 and §4.3.3) at lower oxygen partial pressures. Under these conditions, the imposed deviation from stoichiometry is small and it is reasonable to assume that oxygen defect clustering is negligible.

As indicated previously (Equation 6.2), an approximate expression for the tracer diffusion coefficient may be given in the case of a purely interstitial mechanism:

$$D^*_O = f_{O_i} \cdot D_{O_i} \cdot \frac{K_{O_i}\sqrt{pO_2}}{[h^\circ]^2} \tag{6.5}$$

Therefore, if one considers two sample types for which this equation applies at identical temperatures, it follows that:

$$\alpha \approx \frac{\log\left(\frac{D_{ref}\sqrt{pO_{2,X}}}{D_X\sqrt{pO_{2,ref}}}\right)}{\log\left(\frac{\overset{\circ}{h}_X}{\overset{\circ}{h}_{ref}}\right)} \sim 2 \tag{6.6}$$

where the subscripts refer to a reference sample (subscript *ref*) or a sample type for which the diffusion mechanism is unknown (subscript *X*). Following Dorado and co-workers [68], we take the reference sample set to be the polycrystalline samples in Figure 6.9 (sample set 1). Figure 6.10a) shows parameter α derived for chromium doped samples annealed at the lowest oxygen potentials and obtained from Dorado *et al.*'s study whilst Figure 6.10b) shows the α parameter estimated at 800°C for 5 different oxygen partial pressures. Figure 6.10 shows that the data obtained at 870°C and collected at 800°C and at oxygen potential values of 1.1 10^{-19} and 3.0 10^{-19} atm only are consistent with purely interstitial diffusion mechanisms.

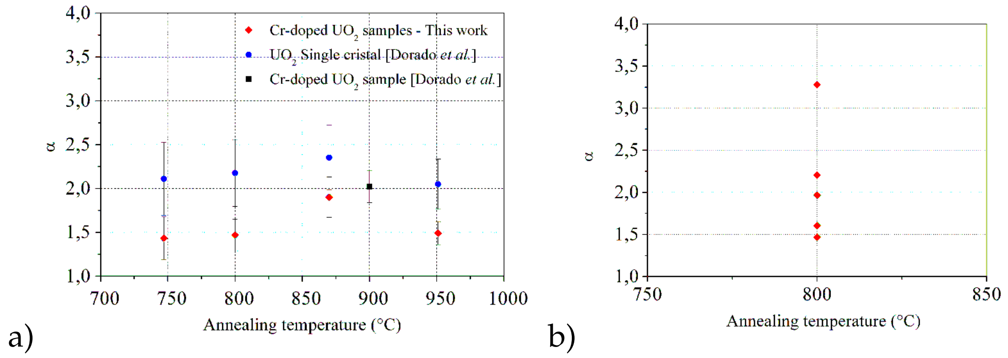

Figure 6.10: Estimate of the α parameter (see text for details) for our sample set and comparison with previously published data [68] at different temperatures (a) and at 800°C (b).

D_{O_i} values only corresponding to the Cr-doped samples with α equal to 2 are plotted in an Arrhenius representation equivalent to Figure 6.9. From the linear trend relative to the Cr-doped samples, $\Delta H^m_{O_i}$ for the sample set n°3 is estimated at 1.3±0.2 eV, value close to the ones found for sample sets 1 and 2 in §6.2.1. Moreover, our data points can improve the estimate of $\Delta H^m_{O_i}$ obtained interpolating all the available estimates for D_{O_i}. From linear interpolation plotted in Figure 6.11, the oxygen interstitial migration barrier is estimated at 1.2±0.4 eV and the pre-exponential term 1.5 10^{-4} $\mathrm{m^2/s}$. This value of D_{0,O_i} (see Equation 6.4) provides a $\frac{\Delta S^m_{O_i}}{k_B}$ estimate of 3.5.

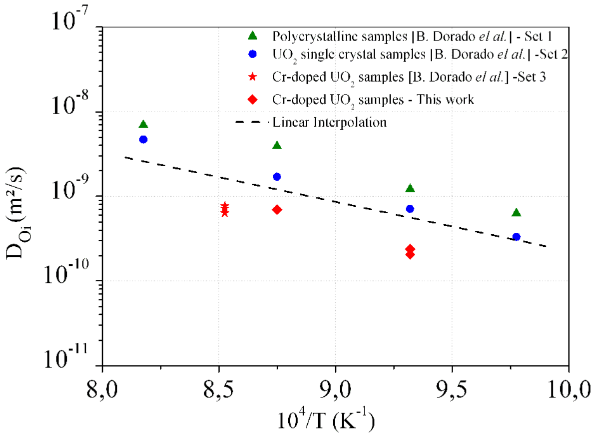

Figure 6.11: Arrhenius relationship of the oxygen interstitial self-diffusion coefficient for each of the three kinds of samples studied: Cr-doped samples (our data + data of [68]), un-doped UO_2 polycristalline and UO_2 single cristals [68].

Because the α parameter was low at 800°C, we carried out a self-diffusion study as a function of oxygen partial pressure at that temperature in order to quantify a possible contribution of oxygen vacancies. As can be seen in Figure 6.10b), there appears to be a contribution of vacancies below an oxygen potential of 10^{-19} atm.

If only isolated oxygen interstitials and vacancies prevail, the oxygen tracer diffusion coefficient is given by:

$$D_O^* = f_{O_i} \cdot D_{0,O_i} \exp\left[-\frac{\Delta H_{O_i}^m}{k_B T}\right] [O_i"] + f_{V_O} \cdot D_{0,V_O} \exp\left[-\frac{\Delta H_{V_O}^m}{k_B T}\right] [V_O{}^{\circ\circ}] \quad (6.7)$$

Further expressing, for small variations of deviation from stoichiometry, the oxygen Frenkel equilibrium (Equation 3.9 - Chapter 3) and the oxygen interstitial formation equilibrium yields the following general expression for the tracer diffusion coefficient in an isolated defect regime:

$$D_O^* = f_{O_i} \cdot D_{0,O_i} \exp\left[-\tfrac{\Delta H_{O_i}^m}{k_B T}\right] \tfrac{K_{O_i}\sqrt{pO_2}}{[h^\circ]^2} + f_{V_O} \cdot D_{0,V_O} \exp\left[-\tfrac{\Delta H_{V_O}^m}{k_B T}\right] \tfrac{K_{AF}}{K_{O_i}} \tfrac{[h^\circ]^2}{\sqrt{pO_2}}$$

$$D_O^* \sim A \cdot \sqrt{pO_2} + \tfrac{B}{\sqrt{pO_2}} \quad (6.8)$$

Term A above is determined from the expression derived previously for the oxygen interstitial diffusion coefficient and K_{O_i} determined in Chapter 3. Term B is then deduced for various values of the self-diffusion coefficient determined at 800°C. Table 6.4 gives the value of B for the two lowest oxygen partial pressures. Based on this value, we have plotted Equation 6.8 in Figure 6.12a). The figure shows that the tracer diffusion coefficient does indeed follow the law predicted by Equation 6.8 for a value of B approximately equal to $5\ 10^{-28}$. At higher oxygen potentials, it is expected that oxygen clusters become the predominant species as indicated in Figure 6.12b) (in which the defect concentrations are given for values of K_{O_i}, K_e and K_{W_b} given in Chapter 3 - §3.4 and Chapter 6 - §6.1). It is the mergence of this more complex defect population which explains why the tracer diffusion coefficient deviates from the law corresponding to Equation 6.8.

pO_2 **(atm)**	***Term B***
$1.3\ 10^{-20}$	$4.7\ 10^{-28}$
$2.3\ 10^{-20}$	$4.2\ 10^{-28}$

Table 6.4: B values obtained by our oxygen diffusion coefficients.

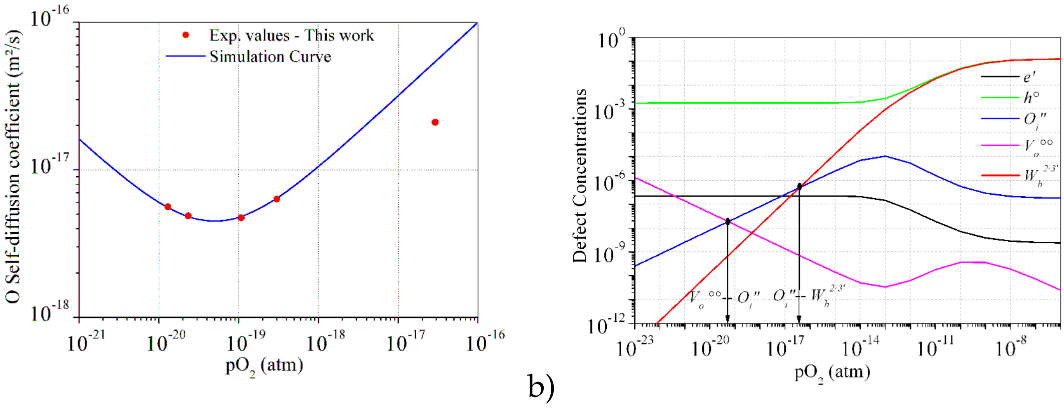

a) b)

Figure 6.12: a) Application of the point defect model developed in Chapter 3 (T=800°C) to oxygen self-diffusion coefficients relative to Cr-doped UO$_2$ samples. b) defect concentrations as a function of oxygen potential.

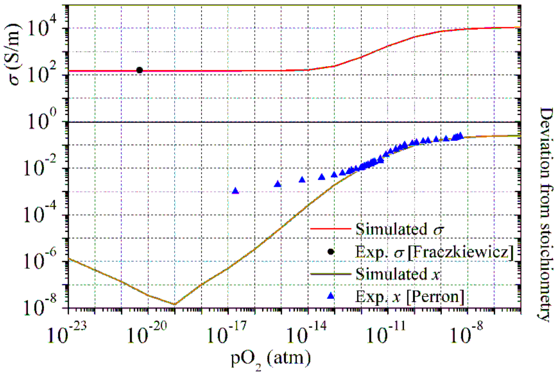

Figure 6.13: Application of our point defect model developped to simulate electrical conductivity of Cr-doped UO$_2$ sample set [73] and deviation from stoichiometry [151] at 800°C.

As indicated in Figure 6.13, the model reproduces available electrical conductivity data and deviation from stoichiometry adequately.

6.2.3 Analysis of data obtained at higher oxygen potentials

6.2.3.1 Comparison of model results with our oxygen self-diffusion measurements

In this section we aim to discuss oxygen self-diffusion results obtained with Cr-doped and undoped samples annealed at high oxygen potentials and determine whether this behaviour is consistent with the presence of isolated point defects.

In Chapter 4 - §4.3.4, we observed that there exists a threshold partial pressure beyond which the oxygen tracer-diffusion coefficient decreases (see Figures 4.9

and 4.10). The oxygen partial pressure values at which this change is experimentally observed are summarized in Table 6.5.

Studied Sample	***Temperature* (°C)**	***Model* $pO_{2,trans}$ (atm)**	***Exp.* $pO_{2,trans}$ (atm)**
Cr-doped	893	5 10^{-15}	$(1.1\pm0.3)\ 10^{-15} < pO_2 < (5.5\pm1)\ 10^{-15}$
Cr-doped	993	6.6 10^{-14}	$(8\pm2)\ 10^{-13} < pO_2 < (1.3\pm0.3)\ 10^{-11}$
Undoped	893	8.5 10^{-14}	$(5.5\pm1)\ 10^{-15} < pO_2 < (1.2\pm0.3)\ 10^{-13}$
Undoped	993	7.4 10^{-13}	$(1.2\pm0.3)\ 10^{-13} < pO_2 < (8\pm2)\ 10^{-13}$

Table 6.5: pO_2 of transition between oxygen isolated and cluster defects for Cr-doped and undoped samples: comparison between the theoretical and the experimental estimates.

In Chapter 4 we interpreted the change in oxygen self-diffusion with pO_2 as being due to a change in the type of oxygen defect that predominates. To further investigate the consistency of this interpretation, we compared the values of oxygen potentials collected in Table 6.5 with the theoretical estimates of transition oxygen partial pressures corresponding to a change from an isolated oxygen defect to defect clusters found with our model in §6.1 (see Tables 6.1 and 6.2). Considering also the experimental error bars that affect our oxygen partial pressure measurements, the $pO_{2,trans}$ evaluated with both the approaches are comparable for each temperature and sample type studied. We conclude that oxygen self-diffusion in UO_{2+x} is inhibited at higher oxygen potentials because of clustering of oxygen interstitials. In fact their progressive increase in concentration is always associated to the diminution of oxygen interstitials, which constitutes the defect responsible of oxygen self-diffusion in hyperstoichiometric UO_2. Unfortunately, no quantitative analysis of the reported oxygen self-diffusion coefficients may be given due to the fact that diffusion coefficient dependences upon pO_2 do not follow entirely reproducible trends.

Despite the experimental difficulties encountered in estimating oxygen self-diffusion coefficients (see §4.3.1), there appears to be some consistency between the observed trends and those expected from our theoretical model.

6.2.3.2 Consistency with collected oxygen K-edge spectra

In Chapter 5 - §5.4, we show that oxidation-induced modifications as observed from the oxygen K-edge spectra first appear to decrease and then, beyond a threshold partial pressure increase as would be expected (see Figure 5.22). The threshold oxygen potential value is estimated at between (5.5±1) 10^{-15} and (1.2±0.3) 10^{-13} atm for Cr-doped samples at 890°C lies at about 10^{-13} atm at 890°C or 990°C for undoped material.

For both types of samples and at the temperatures studied, these values are comparable to the theoretical estimates reported in Table 6.5. This is not inconsistent with the interpretation to put forward in Chapter 5: the surface of the samples is unstable when exposed to air with respect to oxidation since it is reactive and the low defect concentration enables diffusion to proceed at high rates. Formation of oxygen clusters at high oxygen partial pressures stabilises the surface when subsequently exposed to air. Moreover, at these higher oxygen partial pressures, doping effects upon K-edge spectra are not observed. This behaviour can be thought of as indicating that in the intrinsic region (*i.e.* when defect clusters predominate) the effect of Cr-doping becomes negligible because its concentration lies below the defect cluster concentration brought about by the annealing conditions.

6.2.3.3 Analysis of the oxygen chemical diffusion dependence upon oxygen potential

In this section we aim to deduce the theoretical oxygen chemical diffusion dependence upon oxygen partial pressure and compare it with the trend observed experimentally (see §4.2.3 in Chapter 4). This comparison helps us to consolidate the determination of the oxygen potential regions of predominance of different oxygen defects studied above. It enables also to evaluate the consistency of our results with the theory reported in Chapter 1, §1.3.2.3.

In Figure 4.5, we observed that at 890°C and at oxygen potentials below 10^{-13} atm, oxygen chemical diffusion of undoped samples is relatively constant, while at higher pO_2 values oxygen chemical diffusion varies as $pO_2^{-1/2}$. As seen in the previous section (see Figures 6.4 and 6.8), oxygen interstitials are no longer the predominant defect species at oxygen partial pressures above 10^{-13} atm as oxygen interstitial aggregates predominate.

Chemical diffusion is related to the self-diffusion coefficient through the molar fraction of uranium (x_U) and the quantity $\frac{\partial \ln(pO_2)}{\partial \ln(x_O)}$ (see Chapter 1 - Equation 1.7). This factor is clearly dependent upon the molar fraction of oxygen (x_O) in the oxide. This variable, as well as x_U, can be expressed as a function of the deviation from stoichiometry x:

$$\begin{cases} x_O = \frac{2+x}{3+x} \\ x_U = \frac{1}{3+x} \end{cases} \tag{6.9}$$

As a result, the thermodynamic factor $\frac{\partial \ln(pO_2)}{\partial \ln(x_O)}$ can be expressed as follows:

$$\frac{\partial \ln(pO_2)}{\partial \ln(x_O)} = \frac{\partial pO_2}{\partial x}(3+x)^2 \cdot \frac{(2+x)}{(3+x)\cdot pO_2} \tag{6.10}$$

Thanks to the expression 6.10 we can finally express the oxigen chemical diffusion in the following way:

$$\tilde{D_O} = \frac{1}{2} D_O^* \cdot \frac{2+x}{pO_2} \cdot \frac{\partial pO_2}{\partial x} \tag{6.11}$$

Let's focus first on the oxygen partial pressure range in which oxygen interstitials predominate (*i.e.* at low oxygen partial pressures). At oxygen partial pressures above 10^{-17} atm and below roughly 10^{-13} atm, the electroneutrality equation is given by $[h°] \sim 2 \cdot [O_i'']$. Assuming $x \sim [O_i'']$, one may substitute these expressions for $[h°]$ and $[O_i'']$ into Equation 3.7, so that $pO_2 \propto x^6$; as a result:

$$\tilde{D_O} \propto D_O^* \cdot \frac{2+x}{x} \approx D_O^* \cdot \frac{2}{x} \tag{6.12}$$

In case of isolated defect predominance, oxygen self-diffusion is proprortional to $[O_i'']$ [68]. As a consequence of equation 6.12, at low pO_2 $\tilde{D_O}$ assume constant values. This result is in coherence with the first part of the curve represented in Figure 4.5.

We focus now our attention on the region above 10^{-13} atm (cluster predominance). In this case, deviation from stoichiometry is assumed proportional to the concentration of defect clusters ($x \sim [W']$), whose formation reaction constant is expressed by Equation 3.8. Simplifying assumptions outlined in section §3.3.2.1 yield $x \propto \left[W'\right] \propto \sqrt{pO_2}$ and finally:

$$\tilde{D_O} \propto D_O^* \cdot \frac{2+x}{x} \tag{6.13}$$

Equations 6.12 and 6.13 demonstrate that $\tilde{D_O}$ shows the same dependence upon D_O^* and x in both the domains. However, we can show that in cluster domain the quantity $D_O^* \cdot \frac{2+x}{x}$ is a decreasing function of x.

The results obtained by Contamin *et al.* [50] at 800°C for example show that oxygen self-diffusion is constant for deviations from stoichiometry higher than 0.1 (following [183], in this range of x there is predominance of clusters). From equation 6.13, increasing values of x and constant values of D_O^* lead $\tilde{D_O}$ to decrease. However, if all data points in [50] are considered, $\tilde{D_O}$ decreases by a factor of 5 also for lower values of x, comprised between 0.0055 and 0.164: our model links this deviation from stoichiometry range to cluster defect predominance too (see Figure 3.5). Our experimental data of $\tilde{D_O}$ taken at the highest values of pO_2 (see again Figure 4.5) show once again that $\tilde{D_O}$ decreases for increasing values of pO_2. We can therefore conclude that our results are in line with literature and that the overall dependence of $\tilde{D_O}$ with oxygen partial pressure appears to be consistent with the model developed in Chapter 3.

6.2.4 Comparison with literature of our diffusion coefficients

6.2.4.1 Oxygen self-diffusion

In the past (see Chapter 1 - Figure 1.15), oxygen self-diffusion coefficients were evaluated as a function of the oxide composition at much higher deviations from stoichiometry because the solid diffusion couple method [50] was used as opposed to the solid-gas isotopic exchange method in our case. This latter method restricts the deviation from stoichiometry value investigated because the maximum oxygen partial pressure is prescribed by the H_2O, O_2, H_2 equilibrium (see §2.2.2). Nonetheless, in order to compare literature results with ours, we determined the deviation from stoichiometry in our samples during the annealing based on our model analysis which provides an estimate of x. Our data together with the results published by Contamin *et al.* [50] and Marin and Contamin [128] are compared at 800°C and 890°C in Figure 6.14.

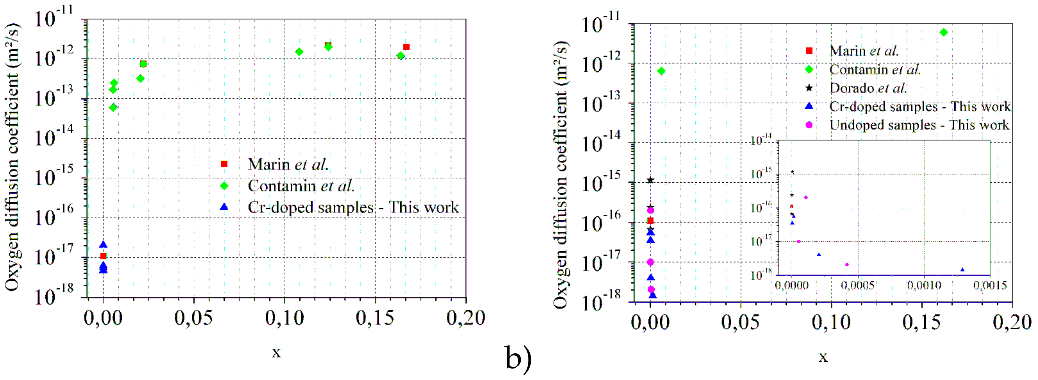

a) b)

Figure 6.14: Oxygen diffusion coefficient dependence upon UO_{2+x} composition: comparison between published results [50, 68, 128] and our data, collected at 800°C (graph a) and at 900°C (graph b).

As shown in both the graphs of Figure 6.14, the composition range we studied is more restricted than the one evaluated by previous authors [50, 128].

At 800°C, Figure 6.14a) demonstrates that our estimates of oxygen self-diffusion coefficients are comparable to existing data. This gives credit also to the interpretation given in §6.2.2 to our oxygen self-diffusion data collected at extremely low pO_2: they correspond to a nearly stoichiometric material. Figure 6.14b) shows clearly that while Dorado *et al.*'s [68] coefficients obtained at low oxygen partial pressures are comparable to the data of Marin and Contamin [50, 128], our self-diffusion data collected at 890°C are systematically lower than the published results of the past.

Also Figure 4.9 shows that all the oxygen self-diffusion estimates collected at high oxygen potentials are significantly lower than those previously published. This is inconsistent because, as our data were collected on the same sample set but at higher oxygen potentials than those studied by Dorado *et al.*, we expected our oxygen diffusion coefficients to be at least comparable, if not higher. These differences can be ascribed to the sample preparation procedure. First of all, in our study carried out at 890°C and 990°C, the high oxygen potentials imposed during annealing may have resulted in enriched water condensating in areas of the gas circuit. As a result samples may have been bulk-contaminated with ^{18}O during the first annealing stage aimed at equilibrating the samples. Consequently, the depth over which the concentration profile could actually be used to determine oxygen self-diffusion coefficients was reduced to the near surface region, which is most affected by the various initial sample polishing stages. Note that the samples examined in this high oxygen potential study and in [68] or the one described in section §6.2.2 are identical bar the last polishing stage, which was in previous work carried out using an OPU suspension with a 50 nm grain size. As a consequence, the second reason identified to explain the discrepancies observed for the study at high pO_2 is the surface roughness of the samples. Polishing the surface with a 1 μm grain instead of 50 nm may modify oxygen exchange between solid and gas phases and possibly even bulk diffusion properties.

6.2.4.2 Oxygen chemical diffusion

In this section we compare our chemical diffusion coefficient measurements to those published by Ruello [162]. This comparison may be seen in the Arrhenius graph reported in Figure 6.15.

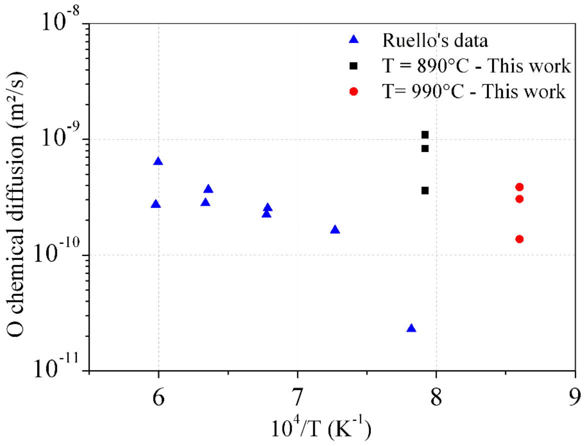

Figure 6.15: Arrhenius representation of estimated oxygen chemical diffusion coefficients: comparison with Ruello's data [162] estimated for a deviation from stoichiometry range between 0.005 and 0.01.

In Figure 6.15 we report only Ruello's data associated to the smallest deviation from stoichiometry range (between 0.005 – 0.01) he studied. The deviation from stoichiometry which corresponds to annealing conditions and samples may be estimated from our previous model analyses. Our annealing conditions correspond to low deviations from stoichiometry (the highest deviation from stoichiometry are in fact roughly equal to 0.001). We have plotted Ruello's data with ours because they correspond to the lowest composition range available in the literature.

As Ruello's data are measured on samples with greater deviation from stoichiometry than ours, his estimates of $\tilde{D}$ are expectedly lower. This fact is consistent with the fact that annealing at higher oxygen potential leads to an increase in deviation from stoichiometry and a decrease in the oxygen chemical diffusion coefficients. However, a more precise comparison of our data with Ruello's is difficult as he derived and reported only a range of composition for which he estimated $\tilde{D}$.

6.3 Conclusions

In this chapter we have tried to apply the point defect model described in Chapter 3 to analyse our oxygen tracer diffusion coefficients, chemical diffusion coefficients and electrical conductivity data reported in Chapter 4. We have also analysed electrical conductivity data of Gd-doped material previously reported [177].

The electrical conductivity data of gadolinium doped, chromium doped and low impurity content samples were first analysed with the model following the same methodology as in Chapter 3. The data relating to the Gd-doped material was consistent with the presence of oxygen clusters for which "the absolute charge to additional oxygen ion" ratio was lower than that determined in Chapter 3. The formation energy for this defect cluster was estimated at roughly -2.9 eV which is consistent with -2.2 eV determined for a di-interstitial, singly charged cluster. The analysis of electrical conductivity data relating to low impurity material, for which an intrinsic behaviour is observed, provides electron-hole, di-interstitial cluster and doubly ionised oxygen interstitial reaction constants in line with those determined in Chapter 3 on different sample sets. This preliminary study enabled us to determine a Brouwer diagram for the subsequent interpretation of self-diffusion and chemical diffusion coefficients.

Self-diffusion data collected on Cr-doped material at different temperatures and at the lowest possible oxygen potentials were analysed. Using the point defect model and applying it to those self-diffusion data available for which it is assumed that doubly ionised oxygen interstitials predominate, it is possible to estimate the oxygen interstitial diffusion coefficient and therefore the migration barrier for interstitial diffusion which is estimated at about 1.3 eV. This value compares relatively well with first principles estimates assuming an indirect interstitial mechanism [68]. The fact that interstitial diffusion coefficients for samples containing different types of impurities lie on roughly parallel lines suggests an influence of the doping agent, although further investigations would be required to conclude for certain. In particular, if the hole mobility were specific to a sample set then the defect concentrations, hence estimated defect diffusion coefficients, would be affected.

Oxygen diffusion measurements carried out at higher oxygen partial pressures and at roughly 900°C and 1000°C show that there is a threshold partial pressure above which the self-diffusion coefficient appears to decrease. We interpret this as resulting from the aggregation of oxygen interstitials into less mobile clusters. The threshold partial pressures are in reasonable agreement with the partial pressure values above which, according to the model, single oxygen interstitials cease to be the predominant defect species. These threshold partial pressures are also comparable with the oxygen partial pressures above which sample oxidation, as estimated from post-annealing XAS characterizations, is seen to increase monotonously.

Chemical diffusion experiments were also carried out at 900°C on low impurity content material. The substantial decrease in chemical diffusion coefficient above a threshold oxygen partial pressure is again very close to the partial pressure at which the model predicts that oxygen clusters become the predominant defect species.

Finally, all the results we obtained on oxygen self- and chemical diffusion were compared to literature data. Such analysis demonstrates that at 800°C our estimates of oxygen self-diffusion coefficients are comparable to existing data [50, 128]. Also our chemical diffusion coefficients estimates were consistent with published results [162]. Conversely, the oxygen self-diffusion estimates collected at high oxygen potentials are significantly lower than Dorado *et al.*'s [68] coefficients. We ascribed such difference to the sample preparation procedure: the high oxygen potentials imposed during the annealing resulted in enriched water condensating in the device and causes samples to be bulk-contaminated with ^{18}O. As a consequence, the concentration profile useful to determine oxygen self-diffusion coefficients was reduced to the near surface region, which is most affected by the initial sample polishing stages. Polishing the surface with a 1 µm grain (as done for our samples) instead of 50 nm (as done for Dorado *et al.*'s ones) may worsen oxygen exchange between solid and gas phases and even may affect bulk diffusion properties.

Conclusions and Prospects

In this work, we have strived to relate some macroscopic properties of UO_2 to point defect behaviour and characteristics by applying trusted methodologies set up originally in relation to transition metal oxides [64]. We have focused in particular upon measuring and analysing electrical and atomic transport properties of oxygen (self- and chemical diffusion). Prior to this work, although some experimental data regarding these properties were available, there had been no comprehensive effort to relate defect concentrations to them.

As detailed in Chapter 3, the starting point was to set up a charged oxygen and electronic defect model which was subsequently used to simultaneously analyse existing electrical conductivity and deviation from stoichiometry data. This simultaneous analysis enabled us to propose a reassessed value for the pre-exponential factor of the hole mobility, assuming an adiabatic hopping process, of 0.26 $m^2 \cdot K \cdot V^{-1} \cdot s^{-1}$, which is approximately five times greater than values previously reported. Our analyses as a function of oxygen partial pressure, at different temperatures, enabled us to estimate defect equilibrium constants with reasonable precision. Formation energies of -0.8 eV, -2.3 eV and 2.2 eV are suggested for doubly charged oxygen mono-interstitials, singly negatively charged oxygen di-interstitials and the electron-hole pair respectively. An important feature of this analysis is that at a given temperature, the dependence of electrical conductivity upon oxygen potential is consistent with a change in the predominant oxygen defect. Although the exact nature of these clusters is impossible to identify unequivocally based upon property measurements alone, it seems that their composition and charge do not follow a simple ionic model. So at relatively low oxygen partial pressures, oxygen clusters take over from single interstitials as the predominant oxygen defect species and the model we have derived enables us to estimate the value of deviation from stoichiometry at which this occurs. Our model enables us to estimate that the regime change occurs for deviation from stoichiometries of the order of 10^{-3}, *i.e.* below the accuracy usually available through thermogravimetric measurements. An important consequence is that any defect property derived from thermogravimetry probably relates to oxygen clusters.

As outlined in Chapter 6, the model applied equally well to electrical conductivity data acquired in this study (concerning low impurity content and Cr-doped sintered samples) and previous studies (Gd-doped sintered material and high impurity content single crystals). The data relating to the Gd-doped material however was consistent with the presence of oxygen clusters for which "the absolute charge to additional oxygen ion" ratio was lower than that determined for a material containing no or much fewer trivalent cations (as in Ruello [162]). The formation energy for this defect cluster was estimated at roughly -2.9 eV.

Two self-diffusion coefficient studies were carried out. The first was performed at relatively low oxygen partial pressures and at different temperatures between *circa* 750°C and 950°C; it concerned Cr-doped material only. The second was carried out at higher oxygen partial pressures and at *circa* 900°C and 1000°C for Cr-doped and low impurity content material. The oxygen potentials for this latter study were chosen so as to try to quantify the effect of radical changes in the defect populations upon self-diffusion.

Regarding the low oxygen partial pressure self-diffusion studies, an analysis was first carried out so as to identify the conditions (*i.e.* temperature and oxygen partial pressure) for which it was reasonable to assume that no oxygen clustering occurred and that oxygen diffusion was due mainly to interstitials. Using the defect concentrations calculated with the model, it was possible to estimate the oxygen interstitial diffusion coefficient. The analyses carried out of our self-diffusion coefficients and those reported in previous studies provide a consistent migration barrier for oxygen interstitial migration of roughly 1.3 eV (see Chapter 6, §6.2.2).

Self-diffusion coefficient measurements were also carried out at higher oxygen partial pressures at two temperatures (900°C and 1000°C) for Cr-doped material and low impurity content samples. The measurements showed that there is a threshold partial pressure above which the self-diffusion coefficient appears to decrease which was interpreted as the manifestation of the aggregation of oxygen interstitials into less mobile clusters. These threshold partial pressures are indeed in reasonable agreement with the partial pressure values above which, according to the model, single oxygen interstitials cease to be the predominant defect species. However, in comparison to data previously reported in the literature (notably Dorado *et al.* [68] and Marin and Contamin [128]), our self-diffusion coefficients appear to be rather low. It is possible that measurements were marred by the accumulation of ^{18}O enriched water which contaminated the samples during the equilibrium annealing stage of the diffusion experiment. This made it virtually impossible to quantitatively interpret ^{18}O concentration values beyond a micron from the sample surface. More experimental work is therefore necessary to clarify this point.

In order to identify possible effects upon the electronic structure of the material of different defect populations, XAS characterisations were carried out at the oxygen K-edge and uranium N edges ($N_{4,5}$ and $N_{6,7}$) of samples equilibrated under the same conditions as in the high oxygen potential self-diffusion study. The spectra obtained were interpreted from data relating to one UO_2 reference sample and two U_4O_9 and U_3O_7 samples obtained from controlled oxidation of uranium dioxide specimens. Hybridisation of the oxygen 2p and uranium 5f and 6d orbitals was demonstrated experimentally as was the change in Fermi energy resulting from the oxidation process. The loss of symmetry as the material changes from a cubic (UO_2, UO_{2+x}, U_4O_9) structure to tetragonal U_3O_7 is also manifest in the collected spectra. Indeed, the cubic symmetry of uranium oxide over the composition range extending from UO_2 to U_4O_9 produces a crystal field which lifts the degeneracies of the uranium 6d orbitals into e_g/t_{2g} levels that are no longer observed in the U_3O_7 spectra.

We have also seen from this study that the oxygen K-edge data of a uranium oxide sample with a composition intermediate between UO_2 and U_3O_7 may be expressed as a linear combination of UO_2 and U_3O_7 spectra. This important result is consistent with the fact that the long range structure of the material results from ordering of defects which have similar short range characteristics, as demonstrated from neutron diffraction studies [61]. This result to some extent justifies using a defect model that spans the whole composition range from UO_2 to U_4O_9. A detailed analysis of the spectra obtained from samples annealed under conditions identical to those corresponding to diffusion experiments shows that the level of oxidation does not increase monotonously with oxygen partial pressure. This unexpected result is interpreted as being due to the fact that the degree of surface oxidation of the sample exposed to air for some time following the annealing treatment, is the result of a combination of post-annealing surface reactivity and transport of oxygen in the bulk material.

Throughout this work we have endeavoured to compare, quantitatively when possible, results from first principles calculations and results from the analyses of our or previously reported experimental data. For instance, in Chapter 3 we saw that the electron hole pair, the doubly ionised mono-interstitial and the singly ionised di-interstitial formation energies determined from experiment were all within less than half an eV of the DFT+U values. In a similar way, the migration energy for the oxygen interstitial determined experimentally (1.3 eV) is reasonably close to the value determined from first principles assuming an interstitialcy mechanism (0.9 eV). From a qualitative standpoint also, we saw in Chapter 3 from deviation from stoichiometry data at low temperature and as stoichiometry rises, the signs of a defect more stable than a singly charge di-interstitial. The absolute charge per additional atom was lower than for the di-interstitial which is entirely consistent with the most recent theoretical studies of charged defect aggregates. Finally despite being a ground state theory and not taking into account core-hole effects, DFT was extremely useful in interpreting XAS spectra.

A number of studies should now be carried out in order to tackle some of the unresolved issues raised in this work. Firstly the effect of high oxygen partial pressures on self-diffusion should be further investigated so that the consistency with previously published data (notably Marin [128]) be definitively established. This probably requires improving the experimental methodology by for instance annealing the system out thoroughly between two diffusion experiments in addition to testing for the presence of undesired enriched water vapour in the gas phase. As regards electrical properties, we proposed in Chapter 3 a revised hole mobility. This should really be confirmed from Hall effect measurements which would provide an independent estimate of the charge carrier concentration and the sample conductivity whence mobility may be derived. This could possibly improve the consistency between interstitial diffusion coefficients derived from samples containing different impurity or doping levels.

Neutron diffraction provides a vision of oxidation of the material in which the long range ordering of cuboctahedra leads to the formation of U_4O_9. As oxidation proceeds still further U_3O_7 will form as a result of cuboctahedra moving still closer together. Since the absorption work carried out in our study shows that the UO_{2+x} spectra can be described as a linear combination of spectra relating to U_3O_7 and UO_2, one wonders whether these more complex oxygen clusters already exist in hyperstoichiometric UO_2 and to what extent this contradicts Willis's original assumptions. Answering this question requires carrying out specific in-situ neutron diffraction experiments on samples carefully equilibrated and would no doubt yield a detailed vision of the structure of UO_{2+x} for technologically relevant values of deviation from stoichiometry.

Regarding the defect model, it is expected that improvements could come from one of two efforts. The first would require setting up a specific theory that may be substituted to the one we have used which assumes infinite dilution. This could enable us to do away with the composition constraint which is build into the model at the moment in a somewhat arbitrary fashion. The second could involve describing uranium defects (vacancies and interstitials) which have been entirely neglected in this work. This actually is an indication that electronic and oxygen type defects are present in much greater concentrations. However, it is essential to build upon our approach by determining uranium self-diffusion coefficients which could lead to identifying diffusion mechanisms and associated defect concentrations.

Bibliography

[1] Internet: http://www.allaboutcircuits.com/vol_1/chpt_8/10.html.

[2] Internet: http://class.phys.psu.edu/p457/experiments/html/esr_long_2004_files/Lock-in-Amp.pdf.

[3] Internet: http://www.bentham.co.uk/pdf/F225.pdf.

[4] Internet: www.ing.unitn.it/ luttero/laboratoriomateriali/Rietveld.pdf.

[5] Internet: www.ccp14.ac.uk/ccp/web-mirrors/fullprof.

[6] Internet: www.lightsource.ca.

[7] Internet: http://www.stilsa.com.

[8] Internet: http://bruceravel.github.com/demeter/.

[9] Internet: JP-minerals.org/vesta/en.

[10] Internet: http://henke.lbl.gov/optical_constants/.

[11] Internet: http://www.srim.org/.

[12] Internet: http://www.cactus2000.de/uk/unit/masshum.shtml.

[13] *IMS 6F/IMS 1270 CAMECA User's Guide*.

[14] G. Allen and N. R. Holmes, *A mechanism for the UO_2 to α-U_3O_8 phase transformation*, J. Nucl. Mater., 223 (1995), pp. 231 – 237.

[15] G. Allen, P. Tempest, and J. W. Tyler, *Coordination model for the defect structure of UO_{2+x} and U_4O_9*, Nature, 295 (2010), pp. 48 – 49.

[16] S. Allen, *Spin-lattice interaction in UO_2 II. Theory of the first-order phase transition*, Phys. Rev., 167 (1968), pp. 492 – 496.

[17] D. A. Andersson, F. J. Espinosa-Faller, B. P. Uberuaga, and S. D. Conradson, *Stability and migration of large oxygen clusters in UO_{2+x}: Density functional theory calculations*, J. Chem. Phys., 136 (2012), p. 234702.

[18] D. A. ANDERSSON, B. P. UBERUAGA, P. V. NERIKAR, C. UNAL, AND C. R. STANEK, *U and Xe transport in UO_{2+x}: Density functional theory calculations*, Phys. Rev. B, 84 (2011), p. 054105.

[19] D. A. ANDERSSON, T. WATANABE, C. DEO, AND B. P. UBERUAGA, *Role of di-interstitial clusters in oxygen transport in UO_{2+x} from first-principles*, Phys. Rev. B, 80 (2009), p. 060101(R).

[20] V. I. ANISIMOV, J. ZAANEN, AND O. K. ANDERSEN, *Band theory and Mott insulators : Hubbard U instead of Stoner I*, Phys. Rev. B, 44 (1991), pp. 943 – 954.

[21] A. APELBLAT, *Vapour pressures of $H^{16}O$ and $H^{18}O$, and 2 2 saturated aqueous solutions of KCl from T_S=298k to T_S=318k by the isoteniscopic method*, J. Chem. Thermodynamics, 30 (1998), pp. 1191 – 1198.

[22] S. ARONSON AND J. BELLE, *Nonstoichiometry in uranium dioxide*, J. Chem. Phys., 29 (1958), pp. 151 – 158.

[23] S. ARONSON, R. B. ROOF, AND J. BELLE, *Kinetics study of the oxydation of uranium dioxide*, J. Chem. Phys., 27 (1957), pp. 137 – 144.

[24] M. AUCOUTURIER, G. BLAISE, AND E. DARQUE-CERETTI, *Microcaractérisation des solides*, M. Ammou, CRAM, 1989.

[25] A. B. AUSKERN AND J. BELLE, *Oxygen ion self-diffusion in uranium dioxide*, J. Nucl. Mater., 3 (1961), pp. 267 – 276.

[26] Y. BAER AND J. SCHOENES, *Electronic structure and Coulomb correlation energy in UO_2 single crystal*, Solid State Commun., 33 (1980), pp. 885 – 888.

[27] M. BAICHI, C. CHATILLON, G. DUCROSA, AND K. FROMENT, *Thermodynamics of the O-U system. IV - Critical assessment of chemical potentials in the U-$UO_{2.01}$ composition range*, J. Nucl. Mater., 359 (2006), pp. 17 – 56.

[28] M. W. BARSOUM, *Foundamental of Ceramics*, IoP, 2003.

[29] J. L. BATES, C. A. HINMAN, AND T. KAWADA, *Electrical conductivity of uranium dioxide*, J. Am. Ceram. Soc., 50 (1967), pp. 652 – 656.

[30] J. BELLE, *Oxygen and uranium diffusion in uranium dioxide (a review)*, J. Nucl. Mater., 30 (1969), pp. 3 – 15.

[31] C. BERTHINIER AND F. H. C. RADO, C. CHATILLON, *Thermodynamic assessment of oxygen diffusion in non-stoichiometric $UO_{2\pm x}$ from experimental data and Frenkel pair modeling*, J. Nucl. Mater., 433 (2013), pp. 265 – 286.

[32] D. J. M. Bevan, I. E. Grey, and B. T. M. Willis, *The crystal structure of β-U_4O_9*, J. Solid State Chem., 61 (1986), pp. 1 – 7.

[33] P. E. Blackburn, *Oxygen dissociation pressures over uranium oxides*, J. Phys. Chem., 62 (1958), pp. 897 – 902.

[34] P. E. Blackburn, J. Weissbart, and E. A. Gulbransen, *Oxidation of uranium dioxide*, J. Phys. Chem., 62 (1958), pp. 902 – 908.

[35] P. E. Blöchl, *Projector augmented-wave method*, Phys. Rev. B, 50 (1994), pp. 17954 – 17979.

[36] A. H. Booth, *A method of calculating fission gas diffusion from UO_2 fuel and its application to the X-2-f loop test*, Report AECL CRDC-721, 1957.

[37] G. Boureau, C. Giaconia, and R. Tétot, *Defect modelling in non-stoichiometric oxides*, Solid State Ionics, 101 - 103 (1997), pp. 397 – 401.

[38] G. Brillant, F. Gupta, and A. Pasturel, *Fission products stability in uranium dioxide*, J. Nucl. Mater., 412 (2011), pp. 170 – 176.

[39] G. Busker, R. Grimes, and M. Bradford, *The diffusion of iodine and caesium in the $UO_{2\pm x}$ lattice*, J. Nucl. Mater., 279 (2000), pp. 46 – 50.

[40] D. Cabaret, F. Mauri, and G. S. Henderson, *Oxygen K-edge XANES of germanates investigated using first-principles calculations*, Phys. Rev. B, 75 (2007), p. 184205.

[41] A. Caneiro, N. Bonnat, and J. Fouletier, *Measurement and regulation of oxygen content in selected gases using solid electrolyte cells. IV. Accurate preparation of CO_2-CO and H_2O-H_2 mixtures*, J. Appl. Electrochem., 11 (1981), pp. 83 – 90.

[42] G. Carlot and P. Garcia, *Etude bibliographique et proposition d'expériences relatives à la diffusion thermique de xénon et du krypton dans le dioxyde d'uranium - Premiers résultats de caractérisation*, Note Tecnique CEA-SESC/LLCC 03-010 (2003).

[43] J. M. Casado, J. H. Herding, and G. J. Hyland, *Small-polaron hopping in mott-insulating UO_2*, J. Phys.: Condens. Matter, 6 (1994), pp. 4685 – 4698.

[44] Y. Chen, H. Y. Geng, Y. Kaneta, M. Kinoshita, and S. Iwata, *First principles modelling of stability mechanism of nonstoichiometric uranium dioxide*, Comput. Mater. Sci., 49 (2010), pp. S364 – S368.

[45] P. Y. CHEVALIER, E. FICHER, AND B. CHEYNET, *Progress in the thermodynamic modelling of the O-U binary system*, J. Nucl. Mater., 303 (2002), pp. 1 – 28.

[46] K. CLAUSEN, W. HAYES, R. O. J. E. MACDONALD, AND M. T. HUTCHINGS, *Observation of oxygen frekel pair disorder in uranium dioxide above 2000 K by use of neutron-scattering techniques*, Phys. Rev. Lett., 52 (1984), pp. 1238 – 1241.

[47] K. COMPAAN AND Y. HAVEN, *Correlation factors for diffusion in solids. Part 2 - Indirect interstitial mechanism*, Trans. Faraday Soc., 43 (1958), pp. 1498 – 1508.

[48] S. D. CONRADSON, B. D. BEGG, D. L. CLARK, M. D. C. DEN AUWER, P. K. DORHOUT, F. J. ESPINOSA-FALLER, R. G. H. P. L. GORDON, N. J. HESS, R. F. HESS, D. W. KEOGH, G. H. LANDER, D. MANARA, L. A. MORALES, M. P. NEU, P. PAVIET-HARTMANN, J. REBIZANT, V. V. RONDINELLA, W. RUNDE, C. D. TAIT, D. K. VEIRS, P. M. VILLELLA, AND F. WASTIN, *Charge distribution and local structure and speciation in the UO_{2+x} and PuO_{2+x} binary oxides for $x<0.25$*, J. Solid State Chem., 178 (2005), pp. 521 – 535.

[49] S. D. CONRADSON, D. MANARA, F. WASTIN, D. L. CLARK, G. H. LANDER, L. A. MORALES, J. REBIZANT, AND V. V. RONDINELLA, *Local structure and charge distribution in the UO_2-U_4O_9 system*, Inorg. Chem., 43 (2004), pp. 6922 – 6935.

[50] P. CONTAMIN, J. BACMANN, AND J. F. MARIN, *Autodiffusion de l'oxygène dans le dioxide d'uranium surstœchiométrique*, J. Nucl. Mater., 42 (1972), pp. 54 – 64.

[51] R. I. COOPER AND B. T. M. WILLIS, *Refinement of the structure of β-U_4O_9*, Acta Crystallogr., Sect. A: Found. Crystallogr., 60 (2004), pp. 322 – 325.

[52] B. COX, *Pellet-Clad interaction (PCI) failures of zirconium alloy fuel cladding - A review*, J. Nucl. Mater., 172 (1990), pp. 249 – 292.

[53] J.-P. CROCOMBETTE, *Ab-initio energetics of some fission products (Kr, I, Cs, Sr and He) in uranium dioxide*, J. Nucl. Mater., 305 (2002), pp. 29 – 36.

[54] ——, *First-principles study with charge effects of the incorporation of iodine in UO_2*, J. Nucl. Mater., 429 (2012), pp. 70 – 77.

[55] ——, *Influence of charge states on energies of point defects and clusters in uranium dioxide*, Phys. Rev. B, 85 (2012), p. 144101.

[56] J.-P. CROCOMBETTE, F. JOLLET, L. T. NGA, AND T. PETIT, *Plane-wave pseudopotential study of point defects in uranium dioxide*, Phys. Rev. B, 64 (2001), p. 104107.

[57] J.-P. CROCOMBETTE, D. TORUMBA, AND A. CHARTIER, *Charge states of point defects in uranium oxide calculated with hybrid functional for correlated electrons*, Phys. Rev. B, 83 (2011), p. 184107.

[58] E. DARQUE-CERETTI, H.-N. MIGEON, AND M. AUCOUTURIER, *Emission ionique secondaire SIMS - Principes et appareillages*, Ed. Techniques Ingénieur, 1998.

[59] ——, *Emission ionique secondaire SIMS - Procédures d'analyse*, Ed. Techniques Ingénieur, 1998.

[60] P. DEBYE AND E. HÜCKEL, *Zur theorie der elektrolite. I. Gefrierpunktserniedrigung und verwandte erscheinungen*, Phsikalische Zeitschrift, 24 (1923), pp. 185 – 206.

[61] L. DESGRANGES, G. BALDINOZZI, G. ROUSSEAU, J.-C. NIÈPCE, AND G. CALVARIN, *Neutron diffraction study of the in situ oxidation of UO_2*, Inorg. Chem., 48 (2009), pp. 7585 – 7592.

[62] L. DESGRANGES, G. BALDINOZZI, D. SIMÉONE, AND H. E. FISCHER, *Refinement of the α-U_4O_9 crystalline structure: new insight into the $U_4O_9 \rightarrow U_3O_8$ transformation*, Inorg. Chem., 50 (2011), pp. 6146 – 6151.

[63] L. DESGRANGES, H. PALANCHER, M. GAMALÉRI, J. MICHA, V. OPTASANU, L. RACEANU, T. MONTESIN, AND N. CRETON, *Influence of the U_3O_7 domain structure on cracking during the oxidation of UO_2*, J. Nucl. Mater., 402 (2010), pp. 167 – 172.

[64] R. DIECKMANN, *Point defects and transport properties of binary and ternary oxides*, Solid State Ionics, 12 (1984), pp. 1 – 22.

[65] B. DORADO, *Etude des propriétés de transport atomique dans le dioxyde d'uranium par le calcul de structure electronique : influence des fortes corrélations*, PhD thesis, Université de Marseille, 2010.

[66] B. DORADO, D. A. ANDERSSON, C. R. STANEK, B. P. UBERUAGA, G. MARTIN, M. BERTOLUS, M. FREYSS, AND P. GARCIA, *First-principles calculations of uranium diffusion in uranium dioxide.* 2012.

[67] B. DORADO, M. FREYSS, AND G. MARTIN, *GGA+U study of the incorporation of iodine in uranium dioxide*, Eur. Phys. J. B, 69 (2009), pp. 203 – 209.

[68] B. Dorado, P. Garcia, G. Carlot, C. Davoisne, M. Fraczkiewicz, B. Pasquet, M. Freyss, C. Valot, G. Baldinozzi, D. Siméone, and M. Bertolus, *First-principles calculation and experimental study of oxygen diffusion in uranium dioxide*, Phys. Rev. B, 83 (2011), p. 035126.

[69] B. Dorado, G. Jomard, M. Freyss, and M. Bertolus, *Stability of oxygen point defects in* UO_2 *by first-principles DFT+U calculations: Occupation matrix control and Jahn-Teller distortion*, Phys. Rev. B, 82 (2010), p. 035114.

[70] N. J. Dudney, R. L. Coble, and H. L. Tuller, *Electrical conductivity of pure and yttria-doped uranium dioxide*, J. of Am. Ceram. Soc., 64 (1981), pp. 627 – 631.

[71] K. L. Duncan, Y. Wang, S. R. Bishop, F. Ebrahimi, and E. D. Wachsman, *Role of point defects in the physical properties of fluorite oxides*, J. Am. Ceram. Soc., 89 (2006), pp. 3162 – 3166.

[72] J. Faber and G. H. Lander, *Neutron-diffraction study of* UO_2*: antiferromagnetic state*, Phys. Rev. B, 14 (1976), pp. 1151 – 1164.

[73] M. Fraczkiewicz, *Dopage au chrome du dioxide d'uranium : modifications physiques induites*, PhD thesis, Université de Grenoble, 2009.

[74] M. Freyss, T. Petit, and J.-P. Crocombette, *Point defects in uranium dioxide: Ab initio pseudopotential approach in the generalized gradient approximation*, J. Nucl. Mater., 347 (2005), pp. 44 – 51.

[75] M. Freyss, N. Vergnet, and T. Petit, *Ab initio modeling of the behavior of helium and xenon in actinide dioxide nuclear fuels*, J. Nucl. Mater., 352 (2006), pp. 144 – 150.

[76] C. A. Friskney and J. A. Turnbull, *The characterization of fission gas release from uranium dioxide during irradiation*, J. Nucl. Mater., 79 (1979), pp. 184 – 198.

[77] P. Garcia, *Etude de la mobilité thermique et sous irradiation de l'iode dans le dioxyde d'uranium*, Note Technique SESC/LLCC 06-018 (2007).

[78] P. Garcia, M. Fraczkiewicz, C. Davoisne, G. Carlot, B. Pasquet, G. Baldinozzi, D. Siméone, and C. Petot, *Oxygen diffusion in relation to p-type doping in uranium dioxide*, J. Nucl. Mater., 400 (2010), pp. 112 – 118.

[79] F. GARRIDO, L. NOWICKI, AND L. THOMÉ, *Channeling investigation of the crystalline structure of* $U_4O_{9\text{-}y}$, Phys. Rev. B, 74 (2006), p. 184114.

[80] H. Y. GENG, Y. CHEN, Y. KANETA, M. IWASAWA, T. OHNUMA, AND M. KINOSHITA, *Point defects and clustering in uranium dioxide by LSDA+U calculations*, Phys. Rev. B, 77 (2008), p. 104120.

[81] H. Y. GENG, Y. CHEN, Y. KANETA, AND M. KINOSHITA, *Ab-initio investigation on oxygen defect clusters in* $U0_{2+x}$, Appl. Phys. Lett., 93 (2008), p. 201903.

[82] P. GERDANIAN AND M. DODÉ, *Etude thérmodynamique des oxides* $UO_{2\pm\,x}$, J. Chim. Phys. Phys. Chim. Biol., 62 (1965), pp. 171 – 184.

[83] R. W. GRIMES, R. G. J. BALL, AND C. R. A. CATLOW, *Site preference and binding of iodine and caesium in uranium dioxide*, J. Phys. Chem. Solids, 53 (1992), pp. 475 – 484.

[84] R. W. GRIMES AND C. R. A. CATLOW, *The stability of fission products in uranium dioxide*, Phil. Trans. R. Soc. London, Ser. A, 335 (1991), pp. 609 – 634.

[85] F. GRØNVOLD, *High-temperature x-ray study of uranium oxides in the* UO_2 *-* U_3O_8 *region*, J. Inorg. Nucl. Chem., 1 (1955), pp. 357 – 370.

[86] F. M. F. D. GROOT, M. GRIONI, J. C. FUGGLE, J. GHIJSEN, G. SAWATZKY, AND H. PETERSEN, *Oxygen 1s X-ray absorption edges of transition metal oxides*, Phys. Rev. B, 40 (1989), pp. 5715 – 5723.

[87] A. GUINIER, *Théorie et Technique de la Radiocrystallographie*, Dunod, Paris, 1964.

[88] C. GUÉNAU, M. BAICHI, D. LABROCHE, C. CHATILLON, AND B. SUNDMAN, *Thermodynamic assessment of the uranium-oxygen system*, J. Nucl. Mater., 304 (2002), pp. 161 – 175.

[89] F. GUPTA, G. BRILLANT, AND A. PASTUREL, *Correlation effects and energetics of point defects in uranium dioxide : a first principle investigation*, Philos. Mag., 87 (2007), pp. 2561 – 2569.

[90] Z. HADARI, M. KROUPP, AND Y. WOLFSON, *Self-diffusion measurements of oxygen in* UO_{2+x} *by the nuclear reaction* $^{18}0(p,\gamma)^{19}F$, J. Appl. Phys., 42 (1971).

[91] K. HAGEMARK AND M. BROLI, *Equilibrium oxygen pressures over the nonstoichiometric uranium oxides* UO_{2+x} *and* $U_3O_{8\text{-}z}$ *at higher temperatures*, J. Inorg. Nucl. Chem., 28 (1966), pp. 2837 – 2850.

[92] J. D. HIGGS, W. T. THOMPSON, B. J. LEWIS, AND S. C. VOGEL, *Kinetics of precipitation of* U_4O_9 *from hyperstoichiometric* $U0_{2+x}$, J. Nucl. Mater., 366 (2007), pp. 297 – 305.

[93] W. H. HOCKING, R. A. VERRAL, AND I. J. MUIR, *Migration behaviour of iodine in nuclear fuel*, J. Nucl. Mater., 294 (2001), pp. 45 – 52.

[94] H. HOEKSTRA, S. SIEGEL, AND P. CHARPIN, *The synthesis of* $UO_{2.37}$ *at high pressure*, J. Inorg. Nucl. Chem., 30 (1968), pp. 519 – 523.

[95] H. R. HOEKSTRA, A. SANTORO, AND S. SIEGEL, *The low temperature oxidation of* UO_2 *and* U_4O_9, J. Inorg. Nucl. Chem., 18 (1961), pp. 166 – 178.

[96] P. HOHENBERG AND W. KOHN, *Inhomogeneous electron gas*, Phys. Rev., 136 (1964), pp. B864 – B871.

[97] J. M. HUBERTY, N. T. KITA, R. KOZDON, P. R. HECK, J. H. FOURNELLE, M. J. SPICUZZA, H. XU, AND J. W. VALLEY, *Crystal orientation effects in* $\delta^{18}O$ *for magnetite and hematite by SIMS*, Chemical Geol., 276 (2010), pp. 269 – 283.

[98] Y. IWANO, *A defect structure study of nonstoichiometric uranium dioxide by statistical-mechanical models*, J. Nucl. Mater., 209 (1994), pp. 79 – 91.

[99] M. IWASAWA, Y. CHEN, Y. KANETA, T. OHNUMA, H.-Y. GENG, AND M. KINOSHITA, *First-principles calculations of point defects in uranium dioxide*, Mater. Trans., 47 (2006), pp. 2651 – 2657.

[100] J.A.AGUIAR, N. GRÖNBECH-JENSEN, A. PERLOV, V. MILMAN, S. P. GAO, C. J. PICKARD, AND N. D. BROWNING, *Electronic structure of oxide fuels from experiment and first principles calculations*, J. Phys.: Conf. Ser., 241 (2010), p. 012062.

[101] N. A. JAVED, *Thermodynamic study of hypostoichiometric urania*, J. Nucl. Mater., 46 (1972), pp. 219 – 224.

[102] L. JOHNSON, C. FERRY, C. POINSSOT, AND P. LOVERA, *Spent fuel radionuclide source-term model for assessing spent fuel performance in geological disposal. Part I: Assessment of the instant release fraction*, J. Nucl. Mater., 346 (2005), pp. 56 – 65.

[103] F. Jollet, P. Petit, S. Gota, N. Thromat, M. Gautier-Soyer, and A. Pasturel, *The electronic structure of uranium dioxide: an oxygen K-edge X-ray absorption study*, J. Phys.: Condens. Matter, 9 (1997), pp. 9393 – 9401.

[104] W. Jost and E. M. Loebl, *Diffusion in solid, liquids, gases*, Accademic Press Inc. Publishers, 3 ed., 1960.

[105] W. Kang, J. Park, Y. Kim, and S. Hong, *A thermodynamic evaluation of the U-O system from UO_2 to U_3O_8*, W. Interscience, (1972).

[106] M. Kato, K. Konashi, and N. Nakae, *Analysis of oxygen potential of $(U_{0.7}Pu_{0.3})O_{2\pm x}$ and $(U_{0.8}Pu_{0.2})O_{2\pm x}$*, J. Nucl. Mater., 389 (2009), pp. 164 – 169.

[107] M. Kato, K. Morimoto, T. Tamura, T. Sunaoshi, K. Konashi, S. Aono, and M. Kashimura, *Oxygen chemical diffusion in hypo-stoichiometric MOX*, J. Nucl. Mater., 389 (2009), pp. 416 – 419.

[108] W. Khon and L. J. Sham, *Self-consistent equations including exchange and correlation effects*, Phys. Rev., 140 (1965), pp. A1133 – A1138.

[109] K. C. Kim and D. R. Olander, *Oxygen diffusion in UO_{2-x}*, J. Nucl. Mater., 102 (1981), pp. 192 – 199.

[110] K. Kiukkola, *High-temperature electrochemical study of uranium oxides in the UO_2-U_3O_8 region*, Acta Chem. Scand., 16 (1962), pp. 327 – 345.

[111] P. Kofstad, *Nonstoichiometry, Diffusion, and Electrical Conductivity in Binary Oxides*, Accademic Press Inc. Publishers, 3 ed., 1960.

[112] A. Kotani and H. Ogasawara, *Theory of the core-level spectroscopy in actinide systems*, Physica B, 186-188 (1993), pp. 16 – 20.

[113] F. A. Kröger, *The chemistry of imperfect crystals*, North Holland publishing Company, Amsterdam, 1964.

[114] ——, *Search for a defect model for UO_2*, Zeitschrift für Physikalische Chemie Neue Folge, 49 (1966), pp. 178 – 197.

[115] ——, *The role of imperfection chemistry in the characterization of materials*, Mater. Res. Bull., 2 (1967), pp. 203 – 216.

[116] O. Kubaschewski and C. B. Alcock, *Metallurgical Thermochemistry*, Pergamon Press, 1967.

[117] K. Kvashnina, *High energy resolution X-ray spectroscopy of lanthanide and actinide systems*, ACTINET Workshop, Avignon (F), 2010.

[118] D. LABROCHE, O. DUGNE, AND C. CHATILLON, *Thermodynamics of the O-U system. I - Oxygen chemical potential critical assessment in the* UO_2*-*U_3O_8 *composition range*, J. Nucl. Mater., 312 (2003), pp. 21 – 49.

[119] G. H. LANDER, J. FABER, A. J. FREEMAN, AND J. P. DESCLAUX, *Neutron-diffraction study of* UO_2*: paramgnetic state*, Phys. Rev. B, 13 (1976), pp. 1177 – 1182.

[120] G. T. LAWRENCE, *A review of the diffusion coefficient of fission-product rare gases in uranium dioxide*, J. Nucl. Mater., 71 (1978), pp. 195 – 218.

[121] A. B. LIDIARD, *Self-diffusion of uranium in* UO_2, J. Nucl. Mater., 19 (1966), pp. 106 – 108.

[122] A. I. LIECHTENSTEIN AND M. I. KATSNELSON, *Ab-initio calculations of quasi-particle bond structure in correlated systems: LDA++ approach*, Phys. Rev. B, 57 (1998), pp. 6884 – 6895.

[123] W. V. LIERDE AND L. D. JONGHE, *The controlled oxidation of single crystals of* UO_2 *to* U_4O_9, Solid State Commun., 2 (1964), pp. 129 – 131.

[124] W. V. LIERDE, J. PELSMAEKERS, AND A. LECOCQ-ROBERT, *On the phase limits of* U_4O_9, J. Nucl. Mater., 37 (1870), pp. 276 – 285.

[125] T. B. LINDEMER AND T. M. BESMANN, *Chemical thermodynamic representation of* $UO_{2\pm x}$, J. Nucl. Mater., 130 (1985), pp. 473 – 488.

[126] S. LING, *High-concentration point-defect chemistry: statistical-thermodynamic approach applied to nonstoichiometric cerium dioxides*, Phys. Rev. B, 49 (1994), pp. 864 – 880.

[127] B. O. LOOPSTRA, *The structure of* β*-*U_3O_8, Acta Crystallogr., Sect. B: Struct. Sci., 26 (1970), pp. 656 – 657.

[128] J. F. MARIN AND P. CONTAMIN, *Uranium and oxygen self-diffusion in* UO_2, J. Nucl. Mater., 30 (1969), pp. 16 – 25.

[129] T. MARKIN AND R. BONES, *The determination of changes in free energies for uranium oxides using a high temperature galvanic cell*, AERE-Report R-4042, 1962.

[130] ——, *The determination of some thermodynamic properties of uranium oxides with O/U ratios between 2.00 and 2.03 using a high temperature galvanic cell*, AERE-Report R-4178, 1962.

[131] P. MARTIN, M. RIPERT, G. CARLOT, P. PARENT, AND C. LAFFON, *A study of molybdenum behaviour in* UO_2 *by X-ray absorption spectroscopy*, J. Nucl. Mater., 326 (2004), pp. 132 – 143.

[132] P. MARTIN, C. SABATHIER-DEVALS, M. FRACZKIEWICZ, AND G. CARLOT, *Comparaison de l'état chimique du chrome par spectroscopie d'absorption X dans les combustibles industriels* UO_2 *dopés chrome CONCERTO et AFA3GLAA*, Note technique SESC/LLCC 09-003 (2009).

[133] N. MASAKI AND T. ISHII, *The preparation of* U_4O_9 *single crystal*, J. Cryst. Growth, 6 (1970), pp. 207 – 209.

[134] P. MATHERON AND L. SILVESTRE, *Fabrication d'échantillons d'*UO_2 *dopés chrome destines à la validation du modèle thermodynamique de solubilité de Cr dans l'*UO_2, Note Technique SPUA/LCU 08-003 (2008).

[135] H. MATZKE, *Atomic transport properties in* UO_2 *and mixed oxides* $(U,Pu)O_2$, J. Chem. Soc. Faraday Trans. 2, 83 (1987), pp. 1121 – 1142.

[136] S. MAZEVET, M. TORRENT, V. RECOULES, AND F. JOLLET, *Calculations of the transport properties within the PAW formalism*, High Energy Density Phys., 6 (2010), pp. 84 – 88.

[137] R. J. MCEACHERN, *A review kinetic data on the rate of* U_3O_7 *formation on* UO_2, J. Nucl. Mater., 245 (1997), pp. 238 – 247.

[138] R. J. MCEACHERN AND P. TAYLOR, *A review of the oxidation of uranium dioxide at temperatures below 400°C*, J. Nucl. Mater., 254 (1998), pp. 87 – 121.

[139] S. K. MITRA AND A. R. ALLNAT, *The configurational entropy of defect complexes in* UO_{2+x}, J. Phys. C: Solid State Phys., 12 (1979), pp. 2261 – 2275.

[140] A. MODIN, Y. YUN, M. T. SUZUKI, J. VEGELIUS, L. WERME, D. P. M. O. J. NORDGREN A, AND S. M. BUTORIN, *Indication of single-crystal* PuO_2 *oxidation from O 1-s x-ray absorption spectra*, Phys. Rev. B, 83 (2011), p. 075113.

[141] G. E. MURCH, D. H. BRADHURST, AND H. J. DE BRUIN, *Oxygen self-diffusion in non-stoichiometric uranium dioxide*, Philos. Mag., 32 (1975), pp. 1141 – 1150.

[142] G. E. MURCH, C. RICHARD, AND A. CATLOW, *Oxygen diffusion in* UO_2, ThO_2 *and* PuO_2, J. Chem. Soc., Faraday Trans. 2, 83 (1987), pp. 1157 – 1169.

[143] G. M. MURCH AND R. THORN, *The mechanism of oxygen diffusion in near stoichiometric uranium dioxide*, J. Nucl. Mater., 71 (1978), pp. 219 – 226.

[144] P. NAGELS, J. DEVREESE, AND M. DENAYER, *Electrical conduction in single crystals of uranium dioxide*, J. Appl. Phys., 35 (1964), pp. 1175 – 1180.

[145] A. NAKAMURA AND T. FUJINO, *Thermodynamic analysis on point defects of* UO_{2+x} *at relatively small deviation from stoichiometry between 600 and 1400°C*, J. Nucl. Mater., 140 (1986), pp. 113 – 130.

[146] ——, *Thermodynamic model of* UO_{2+x}, J. Nucl. Mater., 167 (1989), pp. 36 – 46.

[147] M. NEWVILLE, *Fundamentals of XAFS*, Revision 1.6. (2004), Univ. of Chicago.

[148] P. OCHIN, C. PETOT, AND G. PETOT-ERVAS, *Thermodynamic study of point defects in* $Cu_{2\text{-}\delta}O$*. Electrical conductivity measuments at low oxygen partial pressures*, Solid State Ionics, 12 (1984), pp. 135 – 143.

[149] K. PARK AND D. R. OLANDER, *A defect model for the oxygen potential of urania*, High Temp. Sci., 29 (1990), pp. 203 – 222.

[150] W. PARRISH AND J. LANGFORD, *Powder and related techniques: X-ray techniques, International Tables of Crystallography - Volume C*, edited by A. J. C. Wilson, Kluwer Accademic Publishers, 1992, p. 517.

[151] P. O. PERRON, *Thermodynamics of non-stoichiometric uranium dioxide*, Report AECL-3072, 1968.

[152] G. PETOT-ERVAS AND C. PETOT, *Experimental procedure for the determination of diffusion coefficients in ionic compounds - Application to yttrium-doped zirconia*, Solid State Ionics, 117 (1999), pp. 27 – 39.

[153] J. PHILIBERT, *Atom movements: Diffusion and Mass transport in solids*, Editions de Physique, Les Ulis, France, 1991.

[154] E. PIZZI, P. GARCIA, G. CARLOT, H. PALANCHER, S. MAILLARD, B. PASQUET, I. ROURE, C. POZO, AND C. MAURICE, *Iodine volume diffusion measurements in uranium dioxide*, Def. Diff. Forum, 323 - 325 (2012), pp. 197 – 202.

[155] S. PORTIER, S. BRÉMIER, AND C. WALKER, *Secondary ion mass spectrometry of irradiated nuclear fuel and cladding: An overview*, Int. J. Mass Spectrom., 263 (2007), pp. 113 – 126.

[156] A. POULESQUEN, L. DESGRANGES, AND C. FERRY, *An improved model to evaluate the oxidation kinetics of uranium dioxide during dry storage*, J. Nucl. Mater., 362 (2007), pp. 402 – 410.

[157] S. G. PRUSSIN, D. R. OLANDER, W. K. LAU, AND L. HANSSON, *Release of fission products (Xe, I, Te, Cs, Mo and Tc) from polycrystalline* UO_2, J. Nucl. Mater., 154 (1988), pp. 25 – 37.

[158] L. QUÉMARD, L. DESGRANGES, V. BOUINEAU, M. PIJOLAT, G. BALDINOZZI, N. MILLOT, J. C. NIÈPCE, AND A. POULESQUEN, *On the origin of the sigmoid shape in the* UO_2 *oxidation weight gain curves*, J. Eur. Ceram. Soc., 29 (2009), pp. 2791 – 2798.

[159] C. RIGLET-MARTIAL, *Proposition d'un modèle thermodynamique de solubilité du chrome dans le dioxyde d'uranium*, Note technique SESC/LLCC 06-010 (2006).

[160] L. ROBERTS AND A. WALTER, *Equilibrium pressures and phase relationsin the uranium oxide system*, J. Inorg. Nucl. Chem., 22 (1961), pp. 213 – 229.

[161] G. ROUSSEAU, L. DESGRANGES, F. CHARLOT, N. MILLOT, J. C. NIÈPCE, M. PIJOLAT, F. VALDIVIESO, G. BALDINOZZI, AND J. F. BÉRAR, *A detailed study of* UO_2 *to* U_3O_8 *oxidation phases and the associated rate-limiting steps*, J. Nucl. Mater., 355 (2006), pp. 10 – 20.

[162] P. RUELLO, *Etude du changement de comportement du dioxide d'uranium au voisinage de 1300 K : propriétés électriques, optiques et structurales*, PhD thesis, Ecole Centrale Paris, 2001.

[163] P. RUELLO, K. D. BECKER, K. ULLRICH, L. DESGRANGES, C. PETOT, AND G. PETOT-ERVAS, *Thermal variation of the optical absorption of* UO_2*: determination of the small polaron self-energy*, J. Nucl. Mater., 328 (2004), pp. 46 – 54.

[164] P. RUELLO, G. PETOT-ERVAS, AND C. PETOT, *Electrical conductivity and thermoelectric power of uranium dioxide*, J. Am. Ceram. Soc., 88 (2005), pp. 604 – 611.

[165] M. SAIDY, W. H. HOCKING, J. F. MOURIS, P. GARCIA, G. CARLOT, AND B. PASQUET, *Thermal diffusion of iodine in* UO_2 *and* UO_{2+x}, J. Nucl. Mater., 372 (2008), pp. 405 – 415.

[166] J. SCHOENES, *Optical properties and electronic structure of* UO_2, J. Appl. Phys., 49 (1978), pp. 1463 – 1465.

[167] M. SCHROEDER, J. H. LEE, AND M. MARTIN, *Influence of impurity and dopant ions on the electrotransport properties in oxides*, Solid State Ionics, 101 - 103 (1997), pp. 403 – 409.

[168] H. SOLMON, *Autodiffusion de l'oxygène, du zirconium et de l'yttrium dans la zircone cubique stabilisée par l'yttrium*, PhD thesis, Université de Paris 6, 1992.

[169] W. H. STEVENS, J. R. MACEWANS, AND A. M. ROSS, *The diffusion behaviour of fission xenon in uranium dioxide*, US Report, 7610 (1960), pp. 7 – 22.

[170] A. M. STONEHAM, *Ionic solids at high temperature*, World scientific Publishing, 1989.

[171] R. J. TARENTO, *Influence of evaporation and exchange reactions at the surface on the evolution of an arbitrary tracer distribution by diffusion*, Rev. Phys. Appl., 24 (1989), pp. 11 – 16.

[172] S. R. TEIXEIRA AND K. IMAKUMA, *High temperature X-ray diffraction study of the U_4O_9 formation on UO_2 sintered plates*, J. Nucl. Mater., 178 (1991), pp. 33 – 39.

[173] M. TETEMBAUM AND P. D. HUNT, *High-temperature thermodynamic properties of oxygen-deficient urania*, J. Chem. Phys., 49 (1968), pp. 4739 – 4744.

[174] R. TETOT AND P. GERDANIAN, *Thermodynamic test of defect formation energies calculated by simulation techniques for non-stoichiometric oxides. application to $Ce_{2\text{-}x}O$, $UO_{2\pm x}$, $Ti_{2\text{-}x}O$, $Mn_{1\text{-}x}O$, $Fe_{1\text{-}x}O$*, J. Phys. Chem. Solids, 46 (1985), pp. 1131 – 1139.

[175] J. TÖPFER, L. LIU, AND R. DIECKMANN, *Deviation from stoichiometry and point defects in $(Zn_xMn_{1\text{-}x}Fe_2)_{1\text{-}\delta/3}O_4$*, Solid State Ionics, 159 (2003), pp. 397 – 404.

[176] E. VATHONNE AND M. FREYSS, *Personal communication*, 2012.

[177] E.-L. VEZITEU, *Etude des propriétés de transport de $UO_{2\pm x}$ dopé Gd*, Mastère franco-roumain "Science et Technologie des Matériaux, CNRS UMR 8580 - Laboratoire SPMS, 2006.

[178] C. VIAUD, L. DESGRANGES, C. VALOT, G. ROUSSEAU, AND P. TAYLOR, *Etude des phases cristallines créées lors de l'oxydation de pastilles d'UO_2 vierges en condition d'entreposage par l'analyse Rietveld de diffractogrammes de DRX*, Note Technique CEA SA3C-L2EC 2008-003.

[179] H. Werner, *Quantitative analysis of films by ion microbeam methods. II:SIMS*, Mikrochim. Acta, 114/115 (1994), pp. 107 – 127.

[180] S. Whillock and J. H. Pearce, *A method of determining the distribution of U_4O_9 in oxidised UO_2*, J. Nucl. Mater., 175 (1990), pp. 121 – 128.

[181] B. T. M. Willis, *Neutron diffraction studies of the actinides oxides. I. Uranium dioxide and thorium dioxide at room temperature*, Proc. R. Soc. London, Ser. A, 274 (1963), pp. 122 – 133.

[182] ——, *The defect structure of hyper-stoichiometric uranium dioxide*, Acta Crystallogr., Sect. A: Found. Crystallogr., 34 (1978), pp. 88 – 90.

[183] ——, *Crystallographic studies of anion-excess uranium oxides*, J. Chem. Soc., Faraday Trans., 83 (1987), pp. 1073 – 1081.

[184] P. W. Winter, *The electronic transport properties of UO_2*, J. Nucl. Mater., 161 (1989), pp. 38 – 43.

[185] Z. Y. Wu, F. Jollet, S. Gota, N. Thropmat, M. Gautier-Soyer, and T. Petit, *X-ray absorption at oxygen K edge in cubic f oxides examined using a full multiple-scattering approach*, J. Phys.: Condens. Matter, 11 (1999), pp. 7185 – 7194.

[186] E. Yakub, C. Ronchi, and I. Iosilevski, *Thermodynamic model of solid non-stoichiometric uranium dioxide*, J. Phys.: Condens. Matter, 18 (2006), pp. 1227 – 1248.

[187] S. W. Yu, J. Tobin, J. C. Crowhurst, S. Sharma, J. K. Dewhurst, P. O. Velasco, W. L. Yang, and W. J. Siekhaus, *f-f origin of the insulating state in uranium dioxide: X-ray absorption experiments and first-principles calculations*, Phys. Rev. B, 83 (2011), p. 165102.

List of Figures

List of Tables

Appendix A

Theoretical determination of the oxygen potential imposed with an humidified mixture of Ar and H_2

This appendix aims to determine the theoretical oxygen partial pressure of the atmosphere imposed during UO_2 specimen annealing.

In the device conceived for oxygen diffusion (see §2.2.1), the oxygen partial pressure imposed to a sample (maintained at the temperature *T*) is controlled by the water dissociation reaction:

$$H_2 + \frac{1}{2}O_2 \rightleftharpoons H_2O \tag{A.1}$$

The equilibrium constant K_{eq} of this chemical reaction is defined as follows:

$$K_{eq} = \frac{[H_2O]}{[H_2]\,[O_2]^{1/2}} \tag{A.2}$$

From Equation (A.2), oxygen partial pressure can be written as following:

$$p_{O_2} = \left(\frac{p_{H_2O}}{p_{H_2} \cdot K_{eq}\,(T)}\right)^2 \tag{A.3}$$

Here, the reaction constant K_{eq} figures as a function of temperature. In fact, Kubachewscki [116] found the relationship governing the Gibbs free energy of the water dissociation reaction as a function of the temperature at which the reaction is produced:

$$\Delta G\,(T)\,[cal] = -RT\ln\left(K\,(T)\right) = -58900 + 13.1 \cdot T\,[K] \tag{A.4}$$

The dissociation reaction A.1 is activated inserting in a gas mixture controlled quantites of hydrogen and water vapour. Hydrogen presence is guaranteed because of gas mixture composition: Ar (inert) and H_2 (reductor). Our oxygen diffusion device in fact has two types of bottles available: Argon and Ar/10%H_2. Such gases are mixed together through fluxmeters to obtain the desired composition of the gas to send in the furnace. Therefore, it's possible to rely the hydrogen partial pressure (hereafter, p_{H_2}) of the gas mixture to the fluxes of Ar and Ar/10%H_2 through the following expression:

$$\frac{p_{H_2}}{p_{Ar}+p_{H_2}} = \frac{0.1 \cdot \dot{V}_{Ar/10\%H_2}}{\dot{V}_{Ar}+\dot{V}_{Ar/10\%H_2}} \equiv \frac{1}{r} \tag{A.5}$$

where$\dot{V}_{Ar/10\%H_2}$ and $\dot{V}_{Ar}$ are respectively the fluxes of Ar/10%H_2 and Ar regulated by the fluxmeters, while p_{Ar} and p_{H_2} the argon and hydrogen partial pressures.

Water vapour molecules are assured by the constant circulation of the gas mixture in a bubbler, filled with water and maintained at the temperature of 5°C (hereafter T_{th}); this imposes water vapour partial pressure to correspond to the water vapour partial pressure of saturation at T_{th}:

$$\ln\left(p_{H_2O}\right) = -\frac{6640.2}{T_{th}} - 4.517 \cdot \ln\left(T_{th}\right) + 44.55 \tag{A.6}$$

Assuming that the oxygen partial pressure of the gas mixture is negligible compared to the ones of argon, hydrogen and water vapour[1], we can write:

$$p_{Ar} + p_{H_2} + p_{H_2O} \approx 1 \tag{A.7}$$

Coupling together equations A.5 and A.7, p_{H_2} is found to be:

$$p_{H_2} = \frac{1}{r} \cdot \left(p_{Ar} + p_{H_2}\right) = \frac{1}{r} \cdot \left(1 - p_{H_2O}\right) \tag{A.8}$$

From equation A.8, the ratio between p_{H_2O} and p_{H_2} appearing in equation A.3 can be expressed as follows:

$$\frac{p_{H_2O}}{p_{H_2}} = r \cdot \frac{p_{H_2O}}{1 - p_{H_2O}} \tag{A.9}$$

---

[1] For oxygen partial pressures of about 10^{-4} atm, the term p_{O_2} can be nomore neglected and equation A.7 must be written as follows:

$$p_{Ar} + p_{H_2} + p_{H_2O} + p_{O_2} = 1$$

Combining together equations A.3 and A.9, oxygen partial pressure results:

$$p_{O_2} = r^2 \cdot \left(\frac{p_{H_2O}}{\left(1 - p_{H_2O}\right) K_{eq}\left(T\right)} \right)^2 \tag{A.10}$$

For given temperatures of the furnace (T) and of the bubbler (T_{th}), Equation A.10 shows that the oxygen partial pressure imposed to the sample depends upon r^2 (*i.e.* the composition of the gas mixture sent in the device).

Appendix B

Solutions of the diffusion equations

This appendix aims to shortly present the mechanisms and the laws that govern atomic diffusion (Fick's equations). Moreover, some analytical solutions to the second Fick law are given: attention will be directed towards the boundary conditions gouverning the exchange reaction between the sample surface and the atmosphere surrounding it.

B.1 The various mechanisms of bulk diffusion and the Fick laws

The phenomenon of diffusion appears with the presence and the migration of defects of different nature inside a material. For example, point defects (such as vacancies or interstitials) give birth to the phenomenon of the lattice diffusion (*i.e.* the bulk or volume diffusion). Three different diffusion mechanisms are generally cited in the books [111, 153]:

- Vacancy mechanism: an atom situated in a normal lattice position can jump in a lattice vacant site, leaving empty its nominal site; note that vacancy movement is opposite to the one of the atom.

- Direct interstitial mechanism: an atom situated in an interstitial site jumps directly to the neighbour one. Note that this kind of migration leads to a strong distortion of the crystal lattice.

- Indirect interstitial (or interstitialcy) mechanism: the interstitial atom pushes away an atom from its regular site taking its place in the lattice; the displaced atom will take the neighbour interstitial position. Depending on the jump direction of this second atom, the jump can be collinear or not-collinear.

Note that jumps made by atoms of the same nature are completely random, independent and uncorrelated. But diffusion phenomenon is commonly studied using isotopes of the diffusing species as tracers of the atomic movement. In vacancy and interstitialcy mechanisms, the use of isotopes leads to consider no more jumps as uncorrelated, as the probability to make the reverse movement is greater than the others. Therefore, a correlation factor has to be introduced. The diffusion coefficient of the tracer can be expressed in the following way:

$$D^* = f \cdot D \tag{B.1}$$

Where D^* is the diffusion coefficient of the tracer, D is the one of the diffusing species under analysis and f is the correlation factor.

In direct analogy with the heat transfer phenomenon, diffusion can be expressed with the following equation (the first Fick law):

$$J = -D \cdot \frac{\partial c\,(x,t)}{\partial x} \tag{B.2}$$

Where J is the flux of the diffusing species, c is its concentration and D is the diffusion coefficient. Equation (B.2) is referred to the simple one-dimensional case.

In a not-stationary diffusion regime, time evolution of the diffusing species concentration can be expressed with a combination of the first Fick law and the mass balance equation, giving birth to the following relationship:

$$\frac{\partial c\,(x,t)}{\partial t} = -\frac{\partial J}{\partial x} = \frac{\partial}{\partial x}\left(D \cdot \frac{\partial c\,(x,t)}{\partial x}\right) \tag{B.3}$$

This equation is universally known as the second Fick law. It can be simplified only if the diffusion coefficient D is not dependent upon position. In this case equation (B.3) can be written in the following way:

$$\frac{\partial c\,(x,t)}{\partial t} = D \cdot \frac{\partial^2 c\,(x,t)}{\partial x^2} \tag{B.4}$$

More generally, if the temperature at which diffusion occurs is sufficiently high, sample presents also the phenomenon of surface evaporation. In case of UO_2, some authors (reviewed in [120]) fixed this threshold temperature in the range 1400-1600°C. Mathematically, this phenomenon is represented by adding to the second member of the equation (B.4) a term proportional to the surface evaporation rate. Equation (B.4) then becomes:

$$\frac{\partial c\,(x,t)}{\partial t} = D \cdot \frac{\partial^2 c\,(x,t)}{\partial x^2} + v\frac{\partial c\,(x,t)}{\partial x} \tag{B.5}$$

Here all the symbols have the same meanings of the ones used in equation (B.4); v expresses the sample evaporation rate.

In case of oxygen, the highest temperature at which anneals are carried out is equal to 1000°C. At this temperature evaporation doesn't occur, so the most suited diffusion equation to simulate oxygen self-diffusion profiles is the equation B.4. Conversely, iodine diffusion is activated at higher temperatures, *i.e.* $T \geq 1300$°C: in this case, the most suited equation to use is B.5.

Both equations (B.4) and B.5 have to be coupled with some initial and boundary conditions to be solved. In particular, these conditions have to represent mathematically what happens in a diffusion experiment. Next subsection presents the diffusion equation solutions that are used during our work.

B.2 Analytical solutions of the Fick equation

B.2.1 Tracer exchange between the sample surface and the atmosphere without sample surface evaporation: case of initial condition equal to a constant

In this case the boundary and the initial conditions to associate to the equation (B.4) are the followings:

$$\begin{cases} \left[\frac{\partial c(x,t)}{\partial x}\right]_{x=0} = \frac{K}{D} \cdot \left(c\left(0,t\right) - c_{gas}\right) \\ c\left(\infty, t\right) = c_0 \\ c\left(x, 0\right) = c_0 \end{cases} \tag{B.6}$$

Here K is the exchange coefficient, c_{gas} is the tracer concentration of the atmosphere surrounding the sample and c_0 is the tracer natural isotopic concentration.

Solution of the diffusion equation (B.4) coupled with the conditions B.6 is provided by Philbert [153]:

$$\frac{c\left(x\right) - c_0}{c_{gas} - c_0} = erfc\left[\frac{x}{\sqrt{4Dt_{diff}}}\right] - \exp\left[\left(\frac{K}{D}\right)x - \left(\frac{K}{D}\right)^2 Dt_{diff}\right] \cdot erfc\left[\frac{x + 2Kt_{diff}}{\sqrt{4Dt_{diff}}}\right] \tag{B.7}$$

where all the symbols have the same meaning of the equations above and t_{diff} is the duration of the tracer diffusion annealing.

B.2.2 Tracer exchange between the sample surface and the atmosphere with and without sample surface evaporation: initial condition equal to a generic function *F*(*x*)

In litterature, the Fick equation B.5 associated to the boundary condition expressing the tracer exchange between the sample surface and a gaseous atmosphere and to the initial condition equal to a generic function is already solved. In fact, Tarento [171] found a solution to the equation B.5 for the following boundary and initial conditions:

$$\begin{cases} \left[\frac{\partial c(x,t)}{\partial x}\right]_{x=0} = \frac{K}{D} \cdot \left(c\left(0,t\right) - c_{gas}\right) \\ c\left(\infty, t\right) = 0 \\ c\left(x, 0\right) = F\left(x\right) \end{cases} \tag{B.8}$$

Here K is the exchange coefficient, c_{gas} is the tracer concentration of the atmosphere surrounding the sample and $F(x)$ is a generic function that expresses the initial tracer concentration profile inside the sample bulk. The following equation reports the found solution to this problem:

$$\begin{aligned} c\left(x,t\right) = & \frac{1}{2}\int_0^\infty \frac{F\left(y\right)}{\sqrt{\pi D t}} \cdot \exp\left[-\frac{\left(y-x-vt\right)^2}{4Dt}\right] dy \\ & + \frac{1}{2}\int_0^\infty \frac{F\left(y\right)}{\sqrt{\pi D t}} \cdot \exp\left[-\frac{\left(y+x+vt\right)^2}{4Dt}\right] \exp\left[\frac{vy}{D}\right] dy \\ & - \left(H + \frac{v}{2D}\right) \int_0^\infty F\left(y\right) \cdot \exp\left[H^2 Dt + H \cdot \left(x+y+vt\right)\right] \exp\left[\frac{vy}{D}\right] \cdot \\ & \qquad \cdot erfc\left[\frac{x+y+vt}{4Dt} + H\sqrt{Dt}\right] dy \\ & + c_{gas} \frac{H}{2\left(H+\frac{v}{D}\right)} \exp\left[-\frac{vx}{D}\right] \cdot erfc\left[\frac{x-vt}{\sqrt{4Dt}}\right] + \frac{1}{2} erfc\left[\frac{x-vt}{\sqrt{4Dt}}\right] \\ & - c_{gas} \frac{H+\frac{v}{2D}}{H+\frac{v}{D}} \exp\left[H^2 Dt + H \cdot \left(x+vt\right)\right] \cdot erfc\left[\frac{x+vt}{4Dt} + H\sqrt{Dt}\right] \end{aligned} \tag{B.9}$$

where H is defined as the ratio between the exchange coefficient K and the diffusion coefficient D.

Equation B.9 leads us to simply deduce the solution of the diffusion equation also for a material that doesn't evaporate during the annealing. In this case we simply impose the evaporation rate v equal to 0:

$$
\begin{aligned}
c\left(x,t\right) = & \frac{1}{2}\int_{0}^{\infty}\frac{F\left(y\right)}{\sqrt{\pi Dt}}\cdot\exp\left[-\frac{\left(y-x\right)^{2}}{4Dt}\right]dy \\
& +\frac{1}{2}\int_{0}^{\infty}\frac{F\left(y\right)}{\sqrt{\pi Dt}}\cdot\exp\left[-\frac{\left(y+x\right)^{2}}{4Dt}\right]dy \\
& -H\int_{0}^{\infty}F\left(y\right)\cdot\exp\left[H^{2}Dt+H\cdot\left(x+y\right)\right]\cdot erfc\left[\frac{x+y}{4Dt}+H\sqrt{Dt}\right]dy \\
& +\frac{1}{2}\left(c_{gas}+1\right)\cdot erfc\left[\frac{x}{\sqrt{4Dt}}\right] \\
& -c_{gas}\exp\left[H^{2}Dt+Hx\right]\cdot erfc\left[\frac{x}{4Dt}+H\sqrt{Dt}\right] \qquad \text{(B.10)}
\end{aligned}
$$

Note that such equation (B.10) constitutes the solution of the Fick law B.4 coupled with the initial and boundary conditions B.8.

Appendix C

Iodine diffusion coefficients in $UO_{2\pm x}$: study of their dependence upon oxygen partial pressure

This thesis is all dedicated to study UO_2 anionic sublattice. In particular, we ascertained how oxidation influences oxygen transport properties and UO_2 electronic structure. Conversely, from a complementary standpoint, this appendix aims to analyse the cationic sublattice through the study of fission product diffusion. Here attention is focused on iodine. After a review of past articles studying diffusion of fission product in general and iodine in particular, the experiments carried out to evaluate iodine diffusion dependence upon the oxygen partial pressure are reported. This study was studied through this methodology: iodine-implanted UO_2 polycrystalline samples were annealed at 1500°C under strictly controlled oxygen partial pressures. Iodine diffusion profiles were then characterized experimentally by SIMS and simulated with the 2nd Fick law to obtain iodine diffusion coefficients. The analysis of iodine diffusion dependence upon oxygen partial pressure aims to shear light upon the nature of the defect that promotes iodine diffusion in $UO_{2\pm x}$.

C.1 Literature review

In Chapter 1- Figure 1.13, we showed that oxygen diffusion is activated at relatively low temperatures (at about 600°C) and allows to study oxygen redistribution in the UO_2 anionic sublattice. On the contrary, the complementary study of the cationic sublattice is based on the study of those ionic species whose diffusion is activated at much higher temperatures (*i.e.* 1300°C). In particular, fission products (such as Xe, Cs and I) moves in UO_2 at temperatures similar to those uranium atoms move. Therefore, these elements can be considered as model systems to study UO_2 cationic sublattice. This paragraph aims to summarize the major results of past studies effectuated on fission product diffusion.

C.1.1 Introduction: fission product and iodine diffusion

Historically, much attention was paid to study the diffusion mechanisms of fission products (*i.e.* rare gases, as xenon and krypton, and volatile species, as iodine) in UO_2. The phenomenon of fission gas release is of fundamental importance to evaluate in-pile performance and ultimate disposal behaviour of the nuclear fuel. In fact, it can induce phenomena like fuel swelling, rod overpressure, gap thermal conductivity lowering and thermal feedback [52, 102].
Three different ways to measure out FP diffusion properties were conceived in the past [42, 120]:

1. Post-irradiation annealing experiments. In this case, UO_2 samples are irradiated at values of temperatures not enough to activate diffusion and then out-of-pile annealed to induce the release of fission product gases produced during irradiation. The amount of gases released during the annealing is measured by a gamma counter.

2. In-pile experiments. UO_2 samples are encapsulated and inserted in an experimental reactor; the capsule atmosphere has to be constantly renewed to control sample composition, while its position in reactor has to be fixed to univocally determine sample irradiation rate. This type of experiment is the most similar to the reactor conditions the nuclear fuel is subjected to. However, the diffusion coefficient is more difficult to ascertain, as phenomena like radioelement production-decay processes have to be taken into account.

3. Ion-implantation. The ion species that have to be studied are inserted inside UO_2 through implantation. Parameters as ion energy and fluence have to be determined to know respectively ion penetration depth and concentration inside the UO_2 lattice. This type of experiments is the most

flexible and allows to study fission gas diffusion through the separate effect method.

Fission gas diffusion coefficient can be estimated by measuring over time the fraction of gas released from the sample during a thermal annealing. In this case, gas release curves are analysed with the Booth model [36], that consider UO_2 as an assembly of spheres that communicate with the surrounding atmosphere through channels of open porosity. This model yields an effective diffusion coefficient, D/a^2, where a is the hypothetical radius of these ideal spheres. The major difficulty of this approach consists in defining a reliable value for a, which Booth defined as follows:

$$a = \frac{3}{S/V} \tag{C.1}$$

Here, S is the total microscopic surface area while V is the volume of the bulk UO_2. According to [93], the most reliable technique to determine precisely diffusion coefficients consists in measuring the gas concentration profile in the UO_2 bulk with the Secondary Ion Mass Spectrometry (SIMS).

Many authors applied these three different methodologies to evaluate FP diffusion in UO_2; although the huge scatter in the collected data, these studies (critically reviewed by Lawrence [120]) clarify what phenomena impact on FP diffusion:

- UO_2 deviation from stoichiometry. The slightest increase of oxygen content in the annealing atmosphere leads to a strong increase of gas release rates. This phenomenon was for the first time observed by Lindner and Matzke (in ref. [120]) in 1959, analysing rare gas release curves of UO_2 powder specimens with different stoichiometries.

- Sample irradiation burn-up (or, in case of ion-implantation technique, by the ion dose). Increase in burn up is associated to a diminution of the gas released fraction. MacEwan and Stevens (in ref. [120]) explained this phenomenon affirming that irradiation-induced defects act as traps for gas atoms, inhibiting their release from the lattice.

- Sample density. The effect of reducing the open porosity of the sample leads to a variation the Booth radius a estimation [169]. In this sense, it's still unclear if it leads also to a variation to the true diffusion coefficient D.

- Rating (*i.e.* fission density) influence. For a rating range comprised between 7 and 30 W/g, ion gas concentration inside the lattice increases with rating with no corresponding increase in its release rate. This effect can be explained with the UO_2 change in microstructure during irradiation (as, for example, creation of traps).
- Surface vaporisation. This phenomenon is strongly dependent upon the annealing temperature. In fact, if temperature is high (*i.e.* superior to 1600°C), sample surface can sublimate. As a consequence, the apparent activation energy value that can be inferred in this case is the sublimation heat of UO_2, equal to 147 kcal/mol. Moreover, the control of sample stoichiometry is made more difficult. So, it is still more difficult to ascertain the contribution of the O/M variation from the contribution of vaporisation in the ion diffusion coefficient estimates.

Among all the atomic species that are produced in a fission event, iodine assumes a role of huge importance in nuclear fuel in-pile performance and out-of-pile behaviour. In pressurized water reactors, iodine is produced from a fission reaction of a ^{235}U nucleus with a yield of roughly 1%. In the event of Pellet-Cladding Interaction (PCI) as a result of a power-transient, iodine can be instrumental in the Stress Corrosion Cracking (SCC) of the Zircaloy sheath [52]. Moreover, under long term storage conditions, iodine can contribute in the event of cladding failure to the instantaneous release fraction (IRF) [102]. Next subsections therefore review more in detail the experimental and theoretical studies conducted in the past to analyse iodine migration in UO_2.

C.1.2 Iodine diffusion experiments

Different kinds of studies were experimentally pursued in the past. Iodine diffusion was primarily analysed as a function of temperature to determine its activation energy in UO_2. Authors tried then to determine if deviation from stoichiometry has an impact on iodine diffusion in UO_2 to try to shear light upon the nature of the UO_2 defect responsible of iodine migration.
All the three methodologies cited in §C.1.1 were used to study iodine diffusion:

1. Prussin *et al.* [157] studied with post-irradiation experiments Cs, I and other FP release in UO_2 polycrystalline samples in a range of temperature

of 1450°C – 1750°C. Their diffusion coefficients were obtained using the Booth model.

2. Friskney and Turnbull [76] conducted a study on iodine diffusion in small and large grained UO_2 with the in-pile experiment method.

3. Hocking *et al.* [93] and M. Saidy *et al.* [165] (together with P. Garcia [77]) used the SIMS technique on ion-implanted samples to determine iodine thermally- and radiation-induced diffusion coefficients in stoichiometric UO_2. To deduce iodine diffusion coefficients, each iodine relative concentration profile of the annealed (or irradiated) samples was simulated with the Fick law. Remark that the iodine initial profile is taken equal to the iodine profile of an as-implanted and not-annealed sample.

Figure C.1 reports in a Arrhenius graph the iodine diffusion coefficients found by all of these authors.

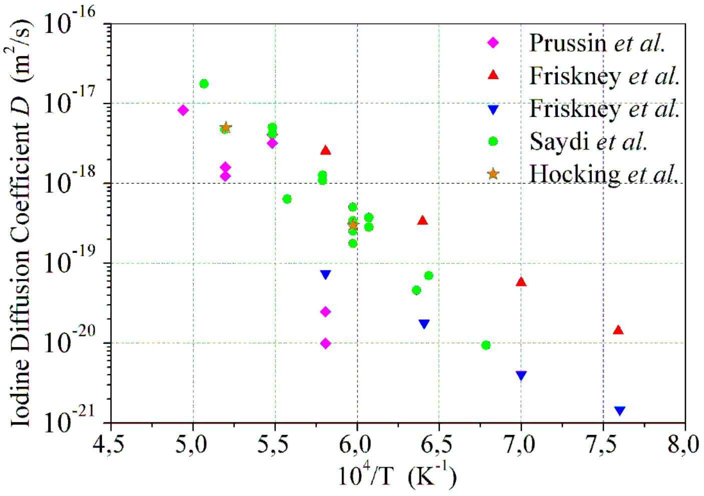

Figure C.1: Arrhenius graph which collects all the literature data [76, 93, 157, 165] referred to iodine thermally activated diffusion coefficients in stoichiometric UO_2. Remark that data collected by Fiskney and Turnbull [76] are indicated with two different colours because they refers to two different sample sets.

As shown in Figure C.1, data acquired with the post-irradiation annealing technique [157] don't really follow an Arrhenius behaviour. In fact, the effective diffusion coefficient estimated with the Booth model decrease from 1550°C to 1650°C. The authors explained this fact as due to the probable negative charge of iodine ions, that leads them to interact with other charged defects created during irradiation. Data acquired with SIMS technique on ion-implanted specimens are instead completely reproducible [93, 165] and follow the Arrhenius relationship here reported [77, 165]:

$$D_I \left(m^2/s\right) = 2.04 \cdot 10^{-8} \cdot \exp\left[-\frac{3.6\ (eV)}{K_B T\ (K)}\right] \tag{C.2}$$

Also the Friskney and Turnbull [76] data are aligned along an Arrhenius trend; however, their estimation of iodine diffusion activation energy is about 1 eV smaller than the one found with the ion-implantation technique [77, 165]. This difference can be ascribed to the technique they used to activate iodine diffusion. In fact, in in-pile experiments sample are exposed not only to high temperatures but also to reactor irradiation. The phenomenon of radiation enhanced diffusion could therefore be activated, modifying the estimation of iodine diffusion coefficients. It seems then that their data cannot be ascribed exclusively to the thermally-induced diffusion. Influence of radiation was reported also by Hocking *et al.* [93]. They stated that irradiation leads to a spreading in the iodine distribution profiles in iodine-implanted samples.

As cited in §C.1.1, not only irradiation but also many other factors can influence FP diffusion in UO_2. Hocking *et al.* [93] demonstrated in fact that the iodine-implantation dose plays an important role in the determination of iodine diffusion coefficients. Above a fluence of 10^{16} atoms/cm^3, iodine trapping is activated and iodine concentration profiles in annealed samples don't show any evidence of bulk diffusive spreading.

M. Saidy *et al.* [165] instead attempted to evaluate if iodine migration is affected by UO_2 deviation from stoichiometry. In a $UO_{2.02}$ sample, iodine diffusion coefficient turns out to be two orders-of-magnitude higher than the value estimated for a stoichiometric specimen. They ascribed this strong difference as due to the presence, inside the hyper-stoichiometric sample, of a higher uranium vacancy concentration that will favour iodine migration.

The reproducible data of Hocking *et al.* [93] and of M. Saidy *et al.* [165] confirms that the ion-implantation is the most reliable technique to clarify the iodine diffusion dependences upon temperature and UO_2 composition. However, more experimental studies have to be yielded to shear light upon the nature of the defect that is responsible for iodine migration inside the UO_2 lattice. Many efforts were done also from a theoretical standpoint to elucidate what UO_2 lattice defect is involved in the incorporation and migration of iodine atoms. The results published in this sense are reviewed in the next subsection.

C.1.3 Iodine incorporation and solution energy estimates by first principle calculations

Literature is full of theoretical study on iodine incorporation and solution in UO_2 [38, 39, 53, 54, 67, 84, 83]. Incorporation energy is defined by theoreticians as the energy needed to insert iodine in a pre-existing trap. Its value can give an indication of what happens in the fuel at low burn-ups, as the FP concentration is still small and traps populations are much higher than at thermal equilibrium. Solution energy is instead related to what happens at thermal equilibrium: its value is defined as the FP incorporation energy plus the apparent formation energies of the trap site. Note that trap formation energy (and consequently the FP solution energy too) is dependent upon deviation from stoichiometry. Next table (C.1) aims to summarize the defects that, from calculations, own the lowest iodine solution energies in case of hypo-, hyper- or exactly stoichiometric material.

The little summary of Table C.1 shows strong discrepancies among the published results. Even the iodine solubility in the UO_2 matrix is not yet completely assessed. While many authors found iodine atoms quite insoluble (see for example [39, 53, 84, 83]), the slightly positive or negative values of [67, 38] may account for an eventual solubility of iodine ions in $UO_{2\pm x}$. Despite this variability, all these studies seem to indicate that solubility of iodine is favoured in case of UO_2 hyper-stoichiometry. Some authors refers also to the charge iodine can assume inside UO_2 and, also in this field, published results disagree: while B. Dorado *et al.* [67] found iodine ions always charged -1, Grimes *et al.* [84, 83] found that the iodine charge state may change with UO_2 stoichiometry, acting as a buffer to the fuel redox potential. Their calculations seem to indicate that iodine is more stable as an anion in hypo- and stoichiometric UO_2, and as cation in case of a hyper-stoichiometric lattice. Very recently, J. P. Crocombette [54] developed *ab-initio* calculation in charged (and not neutral as in all the other studies) supercells to evaluate the interaction between the iodine charge with the charge of the defect iodine is incorporated into. Insertion of an iodine ion inside a defect tends to decrease the total defect charge, in accord with the iodine elevated electronegativity. Moreover, he remarked that to take into account the charge of point defects leads to an appreciable decrease in the iodine incorporation and solution energies.

The only study that reports an estimation of activation energies for iodine diffusion in hypo-, hyper- or exactly stoichiometric UO_2 is the one of Busker *et al.* [39]. They found that activation energy is quite dependent upon the defect

Ref.	***Method***	***UO_{2-x}***		***UO_2***		***UO_{2+x}***	
		Trap site	**E_{sol} (eV)**	***Trap site***	**E_{sol} (eV)**	***Trap site***	**E_{sol} (eV)**
[84]	Mott-Littleton	O di-vacancy	8.92	Schottky, type 1	10.39	U vacancy	2.59
[83]	Mott-Littleton	O di-vacancy	8.05	Schottky, type 1	10.39	U vacancy	2.59
[39]	Mott-Littleton	O vacancy	7.99	U-O divacancy	10.66	U vacancy	2.71
[53]*	LDA+U	U vacancy	11.6	U vacancy	7.7	U vacancy	3.8
[67]	GGA+U			Schottky, type 2	0.5		
[38]	GGA+U	Schottky defect	0.65	Schottky defect	0.65	U-O divacancy	-0.59
[54]‡	GGA+U U ramping	Schottky, type 2 (charged -1 or -2)	decreasing until 2	U-O divacancy (charged -3)	2.97	U-O divacancy (charged -3, -1, -2 or 0)	increasing until 4

* Atom relaxation and clusters not taken into account

‡The defect charges are dependent upon the Fermi energy level. The reported order coincides with a progressive increase of deviation from stoichiometry.

Table C.1: Summary of iodine solution energies referred to the defect that is calculated to be the most probable trap of iodine atoms in UO_2 and $UO_{2\pm x}$.

iodine is trapped and, as a consequence, upon UO_2 deviation from stoichiometry. They estimated it equal to 1 eV, 5.6 eV or 6.3 eV respectively for hypo-, exactly or hyper-stoichiometric UO_2. Remark that their value found for the exact stoichiometry doesn't correspond to the activation energy experimentally assessed [165]. This may be explained saying that they take into account wrong defect migration mechanisms.

As a conclusion, we can say that despite all the studies conducted on unravelling the iodine behaviour in UO_2, until nowadays theoretical approaches lack of a clear picture of iodine incorporation, solubilisation and migration in the UO_2 lattice. Big tendencies however can be deduced by the conducted simulations: for all the values of deviation from stoichiometry uranium dioxide can assume, iodine seems to be insoluble. Moreover, as this ionic species is strongly electronegative, each defect that traps an iodine ion sees its charge modified.

C.2 Iodine diffusion experiences carried out

C.2.1 Sample preparation

To study iodine diffusion in UO_2, we used some undoped polycrystalline samples, the preparation conditions of which were already discussed in Chapter 2 - §2.1. After their preparation, these samples were annealed at 1400°C for 4 hours and then implanted with $^{127}I^{2+}$ ions of 800 keV and with a very low implantation dose ($\sim 10^{11}$ at/cm^2). SRIM software [11] calculated that iodine beam energy of 800 keV leads ions to penetrate in UO_2 at an average depth of 130 nm. The implantation dose used rather corresponds to an iodine concentration in the UO_2 lattice of about 6 10^{15} at/cm^3 (see Figure C.2). Note that such low concentration limits the damage of the UO_2 lattice and reduces the probability for iodine ions to interact and cluster together. Moreover, this low concentration is still sufficient for a reliable SIMS characterisation, since this technique is extremely sensitive to the presence of iodine in UO_2 [93].

C.2.2 Sample anneals

C.2.2.1 Thermal treatment device used to control oxygen partial pressure

The setup in which iodine diffusion experiments are performed is made up of a furnace with two gas inputs: Ar and Ar/5%H_2. The gas flow rates are regulated by ball flowmeters. A fraction of the carrier gas mixture is then diverted

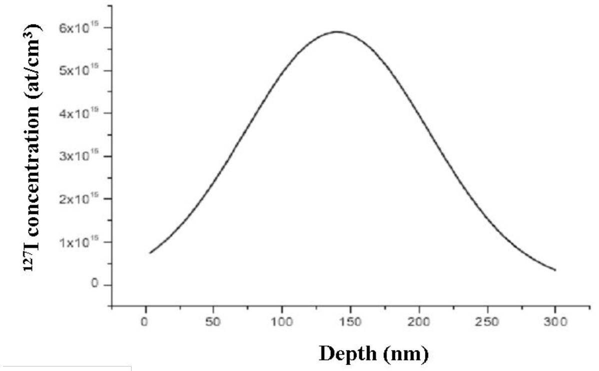

Figure C.2: SRIM simulation corresponding to the implantation of iodine ions of 800 keV at the dose of 10^{11} at/cm² into the UO_2 lattice.

from the main gas stream and sent through a bubbler containing water at constant temperature (20°C). The output gas is then sent back into the main gas stream. Before sending the the furnace input, a part of it is sampled to control its oxygen partial pressure: its dew point temperature is measured with an hygrometer equipped with a mirror system. The water vapour pressure is then determined from the dew point temperature [12] instead of using the same relationship as that used to derive the saturation water vapour pressure in the previous paragraph. The oxygen partial pressure of the gas can be deduced from the thermodynamic equilibrium constant of the reaction corresponding to water vapour formation:

$$pO_2 = \left(\frac{pH_2O}{pH_2 \cdot K\left(T\right)}\right)^2 \tag{C.3}$$

Here pH_2O, pH_2 and pO_2 are the partial pressures of water, hydrogen and oxygen respectively while $K(T)$ is the water formation equilibrium constant at temperature T [116]. The fraction of gas initially diverted from the main gas stream is adjusted in such a way that the final gas flow reaches the desired oxygen potential. The thermal cycle can be started only after having waited long enough for the oxygen partial pressure to stabilise.

This molybdenum furnace is not equipped with a quenching system. To reduce the possibility of any atomic movement during the cooling process, the temperature decreases at the highest possible rate: in this case, 16.6°C/min.

C.2.2.2 Conditions under which sample anneals are carried out

To focalize on iodine diffusion dependence upon oxygen partial pressure, we realized 4 thermal treatments of 2 hours at the fixed temperature of 1500°C. Oxygen partial pressures are controlled by imposing different humidity contents in the gas mixture surrounding the sample during the annealing (see §C.2.2.1). By checking the humidification limits of the available furnace, the imposed 4 oxygen partial pressures are ranging between 10^{-17} and 10^{-12} atm. Table C.2 summarizes the experimental conditions of the anneals.

Employed gas	***Added H_2O* (ppm)**	***Dew point temperature* (°C)**	***Estimated pO_2* (atm)**
H_2	100	-42.5± 0.1	$(9.6\pm0.3)10^{-18}$
H_2	500	-25.6 ± 0.4	$(4.6\pm0.4)10^{-16}$
H_2	3000	-6.5 ± 0.4	$(1.7\pm0.1)10^{-14}$
$Ar/5\%H_2$	1200	-16.2 ± 1	$(1.1\pm0.2)10^{-12}$

Table C.2: Imposed atmosphere, measured dew point temperature and oxygen partial pressure estimates obtained for each annealing carried out.

Remark that, together with the annealed samples, we dispose also of a not-annealed specimen that was implanted at the same time of the others. This sample constitutes the reference useful to determine the iodine concentration profile present in the sample before the annealing. The reference and the four annealed samples were therefore characterized by SIMS and by confocal microscopy to evaluate iodine concentration profiles: the following subsection gives details of this sample characterization.

C.2.3 Determination of iodine spreading induced by sample anneals by SIMS and confocal microscopy

SIMS depth profiling is used to determine diffusion coefficients derived from depth profile modifications due to annealing. *A priori*, a SIMS analysis is only qualitative. However, the analysis of iodine diffusion can be rendered quantitative. This requires having an as-implanted reference sample for which the $\frac{^{127}I}{^{238}U}$ ratio may be used to evaluate an iodine concentration profile (assuming the total number of implanted ions is known)[1].

---

[1] Case of iodine diffusion characterisation treated here is quite different to oxygen diffusion characterisation reported in Chapter 2 and requires a different approach. As regards the implanted iodine (^{127}I) samples, previous works [77, 165] appeared to indicate that ionisation and collection yields of both iodine and uranium species were very much dependent upon experimental conditions and texture. As a result, it is virtually impossible to define a relative sensitivity factor (see equation 2.15). However, normalising the iodine signal to a matrix species does enable sputtering effects to be corrected. Also, we have shown (see [77]) that doing this greatly reduces variations in depth profiles characterised under identical experimental conditions at the surface of implanted samples.

In our experience, primary beam is constituted by a 20 nA current of Cs^+ ions, previously accelerated with a 15 kV high voltage. The sputtered secondary ions are instead negatively charged and extracted from the sample by the extraction voltage of -5 kV. Note that, due to the low iodine concentration studied, all the iodine secondary ions were collected, including those which are less energetic (*i.e.* energy slit - see §2.4.3.1 - was placed in largely opened position). In the depth-profiling mode, while primary beam rasters a sample surface equal to 150x150 μm^2, the secondary ions are collected at the centre of the crater from a circular area of 60 µm of diameter (see again §2.4.3.1). These ions are then counted by the mass spectrometer which SIMS is equipped with. In each sample we made 2 or 3 craters, in order to assure result reproducibility; for each crater we collected the signal of the iodine isotope ^{127}I and of some elements constituting the lattice, such as ^{238}U.

After having analysed the craters with the confocal microscopy (see §2.4.4), SIMS signals can be converted into depth-dependent profiles (see §2.5.1) to be analysed (see the next subsection).

C.2.4 Simulation of depth profiles

Diffusion coefficients are deduced by solving Fick's second law:

$$\frac{\partial c\left(x,t\right)}{\partial t} = D \cdot \frac{\partial^2 c\left(x,t\right)}{\partial x^2} + v \cdot \frac{\partial c\left(x,t\right)}{\partial x} \tag{C.4}$$

The second term of Equation C.4 describes surface evaporation effects that occurs at the high annealing temperatures (T >1400°C) [168, 171] necessary to activate iodine diffusion (see Appendix B). Surface evaporation rate v is considered as a model parameter determined from fitting the model to the experimental data, in much the same way as D is. The boundary and initial conditions used to simulate the diffusion in UO_2 of the pre-implanted iodine ions are:

$$\begin{cases} c\left(0,t\right) = 0 \\ c\left(\infty,t\right) = 0 \\ c\left(x,0\right) = F\left(x\right) \end{cases}$$

Here $F(x)$ is the as-implanted iodine concentration profile. The depth profile in this reference sample was analysed with SIMS just prior to analysing the annealed sample (*i.e.* under identical experimental conditions).

Note that in both the oxygen and the iodine analyses, the physical parameters are fitted to the experimental data by minimizing the following estimator:

$$e = \sqrt{\sum_{i=1}^{n} \left(c_{exp}^{i} - c_{sim}^{i}\right)^2} \tag{C.5}$$

Here n is the number of experimental points, c_{exp}^{i} defines the i^{th} experimental data point and c_{sim}^{i} is the simulated concentration estimate at the same distance from the sample surface.

C.3 Results

Next Figure aims to compare the iodine depth-dependent profiles found for all annealed samples with the reference profile.

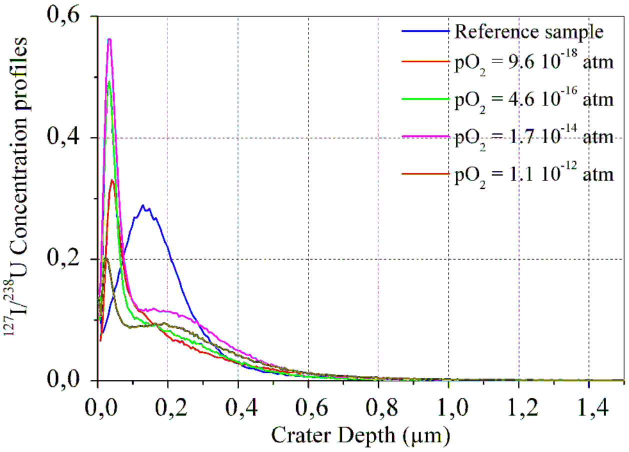

Figure C.3: Iodine diffusion profiles obtained experimentally: comparison of the annealed sample iodine profiles with the one of the reference.

As shown in Figure C.3, the thermal anneals carried out on our samples activated the iodine volume migration in UO_2. Moreover, in this figure we can observe that relative iodine concentration strongly increases just below the sample surface. This peak may be due to a chemical reaction between the implanted iodine ions with the hydrogen of the atmosphere: peak intensities in fact decrease with decreasing hydrogen amounts. Consequently, simulations with the Fick law of these iodine diffusion profiles were pursued starting from a sample depth of about 150 nm, where hydrogen has no-more impact on the experimental curve.

Figure C.4 reports an example of iodine relative concentration profile simulation, together with the profile of the reference sample (taken as initial condition for the Fick law resolution).

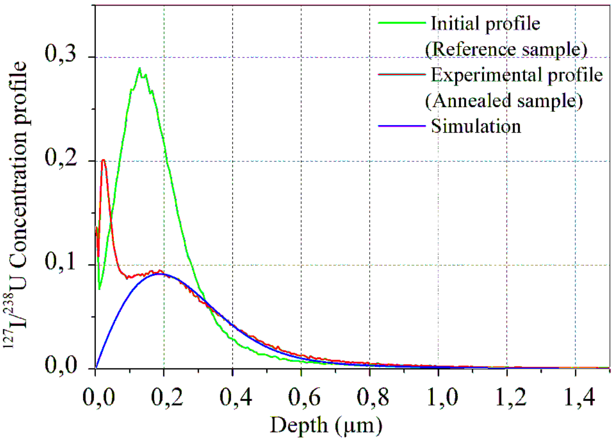

Figure C.4: Simulation of iodine diffusion profiles for the sample annealed at 1.1 10^{-12} atm. Here, the experimental iodine diffusion profile of the annealed samples is plotted in red while its simulations are represented in bleu. Green profile is the iodine concentration profile present inside the sample before the annealing (iodine profile of the reference sample).

Table C.3 reports the iodine diffusion coefficient D and the evaporation rate v of each examined sample, together with their corresponding errors. As previously done with oxygen, both of these estimates were calculated as the average and the standard deviation of all the D and v values obtained analysing all the craters made on a single sample.

Figure C.5 represents these values as a function of pO_2 and reports their comparison with the most recent published results [165]. In this Figure the green point is calculated through the Arrhenius relationship reported in [165] (see Chapter 1 - Equation C.2): for an annealing temperature of 1500°C the iodine diffusion coefficient measured in a stoichiometric UO_2 sample is estimated to be 1.24 10^{-18} m²/s. For aim of completeness we added also the only iodine diffusion coefficient evaluated on a hyper-stoichiometric UO_{2+x} sample (with $x \approx 0.02$), although annealed at 1400°C [165].

***Annealing pO_2* (atm)**	***Diffusion Coeff. D* (m²/s)**	***Evaporation rate v* (m/s)**
$(9.6\pm0.3)10^{-18}$	$(2.65\pm0.07)\ 10^{-18}$	$(2.3\pm0.4)\ 10^{-11}$
$(4.6\pm0.4)10^{-16}$	$(2.1\pm0.3)\ 10^{-18}$	$(1.2\pm0.3)\ 10^{-11}$
$(1.7\pm0.1)10^{-14}$	$(1.6\pm0.4)\ 10^{-18}$	$(2.5\pm3)\ 10^{-12}$
$(1.1\pm0.2)10^{-12}$	$(1.7\pm0.2)\ 10^{-18}$	$(2.5\pm3)\ 10^{-12}$

Table C.3: Evaluation of iodine diffusion coefficients D and of the sample surface evaporation rate v for the four diffusion annealings carried out.

As reported in Table C.3 and shown in Figure C.5, in this range of oxygen

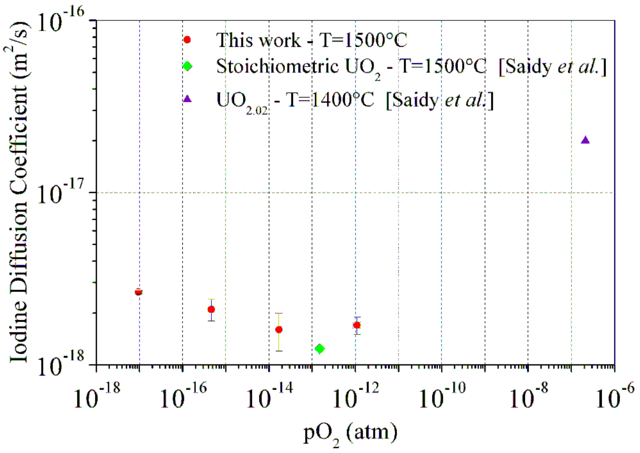

Figure C.5: Iodine diffusion coefficient dependence upon pO_2: comparison with the estimations reported in the published study [165].

potential considered iodine diffusion coefficients do not strongly depend upon the oxygen partial pressure imposed in the anneals.

The next graph in Figure C.6 plots our results together with all the literature data used to evaluate the Arrhenius trend describing iodine diffusion coefficients in UO_2 [165]. There, all our data well align on the Arrhenius relationship traced for UO_2: this demonstrates once again that in the entire pO_2 range probed here our diffusion coefficients are equivalent to the one assumed by iodine diffusing in a stoichiometric material. Analysis of all these data is postponed to the next section to find the mechanism iodine ions use to migrate in the UO_2 lattice.

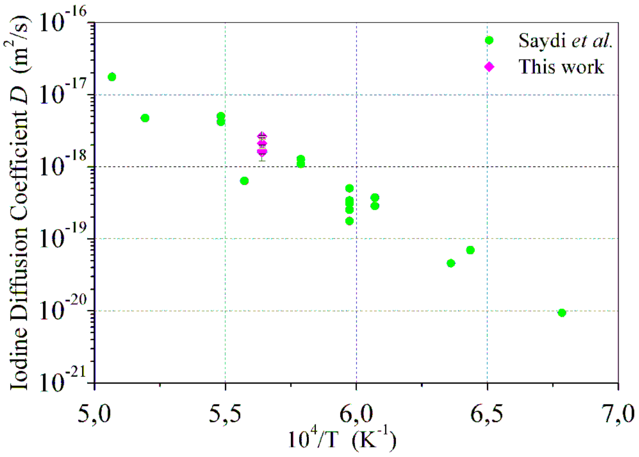

Figure C.6: Insertion of our diffusion coefficients into the Arrhenius graph referred to iodine diffusion in stoichiometric UO_2 [165].

C.4 Discussion

A critical discussion of the obtained results needs firstly to correlate the observed iodine diffusion behaviour to a particular UO_2 deviation from stoichiometry domain (*i.e.* hypo-, near- or hyper-stoichiometry). The oxygen partial pressure imposed during each anneal in fact fixes a particular uranium dioxide composition. For this reason we try to compare our data, spreading over a wide range of oxygen partial pressures, with the experimental iodine diffusion coefficients published by [77, 165] for UO_2 stoichiometric samples. These authors considered a UO_2 sample as stoichiometric when it is annealed under a not-humidified $Ar/5\%H_2$ gas mixture. Because at 1500°C they gave no indication of the oxygen potential reached by this atmosphere, we measured the dew point temperature of a gas with an identical composition to evaluate its corresponding oxygen partial pressure. This measurement enabled us to find a pO_2 value equal to $1.5\ 10^{-13}$ atm. Its comparison to our oxygen partial pressures ranging between 10^{-17} and 10^{-12} atm leads us to consider our UO_2 samples as hypo- or nearly stoichiometric.

In a hypo-stoichiometric lattice, the experimental results previously reported (see section §C.3) give evidence of an iodine diffusion independent upon UO_2 composition. But Figure C.5 shows also that iodine behaves differently in a hyperstoichiometric lattice: UO_2 hyperstoichiometry in fact induces a strong increase of iodine diffusion [165].

This difference clearly indicates that in these two stoichiometry domains iodine diffusion is assisted by defects of different nature. In particular, in hypostoichiometric uranium dioxide the defect assisting iodine migration is present with a concentration independent upon oxygen partial pressure. Supposing that iodine diffusion is assisted by Schottky defects, we can write the following relationship:

$$D_I \propto [Sch]\, D_{sch} \tag{C.6}$$

where D_I is the iodine diffusion coefficient, while $[Sch]$ and D_{Sch} are respectively the concentration and the diffusion coefficient of the Schottky defect. To verify if this hypothesis is consistent with our experimental results, we need to evaluate if its concentration is independent on oxygen potential. As the concentration of a defect generally vary together with its formation rate, we need to analyze the formation reaction of a Schottky defect by evaluating its formation reaction constant K_{Sch} as a function of pO_2. Following [66], K_{Sch} can be written as follows:

$$K_{Sch} = \left[V_o^{\circ\circ}\right]^2 \left[V_U^{''''}\right] \tag{C.7}$$

where $V_O{}^{\circ\circ}$ is a doubly positive charged oxygen vacancy, while $V_U{}''''$ is a four-times negatively charged uranium vacancy. As $[V_O{}^{\circ\circ}]$ is dependent upon $pO_2{}^{1/2}$ [68, 78] and $[V_U{}'''']$ upon $pO_2{}^{-1}$ [66], Equation C.7 demonstrates that K_{Sch} (and consequently the corresponding Schottky defect concentration) doesn't depend upon oxygen potential. Therefore, Equation C.6 enables us to demonstrate that also iodine diffusion coefficients don't depend upon oxygen potential too, if assisted by Schottky defects. This theoretical result full matches with our experimental evidences and allows us to validate our starting hypothesis. Moreover, our analysis is also consistent to the most recent first-principle calculations of Crocombette [54], that indicates the Schottky defects, together with the di-vacancies, as the most probable hosts of iodine in UO_{2-x}.

C.5 Conclusions

This appendix summarizes the major results obtained for iodine diffusion. Iodine-implanted UO_2 samples were annealed at 1500°C under four strictly controlled oxygen partial pressures (comprised between 10^{-17} and 10^{-12} atm) and later on characterised with SIMS to evaluate iodine thermally activated volume diffusion. Iodine diffusion coefficients were then estimated by simulating the experimental profiles with the 2nd Fick law. In the studied pO_2 range, the annealed UO_2 samples were hypo- or nearly stoichiometric and had iodine diffusion coefficients independent upon oxygen potential and comparable with literature results [77, 165]. A theoretical analysis of our experimental data succeeded in demonstrating that, in a hypostoichiometric UO_2 lattice, diffusion of iodine ions can be assisted by Schottky defects. This thesis is consistent also to the most recent *ab-initio* simulations, that indicate the Schottky defects as the traps that incorporate iodine in a hypo-stoichiometric lattice [54]. This analysis, although interesting, should be confirmed by a much more detailed study that would take into account a more extended range of oxygen partial pressures and temperatures. Repeated breakdowns of the ion implanter don't allow us to pursue this aim. Consequently, it can be considered as an outlook of the present work.

Résumé

Parmi les nombreuses phases présentes dans le système binaire U-O, la phase UO_{2+x} s'etend sur une large gamme de températures et de compositions: la phase d'UO_2 donc peut s'éloigner très fortement de la stricte stœchiométrie avant de se transformer en U_4O_9 [92]. Le réseau cristallin de l'UO_2 est capable d'accommoder un grand nombre de défauts sans changer notablement sa structure cristalline à longue distance [85]. L'écart à la stœchiométrie est surtout accommodé par des défauts chargés de type anionique [182]. L'incorporation dans la maille de ces défauts oxygène chargés doit toutefois être compensée par un changement de valence de l'uranium pour pouvoir conserver l'électroneutralité du matériau. Le même type de compensation de charge intervient en présence d'impuretés. En conséquence, le dopage et la simple oxydation du matériau modifient les concentrations en défauts anioniques et donc leurs propriétés de transport atomique. Cette caractéristique est essentielle dans les conditions d'usage du matériau comme combustible nucléaire, combustible le plus exploité dans les réacteurs de puissance actuels (production d'électricité). Chaque variation de composition de cet oxyde influence donc de manière importante son comportement, non seulement pendant son utilisation en réacteur mais aussi en situation d'entreposage. Ainsi, la diffusion de l'oxygène dans l'UO_2 induit des modifications microstructurales importantes. De plus, par des jeux d'équilibres entre populations de défauts sur les deux sous-réseaux, les modifications du sous-réseau anionique sont susceptibles de modifier les concentrations d'équilibres de défauts sur le sous-réseau cationique et donc de contrôler les évolutions microstructurales du matériau y compris sous irradiation. Dans la mesure où les produits de fission sont sensibles au premier ordre à la présence de défauts sur le réseau cationique, les modifications de la nature et de la concentration en défauts oxygène sont susceptibles d'affecter aussi la mobilité des produits de fission dits gazeux ou réputés corrosifs tels le xénon ou l'iode dont le comportement détermine la durée de vie de l'élément combustible lui-même. En conclusion, la maitrise et la prédiction du comportement de l'UO_2 sous irradiation nécessite une profonde compréhension des relations entre microstructure, composition d'une part et transport atomique d'autre part.

Dans la littérature des années 1960-1970, beaucoup d'auteurs ont étudié l'autodiffusion de l'oxygène dans l'UO_2 et dans l'UO_{2+x} mais aucun d'entre eux n'a identifié clairement de mécanisme (barrière de migration et nature du défaut assistant cette diffusion) [30, 50, 142]. La raison principale de cette incertitude réside dans la difficulté qu'il y a à maitriser et mesurer tous les paramètres qui influencent le phénomène de diffusion, c'est-à-dire la pression partielle d'oxygène, la température et la concentration en impuretés du matériau. En contrôlant ces trois paramètres, un mécanisme d'autodiffusion de l'oxygène a pu être récemment proposé. Toutefois, celui-ci n'a pu être validé que dans le domaine d'une faible sur-stœchiométrie (*i.e.* à l'équilibre avec les faibles pressions partielles d'oxygène) [78].

Par le passé, beaucoup d'études ont été menées sur la diffusion des produits de fission. Parmi eux, un des plus importants est l'iode, qui constitue un élément chimique volatile et qui peut provoquer le phénomène de corrosion sous contrainte de la gaine (c'est-à-dire qu'en cas de rampe de puissance, il peut être relâché de la pastille et réagir chimiquement avec la gaine en Zircaloy et ainsi causer sa rupture) [52]. Au niveau expérimental, seule l'énergie d'activation de la diffusion de l'iode a été déterminée et uniquement dans un matériau proche de la stœchiométrie [165] : la littérature manque ainsi d'une étude systématique dédiée à la complète compréhension du type de défaut impliqué dans la migration de l'iode dans l'$UO_{2\pm x}$.

Pour compléter cet état de la connaissance, deux thèmes principaux sont abordés dans ce travail : l'autodiffusion de l'oxygène dans une gamme de pO_2 plus étendue que celle déjà étudiée dans la littérature [68, 78] et la migration de l'iode dans l'UO_2 sous-stœchiométrique. Pour y parvenir, il a été choisi d'étudier respectivement le sous-réseau anionique dans UO_{2+x} et le sous-réseau cationique dans UO_{2-x}. L'approche générale utilisée pour ces deux axes de recherche est celle développée par Dieckmann [64]. Elle s'appuie sur la mise à l'équilibre d'un oxyde à stœchiométrie variable (par exemple, l'UO_{2+x}) dans des atmosphères (potentiels d'oxygène) et à des températures contrôlées. Ainsi, les concentrations en défauts dans le matériau sont fixées par les conditions extérieures et *a priori* reproductibles. Pour avoir une vision générale et complète du système analysé, les échantillons ainsi traités peuvent être étudiés avec plusieurs méthodes expérimentales et les résultats analysés de la manière suivante :

1. la caractérisation structurale directe qui permet de déterminer directement la nature des défauts présents. Un nombre important des résultats est disponible dans la littérature
2. la détermination des propriétés de transport atomique, qui sont influencées par la concentration de chaque défaut. L'étude de la dépendance

des coefficients de diffusion d'une espèce atomique à la température, la pO_2 et la concentration en dopant donne ainsi des informations sur la nature du défaut responsable de sa migration dans la maille cristalline.

3. le travail précédent nécessite une analyse de ces propriétés avec un modèle thermodynamique de défauts qui permet de décrire l'évolution de leur concentration en fonction des conditions thermodynamique considérées (T, pO_2 et concentration en impuretés)

4. la caractérisation de la structure électronique des différents atomes constitutifs du matériau, qui est affectée par la présence de défauts chargés dans la maille

5. le calcul d'énergie de formation et de migration des défauts (par exemple, par DFT) ainsi que du mécanisme de migration.

La majorité de ce travail a été consacrée à l'étude du comportement de l'oxygène qui a fait l'objet des points 2, 3 et 4 ci-dessus.. L'étude relative à la diffusion de l'iode s'est limitée à une caractérisation des propriétés de transport dans un domaine limité.

Sur la base de l'étude bibliographique établie au Chapitre 1, un modèle de défauts ponctuels prenant en compte les défauts de type électronique et anioniques a d'abord été développé (voir Chapitre 3). Ce modèle prend en compte des défauts rapportés dans la littérature : les défauts ponctuels électroniques (trous et électrons) [70, 164], les défauts oxygène (lacunes et interstitiels) [78, 109, 143] et les défauts de type agrégés tels les di-interstitiels proposés par Willis [183]. Sous l'hypothèse d'une mobilité relative des électrons égale à celle de trous, ce modèle reproduit simultanément les données de la littérature relatives à la conductivité électrique [162] et à l'écart à la stœchiométrie [151]. Ce modèle a été validé dans une gamme de températures (entre 700°C et 1400°C) et de pO_2 étendues. Les constantes de réaction de formation de défauts sont les paramètres de ce modèle thermodynamique et leur détermination est optimisée à partir des données de littérature. Les lois d'Arrhenius qui gouvernent ces constantes de réaction permettent ainsi d'estimer les énergies de formation de chaque défaut du modèle ou plus exactement de l'énergie associée à l'équilibre quasi-chimique décrivant le défaut. Il apparaît que les estimations des énergies de formation de la paire électron/trou, de l'interstitiel d'oxygène et du défaut de Willis sont très proches des estimations des mêmes grandeurs physiques calculées à l'aide de méthodes *ab-initio* [18, 65]. Par contre, l'évaluation de l'énergie de formation d'une paire de Frenkel d'oxygène est entachée d'une plus grande incertitude, car peu de données expérimentales sont disponibles dans des conditions thermodynamiques où les lacunes d'oxygène constituent un défaut présent en concentration suffisante.

La deuxième étude rapportée dans ce document concerne la caractérisation expérimentale du sous-réseau anionique dans le système UO_{2+x} dans des gammes de températures et potentiels d'oxygène plus étendues que celles étudiées antérieurement [78] et [68] (Chapitre 4). Deux types d'échantillons ont été considérés : des polycristaux dopés au chrome et d'autres présentant une faible teneur en impuretés (et donc non dopés). Dans un premier temps, ceux-ci ont été recuits sous atmosphères contrôlées (humidifiées avec $H_2{}^{16}O$) pour fixer leur concentration en défauts. La population de défauts électroniques a été caractérisée par conductivité électrique et la densité d'états électroniques a été déterminée par Spectroscopie d'Absorption X (XAS). Dans un deuxième temps ces échantillons ont été recuits dans une atmosphère enrichie en ^{18}O dans les mêmes conditions thermodynamiques que lors de leur mise à l'équilibre et ultérieurement analysés par SIMS et par microscopie confocale. Cela nous a permis de déterminer les profils de concentration isotopique. Ces profils ont finalement été reproduits avec la deuxième loi de Fick et les coefficients d'autodiffusion de l'O ont ainsi été évalués.

Les données de conductivité électrique à 890°C et 990°C ont permis, pour ces deux types d'échantillons, de déterminer la gamme de pO_2 où la concentration en dopants fixe la concentration en trous : ce domaine définit le comportement extrinsèque du matériau. Du fait de la forte teneur en impuretés dans les échantillons dopés au Cr, le domaine extrinsèque s'étend jusqu'à de fortes pO_2 (c'est-à-dire, dans toutes les conditions thermodynamiques analysées dans cette étude). Ainsi, à une température donnée et sur toute la gamme de pression partielle étudiée, la concentration en trous est indépendante de la pression partielle d'oxygène. Par conséquent, la dépendance à la pression partielle d'oxygène du coefficient d'autodiffusion fournit directement des indications relatives à la nature du défaut qui contrôle la migration de l'oxygène. Dans les échantillons non-dopés, il a été montré que le faible niveau d'impuretés limite le domaine extrinsèque à de plus faibles pO_2. Pour les fortes valeurs de pO_2, les défauts anioniques introduisent des trous dont la concentration est du même ordre de grandeur que la concentration en trous présents du fait de la présence des dopants. Leur contribution est donc visible sur les courbes de conductivité électrique. Ainsi pour les fortes valeurs de pO_2, la simulation de l'évolution de la conductivité électrique en fonction du temps à la suite d'une modification de la pression partielle d'oxygène permet l'estimation des coefficients de diffusion chimique dans différentes conditions thermodynamiques et l'évaluation de leur dépendance au potentiel d'oxygène. Il en résulte, en cohérence avec les résultats de la littérature [162], que les coefficients de diffusion chimique diminuent avec l'augmentation du potentiel d'oxygène.

La dépendance des coefficients d'autodiffusion de l'oxygène à la température dans les échantillons dopés Cr a été analysée et une énergie d'activation apparente pour l'autodiffusion de l'O a été évaluée à 3 eV, comparable aux valeurs estimées antérieurement [68].

Les spectres d'absorption X ont été acquis et interprétés au seuil K de l'oxygène (532 eV) et aux seuils $N_{4,5}$ (778.3 et 736.2 eV) et $N_{6,7}$ (388.2 et 377.4 eV) de l'uranium (voir Chapitre 5). Tout d'abord, ces spectres ont été collectés sur trois phases de référence, l'une étant de l'UO_2 et les deux autres élaborées par oxydation ménagée afin d'obtenir U_4O_9 et U_3O_7. Les densités d'états ainsi obtenues sont en très bon accord avec celles calculées récemment par *ab-initio* (théorie de la fonctionnelle de densité) [176]. L'hybridation des orbitales 2p de l'oxygène avec les orbitales 5f et 6d de l'uranium de même que la diminution de l'énergie de Fermi induite par le processus d'oxydation ont pu être ainsi confirmées expérimentalement. On observe aussi la perte de symétrie liée au passage d'une structure cubique à une structure tétragonale. Ainsi la levée de dégénérescence des orbitales 6d de l'uranium en niveaux e_g/t_{2g} induite par le champ cristallin et liée à la symétrie cubique des phases UO_2 et U_4O_9 est clairement observée dans les spectres collectés sur ces deux phases. Ce dédoublement disparaît dans le spectre collecté sur U_3O_7 et s'explique par la perte de symétrie liée à la structure tétragonale de cette phase. De plus, nous avons démontré que les spectres au seuil K de l'oxygène des échantillons de stœchiométrie intermédiaire sont reproduits par combinaison linéaire des spectres d'UO_2 et d'U_3O_7. Ceci permet de montrer que l'augmentation du rapport O/U n'implique pas une variation du type du défaut, mais seulement une augmentation de la concentration du même défaut dans la gamme de composition qui va de UO_2 à U_3O_7. Ceci est en accord avec les résultats de diffraction neutronique [61] selon lesquels le défaut oxygène présent dans les deux phases pures U_4O_9 et U_3O_7 est le cuboctaèdre. Les oxydes intermédiaires peuvent donc être décrits par l'accumulation de ce défaut dans la structure fluorine. Cette méthodologie a été appliquée aux spectres collectés sur des échantillons d'UO_2 sur-stœchiométriques provenant des deux lots étudiés en diffusion. L'évolution des spectres à mesure qu'augmente la pression partielle d'oxygène à laquelle les échantillons sont mis à l'équilibre ne suit pas l'évolution monotone attendue. Ceci a été interprété comme étant lié aux propriétés de volume (diffusion chimique même à température ambiante) et de surface (réactivité de la surface d'autant plus forte que le matériau est exposé à une atmosphère humidifiée).

Dans la dernière partie de ce travail une synthèse de l'ensemble des résultats est proposée (Chapitre 6). Le modèle de défauts ponctuels développé à partir de données de la littérature est appliqué aux mesures de conductivité électrique réalisées dans ce travail (sur des échantillons dopés Cr et non dopés). Le défaut majoritaire pour chaque température considérée et gamme de potentiel d'oxygène a été déterminé et sa concentration estimée. Dans une gamme de pO_2 où les interstitiels d'O prédominent, une expression pour le coefficient de diffusion du défaut oxygène interstitiel est proposé, son énergie de migration étant estimée à 1±0.4 eV. Ce coefficient de diffusion est obtenu à partir du coefficient d'auto-diffusion de l'oxygène et de la concentration en défauts calculées avec le modèle. De plus, dans le domaine de défauts isolés (aux basses pO_2), et exclusivement pour les échantillons d'UO_2 contenant du chrome, nous mettons en évidence à 800°C une contribution des lacunes d'oxygène à l'auto-diffusion.

Aux plus fortes $pO_{2,}$ nous montrons qu'à partir d'une valeur critique du potentiel d'oxygène, les coefficients d'autodiffusion diminuent fortement. La valeur mesurée de ce seuil de pO_2 est comparable à la pO_2 de transition entre défauts isolés et agrégés, prédite par le modèle. Ainsi, notre interprétation de la baisse du coefficient d'autodiffusion de l'oxygène à fortes pO_2 est liée à la formation de défauts oxygène complexes. Il est intéressant de noter que cette valeur de seuil en pO_2 délimite également deux types d'évolution des spectres d'absorption mais aussi des coefficients de diffusion chimique mesurés UO_{2+x}. L'ensemble des différentes caractérisations est donc cohérente. La comparaison de nos données d'autodiffusion avec celles déjà publiées [30, 50, 68, 78, 142] a montré que dans certains cas des écarts existaient. Cette différence est attribuée à une la sensibilité de la méthode utilisée pour l'estimation de coefficients d'autodiffusion, à la préparation et au conditionnement des échantillons (polissage, recuit et trempe) : seuls les échantillons polis avec des suspensions de granulométrie très fine (50 nm) donnent des résultats fiables et reproductibles.

Une deuxième partie de ce travail, moins aboutie, est néanmoins présentée en Annexe C. Une étude du sous-réseau cationique a été effectuée au travers de l'analyse de la diffusion de l'iode dans l'$UO_{2\pm x}$. Cette étude a porté sur l'évaluation de la dépendance du coefficient de diffusion en volume de l'iode à la pression partielle d'oxygène, à une unique température (1500°C). Dans la gamme de pO_2 visée, le dioxyde d'uranium est sous- ou proche de la stœchiométrie : dans ce domaine de composition, les coefficients de diffusion estimés ne dépendent pas du potentiel d'oxygène. Cette évolution, en cohérence avec les résultats *ab-initio* les plus récents [54], suggère que la migration de l'iode dans l'UO_{2-x} est assistée par le défaut de Schottky, puisque la concentration de ce type de défaut n'est pas dépendante à la pression partielle d'oxygène.

En conclusion, en associant à l'étude des propriétés de transport électrique et atomiques des méthodes de modélisation à plusieurs échelles (dont les méthodes aux échelles atomiques comme la DFT), il est possible de déterminer les caractéristiques essentielles des défauts du matériau. Ces défauts qui sont à l'origine de la mobilité des atomes dans $UO_{2\pm x}$. Les méthodes que nous avons mises en œuvre sont parfaitement adaptées à l'ensemble des oxydes à base d'actinides. Pour ce qui concerne le matériau étudié ici, plusieurs perspectives émergent:

- l'étude de la conductivité électrique de l'UO_2 dopé avec un cation pentavalent (comme, par exemple, le niobium), pour exacerber la contribution des électrons à la conductivité et l'éventuelle détermination expérimentale de leur mobilité

- l'étude systématique de l'autodiffusion de l'oxygène dans l'UO_2 sous-stœchiométrique, pour mieux caractériser la nature et la charge des lacunes d'oxygène

- l'étude systématique de la dépendance à la température et au potentiel d'oxygène, des coefficients d'autodiffusion de l'uranium et de différents produits de fission, pour définir leurs mécanismes de migration

- l'évaluation des phénomènes de diffusion induite et/ou accrue par l'irradiation, pour mieux comprendre et prévoir le comportement du dioxyde d'uranium pendant son utilisation en réacteur.